

Department of material science

PhD program MATERIALS SCIENCE AND NANOTECHNOLOGY Cycle XXIX

Curriculum in Nanoscience - 79R - 3

DEVELOPMENT OF PLGA HYBRID NPs FOR BIOMEDICAL APPLICATIONS

Surname: Collico Name: Veronica

Registration Number: 787802

Tutor: Prof. Davide Prosperi

Co-tutor: Asst. Prof. Miriam Colombo

Coordinator: Prof. Gian Paolo Brivio

ACADEMIC YEAR 2015/2016

General Index

Abstract	2
List of Abbreviations	3
Chapter I: Nanomedicine and its challenges	6
Chapter II: PLGA-MnO composite nanomaterials for targeted imaging of Crohn's disease	34
Chapter III: General Methods: Gold Nanoparticles Developing of glycolic acid) Chapter III Phase Transfer to Organic Solvent and Developing of Metal Core Poly(lactic-co-glycolic acid) Nanoparticles	131
List of Publications	132

Abstract

Biodegradable polymers are very promising materials for biomedical and pharmaceutical applications thanks to their safe use in human being, tunable biodegradability, desirable mechanical properties and extensive investigation in medical areas. Above all, poly(lactide-*co*-glycolide) (PLGA) polymer has received a considerable attention as excipient in pharmaceutical industry up to be approved by Food and Drug Administration (FDA) and European Medicine Agency (EMA). The main features of PLGA have been discussed in chapter I.

The headline of this work is the application of poly(lactide-*co*-glycolide) polymer as nano-container for metal nanoparticles: inorganic-based NPs (PLGA@metal NPs) entrapped into PLGA nano-containers join the fascinating properties of the metallic nanomaterials with the extreme biocompatibility of the polymer, to make inorganic particles very attractive tools for future biomedical applications.

The thesis focuses on two main tasks: to prepare PLGA@MnO nanocomposite for targeted imaging of Crohn's disease, and to set up and generalize the gold NPs phase transfer procedure and the PLGA@metal NPs synthetic protocol.

The chapter II concerns the development of a manganese-based contrast agent (CA) for MRI application *in vivo* to achieve a highly accurate diagnosis of the stadiation and follow-up of the disease. In this respect, nanomedicine offers a unique opportunity to design novel smart enhancers by combining the safety of PLGA polymer and the paramagnetic behavior of manganese, to generate PLGA@MnO nanocomposites as promising T₁-positive contrast agent for MRI. PLGA@MnO NPs are safe for Hela and SVEC-4-10 cell lines and thus they are more attractive contrast agents compared with gadolinium and Teslascan which are more toxic. In addition, promising results of biofunctionalized MnO NPs for the active targeting of Crohn's disease, have also suggested to conjugate PLGA@MnO NPs with anti-MAcCAM-1 to target mucosal vascular addressin cell adhesion molecule 1 overexpressed in inflamed bowel sites to enhance further the spatial resolution of MR images and providing an early stage diagnosis, with negligible side effect *in vivo*.

In sight of the encapsulation of manganese-based particles, a general method to entrap inorganic nanoparticles in the poly(lactic-*co*-glycolic acid) polymeric matrix was investigated further through

chapter III. The method here discussed has been set up in collaboration with the Luis Liz-Marzan's group at CICBiomaGune, Spain.

The PLGA polymer has been exploited to trap metal NPs of different nature to make them safe for the human organism and at the same time it maintains their fascinating chemical-physical properties. PLGA NPs loading gold nanoparticles (spheres, rods and cages), iron oxide and quantum dots have been synthesized by single emulsion method and characterized by Dynamic Light scattering and Transmission Electron Microscopy.

The efficient encapsulation has been obtained by highly concentrated and stable metal NPs in organic solvent. On this purpose, two different approaches, the biphasic and the monophasic one, have been explored to transfer gold nanoparticles to organic solvent (iron and manganese-based NPs already meet these conditions). Both the procedures have been adaptable to any size and shapes of gold NPs.

These general approaches are attractive strategies toward the fabrication of heterogeneous nanostructures based on inorganic platforms and functional cargo molecules (e.g. drugs, vaccines, nucleic acids, quantum dots, magnetic nanoparticles) located within the hydrophobic spacer. The hybrid particles join the advantages of the biodegradability and the high biocompatibility of PLGA polymer with the unique properties of inorganic nanoparticles, to obtain potential systems for numerous biomedical applications. PLGA loading plasmonic gold particles could be employed for photothermal therapy and diagnosis; iron oxide particles entrapped in the polymer NPs could act as hyperthermic therapeutic agent or MR contrast agent; manganese oxide nanoparticle-loaded PLGA NPs have been demonstrated to be a high performing CA.

Future attempts will be focused on the application of PLGA@inorganic NPs and their functionalizing particles with targeting moieties to enhance even their efficacy as theranostic agents.

List of Abbreviations

API	Active pharmaceutical ingredients
AR	Aspect ratio
AuNP	Gold nanoparticle
Bp	Boiling point
CA	Contrast agent
CD	Crohn's disease
CE	Capsule endoscopy
CEA	Anti-carcinoembryonic antigen
CT	computed tomography
CTAB	Cetyl trimethylammonium bromide
DCM	Dichloromethane
DD	Drug delivery
DDS	Drug Delivery System
DDT	Dodecanethiol
DMAB	Didodecyl dimethyl ammonium bromide
DMF	Dimethylsuloxide
DNA	Deoxyribonucleic acid
DTPA	Diethylenetriamine pentaacetic acid
EGD	Upper endoscopy
EIM	Extraintestinal manifestation
EMA	European Medicines Agency
EPR	Permeabilità and retention effect
ERS	Erythrocyte sedimentation rate
EtAc	Ethylacetate
EUS	Endoscopy ultrasound
FDA	Food and Drug Administration
FID	Free induction decay
GNP	Spherical gold nanoparticle
GNR	Gold nanorod
H _c	Coercive Field
IBD	Inflammatory bowel diseases
IFN	Interferon

IL	Interleukin
IONP	iron oxide nanoparticle
IR	Infrared
M	Net magnetization
MAdCAM-1	mucosal vascular addressin cell adhesion molecule 1
MC	Methylcellulose
MEMRI	Manganese-enhanced magnetic resonance imaging
MnO NP	Manganese oxide nanoparticle
MNP	Magnetic nanoparticle
MPIO	Micrometric paramagnetic iron oxide
MPS	Mononuclear phagocyte system
MRI	magnetic resonance imaging
mRNA	Messenger ribonucleic acid
M _s	Saturation Magnetization
MUA	Mercaptoundecanoic acid
NMR	Nuclear magnetic resonance
NP	Nanoparticle
NSF	Nephrogenic systemic fibrosis
NV	Nanovectors
OA	Oleic acid
PCL	Poly(ϵ -caprolactone)
PEG	Polyethylene glycol
PEG-SH	thiol terminated Polyethylene glycol
PET	Position emission tomography
PGA	Poly(glycolic acid)
PLA	Poly(lactic acid)
PLA-SH	thiol-terminated poly(lactic) acid
PLGA	poly(lactic-co-glycolic acid)
PLGA-SH	thiol-terminated poly(lactic-co-glycolic acid)
PMA	Poly(isobutylene-alt-maleic) anhydride
PVA	Polyvinyl alcohol
RES	Reticuloendothelial system
RF	Radio frequency
RT	Room temperature

PPT	Photothermal therapy
rRNA	Ribosomal ribonucleic acid
rSP	Superparamagnetic radius
SBE	Small bowel enteroclysis
SBFT	Small bowel follow through
SDS	Sodium dodecyl sulfate
SE	Spin echo
SERS	Surface enhanced Raman scattering
SPIO	Superparamagnetic iron oxide
SPR	Surface plasmon resonance
TACE	TNF- α converting enzyme
TE	Echo time
Tg	Transition temperature
Th1	T-helper type 1
THF	Tetrahydrofurane
TNF	Tumor necrosis factor
UA	undecanoic alcohol
UC	Ulcerative colitis
US	Ultrasound
USPIO	Ultrasmall superparamagnetic iron oxide
WBC	White blood cell

Chapter I

Nanomedicine and its challenges

Index

1. Introduction to Nanotechnology	8
1.1. Nanomedicine	8
1.2. Nanoparticles for Biomedical Applications	10
1.2.1. Poly(lactic-co-glycolic acid) polymer	11
1.2.2. Physicochemical Properties	12
1.2.3. Poly(lactic-co-glycolic acid) Nanoparticles Preparation Techniques	13
1.2.4. Degradation of poly (lactic-co-glycolic acid) nanoparticles	15
1.3. Release Kinetic Profile	17
1.4. Biomedical Application of Poly(lactide-co-glycolide) Nanoparticles	18
1.5. Nanoparticle Functionalization for Biomedical Applications	24
List of Figures, Graphs and Tables	26
References	28

1. Introduction to Nanotechnology

Nanotechnology is defined as the intentional design, characterization, production, and application of materials, structures, devices and systems by controlling their size and shape at the nanoscale (from 1 to 100 nm) (Fig. 1.1).

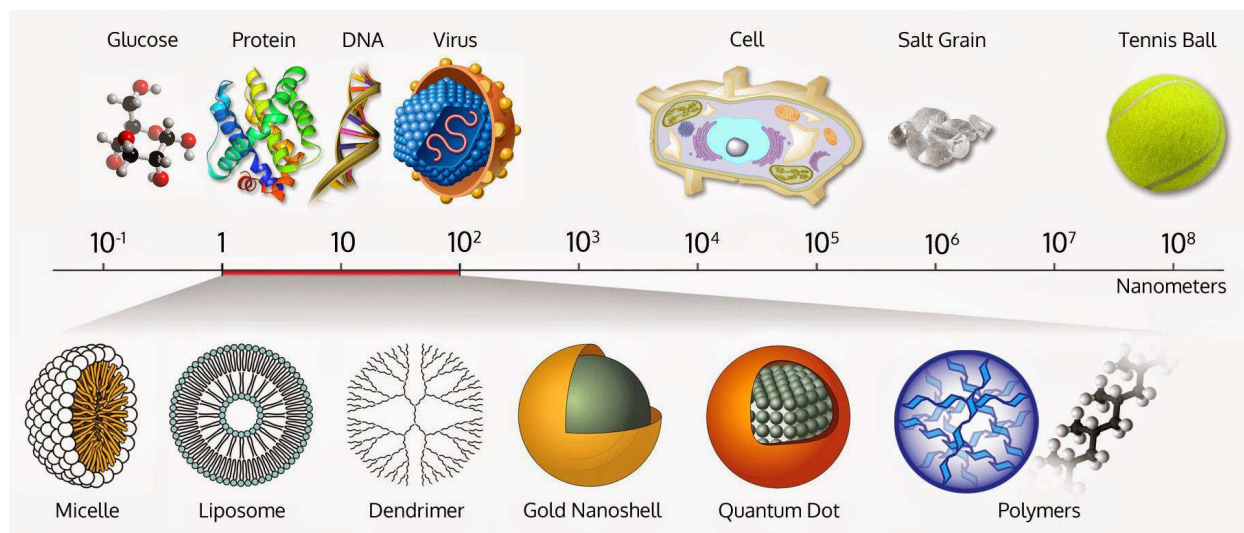


Figure 1.1. Nanometer scale with examples of natural elements.

At the nanoscale dimension, the matter shows different and unexpected properties that allow to overcome the frontiers of scientific disciplines and techniques. Nanomaterials possess several unique properties not found in the bulk counterparts, such as high surface-to-volume ratio, tailorable physical and chemical properties, high surface energy, peculiar mechanical, thermal, electrical, optical behaviors etc.. In addition, nanomatter can be manipulated without modifying its chemical composition. This aspect is of primary importance as the properties of nanomaterials are strongly dependent on their shape and dimensions. All these features allow the use of nanomaterials in a wide range of fields, including electronics, renewable energies, textiles, food industry, healthcare and medicine.¹

1.1. Nanomedicine

In last decades, nanotechnology has gained an even more dominant role in biomedical research and clinical applications. The unique physical-chemical properties of nanomaterials are exploited

for in medical research as well as in clinical practice, for both diagnosis and treatment of several diseases.

Their similarity with the dimensions of biological system is the focal point of the wide application of nanomaterials to the medical field. Biomolecules are considered the natural model to which nanotechnology is inspired, thanks to their attractive extremely definite morphology, with complex and specific functions. Nanobiotechnology indeed is the field that combines the efficacy of biological materials with the laws and tools of life-science, like physics, chemistry and genetics, to fabricate minute synthetic structures.

Within the nanotechnological field, nanomedicine emerged as the study and application of nanoparticles in medicine. It seeks to address various medical challenges and shortcomings faced by conventional medicine, such as poor bioavailability, impaired target specificity, systemic and organ toxicity. In the last decades, many nano-products have been developed and are currently undergoing clinical trials or have been approved by the Food and Drug Administration (FDA) and the European Medicines Agency (EMA) for use in humans, and others are in the proof-of-concept stage in research laboratories (Fig. 1.2 B).

The model which better summarizes the principal aim of biotechnology and nanomedicine points to three main goals: *find* (contrasting agent for molecular/cellular imaging); *fight* (action of drugs on nanoparticles); *follow* (contrasting imaging for monitoring the therapeutic effect).

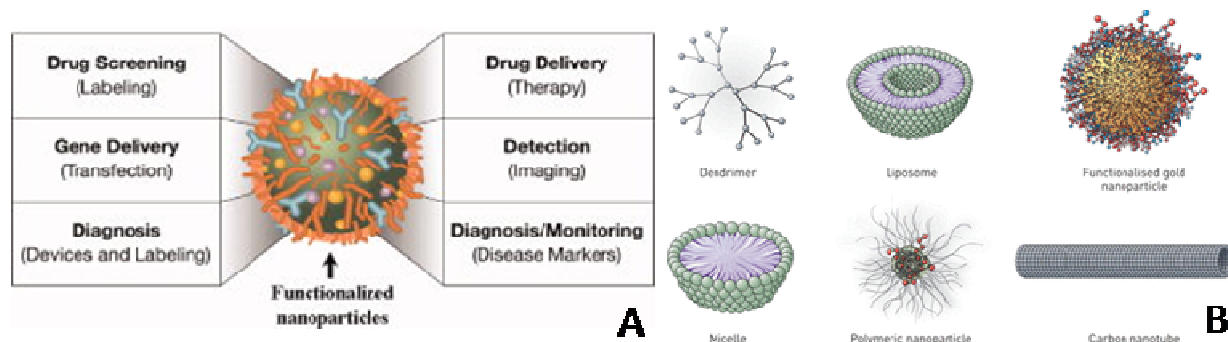


Figure 1.2. (A) Applications and research targets of nanomedicine. Nanoparticles have been designed with chemically modifiable surfaces, with the possibility of linking various ligands, which can turn these nanomaterials into biosensors, molecular-scale fluorescent tags, imaging agents, targeted molecular delivery vehicles, and other useful biological tools;² (B) Nanomaterials commonly used in medicine: liposomes contain amphiphilic molecules, which have hydrophobic and hydrophilic groups that self-assemble in water; dendrimers are branched nanostructures; each terminus contains reactive chemical functional groups that

allow the addition of multiple monomers to increase the size of the nanostructure; gold nanoparticles are solid metal particles that are conventionally coated with drug molecules, proteins or oligonucleotides; fullerenes and carbon nanotubes have only carbon-to-carbon bonds.³

Nanomedicine exploits the properties and physical characteristics of nanomaterials for the diagnosis and treatment of diseases at the molecular level. The discoveries in medical field are really revolutionary, to the point that they are currently changing traditional diagnostic and pharmaceutical techniques.^{2,4-8}

The main features to attempt in designing a medical nanoplatformare drafted in figure 1.3

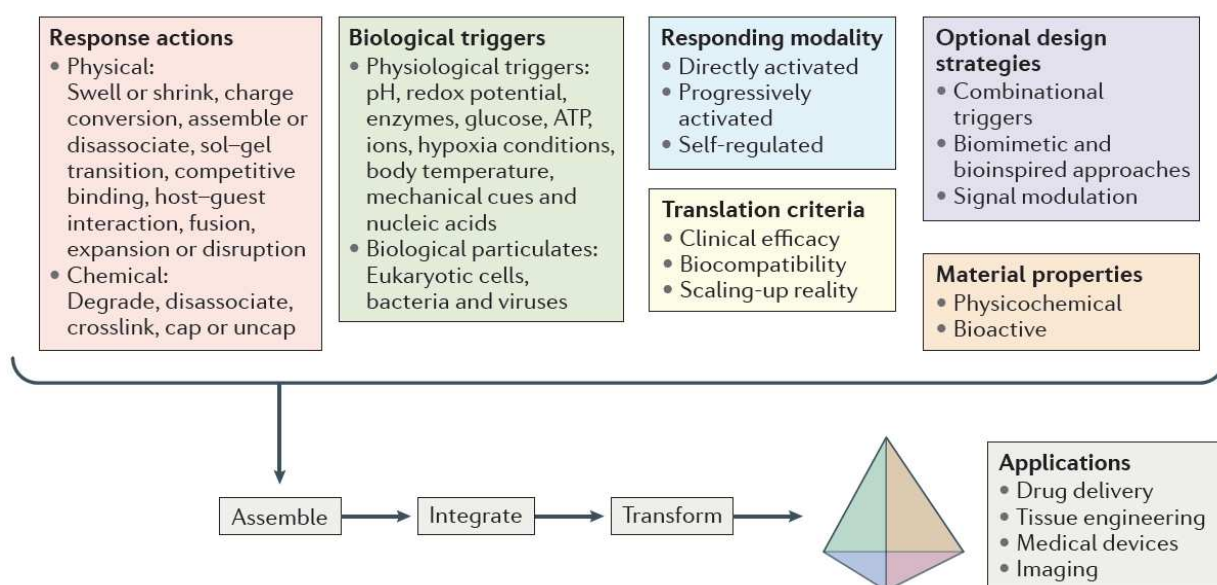


Figure 3.3. General rationale design of bioresponsive materials. Multiple perspectives, including the responding modality, biological triggers, response actions, material properties, design strategies and translation criteria, serve as ‘building blocks’ for engineering bioresponsive materials for different applications.⁹

1.2. Nanoparticles for Biomedical Applications

In the last decades, a wide variety of nanoparticles (NPs) have been developed. They can be mainly classified in two groups: NPs contained organic molecules (protein cages, liposomes, dendrimers, carbon nanotube, polymeric NPs) and constituted by an inorganic core, mostly metal core.

Particularly, in this chapter poly(Lactide-*co*-Glycolide) polymeric nanoparticles (PLGA NPs) are discussed, while brief descriptions of inorganic nanoparticles (mainly gold and magnetic particles) are displayed in chapter II and III.

1.2.1. Poly(lactic-*co*-glycolic acid) polymer

Polymers are a very versatile class of materials and have been changing our daily lives for decades with important applications in the areas of medicine, agriculture, and engineering. There has been a rapid growth in the medical use of polymeric materials in many fields including tissue engineering, implant of medical devices and artificial organs, prostheses, ophthalmology, dentistry, and bone repair. Among the synthetic polymers, the polyester family (i.e., poly(lactic acid) (PLA), poly(ϵ -caprolactone) (PCL), poly(glycolic acid) (PGA) and poly(D,L-lactide-*co*-glycolide) (PLGA)), are of interest in the biomedical area because of their biocompatibility and biodegradability properties.^{19,11,12} PLGA co-polymers could be prepared by the direct polycondensation reaction of lactic acid and glycolic acid units, resulting in copolymers with low molecular weight (Fig. 1.5 A)^{13,14} or by an opening polymerization of cyclic dimers of lactic acid (lactide) and glycolic acid (glycolide), resulting in copolymers with high molecular weight and therefore with better mechanical properties (Fig. 1.5 B).^{15,16,17,18}

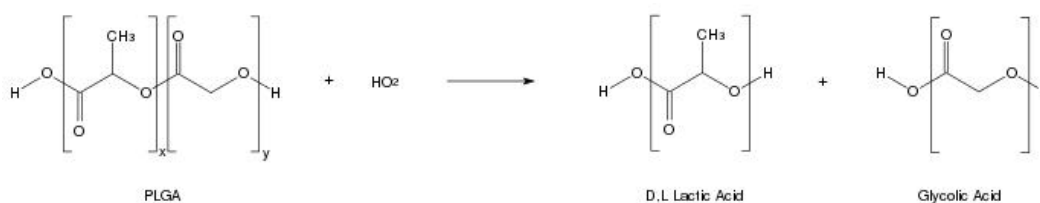


Figure 4.4. Polymers with hydrolysable chains: (A) poly(glycolic acid); (B) poly(lactic acid) and (C) poly(D,L-lactide-*co*-glycolide) copolymer.

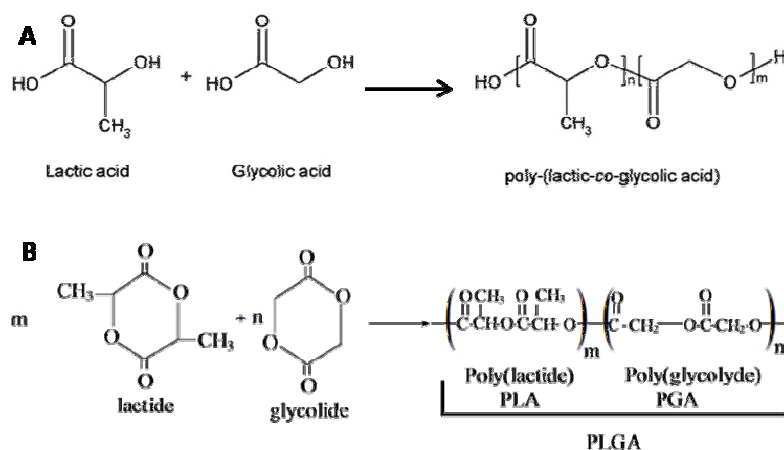


Figure 5.5. (A) Chemical structure of poly(lactic-co-glycolic acid) and direct polycondensation reaction of lactic acid and glycolic acid; (B) chemical structure of the dimers and polymers, and the opening of cyclic dimers of lactic acid (lactide) and glycolic acid (glycolide) polymerization reaction.¹⁷

1.2.2. Physicochemical Properties

To understand the physical, chemical and biological properties of poly(lactic-co-glycolic acid) it is essential to design a suitable nanoparticle for biological applications. The physical properties of PLGA are influenced by various factors, involving initial molecular weight, lactide to glycolide ratio, size of the device and storage temperature.

PLGAs are soluble in a wide range of solvents including chlorinated solvents, tetrahydrofuran, acetone or ethyl acetate; while in water, the polymer biodegrades by hydrolysis of its ester linkages (Fig. 1.4). The presence of methyl side groups in PLA makes it more hydrophobic than PGA and hence lactide rich PLGA copolymers are less hydrophilic, absorb less water and subsequently degrade more slowly.⁴⁰

Hydrolysis process causes the physicochemical parameters of PLGA (e.g., glass transition temperature (T_g), moisture content, inherent viscosity and molecular weight) to change with time. The modulation of the composition of the polymer can result in changes of many other properties, thus it can eventually affect the drug release, polymer degradation, etc. For example, a reduction of glass transition temperature (T_g) leads to plasticization of the polymer matrix²⁰ and consequently to decrease in mechanical properties of the polymer. Ideally PLGA polymer systems should have considerable mechanical strength, since the drug delivery devices formulated using them are subjected to significant physical stress, which can also influence mechanical breakdown of implants

and alter surface area and hydration/hydrolysis.²¹ In addition, extensive research demonstrated that the decrease of the PLGA lactide content results in the decrease of the T_g .²⁰

The degree of *crystallinity* of PLGA influences mechanical strength, swelling behavior and biodegradation rate of the polymer, as it depends upon the monomeric units out of which it is formed during co-polymerization of PGA and PLA.

Commonly, the commercially available polymers are characterized by an inherent viscosity that is directly dependent upon the molecular weight of the polymer.^{19,38,42}

1.2.3. Poly(lactic-co-glycolic acid) Nanoparticles Preparation Techniques

PLGA nanoparticles preparation methods are distinguished in two classes: bottom-up and top-down techniques. The bottom-up techniques (e.g., emulsion or microemulsion polymerization, precipitation polymerization, interfacial polymerization) employ a monomer as a starting point, while top-down techniques (e.g. emulsion evaporation, emulsion diffusion, salting out, solvent displacement) prepare nanoparticles from the polymer. Here it is discussed the top-down technique, particularly a oil-in-water emulsion (single emulsion) method, which was employed for preparing PLGA NPs in this thesis.

The oil-in-water emulsion method (single emulsion) is based on the emulsification of an organic solution which contains the polymer and the active component in an aqueous phase, followed by the evaporation of the organic solvent. Different surfactants such as poly(vinyl alcohol) (PVA) or Pluronic F127 can be dissolved in the aqueous phase. The size reduction of the emulsion droplet is done by sonication or microfluidization. Important parameters to be considered are polymer molecular mass and concentration, *co*-polymer ratio and terminal groups, surfactant nature, phase ratio, solvent nature, evaporation rate, drug entrapment, additives, shear stress and sterilization.²⁴ Many parameters can influence the diameter and are briefly discussed.

Higher is the *polymer concentration* in the organic phase (% w/v) bigger is the nanoparticles.^{24,25}

The increase in *polymer molecular mass* leads to formation of nanospheres of significantly bigger size, but reduce the entrapment of active components.^{24,26}

Co-polymer ratio have no significant influence on the mean size of nanoparticles.^{24,26} On the contrary, *terminal groups* strongly influence the mean size of the particles.

Many *surfactants*, such as PVA, methylcellulose (MC), PLURONIC F127, gelatin and lecithin, have been tested to better stabilize NPs and to decrease the polydispersion. The nature of the surfactant leads to the formation of PLGA NPs of different size. For example, PVA produces smaller particles than MC at the same reaction conditions. Importantly, for biomedical applications the presence of non-toxic surfactant is required. To address this concern, researchers found other surfactants, which are biodegradable and biocompatible, such as vitamin E TPGS (D- α -tocopheryl polyethylene glycol 1000 succinate).^{27,32} Moreover, by increasing the concentration of PVA it is possible to reduce the size of NPs, while MC at the same concentrations increases their dimension.

The organic to aqueous solvent ratio plays an important role in controlling the size of the nanospheres. In general, a lower ratio of organic to aqueous phase produces smaller nanoparticles.^{24,25}

The organic solvents used for the reaction need to be completely immiscible with water and to be able to solubilize the PLGA polymer. Chlorinated solvents are widely used in the emulsion evaporation method.²⁴⁻²⁷

Evaporation rate is also important in determining the size of the particle. The evaporation of organic solvents under vacuum produce particle size 30% smaller than the particles that are obtained under a normal rate of evaporation.^{24,28,29}

During emulsion evaporation, as in other synthesis methods, entrapment of highly *hydrophobic drugs* tends to reduce the size of the nanospheres.^{24,27} The solubility of the drug in water is the main drawback in forming smaller size nanospheres and in improving the drug entrapment efficiency. The drug solubility can be controlled by adjusting the pH.

Additives greatly influence the size of the nanospheres. Addition of hydrophobic additives can improve their size, drug entrapment efficiency and release profile.^{24,30}

Shear stress generated from a strong agitation or sonication is necessary to reduce the droplet size that highly impacts the nanoparticles size.^{24,25}

The *sterilization* process increases a little the size of the NPs, but does not affect the drug release profile and increase only slightly the cellular uptake.^{24,30}

1.2.4. Degradation of poly (lactic-*co*-glycolic acid) nanoparticles

PLGA undergoes degradation in aqueous environment where ester linkages present along the polymer backbone are randomly hydrolyzed.¹⁶ Two main degradation mechanisms have been highlighted: hydrolytic degradation and auto-catalytic degradation.³² Any change in PLGA molecular weight, chemical composition and surface modification may lead to changes in its rate of degradation (e.g., the increase in carboxylic end groups facilitate the further autocatalysis).²⁷

Scission of long polymer chains leads to reduction in the molecular weight of the polymer that increases its hydrophilicity and on further reduction until the formation of water-soluble fragments. These are hydrolyzed to lactic and glycolic acids (Fig. 1.4), subsequently metabolized in the body *via* the Krebs cycle, and finally eliminated from the body as carbon dioxide and water.³³ Glycolic acid is either excreted unchanged in the kidney or it enters the tricarboxylic acid cycle and is eventually eliminated as carbon dioxide and water.

During autocatalytic degradation, acidic by-product remains strapped in polymer bulk, autocatalyzing the degradation process and resulting into a highly acidic microenvironment. In biological systems, the formation of lactic and glycolic acids increases the local acidity, which may irritate the surrounding tissues, adversely affect the stability and even trigger the release of polymer-entrapped moieties. Improved drug stability has been achieved by pH control *via* the incorporation of poorly water-soluble bases, which stabilize small anti-cancer agents and several therapeutic proteins,³³ such as vincristine and basic fibroblast growth factor.²⁴

Particularly, the study of the degradation mechanism of the PLGA polymeric particles as drug delivery systems has attracted much attention. A fundamental understanding of the *in vivo* phenomenon of PLGA biodegradation is important because this determines the rate and mechanism of the release of diagnostic or therapeutic agents.

The therapeutic agent is either dispersed throughout the polymeric matrix or encapsulated in the hydrophobic nanoparticle *core*. The release of a therapeutic agent from nanoparticles has usually been shown to be biphasic, initially by diffusion through the polymer matrix and later by diffusion of the therapeutic agent and degradation of the polymer matrix itself.^{34,35}

Generally, biodegradable polymers as nanobiovector follow any of the two main degradation mechanisms depicted in figure 1.6 A: polymer surface erosion with the consequently release of physically entrapped drug and of polymer-drug bonding scission, followed by drug release

viadiffusion.³⁶ In both cases, the degradation rate of the polymer, the stability and the drug release kinetic are considerably affected by the pH of the surrounding *media*. Increasing the pH decreases the degradation rate and improves the system stability.

Polymer Surface Erosion. When hydrolysis occurs on soft surface, the degradation products can diffuse more easily out of the polymer, which is neutralized by large amount of buffer present on the surface of the polymer.

Bulk Erosion. During bulk erosion the entire polymer matrix is involved in the degradation process and the water uptake is faster than the hydrolysis rate.³⁷ The degradation products diffuse out of the degrading material. Phases with high degree of cristallinity slow the degradation process, whereas amorphous ones show faster degradation due to their high water uptake. These factors affect and vary the degradation time from several weeks up to years, thus modifying the drug release profile accordingly.³⁸

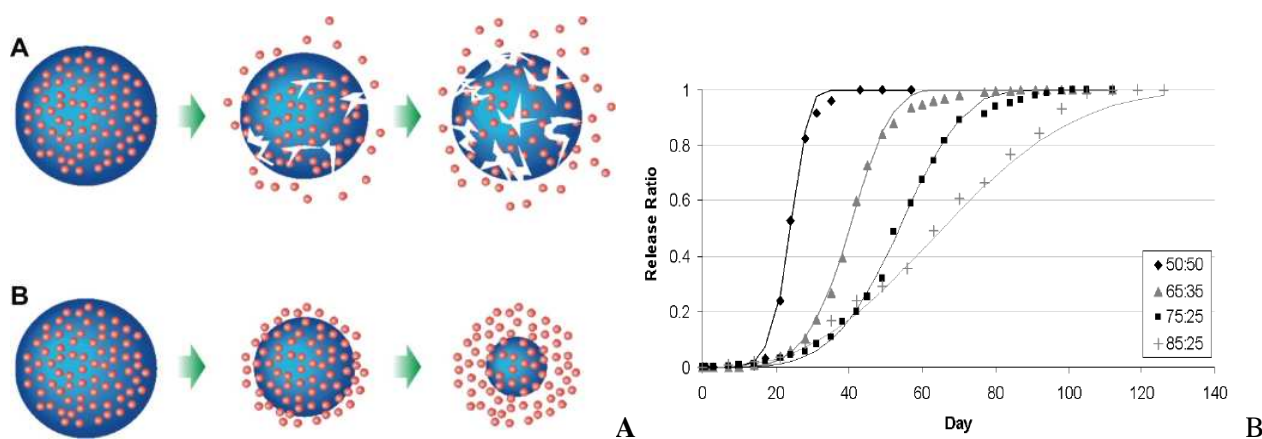


Figure 6.6. (A) Degradation mechanisms of biodegradable polymeric nanoparticles: A) bulk erosion, B) surface erosion;³⁶ (B) Modeled *in vivo* release profiles for 50:50, 65:35, 75:25 and 85:15 poly lactic-co-glycolic acid. A biphasic release profile with an initial zero release period followed by a rapid drug release has been observed. The profiles also show increase in release rate with decrease in lactide to glycolideratio.^{45,47}

The degradation period of biodegradable polymers is significantly affected by six main factors: the chemical structure and composition of the system, the molecular mass distribution of the polymers, the presence of monomers and oligomers, the size and shape of the system surface, the morphology of the system components and the hydrolysis mechanism.⁵⁹

Of primary importance, the monomer ratio (LA: GA) markedly affects the polymeric properties. For example, the *in vivo* resorption period of PLA (100% LA) and PGA (100% GA) is 12 - 24 months and 6 - 12 months, respectively.¹² Thus, the choice of an appropriate LA to GA ratio of the copolymer should be focused on the selection of suitable degradation kinetics in the body for the desired biomedical applications.

The *molecular weight* is directly related to the polymeric chain size.⁶⁰ The high molecular weight polymeric chains exhibit low degradation rate because they require more time to break down and degrade, as compared to small polymeric chains.⁴⁰

The *glass transition temperature* (T_g) and the *crystallinity* of the polymer indirectly affect the degradation rate. At the moment there are conflicting reports on how these parameters affect the degradation rate.

The *in vitro* biodegradable studies concluded that both alkaline and strongly acidic media leads to polymerdegradation.⁴¹ However, the degradation rate becomes slow in slightly acidic and neutral *medium* due to autocatalysis by carboxylic end groups.⁴²

The *loading* and the *chemical properties* of the *drug* play significant role in the rate and duration of the drug release.^{66,67}

The role of *enzymes* in PLGA biodegradation is unclear. Some investigators have suggested an enzymatic role in PLGA breakdown based on the difference in the *in vitro* and *in vivo* degradation rates, but most literature indicate that PLGA biodegradation occurs only through hydrolysis.

In order to tune the degradation and drug release mechanisms all the factors must be considered for desirable application of the polymeric system.²³

1.3. Release Kinetic Profile

The release profile of molecules from PLGA NPs is strongly influenced by the degradation mechanism described above. Drug release kinetic profiles reveal a biphasic behavior (Fig. 1.6 B).^{59,60}

An initial *burst release* affects drug molecules in contact with the environment and it is associated to the nature and concentration of the drug and to the polymer hydrophobicity. Burst

release is related to the drug solubility as well as penetration of water into the polymer matrix. The initial random hydrolysis causes a significantly decrease in PLGA molecular weight, but no appreciable weight loss and no soluble monomer products are formed in this phase.

Secondary, drug is released progressively through the thicker drug depleted layer. The water inside the matrix hydrolyzes the polymer into soluble oligomeric and monomeric products. This creates a passage for the drug to be released by diffusion and erosion until complete polymer solubilization. Drug nature also plays an important role in attracting the aqueous phase into the matrix.

1.4. Biomedical Application of Poly(lactide-co-glycolide) Nanoparticles

Biodegradable polymers are promising materials for biomedical and pharmaceutical applications due to their safety, tunable biodegradability, desirable mechanical properties and extensive investigation in carrier based drug delivery system.^{15,39,44}

Above all, homo and co-polymers derived from lactic and glycolic acids monomers received a considerable attention as excipients in pharmaceutical industry since 1973, due to their attractive properties such as the biodegradability and biocompatibility, the approval in drug delivery systems for parenteral administration by Food and Drug Administration (FDA) and European Medicine Agency (EMA), the well define methods of production for hydrophilic or hydrophobic small molecules or macromolecules in various carrier based drug delivery system, the drug protection from degradation, the sustained release, the easy modification of PLGA for better interaction with biological materials and the possibility to target specific organs or cells.⁴⁸

Polymer-based drug delivery systems can control the rate of drug release, enhance effective drug solubility, minimize drug degradation, contribute to reduced drug toxicity and facilitate the control of drug uptake, which significantly contributes to therapeutic efficiency of a drug. The polymer s for drug delivery system should be non-immunogenic and should degrade *in vivo* at a well-defined rate to give non-toxic products, readily excreted from the body.

The size and size distribution of the PLGA nanoparticles among other physical characteristics, are affected by the technique used for the nanoparticle production and the pertinent synthesis parameters, i.e., PLGA molecular mass, the addition of active components, surfactants and other additives. As a consequence PLGA NPs of different physical characteristics (size, size distribution,

morphology, zeta potential) are synthesized by controlling the parameters specific to the synthetic method employed.⁴⁹

PLGA NPs find a wide range of applications in biomedical area such as drug, vaccine or gene delivery, regenerative tissue engineering, cancer and inflammatory diseases therapy, cell culture supporting and diagnosis.⁵⁰ A lot of recent examples of potential biomedical application of PLGA in the treatment of various diseases and in tissue engineering, recent patents and list of approved marked PLGA products are described in *Recent biomedical applications and patents on biodegradable polymer-PLGA*,⁵¹ and clearly illustrate the promising use of biodegradable PLGA for novel medical concepts.

Here, it is briefly discussed nanoparticles for drug delivery (DD), diagnosis and theranostic. Among all these possibilities, the most important and unique aspect of nanomedicine is multimodality, i.e. the capacity to perform several diagnostic and/or therapeutic functions in tandem, thus paving the way to the construction of innovative theranostic agents.

Poly(lactic-co-glycolic acid) Nanosystem as Delivery System

The PLGA NPs are widely used as drug, gene and vaccine⁵⁰ delivery specific vehicles. They aim to satisfy the payload delivery with appropriate duration, biodistribution and concentration for the intended therapeutic effect. Therefore, design essentials, including material and geometry, must incorporate mechanisms of degradation and clearance of the vehicle as well as active pharmaceutical ingredients (API). Because of its ability to deliver varied types of cargo efficiently and compatibility with other polymers, PLGA is a first choice carrier.

Moreover, nanovectors (NVs) protect active molecules from primary enzymatic degradation, recognition by immune system and metabolism by reticulum endothelial system (RES). In addition, nanoparticles can drive the drug to specific tissues (first order targeting), cells (second order targeting) or intracellular organelles (third order targeting) by active or passive targeting. Passive targeting exploits the nanosystem dimensions and the enhanced permeability and retention (EPR) effect alone to reach only cancer and inflammatory tissues. Profitably, the high *surface to area* ratio of nanomaterial allows the surface functionalization with targeting moieties for the active recognition of receptors expressed on pathological tissue or cells. Furthermore, by tuning the structure and the composition of the DD vectors, it is possible to control the delivery of their

payload and permit sustained, stimuli-responsive or externally activated release.^{9,52} In conclusion, multimodal nanosystems can be designed for a combination of therapies or as theranostic tools.

Biodistribution and pharmacokinetics of PLGA follows a non-linear and dose-dependent profile. Furthermore, previous studies suggest that both blood clearance and uptake by the mononuclear phagocyte system (MPS) may depend on dose and composition of PLGA carrier systems.⁵³ Additionally, quantitative distribution experiments indicate that some PLGA formulations, such as nanoparticles, accumulate rapidly in liver, bone marrow, lymph nodes, spleen and peritoneal macrophages. The biphasic release profiles of drug molecules from PLGA carriers also play importance major role in treatment of diseases.

Drug release profile is of great importance in determining the dose and dosage. PLGA carriers have a typical biphasic curve for drug release, as described in the previous paragraph.⁶⁷ Here reported, the complex picture of physicochemical process occurring within the PLGA carrier polymer matrix leading to the release of drugs or biomolecules (Fig. 1.7).⁵⁴

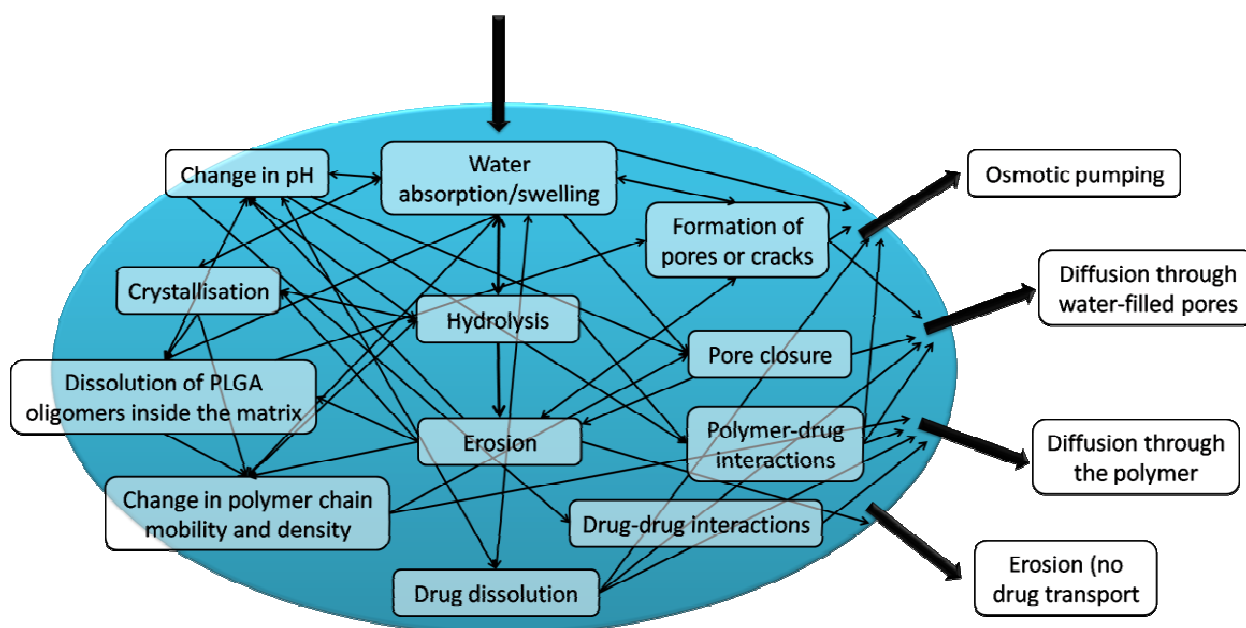


Figure 7.7. Complex web picture showing different processes involved in drug release from PLGA.⁵⁴

PLGA NPs are internalized in cells partly through fluid phase pinocytosis and also through clathrin-mediated endocytosis. NPs rapidly escape the endo-lysosome apparatus and enter the cytoplasm within few time of incubation (Fig.1.8). This facilitates interactions of nanoparticles with the vesicular membranes leading to transient and localized destabilization of the membrane,

resulting in the escape of nanoparticles into the cytosol.⁵⁵ The polymer degradation time can differ from days, to several months or years, depending on the molecular weight and copolymer ratio.⁵⁶

In vivo, the binding of opsonin proteins in the blood stream leads to attachment onto macrophages and subsequently their internalization mediated by phagocytosis.⁵⁷ To threshold these phenomena, several methods of surface modifications have been developed to produce stealthness and many work converged to the surface modification with Polyethylene glycol (PEG), which exhibits excellent biocompatibility and low toxicity. To this aim, PEG coating is essential for avoiding recognition by the reticuloendothelial system, while targeting ligands should be extended away from the nanoparticle surfaces to avoid shielding by the PEG chains.^{58,59} In addition, many different coatings (e.g., PEGylation⁶⁰ or PEI⁶¹ and chitosan⁶² one) are exploited for modulating PLGA surface charge in order to avoid non-specific interactions.

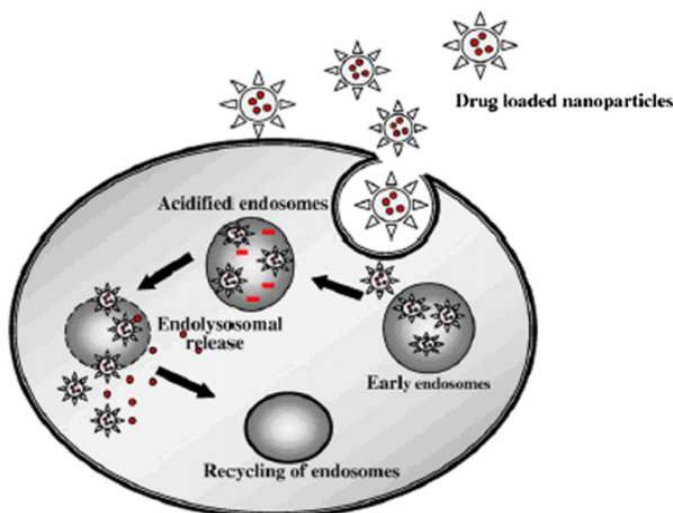


Figure 8.8. Depiction of PLGA NPs internalization in cells. Polymeric PLGA NPs allow efficient entry into cells followed by cargo release in response to acid conditions inside endosomes. Thus the polymer is decomposed through metabolic compounds and the drug can accumulate into the cytoplasm of the cell.^{50,63}

Poly(lactic-co-glycolic acid) nanoparticles for diagnosis

Nanodiagnostic intends to identify diseases at early stage with high sensibility, specificity and affinity by means of nanosystems to target pathological species *in vitro* and/or *in vivo*. Nanoimaging in particular, is becoming a leading science for diagnostic methodologies, with particular relevance in magnetic resonance imaging (MRI), computed tomography (CT) and positron emission tomography (PET), which aims at a personalized medicine by a non-invasive and

real-time evaluation of the patient healthcare during and after therapies or surgery. Nanoimaging exploits smart contrast nanoagents that have demonstrated optimal sensitivity, biocompatibility and biodistribution profile in the current diagnostic methodologies, and also permits to introduce new imaging technologies, such as fluorescence imaging,¹¹ and a combination of techniques with a compact contrast agent. In this perspective, PLGA NPs content confers them the ability to detect disease without severe immunogenicity for human being.

An example of PLGA NPs as diagnostic tools consists of fluorescent dye-loaded particles for *in vitro* application.⁶⁵ Otherwise, PLGA particles containing magnetic tools such as iron oxide particles, are reported having a great potential as theranostic agent. As a matter of fact, they can act as drug delivery, magnetic resonance (MR) imaging and hyperthermic agent at the same time.⁶⁶ For the *in vivo* applications, Gd-based contrast agents⁶⁷ and manganese oxide nanoparticles are incorporated in PLGA NPs by a single emulsion technique, to fabricate a pH-sensitive MRI contrast agent. This nanocomposite provides 35-fold high contrast compared to the common MRI contrast agent yet reported.⁶⁸ Finally, PLGA containing gold nanorods provides the combination of chemotherapeutic and photothermal therapy in mammalian cells and *in vivo* in an animal model.⁶⁹

Poly(lactic-co-glycolic acid) Nanoparticles for Theranostic

Nowadays, several diseases are broadly heterogeneous and the accessible treatments are effective for few patients at certain stages of the disease development. To overcome these limitations, theranostic associates the diagnostic and therapeutic properties of nanoparticles to more specific and personalized therapies. The large capacity of nanoparticles even allows for the tethered of a second or third functionality, a feature that encourages the formation of an all-in-one nanosystem with comprehensive characteristics.⁷

Figure 1.9 reports various combinations to design a PLGA-based theranostic nanoconstruct.

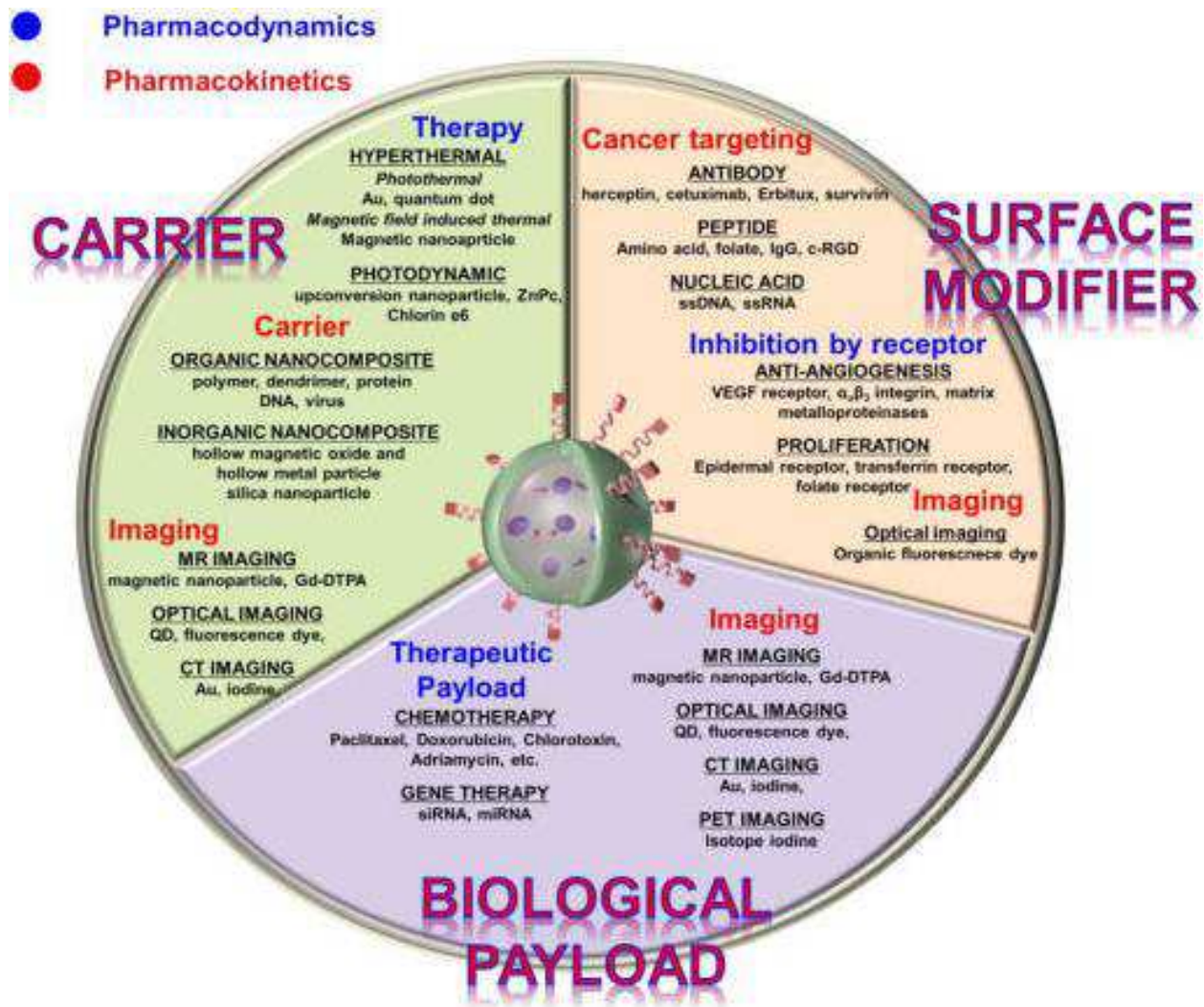


Figure 9.9. Diagram of pharmacokinetics and pharmacodynamic aspects of PLGA-based theranostic nanocomposites.⁷

1.5. Nanoparticle Functionalization for Biomedical Applications

In order to obtain particles for biomedical application it is necessary to take in consideration some important requisites that nanoparticles need to satisfy. NPs must be dispersible in physiological environment, biocompatible, non-toxic, non-immunogenic, and selective for the biologic target. Particle surface chemistry plays a pivotal role in defining these features and consequently the NPs biomedical employment.

In last decades, many surface modification strategies have been developed with the aim to obtain nanoparticles interacting with cells. Nanoparticles can be functionalized directly after synthesis by exploiting the surfactant molecule nature, or by substituting it with others molecules with congruous functional groups for the anchoring of chemical and biological moieties. Nanoparticle functionalization provides two main goals: to make nanoparticle biocompatible and to guarantee the biological activity. Below, the description of the main strategies for surface particle modifications.

Pre-modification. Before NPs biofunctionalization is necessary to prepare NPs for the anchorage of active materials. Requested functional moieties can be present on the as-prepared nanoparticle *core* itself (e.g. carboxylic groups on PLGA NPs surface) or they need to be added on the surface (e.g. most of inorganic NPs). To this aim, pre-modification of NPs surface by ligand exchange is necessary to eliminate the eventual toxic surfactants (such as cetyltrimethylammonium bromide (CTAB) on gold nanorods (GNRs), poly(isobutylene-*alt*-maleic) anhydride (PMA)-coating for iron oxide nanoparticles (IONPs) prepared in organic solvent) and to expose the functional groups required for the next attachment of molecules. Amino groups, carboxylic acid and sulphhydryl groups are the most exploited functional groups for the conjugation of molecules. The amino and carboxyl groups have the potentiality to generate amide bonds with the aid of an activating, and to generate positive and negative charged surfaces, respectively. Another strategy consists in coating NPs with an amphiphilic polymer, (e.g. dodecylamine-modified PMA), which is able to transfer NPs from organic to aqueous phase, in order to stabilize the particles in a cell-friendly environment and to expose further reactive groups for bioconjugation.

Functionalization. The surface reactivity of the nanocarriers, intrinsic or resulted from functional groups added post-synthesis, is exploited for the conjugation of a plethora of molecules (e.g., peptides, proteins, and antibodies; enzymes and ribozymes, oligonucleotides and aptamers; carbohydrates, lipids, drugs, or other biologically active small molecules; reporter molecules or contrast agents, including MRI labels, radiolabels, and fluorescent dyes, etc.), depending on the biomedical applications, being it therapeutic, diagnostic or theranostic. In the last decades, three

main methodologies have been developed for NPs functionalization: ligand attachment by passive or electrostatic forces, chemical modification, or specific interactions. A graphical overview of these strategies is reported in figure 1.10. Many factors could be considered to affect the success of the conjugation, such as biomolecules to nanoparticles ratio, spatial orientation, activity and density of biomolecules on the nanoparticle surface, and non-specific interactions with undesired species.

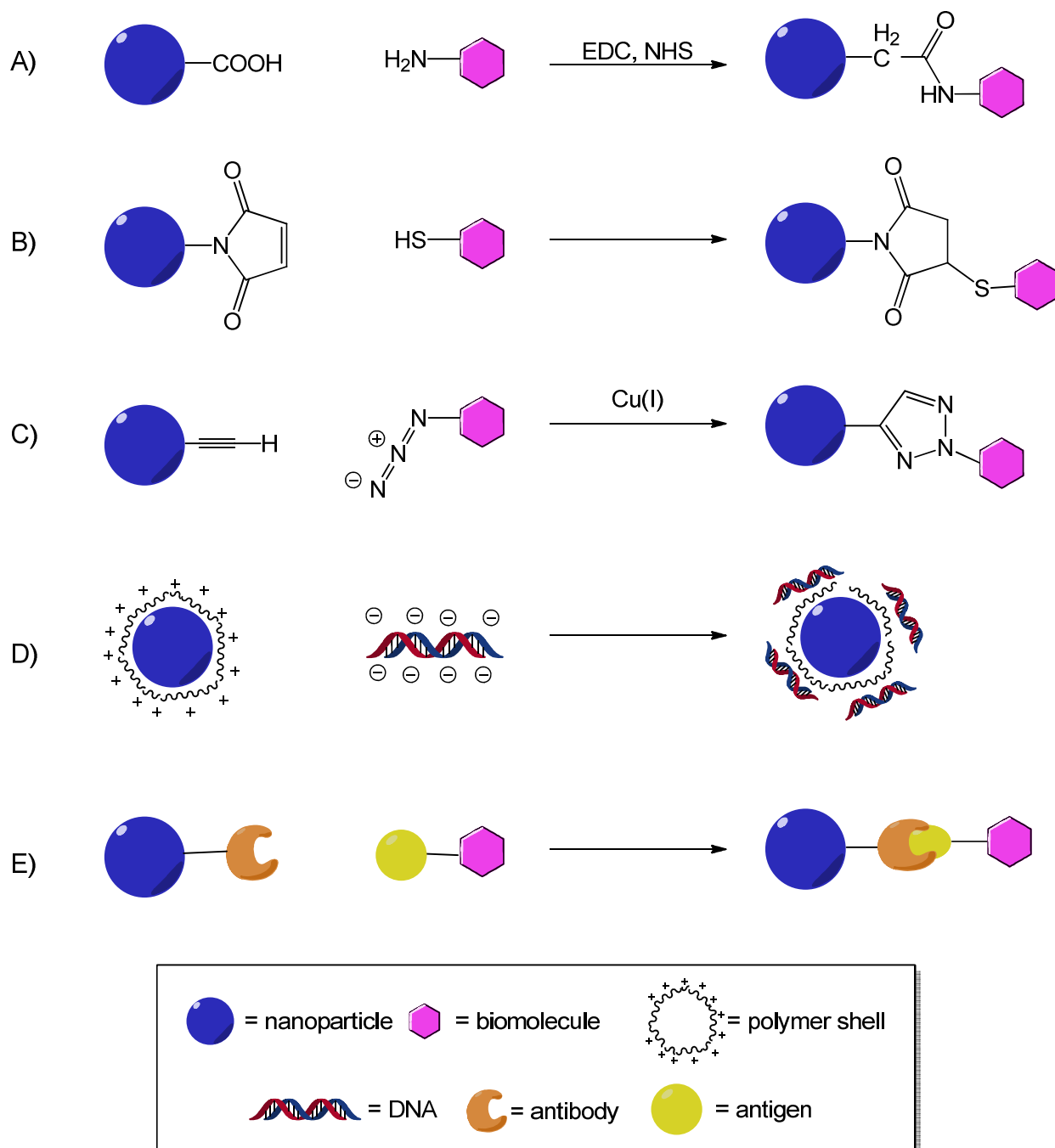


Figure 10.10. Examples of bioconjugation strategies, including covalent linkages (A) peptide bond, (B) Michael addition, (C) click chemistry; non-covalent interactions (D) electrostatic interactions, (E) antibody-antigen recognition.

List of Figures, Graphs and Tables

Figure 1.1. Nanometer scale with examples of natural elements.	8
Figure 1.2. (A) Applications and research targets of nanomedicine. Nanoparticles have been designed with chemically modifiable surfaces, with the possibility of linking various ligands, which can turn these nanomaterials into biosensors, molecular-scale fluorescent tags, imaging agents, targeted molecular delivery vehicles, and other useful biological tools; ² (B) Nanomaterials commonly used in medicine: liposomes contain amphiphilic molecules, which have hydrophobic and hydrophilic groups that self-assemble in water; dendrimers are branched nanostructures; each terminus contains reactive chemical functional groups that allow the addition of multiple monomers to increase the size of the nanostructure; gold nanoparticles are solid metal particles that are conventionally coated with drug molecules, proteins or oligonucleotides; fullerenes and carbon nanotubes have only carbon-to-carbon bonds. ³	9
Figure 1.3. General rationale design of bioresponsive materials. Multiple perspectives, including the responding modality, biological triggers, response actions, material properties, design strategies and translation criteria, serve as ‘building blocks’ for engineering bioresponsive materials for different applications. ⁹	10
Figure 1.4. Polymers with hydrolysable chains: (A) Poly(glycolic acid); (B) Poly(lactic acid) and (C) Poly(D,L-lactide-coglycolide) copolymer.	11
Figure 1.5. (A) Chemical structure of poly(lactic-co-glycolic acid) and direct polycondensation reaction of lactic acid and glycolic acid; (B) Chemical structure of the dimers and polymers, and the opening of cyclic dimers of lactic acid (lactide) and glycolic acid (glycolide) polymerization reaction. ¹⁷	12
Figure 1.6. (A) Degradation mechanisms of biodegradable polymeric nanoparticles: A) bulk erosion, B) surface erosion; ³⁶ (B) Modeled <i>in vivo</i> release profiles for 50:50, 65:35, 75:25 and 85:15 poly lactic-co-glycolic acid. A biphasic release profile with an initial zero release period followed by a rapid drug release has been observed. The profiles also show increase in release rate with decrease in lactide to glycolide ratio. ^{45,47}	16
Figure 1.7. (A) Hydrolysis of PLGA. X and Y represent the number of units of lactic acid and glycolic acid respectively. (B) Complex web picture showing different processes involved in drug release from PLGA. ⁵⁴	20
Figure 1.8. Depiction of PLGA NPs internalization in cells. Polymeric PLGA NPs allow efficient entry into cells followed by cargo release in response to acid conditions inside endosomes. Thus the polymer is decomposed through metabolic compounds and the drug can accumulate into the cytoplasm of the cell. ^{50,63} .	21

Figure 1.9. Diagram of pharmacokinetics and pharmacodynamic aspects of PLGA-based theranostic nanocomposites.⁷ 23

Figure 1.10. Examples of bioconjugation strategies, including covalent linkages (A) peptide bond, (B) Michael addition, (C) click chemistry; non-covalent interactions (D) electrostatic interactions, (E) antibody-antigen recognition. 25

References

1. Mazzucchelli, S. *et al.* Single-Domain Protein A-Engineered Magnetic Nanoparticles: Toward a Universal Strategy to Site-Specific Labeling of Antibodies for Targeted Detection of Tumor Cells. *ACS Nano***4**, 5693–5702 (2010).
2. Liu, Y., Miyoshi, H. & Nakamura, M. Nanomedicine for drug delivery and imaging: A promising avenue for cancer therapy and diagnosis using targeted functional nanoparticles. *ResearchGate***120**, 2527–37 (2007).
3. Rijt, S. H. van, Bein, T. & Meiners, S. Medical nanoparticles for next generation drug delivery to the lungs. *Eur. Respir. J.***44**, 765–774 (2014).
4. Sperling, R. A., Gil, P. R., Zhang, F., Zanella, M. & Parak, W. J. Biological applications of gold nanoparticles. *Chem. Soc. Rev.***37**, 1896–1908 (2008).
5. Liu, G., Gao, J., Ai, H. & Chen, X. Applications and Potential Toxicity of Magnetic Iron Oxide Nanoparticles. *Small***9**, 1533–1545 (2013).
6. Kim, B. Y. S., Rutka, J. T. & Chan, W. C. W. Nanomedicine. *N. Engl. J. Med.***363**, 2434–2443 (2010).
7. Lim, E.-K. *et al.* Nanomaterials for Theranostics: Recent Advances and Future Challenges. *Chem. Rev.***115**, 327–394 (2015).
8. Pautler, M. & Brenner, S. Nanomedicine: promises and challenges for the future of public health. *Int. J. Nanomedicine***5**, 803–809 (2010).
9. Lu, Y., Aimetti, A. A., Langer, R. & Gu, Z. Bioresponsive materials. *Nat. Rev. Mater.***1**, 16075 (2016).
10. Elnashar, M. M. M. Review Article: Immobilized Molecules Using Biomaterials and Nanobiotechnology. *J. Biomater. Nanobiotechnology***1**, 61 (2010).
11. Queiroz, A. & Bolsista de iniciaçãocientífica. Instituto de Química - LQS - LaboratórioQuímica de Superfície, S. POLÍMEROS BIODEGRADÁVEIS: NOVAS PERSPECTIVAS PARA AS CIÊNCIAS FARMACÊUTICAS. *MyScienceWork* (2007).

12. Anderson, J. M. & Shive, M. S. Biodegradation and biocompatibility of PLA and PLGA microspheres. *Adv. Drug Deliv. Rev.***64, Supplement**, 72–82 (2012).
13. Lunt, J. Large-scale production, properties and commercial applications of polylactic acid polymers. *Polym. Degrad. Stab.***59**, 145–152 (1998).
14. Fukuzaki, H., Yoshida, M., Asano, M. & Kumakura, M. Synthesis of copoly(d,l-lactic acid) with relatively low molecular weight and in vitro degradation. *Eur. Polym. J.***25**, 1019–1026 (1989).
15. Reed, A. M. & Gilding, D. K. Biodegradable polymers for use in surgery — poly(glycolic)/poly(lactic acid) homo and copolymers: 2. In vitro degradation. *Polymer***22**, 494–498 (1981).
16. Bendix, D. Chemical synthesis of polylactide and its copolymers for medical applications. *Polym. Degrad. Stab.***59**, 129–135 (1998).
17. Deasy, P. B., Finan, M. P. & Meegan, M. J. Preparation and characterization of lactic/glycolic acid polymers and copolymers. *J. Microencapsul.***6**, 369–378 (1989).
18. Jérôme, C. & Lecomte, P. Recent advances in the synthesis of aliphatic polyesters by ring-opening polymerization. *Adv. Drug Deliv. Rev.***60**, 1056–1076 (2008).
19. Lamprecht, A. *et al.* Influences of process parameters on nanoparticle preparation performed by a double emulsion pressure homogenization technique. *Int. J. Pharm.***196**, 177–182 (2000).
20. Graham, P. D., Brodbeck, K. J. & McHugh, A. J. Phase inversion dynamics of PLGA solutions related to drug delivery. *J. Controlled Release***58**, 233–245 (1999).
21. Kranz, H., Ubrich, N., Maincent, P. & Bodmeier, R. Physicomechanical properties of biodegradable poly(D,L-lactide) and poly(D,L-lactide-co-glycolide) films in the dry and wet states. *J. Pharm. Sci.***89**, 1558–1566 (2000).
22. Musumeci, T. *et al.* PLA/PLGA nanoparticles for sustained release of docetaxel. *Int. J. Pharm.***325**, 172–179 (2006).
23. Kapoor, D. N. *et al.* PLGA: a unique polymer for drug delivery. *Ther. Deliv.***6**, 41–58 (2015).

24. Astete, C. E. & Sabliov, C. M. Synthesis and characterization of PLGA nanoparticles. *J. Biomater. Sci. Polym. Ed.***17**, 247–289 (2006).
25. Julienne, M. C., Alonso, M. J., Amoza, J. L. Góm. & Benoit, J. P. Preparation of Poly(D,L-Lactide/Glycolide) Nanoparticles of Controlled Particle Size Distribution: Application of Experimental Designs. *Drug Dev. Ind. Pharm.***18**, 1063–1077 (1992).
26. Panyam, J., Williams, D., Dash, A., Leslie-Pelecky, D. & Labhasetwar, V. Solid-state solubility influences encapsulation and release of hydrophobic drugs from PLGA/PLA nanoparticles. *J. Pharm. Sci.***93**, 1804–1814 (2004).
27. Mu, L. & Feng, S. S. A novel controlled release formulation for the anticancer drug paclitaxel (Taxol®): PLGA nanoparticles containing vitamin E TPGS. *J. Controlled Release***86**, 33–48 (2003).
28. Chung, T.-W., Huang, Y.-Y., Tsai, Y.-L. & Liu, Y.-Z. Effects of solvent evaporation rate on the properties of protein-loaded PLLA and PDLLA microspheres fabricated by emulsion-solvent evaporation process. *J. Microencapsul.***19**, 463–471 (2002).
29. Chung, T.-W., Huang, Y.-Y. & Liu, Y.-Z. Effects of the rate of solvent evaporation on the characteristics of drug loaded PLLA and PDLLA microspheres. *Int. J. Pharm.***212**, 161–169 (2001).
30. Song, C. X. *et al.* Formulation and characterization of biodegradable nanoparticles for intravascular local drug delivery. *J. Controlled Release***43**, 197–212 (1997).
31. Makadia, H. K. & Siegel, S. J. Poly Lactic-co-Glycolic Acid (PLGA) as Biodegradable Controlled Drug Delivery Carrier. *Polymers***3**, 1377–1397 (2011).
32. Wu, H.-F., Gopal, J., Abdelhamid, H. N. & Hasan, N. Quantum dot applications endowing novelty to analytical proteomics. *PROTEOMICS***12**, 2949–2961 (2012).
33. Crotts, G. & Park, T. G. Protein delivery from poly(lactic-co-glycolic acid) biodegradable microspheres: release kinetics and stability issues. *J. Microencapsul.***15**, 699–713 (1998).
34. Polymer Degradation and in Vitro Release of a Model Protein From Poly(D,L-Lactide-Co-Glycolide) Nano- And Microparticles. *PubMed Journals* Available at: <https://ncbi.nlm.nih.gov/labs/articles/14499195/>. (Accessed: 9th January 2017)

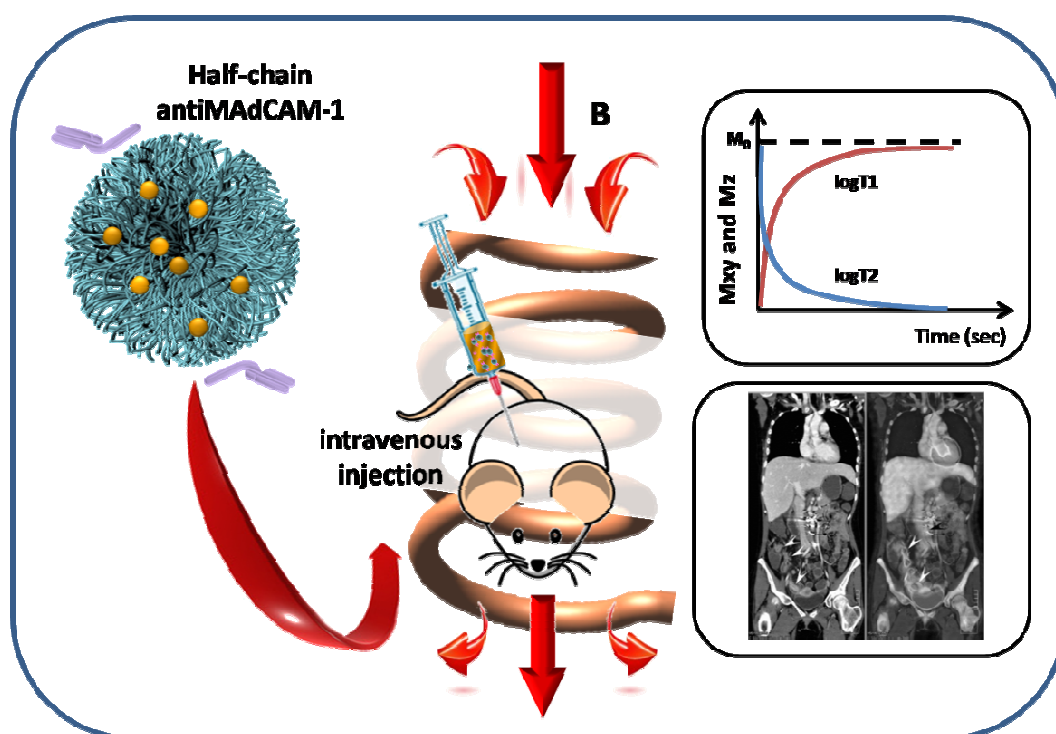
35. Barratt, null. Therapeutic applications of colloidal drug carriers. *Pharm. Sci. Technol. Today***3**, 163–171 (2000).
36. Dinarvand, R., Sepehri, N., Manoochehri, S., Rouhani, H. & Atyabi, F. Polylactide-co-glycolide nanoparticles for controlled delivery of anticancer agents. *Int. J. Nanomedicine***6**, 877–895 (2011).
37. Leemhuis, M., Kruijtzter, J. A. W., van Nostrum, C. F. & Hennink, W. E. In Vitro Hydrolytic Degradation of Hydroxyl-Functionalized Poly(α -hydroxy acid)s. *Biomacromolecules***8**, 2943–2949 (2007).
38. Tyle, P. Controlled drug delivery: Fundamentals and applications. *J. Pharm. Sci.***77**, 94 (1988).
39. Fialho, S. L. *et al.* Biodegradable implants for intraocular drug delivery. *Arq. Bras. Oftalmol.***66**, 891–896 (2003).
40. Park, T. G. Degradation of poly(lactic-co-glycolic acid) microspheres: effect of copolymer composition. *Biomaterials***16**, 1123–1130 (1995).
41. Holy, C. E., Dang, S. M., Davies, J. E. & Shoichet, M. S. In vitro degradation of a novel poly(lactide-co-glycolide) 75/25 foam. *Biomaterials***20**, 1177–1185 (1999).
42. Zolnik, B. S. & Burgess, D. J. Effect of acidic pH on PLGA microsphere degradation and release. *J. Control. Release Off. J. Control. Release Soc.***122**, 338–344 (2007).
43. Frank, A., Rath, S. K. & Venkatraman, S. S. Controlled release from bioerodible polymers: effect of drug type and polymer composition. *J. Controlled Release***102**, 333–344 (2005).
44. Eniola, A. O. A. O. & Hammer, D. A. D. A. Characterization of biodegradable drug delivery vehicles with the adhesive properties of leukocytes II: effect of degradation on targeting activity. *Biomaterials***26**, 661–670 (2005).
45. Ramchandani, M. & Robinson, D. In vitro and in vivo release of ciprofloxacin from PLGA 50:50 implants. *J. Control. Release Off. J. Control. Release Soc.***54**, 167–175 (1998).
46. Fredenberg, S., Wahlgren, M., Reslow, M. & Axelsson, A. The mechanisms of drug release in poly(lactic-co-glycolic acid)-based drug delivery systems--a review. *Int. J. Pharm.***415**, 34–52 (2011).

47. Siepmann, J., Faisant, N. & Benoit, J.-P. A New Mathematical Model Quantifying Drug Release from Bioerodible Microparticles Using Monte Carlo Simulations. *Pharm. Res.***19**, 1885–1893 (2002).
48. Sharma, S., Parmar, A., Kori, S. & Sandhir, R. PLGA-based nanoparticles: A new paradigm in biomedical applications. *ResearchGate***80**, (2015).
49. Biodegradable Nanoparticles for Drug Delivery and Targeting | Nanoparticle. *Scribd* Available at: <https://www.scribd.com/document/131928294/Biodegradable-Nanoparticles-for-Drug-Delivery-and-Targeting>. (Accessed: 9th January 2017)
50. Danhier, F. *et al.* PLGA-based nanoparticles: An overview of biomedical applications. *J. Controlled Release***161**, 505–522 (2012).
51. Gurpreet, S., Tanurajvir, K., Ravinder, K. & Anudeep, K. Recent biomedical applications and patents on biodegradable polymer-PLGA. *ResearchGate***1**, 30–42 (2014).
52. Esmaeili, F. *et al.* PLGA nanoparticles of different surface properties: preparation and evaluation of their body distribution. *Int. J. Pharm.***349**, 249–255 (2008).
53. Panagi, Z. *et al.* Effect of dose on the biodistribution and pharmacokinetics of PLGA and PLGA-mPEG nanoparticles. *Int. J. Pharm.***221**, 143–152 (2001).
54. Kumari, A., Yadav, S. K. & Yadav, S. C. Biodegradable polymeric nanoparticles based drug delivery systems. *Colloids Surf. B Biointerfaces***75**, 1–18 (2010).
55. Prokop, A. & Davidson, J. M. Nanovehicular intracellular delivery systems. *J. Pharm. Sci.***97**, 3518–3590 (2008).
56. Vasir, J. K. & Labhasetwar, V. Biodegradable nanoparticles for cytosolic delivery of therapeutics. *Adv. Drug Deliv. Rev.***59**, 718–728 (2007).
57. Owens, D. E. & Peppas, N. A. Opsonization, biodistribution, and pharmacokinetics of polymeric nanoparticles. *Int. J. Pharm.***307**, 93–102 (2006).
58. Wang, M. & Thanou, M. Targeting nanoparticles to cancer. *Pharmacol. Res.***62**, 90–99 (2010).

59. Karakoti, A. S., Das, S., Thevuthasan, S. & Seal, S. PEGylated inorganic nanoparticles. *Angew. Chem. Int. Ed Engl.***50**, 1980–1994 (2011).
60. Danhier, F., Feron, O. & Pr at, V. To exploit the tumor microenvironment: Passive and active tumor targeting of nanocarriers for anti-cancer drug delivery. *J. Control. Release Off. J. Control. Release Soc.***148**, 135–146 (2010).
61. Song, C., Noh, Y.-W. & Lim, Y. T. Polymer nanoparticles for cross-presentation of exogenous antigens and enhanced cytotoxic T-lymphocyte immune response. *International Journal of Nanomedicine* (2016).
62. Tahara, K. *et al.* Improved cellular uptake of chitosan-modified PLGA nanospheres by A549 cells. *Int. J. Pharm.***382**, 198–204 (2009).
63. Verderio, P., Synthesis and Functionalization of Novel Composite Nanocarriers for Targeted Detection and Treatment of Malignant Cells, in *Chemical Sciences 2014*, University of Milan Bicocca: Milan. - Cerca con Google. Available
64. Andersson-Engels, S., Klinteberg, C. af, Svanberg, K. & Svanberg, S. In vivo fluorescence imaging for tissue diagnostics. *Phys. Med. Biol.***42**, 815 (1997).
65. Kim, J. S. *et al.* In vivo NIR imaging with CdTe/CdSe quantum dots entrapped in PLGA nanospheres. *J. Colloid Interface Sci.***353**, 363–371 (2011).
66. Yang, J. *et al.* Antibody conjugated magnetic PLGA nanoparticles for diagnosis and treatment of breast cancer. *J. Mater. Chem.***17**, 2695–2699 (2007).
67. Zhang, Y. *et al.* Preparation and characterization of gadolinium-loaded PLGA particles surface modified with RGDS for the detection of thrombus. *Int. J. Nanomedicine***8**, 3745–3756 (2013).
68. Bennewitz, M. F. *et al.* Biocompatible and pH-Sensitive PLGA Encapsulated MnO Nanocrystals for Molecular and Cellular MRI. *ACS Nano***5**, 3438–3446 (2011).
69. Cheng, F.-Y., Su, C.-H., Wu, P.-C. & Yeh, C.-S. Multifunctional polymeric nanoparticles for combined chemotherapeutic and near-infrared photothermal cancer therapy *in vitro* and *in vivo*. *Chem. Commun.***46**, 3167–3169 (2010).

Chapter II

PLGA-MnO COMPOSITE NANOMATERIALS FOR TARGETED IMAGING OF CROHN'S DISEASE



Index

1. Introduction	37
1.1. <i>Inflammatory Bowel Disease</i>	37
1.1.1. MAdCAM-1 expression	38
1.1.2. Inflammatory Bowel Disease Diagnosis	40
1.2. <i>Magnetic Resonance Imaging</i>	42
1.2.1. Nuclear Magnetic Resonance Principles	42
1.2.2. Relaxation times T_1 and T_2	49
1.2.3. Time Recovery and Time Echo	53
1.2.4. Contrast Agents for MRI	55
1.3. <i>Magnetic nanoparticles</i>	58
1.3.1. Manganese Oxide Nanoparticles as Contrast Agent for MRI	60
2. Preliminary results on MAdCAM-1 targeted MnO NPs	65
3. The goal	69
4. Materials and Methods	70
4.1. <i>Chemicals and biological materials</i>	70
4.2. <i>Synthesis of nanoparticles</i>	72
4.2.1. Synthesis of manganese oxide nanoparticles	72
4.2.2. Synthesis of polymer poly(Isobutylene- <i>alt</i> -maleic anhydride)	72
4.2.3. Manganese oxide nanoparticles phase transfer to organic solvent	73
4.2.4. Synthesis of polypoly(D,L-lactide-co-glycolide) nanoparticles	75
4.2.5. Synthesis of manganese oxide nanoparticles loaded polypoly(D,L-lactide-co-glycolide) nanoparticles	75
4.3. <i>Nanoparticles Characterization</i>	76
4.3.1. Reaction efficiency	76
4.3.2. UV-visible analysis	76
4.3.3. Dynamic Light Scattering and ζ -potential analysis	77
4.3.4. Inductively Coupled Plasma analysis	78
4.3.5. Stability test and degradation rate of nanoparticles	78
4.3.6. Transmission Electron microscopy and Scanning Electron microscopy	78
4.3.7. Metallic nanoparticles encapsulation efficiency and loading	78
4.3.8. Relaxation analysis	79
4.4. <i>Cytotoxicity assay</i>	79
4.5. <i>In vitro MRI analysis</i>	80
4.6. <i>In vivo experimental IBD model</i>	80
4.6.1. Histological assessment	81
4.6.2. Immunohistochemistry	81
4.6.3. Protein extraction and western blotting	82
5. Result and discussion	82

5.1.	<i>Reaction efficiency</i>	82
5.2.	<i>Calibration curves of manganese oxide nanoparticles</i>	82
5.3.	<i>Encapsulation efficiency and loading of metal nanoparticles</i>	84
5.4.	<i>Dynamic Light Scattering and ζ-potential analysis</i>	85
5.5.	<i>Transmission Electron Microscopy (TEM)</i>	86
5.6.	<i>Stability test and degradation rate of PMA@MnO NPs, PLGA NPs and PLGA@MnO NPs</i>	90
5.7.	<i>Relaxation analysis</i>	91
5.7.1.	Reproducible manganese-loaded poly(lactic-co-glycolic acid) nanoparticles enhancement power	100
5.7.2.	A comparison with commercial manganese-based contrast agent	101
5.7.3.	<i>In vitro</i> Magnetic Resonance Imaging analysis	104
5.8.	<i>Cytotoxicity assay</i>	107
5.9.	<i>MAdCAM-1 expression in experimental IBD model</i>	110
6.	Conclusion and Future perspectives	113
	List of Figures, Graphs and Tables	115
	References	122

1. Introduction

1.1. Inflammatory Bowel Disease

Inflammatory bowel diseases are a group of intestinal disorders that cause prolonged chronic inflammation of the digestive tract. The inflammatory bowel diseases, represented mainly by ulcerative colitis (UC) and Crohn's disease (CD), but including also non-infectious inflammations of the bowel, posed an enigma to gastroenterologists and immunologists since their first modern descriptions some 75 - 100 years ago.¹ Crohn's disease, in particular, is a long-term condition that involves inflammation in all parts of the gastrointestinal tract (from mouth to anus). It has an annual incidence of 12.7 per 100,000 person per year in Europe, 5 person-year in Asia and the Middle East, and 20.2 per 100,000 person-year in North America.² In time-trend analyses, 75 % of CD studies have had an increasing significant statistically incidence ($P < .05$). CD can affect indifferently the two sexes, mostly between 15 and 45 years of age.

Crohn's disease is associated with excess IL-12/IL-23 and IFN- γ /IL-17 production that affects the small bowel and colon with discontinuous ulceration and full thickness bowel wall inflammation often including granulomas.³

Patients have gastrointestinal manifestations of abdominal pain, diarrhea, and rectal bleeding as well as systemic symptoms of weight loss, fever, and fatigue. CD patients also develop fistulae between segments of bowel or between the bowel and skin and other organs.¹ In 25 - 40 % of patients, the typical signs and symptoms of IBD may be accompanied by symptoms in eyes, joints, skin, bones, kidneys, and liver. These non-bowel symptoms are called extra-intestinal manifestations (EIMs). Children who develop IBD often experience growth problems, without outward signs of an inflamed bowel.

Although there are few epidemiologic data from developing countries, the incidence and prevalence of IBD are increasing in time and in different regions around the world, indicating its emergence as a global disease.² In this perspective, it is fundamental to have an efficient diagnostic technique that allows the exact diagnosis and the follow-up of the disease.

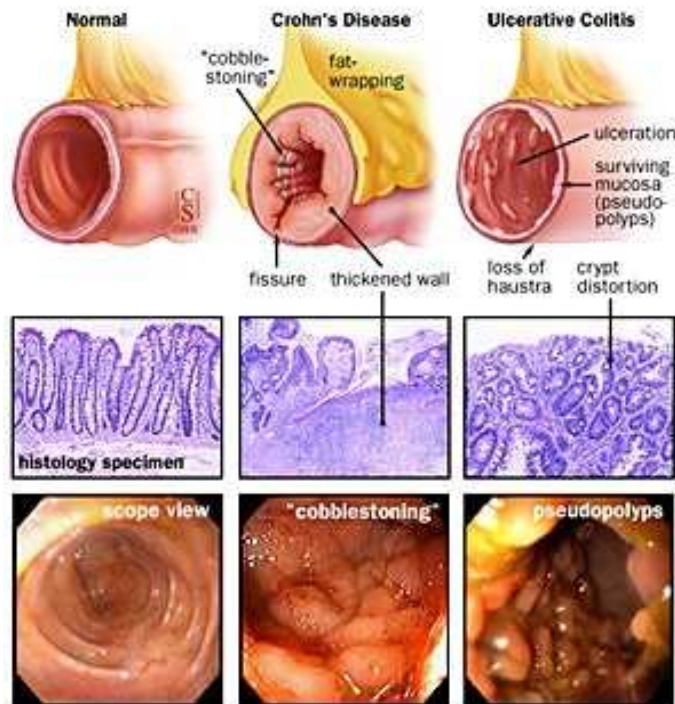


Figure 1.1. Depiction of colon in normal tissue, in Crohn's disease and in ulcerative colitis.⁴

1.1.1. MAdCAM-1 expression

Crohn's disease is characterized by non-caseating granulomas, lymphoid aggregates and extension of inflammation through all layers of the bowel wall. An increased expression of interleukin (IL)-2, interferon (IFN)- α and IL-12 is commonly observed in CD, suggesting the predominance of T-helper type 1 (Th1) response in CD.^{5,6,7} In addition, chemokines induce chemotaxis of leukocytes and their transendothelial migration, by stimulating the expression and the adhesive properties of leukocyte integrins. Tumor necrosis factor (TNF)- α and cell adhesion molecules, in particular, play a central role in the pathogenesis of chronic inflammation as they are involved in the adhesion of leukocytes (lymphocytes and granulocytes) to endothelial cells, and the subsequent activation and transmigration of leukocytes.^{6,7,8}

TNF- α is a transmembrane protein produced by macrophages and T-cells and released from activated cell membranes in response to endotoxins, IL-1 and TNF- α . TNF- α binds to TNF- α receptor on endothelium target cells and mediates the up-regulation of the selectin and adhesion molecules (e.g., E-selectin, VCAM-1 and MAdCAM-1), thus facilitating leukocyte adhesion and migration at the site of inflammation.⁸

In particular, MAdCAM-1 addresssin (mucosal vascular addresssin cell adhesion molecule 1) (Fig. 1.2) is an extracellular protein selectively expressed in the endothelium of venules⁹ and is encoded by the MADCAM-1 gene in human being.¹⁰ MADCAM-1 adesion molecules are responsible of recruiting T cells by linking the integrin $\alpha_4\beta_7$: the bound between the ligand and the correspondent receptor determines which tissue the lymphocyte will enter next. MAdCAM-1 overexpression on the inflamed portal vein/sinusoidal endothelium¹¹ further promotes the chronic inflammation in involved bowel tracts.

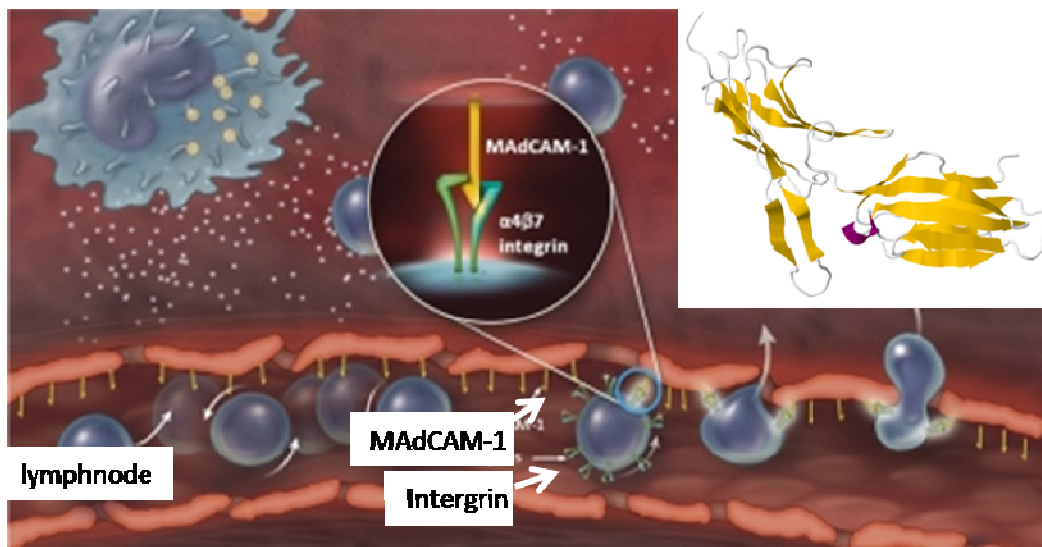


Figure 1.2. Mechanism of interaction between MAdCAM-1 molecules and the receptor integrin $\alpha_4\beta_7$; inset, 3D-structure of MACAM-1, mucosal vascular addresssin cell adhesion molecule 1.

Medical therapies of Crohn's disease rely on common anti-inflammatory, antibiotic and immunosuppressant drugs: corticosteroids, mesalamine compounds, azathioprine, and derivatives of the latter.¹ The drugs only maintain the control of symptoms, but don't constitute a definitively solution for the disease. Emerging therapies for IBD are focusing on major effectors cytokines as they are identified in ongoing investigations.^{12,13}

Natalizumab (brand name Tysabri) and Vedolizumab (brand named Entyvio) are monoclonal antibodies for immune system suppression recently approved for Crohn's disease. The drugs prevent the integrins from binding intestinal cells, thus limiting the immune response. Anti- α_4 integrin monoclonal antibodies bind the α_4 subchain preventing the leukosite adhesion to addresssin and reducing the leukocytes trafficking,¹⁴ thus reducing inflammation in patients.

Recombinant monoclonal antibody technology is used to develop the first generation of anti-inflammatory biological agents directed at neutralizing TNF- α and integrin α_4 subunits to reduce the immune response by blocking the recruitment of white blood cells (WBCs).⁹ The American Food and Drug Administration (FDA) firstly approved the use of Infliximab for the treatment of CD in 1998.¹⁵ Anti-TNF- α -agent monoclonal antibodies reduce inflammation by binding TNF- α and preventing receptor contact mitigating leukocyte recruiting. The most clinically used are Infliximab, Adalimumab, Certolizumab.

Table 1.1. Selected examples of clinical experience with emerging IBD therapies.¹

Agent	Target or action	Reported efficacy in
Anti-IL-12p40/ABT874	IL-12/IL-23	Active CD
Anti-IL-6 receptor	IL-6	Active CD
Fontolizumab	IFN- γ	Active CD
Visilizumab	CD3/apoptosis-activated T cell	Active UC
Basiliximab	IL-2 receptor	Active UC
Daclizumab	IL-2 receptor	No effect in active UC
Natalizumab	α_4 integrins	Active CD
MLN02	$\alpha_4 \beta_7$ integrin	Active UC
Alicaforsen	ICAM-1 (antisense oligonucleotide)	Active UC, maintenance of remission
GM-CSF	Innate immune system	Active CD
EGF	Epithelium	Active UC
Porcine whipworm oocysts	Innate immune system	Active UC

1.1.2. Inflammatory Bowel Disease Diagnosis

Routinely test recommended for IBD patients include the complete blood count to identify anemia, infection, inflammation, and monitor certain medications, the erythrocyte sedimentation rate (ERS) and the C-reactive protein to identify the inflammation, the screening of liver enzymes and the stool markers and cultures to detect complications, and the electrolytes to check for dehydration and medication side effects. None of the current commercially available serological biomarker tests allow high specific and helpful analyses for the diagnosis and the follow-up of IBD.¹⁰ The blood tests can only determine inflammation or complication by IBD, but are not able to diagnose IBD directly, thus more invasive techniques are required.

The standard procedure for IBD diagnosis consists of endoscopy, including sigmoidoscopy, upper endoscopy (EGD), capsule endoscopy (CE), endoscopic ultrasound (EUS), and biopsy. Besides the disadvantage of being invasive, these techniques do not reveal the condition of the entire intestinal tract, but only allow to investigate the small intestine.

For this reason, radiologic exams or diagnostic imaging are complementary techniques to evaluate the other segments of intestines as well as the areas outside the bowel. Crohn's disease evaluation is commonly performed by abdominal magnetic resonance imaging (MRI), by computed tomography (CT) scan or by bowel ultrasound (US).¹¹ The main advantage of MRI over other modalities is the ability to differentiate active inflammation from fibrosis in a thickened bowel segment.

MRI offers static and dynamic imaging capabilities. It does not involve ionizing radiation, it has excellent resolution of soft tissue, and it is safe in renal failure and pregnancy. The use of non-ionizing radiation makes MRI an attractive diagnostic test, particularly in young patients of reproductive age.¹⁶ For a more detailed discussion on MRI, see paragraph 1.3 and 1.4. Computed tomography scan has greater availability and minor costs required in comparison with MRI. Otherwise, CT lacks of dynamic information and differentiation between peristalsis and skip lesions may be difficult compared with the conventional barium studies.¹⁶ Doppler US is another emerging technology which can increase the sensitivity of transabdominal US and potentially may provide information about disease activity. The role of endoscopic US in inflammatory bowel disease is limited to perianal disease. In addition, barium enema, Leukocyte scintigraphy (white blood cell scans), small bowel follow-through (SBFT) and small bowel enteroclysis (SBE)¹⁶, X-rays and position emission tomography (PET)¹⁰ are also used as radiological diagnostic methods.

These techniques rely only on aspecific radiological signs of bowel inflammation, such as contrast enhancement of bowel wall thickening. However, specific imaging targeted for bowel inflammation is still lacking.

In this respect, nanomedicine offers a unique opportunity to design novel smart imaging enhancers, as specific active targeting agents, to achieve a highly accurate diagnosis of the stadiation and follow-up of the disease. To achieve this aim, inorganic manganese oxide nanoparticles (MnO NPs) are very attractive for molecular and cellular imaging due to their ability to provide positive (T_1 -weighted) enhancement of MR images and to their lower toxicity compared to gadolinium-based contrast agents.¹⁷

1.2. Magnetic Resonance Imaging

Magnetic resonance imaging (MRI) is one of the most powerful medical imaging techniques used in daily clinics to visualize the anatomy and the physiological processes of both healthy and sick participants in a non-invasive and real-time manner.¹⁸ MRI was built for the first time in the world by Raymond Damadian and his *post*-doctoral students, Michael Goldsmith and Larry Minkoff at New York's Downstate Medical Center. They achieved the earliest MRI scan of a healthy human body in 1977 and a human body with cancer one year later.

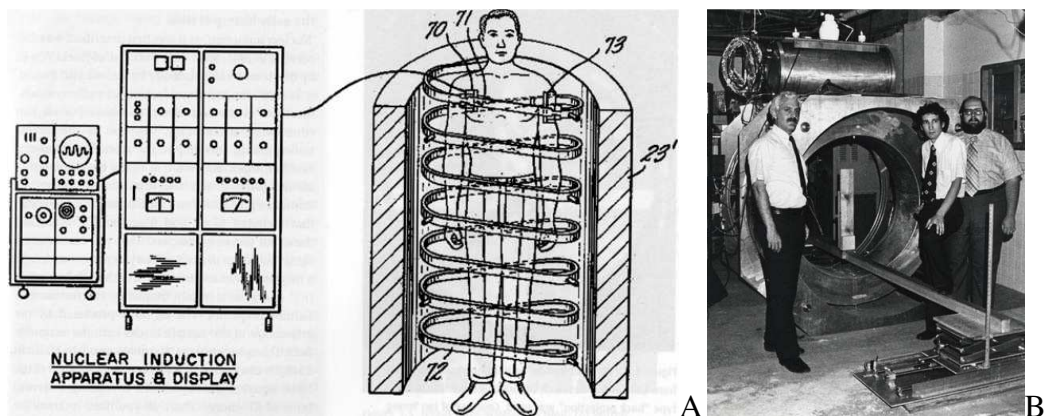


Figure 1.3. (A) Drawing of Damadian's invention of MRI; (B) Raymond Damadian, Larry Minkoff and Michael Goldsmith (from left to right) with Indomitable and its iced liquid helium and liquid nitrogen ports: the first supercooled, superconducting MR scanner and MRI machine in the world.

Magnetic resonance imaging exploits the response of the nuclear spin of hydrogen atoms of water in the body to a radio frequency and a gradient of an external strong magnetic field, taking into account that water protons in different environment will respond differently, thus leading to images with contrast between tissues. Nevertheless, the high cost of analysis and the inability to detect minor entities diseases don't make this technique suitable for routine examinations. In the last decades, contrast agents (CAs) were developed to implement further MRI analysis, thus enhancing the spatial resolution of MR images and increasing the sensitivity of the detection.¹⁹

1.2.1. Nuclear Magnetic Resonance Principles

Nuclear magnetic resonance imaging (MRI) based on the nuclear magnetic resonance (NMR) principles. NMR exploits the magnetic properties only of the nuclei with an odd mass number and an unpaired spin (e.g., hydrogen). Nuclear spin is an intrinsic characteristic of subatomic particles related to the direction of the precession of protons around their axis. For individual protons and

neutrons, spin is identified as a multiple of $\frac{1}{2}$ and can be positive (+) or negative (-). Each spin has an intrinsic angular momentum (or nuclear spin), indicated by the vector I . The rotation of the electric charge proton origins a small current loop and generates the magnetic dipole moment (or magnetic moment) μ . Nucleus with spin behaves like a small magnet, namely equipped with a magnetic dipole moment μ , and generates a weak magnetic field as a consequence (Fig. 1.4).

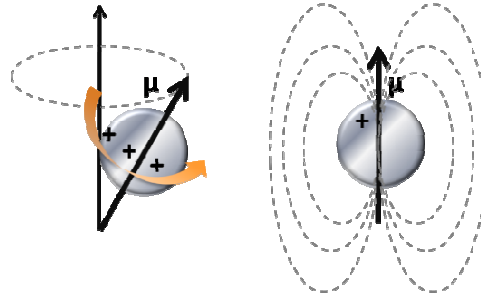


Figure 1.4. The rotation of the electric charge proton origins a small current loop and generates the magnetic dipole moment μ and consequently a weak magnetic field.

The magnetic moment μ is expressed by the following equation:

$$\mu = g \frac{e}{2m_p} = \gamma I, \quad \text{eq. 1.1}$$

$$\mu_z = g \frac{eh}{2m_p} m_I = g\mu_N m_I \quad \text{eq. 1.2}$$

where γ is the constant gyromagnetic ratio. For hydrogen it has the value of 46.2 MHz T^{-1} , and μ_z is the nuclear magneton ($5.05084 \cdot 10^{-27} \text{ J T}^{-1}$ and $3.15245 \cdot 10^{-8} \text{ eV T}^{-1}$).²⁰

Table 1.2. Nuclear spin I and magnetic moment μ of nuclides.²¹

Nuclide	Nuclear Spin I	Magnetic Moment μ (J T-1)
N	$\frac{1}{2}$	-1.9130418
P	$\frac{1}{2}$	+2.7928456
²H(D)	1	+0.8574376
¹⁷O	$\frac{5}{2}$	-1.8927900
⁵⁷Fe	$\frac{1}{2}$	+0.09062293
⁵⁷Co	$\frac{7}{2}$	+4.7330000
⁹³Nb	$\frac{9}{2}$	+6.1705000

When the nuclear magnetic moment μ associated with a nuclear spin I is placed in an external static magnetic field (B_0), the different spin states have different magnetic potential energies.

In the static magnetic field, spins align along its direction, bearing a small spin polarization. Aligning parallel with the magnetic field spins acquire energy and are at lower energy level (spin-up). On the contrary, aligning anti-parallel (spin-down) with the magnetic field spins decrease their energy and leap over energy state (Fig. 1.5). This phenomenon is known as Zeeman effect.

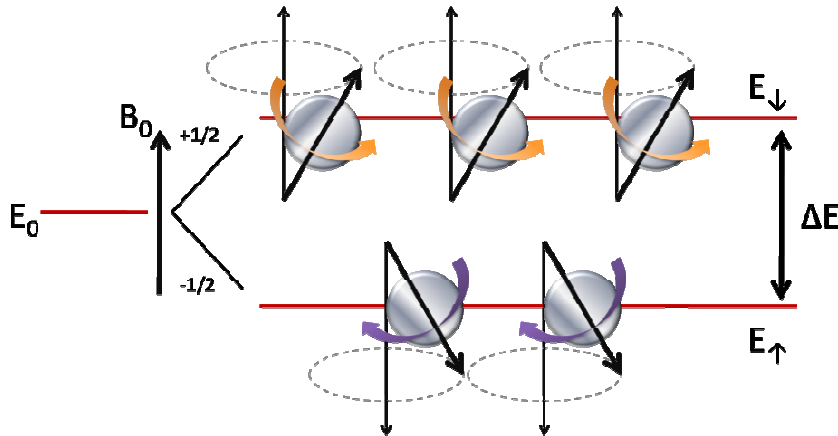


Figure 1.5. Proton spin alignment and energy level occupation follow the Boltzmann distribution in a static magnetic field B_0 . The energy gap (ΔE) between spin-up ($+ 1/2$) and spin-down ($- 1/2$) states is directly proportional to the magnetic field strength (B_0) (Nuclear Zeeman splitting).

The energy gap (ΔE) between two nuclear spin states scales directly with magnetic field strength and is given by the Zeeman equation:

$$\Delta E = \gamma h B_0 \quad \text{eq. 1.3}$$

The energetic distribution of the spin in the magnetic field follows the Boltzmann distribution (Fig. 1.5):

$$\frac{N_\beta}{N_\alpha} = e^{-\frac{\Delta E}{k_b T}} \quad \text{eq. 1.4}$$

Where k_b is the Boltzmann constant ($1.3806488 \cdot 10^{-23} \text{ J K}^{-1}$) and T is the absolute temperature (K).

The sum of all nuclear magnetic moments, both parallel and anti-parallel aligned with B_0 , generates a net vector called magnetization (M , or net magnetization vector) (Fig. 1.6), whose

potential energy is related to its orientation with respect to the magnetic field. At thermal equilibrium, M is aligned with B_0 .

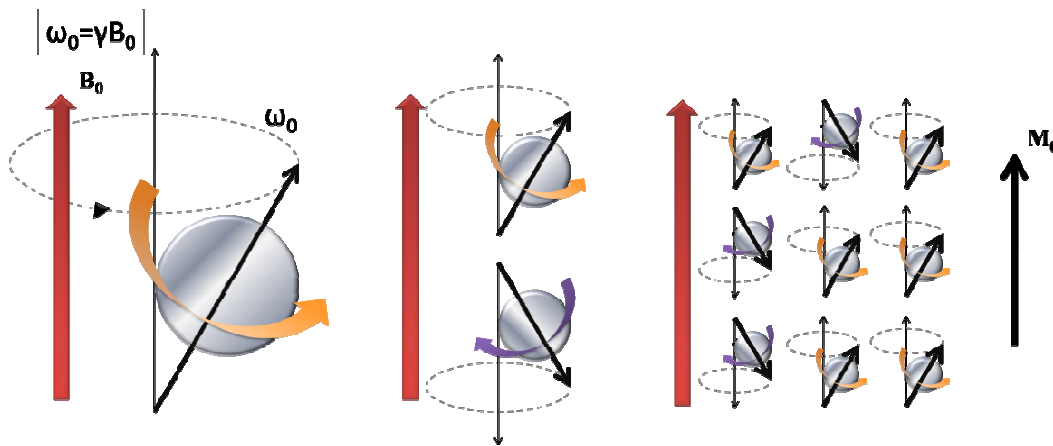


Figure 1.6. Depiction of the net magnetization (M) and the precession of spin as Larmor frequency (ω_0) in the static magnetic field B_0 .²² M is the averaged sum of a lot of individual quantum spins and can be treated as a regular vector in classical physics.

Like individual spins, M precesses around B_0 under a specific frequency (Fig. 1.6), known as the Larmor frequency (ω_0), defined by the Larmor equation (eq. 1.5). This phenomenon is called proton precession.²⁰

$$\omega_0 = \gamma B_0, \quad \text{eq. 1.5}$$

where ω_0 (Hz) is the resonance frequency of protons in a specific field and B_0 (T) is the external magnetic field.

For a 1 Tesla magnetic field the Larmor frequency would be:

$$\omega_{proton\ spin} = \frac{2\mu_p B}{\hbar} = \frac{2(2.79)(3.15 \cdot 10^{-8} eVT^{-1})(1T)}{6.58 \cdot 10^{-16} eVs} = 2.6753 \cdot 10^8 s^{-1} \quad \text{eq. 1.6}$$

$$\text{Larmor frequency: } \nu = \frac{\omega}{2\pi} = 42.5781MH \quad \text{eq. 1.7}$$

The precession of the proton spin in a static magnetic field is exploited in proton NMR to obtain signals. In MRI the unpaired spins of hydrogen protons (H) are used to generate images, mainly because of H abundance in the body, such as in water (H_2O) and in fat ($-CH_2$). When the nuclei are subjected to a radiofrequency pulse, protons absorb energy and are excited to the anti-parallel state.

This leap occurs only at the resonance frequency ω_0 , that is the Larmor frequency. Thus, the Larmor frequency corresponds to the quantum energy provided for the transition between the two possible spin states. The transition energy can be expressed as photon energy according to the Planck relationship; hence the difference of magnetic potential energy is described in equation 1.8:

$$h\nu = 2\mu B \qquad \text{eq. 1.8}$$

As a consequence of the spin transition, M changes direction, way and module.

Net magnetization (M) behaves as a vector using the principles of classical physics. From this point forth we will almost exclusively use the vector M rather than individual nuclear spins to explain the aspects of both NMR and MRI.²⁰

Although the individual nuclei are all precessing, at this time M is not and is aligned with the external field (B_0). Just like a perfectly upright spinning top or gyroscope, there is not yet a precession of M . To induce precession, M must be displaced out of its equilibrium alignment by an external injection of energy at the Larmor frequency. When M tips out of alignment, it precesses in the transverse plane also at the Larmor frequency (Fig. 1.7 c).

Since M is a vector rotating in space it can be resolved into three components: $M_x(t)$, $M_y(t)$, and $M_z(t)$, each function of time. $M_x(t)$ and $M_y(t)$ are named transverse components; $M_z(t)$ is the longitudinal component (Fig.1.7 a).

The modification of each component of the magnetization vector M in time provides a lot of information about materials, such as magnetic properties, viscosity, elasticity, etc.. For this reason, the quantification of the behavior of M_z and M_{xy} is extremely necessary. On this purpose, Felix Bloch published a mathematical analysis of the nuclear induction phenomenon including a set of equations explaining the origin and properties of the NMR signal, in 1946. Bloch's equations are a set of macroscopic equations to calculate the nuclear magnetization M as a function of time when relaxation times T_1 and T_2 are first-order kinetics constant (par. 1.3.2).²³ Bloch assumed that the millions of individual nuclei in a sample could be represented by a single vector M . At equilibrium in the magnetic field, the net magnetization vector M reaches its maximum value ($M_0 = M_z(0)$; $M_{xy}(0) = 0$). As a consequence of a RF pulse, M varies its direction, way and module in few milliseconds, depending on the strength of the magnetic field applied and on the examined tissue type or, more punctually on the mobility of protons within the tissue. When the RF pulse stops, the

excited nuclei relax and return to their equilibrium values of the lower state producing a measurable RF signal at the resonant frequency associated with the spin flip. This process is called nuclear magnetic resonance (NMR). The emission of radiation is associated with the spin relaxation of the protons from their excited state. It induces a radio frequency signal in a detector coil which is amplified to display the NMR signal. Since the Larmor frequency of the detected signal is proportional to the applied magnetic field, changing the magnitude of that field produces a different detected frequency. Placing a magnetic field gradient across a sample allows the source of the proton NMR signal to locate in the sample. This is used to great advantage in the medical imaging process known as Magnetic Resonance Imaging.

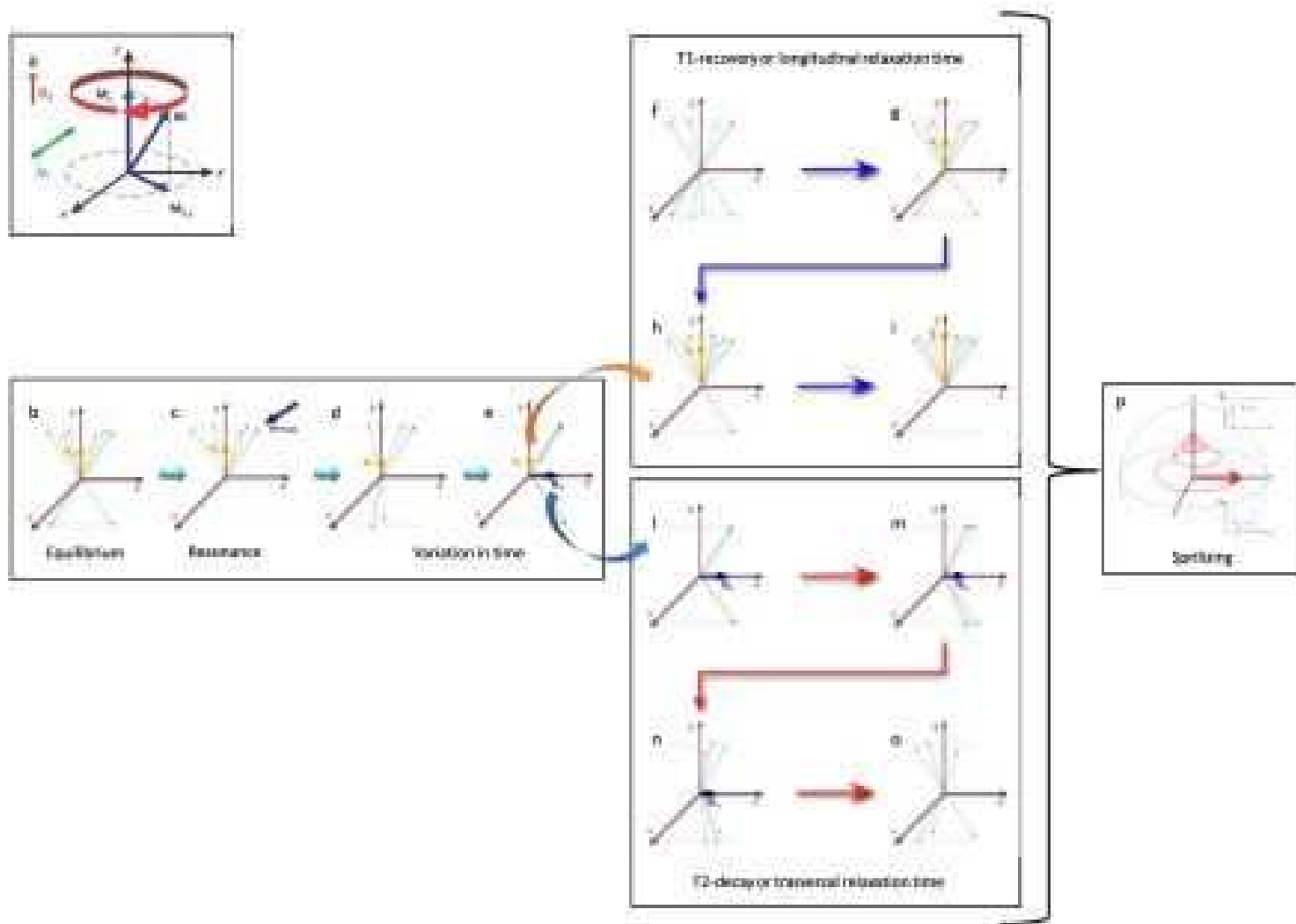


Figure 1.7. (a) Components $M_x(t)$, $M_y(t)$ and $M_z(t)$ of magnetization vector M ; (b) Magnetization vector at equilibrium; (c) Precession of magnetization vector at the Larmor frequency after a RF pulse in a static magnetic field; (d, e) Magnetization vector variation after the RF pulse; (f - i) M_z recovery in time along z axis; (j - o) M_{xy} decay in time in xy plane back to module value 0; (p) M spiralization after the RF pulse to restore the equilibrium state.

1.2.2. Relaxation times T_1 and T_2

MRI is interested in the variation of the component transversal magnetization (M_{xy}) and longitudinal magnetization (M_z) depending on time ($M_{x,y}(t)$ and $M_z(t)$). Conventionally, M_z has the same direction of the applied magnetic field. Before the RF pulse application, the net magnetization M_0 has his maximum value, as all proton spins are aligned along the direction of the external static magnetic field (B_0). In this situation M_0 is equal to M_z while the contribution of the component M_{xy} is nil. When a RF at the Larmor frequency is applied, M_0 varies in module and direction. In particular, the M_z module decreases, while the transverse magnetization M_{xy} increases in the xy plane perpendicular to the direction of the static magnetic field (Fig 1.7 f – i). The change of M_z in way and module is due to energetic transfer, while M_{xy} variation is due to the process of spin dephasing caused by the randomization of the magnetization of excited spins with the same phase coherence immediately after the application of the RF pulse.²²

At the end of the RF pulse, the net magnetization vector tends to reestablish the original state through a process called relaxation.

The two components M_{xy} and M_z of the magnetization vector relax at different speed and follow different pathways. The relaxation of M_z , called longitudinal relaxation T_1 , occurs along the z axis, while the transversal relaxation T_2 of M_{xy} component relaxes in the xy plane. As T_1 and T_2 occur simultaneously, M exhibits a spiralizing precession around B_0 at the Larmor frequency with decay of transverse components back to zero and regrowth of the longitudinal component to its original maximum value M_0 (Fig. 1.7 l - o). T_2 is always shorter than T_1 , so the transverse components typically decay completely before the longitudinal magnetization is fully restored.

Nowadays, no comprehensive quantitative theory has been developed yet about the exhaustive explanation of specific T_1 and T_2 values of tissues. Nevertheless, six basic mechanisms responsible for relaxation are identified: chemical shift anisotropy, molecular translation, flow or diffusion, chemical exchange, scalar (J-coupling), electric-quadrupole coupling and dipole-dipole interactions. The last mechanism is the predominant for the ^1H nuclei relaxation.

In detail, the longitudinal relaxation time T_1 regards the re-growth (T_1 -recovery) of the net magnetization (M_z) in time on the z axis, while the transverse relaxation time T_2 , involves the decay of the magnetization (M_{xy}) in time in the perpendicular plane (T_2 -decay).²⁴ Both relaxation times T_1 and T_2 are first-order kinetics constants. The longitudinal (or spin-lattice) relaxation time T_1 is the

decay constant for the recovery of the z component of the nuclear spin magnetization M , towards its thermal equilibrium value, $M_{z,eq}$ (Fig. 1.8 a).

$$M_z(t) = M_{z,eq}(0) - [M_{z,eq} - M_z(0)]e^{-t/T_1} \quad \text{eq. 1.9}$$

Longitudinal relaxation is modelled as exponential growth curve with time constant T_1 (Fig. 1.8 a). M reaches 63% of its maximum value (M_0) at t equal to T_1 and it is very closed to maximal at t correspondent to $5T_1$.

If M has been tilted into the xy plane, it results $M_z(0) = 0$ and the recovery is simply:

$$M_z(t) = M_{z,eq}(1 - 2e^{-t/T_1}) \quad \text{eq. 1.10}$$

In particular, T_1 is the time the magnetization recovers to 63% of its equilibrium value after the applied RF.

T_1 relaxation redistributes the populations of the nuclear spin states in order to reach the thermal equilibrium. By definition, this is not energy conserving. Moreover, spontaneous emission is negligibly slow at NMR frequencies. Hence truly isolated nuclear spins would show negligible rates of T_1 relaxation. However, a variety of relaxation mechanisms allows nuclear spins to exchange energy with the surroundings, the lattice, allows the spin populations to equilibrate. For this reason, it is also named spin-lattice relaxation. The rates of T_1 relaxation are generally strongly dependent on the NMR frequency and so vary considerably with magnetic field strength.

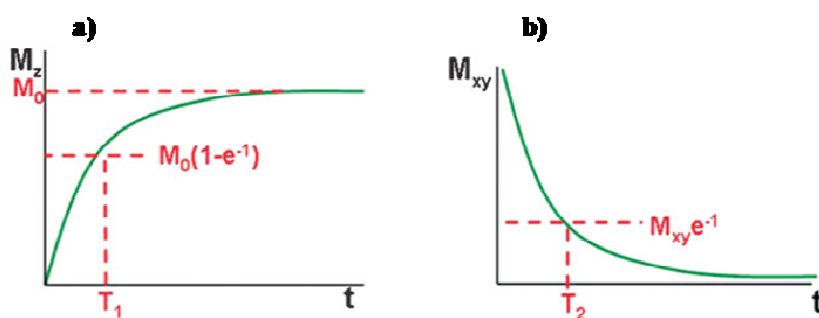


Figure 1.8. (A) Increased magnetization along the z axis. (B) Decay of the magnetization in the xy plane.

On the other hand, the transverse (or spin-spin) relaxation time T_2 is the first order decay constant of the component M_{xy} . For example, initial xy magnetization at time zero will decay to zero to reach the equilibrium and is described by the equation 1.11.

$$M_{xy}(t) = M_{xy}(0)(e^{-t/T_2}) \quad \text{eq. 1.11}$$

The transverse magnetization vector drops to 37% of its original magnitude after the time constant T_2 (Fig. 1.8 b). Transversal relaxation is a complex phenomenon, simply explained as the decoherence of the transverse nuclear spin magnetization. Random fluctuations of the local magnetic field lead to random variations in the instantaneous NMR precession frequency of different spins. As a result, the initial phase coherence of the nuclear spins is lost and no net magnetization is detectable. T_2 relaxation is also called spin-spin relaxation because it involves only the phases of nuclear spins. T_2 values are less dependent on magnetic field strength than T_1 values. T_2 relaxation always proceeds at a faster rate than T_1 relaxation; thus the T_1 relaxation time is always 5-10 times longer than or equal to T_2 (table 1.3).

Table 1.3. Approximate values of T_1 and T_2 at 1.5 T of some elements of the human body.²³

Tissue type	Approximate T_1 (msec)	Approximate T_2 (msec)
Water/CSF	4000	2000
Adipose tissue	240-250	60-80
Whole blood (oxygenated)	1350	200
Cerebrospinal fluid	2200-2400	500-1400
Grey matter	920	100
White matter	780	90
Liver	490	40
Kidneys	650	60-75
Muscle	860-900	50
Fat	250	70
Tendon	400	5
Proteins	250	0,1-1
Ice	5000	0,001

In an ideal system, all nuclei in a magnetic field and in the same chemical environment precess with the equal frequency around the z axis (the direction of B_0). The transverse components of M generate a current in the receiver coil based on the Faraday-Lenz Law of electromagnetism of an NMR apparatus. The signal is a sine wave oscillating at the Larmor frequency (ω_0). Nevertheless, in real systems, there are minor differences in chemical environment which can lead to a distribution of resonance frequencies around the ideal. Over time, this distribution can lead to a dispersion of the tight distribution of magnetic spin vectors, and loss of signal. The initially

coherent transverse components of M dephase as a result of both magnetic field inhomogeneities and intrinsic T_2 mechanisms, and resulting in a Free Induction Decay (FID) (Fig. 1.9):

$$[\sin(\omega_0 t)]e^{-t/T_2^*} \quad \text{eq. 1.12}$$

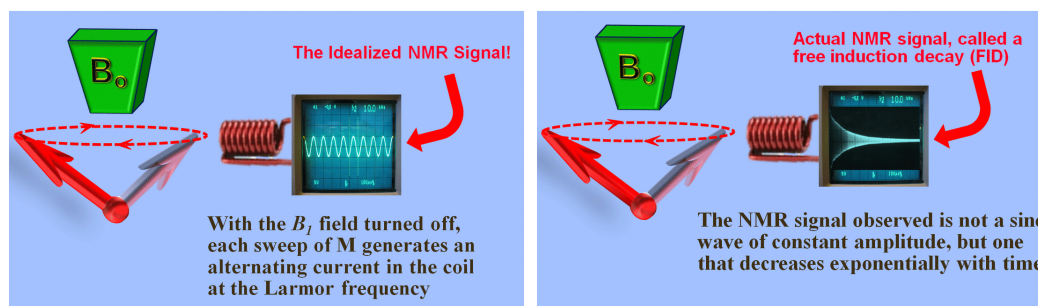


Figure 1.9. Ideal NMR signal is sinusoidal, while actual signal decay over time.¹⁸

T_2 depends on how fast protons in tissue lose their phase coherence and it is associated with their density. High density means more spin-spin interactions and faster phase shift (Table 1.4). Fluids for example have relatively long distances between molecules and therefore long T_2 .

Table 1.4. T_1 and T_2 properties for three different types of tissues.²³

	Fluids	Solid	Fat and Protein rich tissue
T_1	Non efficient energy transfer Very long T_1	Inefficient energy transfer Long T_1	Efficient energy transfer Short T_1
T_2	Less dephasing Long T_2	Most dephasing Short T_2	Intermediate dephasing Intermediate T_2

The characteristics T_1 in a tissue depend on the efficiency of proton transfer. Experimental data have shown the transfer of the proton energy will be more efficient when the vibration or the rotation frequencies of the molecules are similar to Larmor frequency. The Larmor frequency depends on the magnetic field (eq. 1.5), while the vibrational frequencies depend on the physical state of the tissue. Water vibrations cause fluctuations of the protons at the same frequency of the magnetic field and this disturbance in the magnetic field stimulates the relaxation. The rotational frequency of C-C bonds in fatty tissue is close to the Larmor frequency and therefore brings to an efficient transfer of energy. On the contrary small water molecules vibrate at higher frequency leading to a lower efficient transfer of energy. (Tab. 1.4).

1.2.3. Time Recovery and Time Echo

An MR analysis allow to obtain images of the interior body highlighting different areas of it, by exploiting the different relaxation times of tissues (Table 1.3). It is possible to elaborate four classes of images (Fig.1.10): poor contrasted image, proton density (PD), T_1 -weighted and T_2 -weighted images. In this paragraph we focused only on the for last two kind of images. These types of images can be obtained by varying the parameters of acquisition of the MR signal.

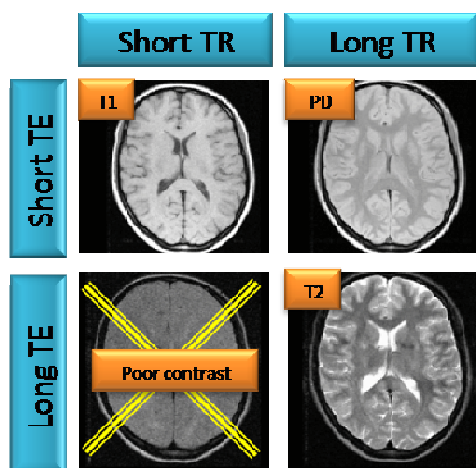


Figure 1.10. The four classes of MRI images obtained by varying TR and TE.²³

Repetition Time (TR) and echo time (TE) are basic pulse sequence parameters, typically measured in milliseconds (ms) (Fig. 1.11). The echo time (TE) represents the time from the center of the RF-pulse to the center of the echo while the repetition time (TR) is the length of time between corresponding consecutive points on a repeating series of pulses and echoes.

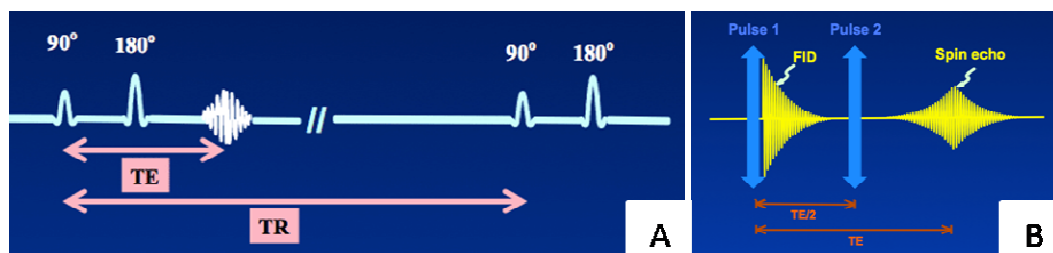


Figure 1.11. (A) Schematic representation of repetition time (TR) and echo time (TE); (B) Schematic representation of Free Induction Decay (FID) and echo time (TE).²³

A single RF pulse generates a free induction decay (FID), but two successive RF pulses produce a spin echo (SE). The time between the middle of the first RF pulse and the peak of the spin echo is called the echo time (TE) (Fig. 1.29).

The SE represents the regeneration of spin phase information apparently lost during the decay of the FID. Most of the FID signals have not been destroyed, but have merely due to the disorganized individual spins that lose their phase coherence. As a lot of processes producing the FID are symmetrically reversible, the application of second RF pulse allows to refocus into SE spins to the original FID and allows to measure the real T₂ value (e.g., by means of the Hahn Echo Decay experiment).

2.1.1. T₁-weighted images and Repetition Time (TR)

To generate a T₁-weighted image, the site of interest must be excited with several RF pulses. Repetition time affects directly the T₁ contrast because it regulates the available time for relaxation after the pulse. A long TR allows a better realignment along the z axis and a bigger angle to overturn a radio frequency. A short TR permits to highlight tissues with short T₁, which are generally able to recover at higher level. This will give bigger net magnetization which provides brighter spots in the MR image. On the other hand, tissues with longer T₁ have shorter time to relax and they will have consequently smaller net magnetization. In conclusion, image given by short TR contains more information about T₁ and is therefore called T₁-weighted.²⁰

2.1.2. T₂-weighted images and echo time (TE)

The echo time (TE) is the time between the RF pulse and the measuring time and it influences directly the T₂ contrast. Using a TE of the same order of magnitude of the T₂ of the tissues, differences in their relaxivities will be underlined. Commonly, tissues with short T₂ have more phase shift and lose much of their net magnetization M_{xy}, while tissues with long T₂ give a strong signal. A short T₂ gives a faster phase shift and a faster signal loss, and as a consequence, tissues with short T₂ appear darker. The greater the difference between the decay curves, the sharper the contrast is. (Fig. 1.12 A). Images acquired with a long TR and a long TE will give a dark spots for tissues with short T₂; for this reason they are called T₂-weighted images.²⁰

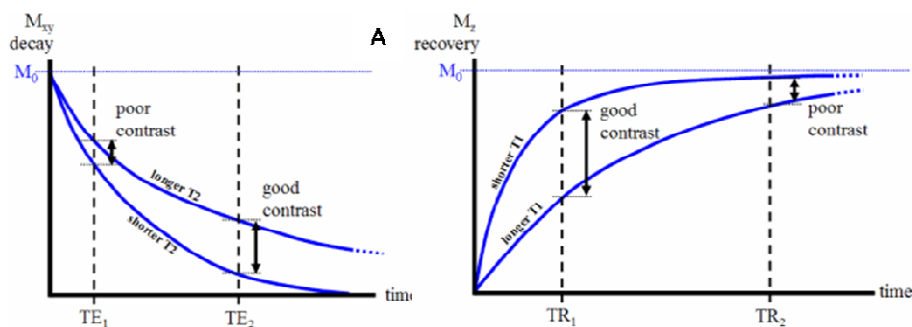


Figure 1.12. Differences between (A) T_2 -decay and (B) T_1 -recovery curves lead to a sharper contrast.

1.2.4. Contrast Agents for MRI

Among the current existing imaging techniques such as X-ray, ultrasound (US), radioactive markers, MRI is the most used diagnostic tool due to its ability to perform images in real-time with a high spatial resolution to discriminate tissues *in vivo*, according to their biochemical composition. Furthermore, MRI is a non-invasive and safe technique since patients are not subjected to ionizing radiation or treated with radioactive isotopes. However, MRI application in clinics is limited by the high costs of technicians and equipment maintenance, and by the time required for the acquiring images. Moreover, it is difficult to distinguish magnetically similar but histological different tissues (e.g., healthy from diseased tissues).

In the last decades, the introduction of chemical moieties able to enhance the spatial resolution of MR images allows to overcome these important limitations. These entities named contrast agents, improve contrast images by shortening the relaxation time constants T_1 and T_2 of the proton spins of tissues of body (par. 1.4), thus the contrast with the surrounding tissues increases and high-quality images are obtained.. CA directly influence the relaxation times T_1 and T_2 , depending on its concentration and on the pulse sequence (or excitation sequence) used to collect data.²⁵

Contrast agents need to satisfy many requirements to be efficient MR enhancers. They should have high susceptibility to attest the magnetic property of the agent. The classification of magnetic properties of material is based on its magnetic susceptibility (χ) (par. 1.2.1), which in turn depends on their atomic structures, temperature, and the external field.

An efficient CA aims at enhancing or modifying the natural contrast between different structures and tissues to allow a detailed characterization of tissue in order to improve the diagnosis. The

efficiency of contrast agents depends on their relaxivity (r). Relaxivity is an intrinsic property of an MR CA that reflects the changing relaxation rate behavior of a solution as a function of the concentration of the contrast enhancer. Relaxivity is calculated by the nuclear relaxation times T of water protons produced by 1 mM of contrast compound. Relaxation times permit to calculate the relaxation rates (R) R_1 and R_2 , as the reciprocal values of T_1 and T_2 , respectively. Plotting R data (s^{-1}) against concentration (mM) it is possible to obtain the relaxivity r ($mM^{-1} s^{-1}$) that coincides with the angular coefficient of the curve. Each contrast agent has a characteristic longitudinal (r_1) and transverse (r_2) relaxivities, obtained by plotting respectively R_1 and R_2 (Fig. 1.13).

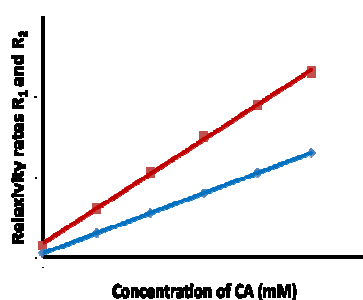


Figure 1.13. Relaxivities r_1 and r_2 , extrapolated by the curve relaxation rates R_1 or R_2 versus the concentration of CAs.

As T_2 is always longer than T_1 (par. 1.3.2), r_2 is higher than r_1 and the ratio between the transversal and longitudinal relaxivities (r_2 / r_1) is equal or major than one. In general, higher r_1 and lower the ratio, better the CA is as T_1 enhancer.

MRI CAs currently used in clinic are classified as T_1 -positive (bright) and T_2 -negative (dark) contrasts and they are selected for detecting anomalies depending on the nature of the tissue analyzed.²⁵ Table 1.5 reported an overview of the contrast agents actually use in clinic, already withdrawn from the market, or being developed.^{24,27,29}

T_1 CAs are primarily paramagnetic elements, while T_2 contrast agents are superparamagnetic materials.

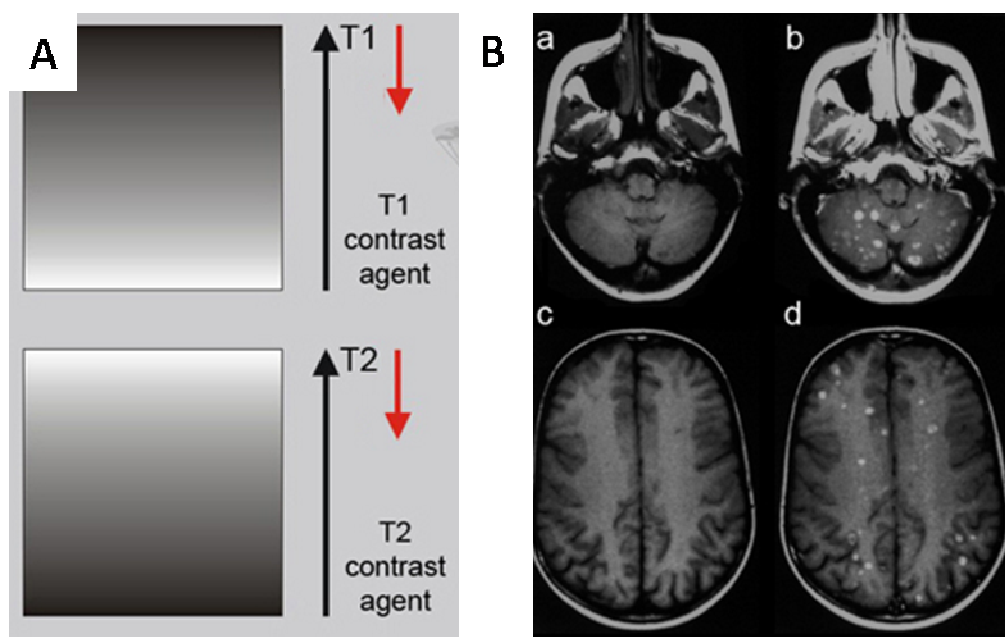























Figure 1.14. (A) Influence of positive (T_1) and negative (T_2) MR contrast agents upon signal intensity. (B) Example of a clinical case where only the application of a positive contrast agent helped the diagnostic process to show the extent of the disease (breast cancer and recent neurological symptoms). The plain MR T_1 -weighted images (pre-contrast a and c) do not reliably reveal brain lesions. However, the contrast-enhanced MR images (post-contrast b and d) show a large number of metastases.²³

Table 1.5. Overview of several MR contrast agents actually use in clinic, already withdrawn from the market, or being developed.²³

Code Name	Generic Name	Trade Name *
Extracellular Fluid (ECF) Space Agents **		
■	Gd-DOTA	Gadoteric acid Dotarem (et al.)
■	Gd-HP-DO3A	Gadoteridol ProHance
■	Gd-DO3A-butrol	Gadobutrol Gadovist Gadovist et al.
■	Gd-BOPTA	Gadobenate dimeglumine MultiHance
■	Gd-DTPA	Gadopentetate dimeglumine Magnevist (et al.)
■	Gd-DTPA-BMA	Gadodiamide injection Omniscan
■	Gd-DTPA-BMEA	Gadoversetamide Optimark
Targeted / Organ-Specific Agents ***		
■	Mn-DPDP	Mangafodipir trisodium Teslascan [new version]
■	Mn-PLD	Manganese pyridoxil ethyl diamine —
■	Ca ₆ Mn(DPDP) ₅	Calmangafodipir —
■	Gd-BOPTA	Gadobenate dimeglumine MultiHance
■	Gd-EOB-DTPA	Gadoxetic acid disodium Primovist Eovist
■	Gd-DTPA mesoporphyrin	Gadophrin —
■	Gadomer-17	— —

	P792	Gadomelitol	Vistarem
	Gadofluorine P	—	—
	Gadofluorine-M	—	—
	AMI-25	Ferumoxides (SPIO)	Endorem Feridex
	SHU 555 A	Ferucarbotran (SPIO)	Resovist Clivist
	NC-100150	PEG-feron (USPIO)	Clariscan
	AMI-227	Ferumoxtran-10 (USPIO)	Sinerem Combidex
	Dy-DTPA-BMA	Sprodiamide injection	—
Blood Pool Agents			
	MS-325	Gadofosveset trisodium	Formerly Angiomark and Vasovist; Albavar
	SH U 555 C	Ferucarbotran (USPIO)	Supravist
Commercial Enteral Agents (orally or rectally administered)			
	Gd-DTPA	Gadopentetate dimeglumine	Magnevist enteral
	—	Ferric ammonium citrate	Ferriseltz
	—	Manganese chloride	LumenHance
	—	Gadolinium-loaded zeolite	Gadolite
	Oral Magnetic Particles (OMP)	Ferristene (MPIO)	Abdoscan
	AMI-121	Ferumoxsil (MPIO)	Lumerem Gastromark

 = agent available for clinical and/or research application;  = agent available for clinical and/or research application with severely limited indications ("high risk");  = agent being developed;  = development interrupted or discontinued;  = agent withdrawn from one or all major markets; * = trademark or registered trademark; ** = with high concentrations, negative contrast can be achieved (e.g., first-track bolus); *** = all ECF agents are also kidney-specific agents; (et al.) = the compound is sold under different trade names.

1.3. Magnetic nanoparticles

Although early research can be dated back to several decades, the recent surge of interest in nanotechnology has significantly gone deeper in magnetic nanoparticles (MNPs) research. Among all inorganic nanocomposites, iron and manganese nanoparticles have attracted lot of attention due to their magnetic properties that make them significant tools in meeting the actual healthcare needs.^{24-27,30}

Several kinds of MNPs have been proposed and evaluated for biomedical applications thanks to magnetic phenomena they exhibit at nanoscale, such as enhanced magnetic moments and superparamagnetism.^{24,30-33} In order to employ MNPs for biomedical applications, magnetic nanoparticles have to be monodisperse MNPs to better control on biodistribution and

bioelimination, and to decrease side effects. Moreover no relevant toxic effect on living organism must be detected.^{34,35}

A significant challenge associated to MNPs application is the *in vivo* behavior. Indeed, the efficacy of the nanocomposite is often compromised by the recognition and the clearance by the reticuloendothelial system (RES) prior to reaching the target tissue, as well as by the inability of to overcome biological barriers, such as the vascular endothelium or the blood brain barrier (BBB). The fate of these MNP upon intravenous administration is highly dependent on their size, morphology, charge, and surface chemistry. The NP physical-chemical properties affect directly pharmacokinetic and pharmacodynamic profiles, and thus, by tailoring particle composition, size, morphology and by grafting non-fouling polymers, it could be possible to improve magnetic properties and influence MNPs *in vivo* behavior, such as the increment of stealthiest and blood circulation time to maximize the likelihood of reaching targeted tissues.³⁶

The simplest magnetic NP-based biomedical nanoplatform consists of a inorganic *core* and a biocompatible surface coating that provides the particle stabilization under physiological conditions and decreases their cytotoxic effects. Additionally, the application of suitable surface chemistry allows for the integration of functional ligands. MNPs tunability and versatility have the potential to overcome some restrictions associated with the systemic distribution of conventional chemotherapies. Moreover, drug in the form of antibody or chemical molecules could be loaded onto NPs surface, opening the possibility of using them as therapeutic agents.³³ This modular design enables MNPs to perform multiple functions simultaneously, such as multimodal imaging, drug delivery and real-time monitoring, as well as combined therapy.

In addition, the penetration of magnetic fields through human tissue and the ability to remotely manipulate MNPs by an external magnetic field, could address particle accumulation upon location of a malignancy or lesion and provide a magnetically controllable tagging of biomolecules, thus leading to an high efficient bioseparation and sensitive biosensing.³⁷ Magnetofection is an example of this type of application, that combines the common biochemical and physical transfection methods with the use of magnetic fields to concentrate particles containing nucleic acids into the target cells, thus improving their efficiency and decreasing their toxicity.

In the last decades MNPs became also one of the most exploited nanoparticles for hyperthermic treatment, especially for cancer care.³⁸⁻⁴⁰ MNP resonant response to an external alternating

magnetic field converts the magnetic energy to heat, and hence warms up the surrounding environment.

A recent and significant application of MNP magnetic properties has been in MR diagnostic field: the potentiality of the actual clinical imaging can be expanded greatly through the use of MNPs to improve differentiation of malignant and healthy tissues. Next-generation MNP-based MR imaging contrast agents and drug delivery systems^{38,40-43} incorporate novel nanocrystalline *cores*, coating materials, and functional ligands to targeted detection and delivery. Concurrently, the use of new surface coatings, such as gold or silica shells and polymeric self-assembled monolayers, allows for the reduction of potential toxicity of the inorganic *core*. Next-generation platforms could incorporate surface qualities that would enable probing and/or monitoring of local physical mechanistic changes greatly improving disease detection, monitoring, and treatment. Although a lot of nanocomposites are in pre-clinical evaluation, many efforts are necessary to conserve the efficacy and evaluate the potential long-term toxicity of MNPs.³⁷

1.3.1. Manganese Oxide Nanoparticles as Contrast Agent for MRI

Paramagnetic ions are mainly used as extracellular contrast agents. In imaging of liver, they provide important information for the detection of lesions and for characterization of focal and diffuse liver pathologies (in general using dynamic imaging). Regarding lesion detection, characteristic enhancement patterns have been identified for several benign and malignant masses of both hepatocellular and non-hepatocellular origin.

Among T_1 paramagnetic contrast agents, gadolinium is the most exploited in clinic diagnosis is contrast medium for magnetic resonance^{43,45,46} due to the highest number of unpaired electrons in the orbital valence ($7 e^-$) conferring it the highest ability to alter the relaxation times of adjacent protons. Free gadolinium (Gd^{+3}) is extremely toxic because it tends to precipitate and to deposit in liver, lymph nodes and bones. It can also obstruct the transport of calcium ions through the muscle cells, blocking the calcium flow into the cells of the nervous tissue, causing arrest of neuromuscular transmission. For these reasons, Gd-based agents are always administered to patients in a chelated form commercially available since 1986. Chelated-complex are thermodynamically and kinetically more stable and less toxic. Chelates of gadolinium distribute without any tissue-specific allocation. The first MR contrast agent introduced into the market is gadopentetate dimeglumine (Magnevist®, Gd-DTPA; Schering AG). Other Gd-chelates include gadoteridol (ProHance®, Gd-HP-DO3A; Bracco Diagnostics), gadodiamide (Omniscan®, Gd-DTPA-BMA; GE Healthcare)

gadoversetamide (Optimark®, Gd-DTPA-BMEA; Mallinckrodt), gadoterate meglumine (Dotarem®, Gd-DOTA; Guerbet), gadobutrol (Gadovist®, Gd-BT-DO3A; Schering AG), and gadofosveset (Vasovist®, Schering AG). In 1998, gadobenate dimeglumine (MultiHance®, Gd-BOPTA; Bracco Diagnostics) has been approved in Europe for MRI of the liver. Another agent with combined extracellular and hepatobiliary properties, gadoxetic acid disodium, or gadolinium-ethoxybenzyltriethylenetriaminepentaacetic acid (Primovist®, Gd-EOB-DTPA; Schering AG), has been approved for use in Europe. Gadolinium oxide (Gd₂O₃), gadolinium fluoride (GdF₃), and gadolinium phosphate (GdPO₄) nanoparticles showed an improvement in the contrast enhancement in T₁-weighted images. Usually, contrast agents based on Gd₂O₃ nanoparticles are composed of a small core of < 5 nm and stabilized with shells of dextran, PEG, and silica. For example, water dispersible GdF₃ nanoparticles (or GdF₃/LaF₃) have been prepared with both positive surface charge, by conjugation with 2-aminoethyl phosphate groups (GdF₃/LaF₃: AEP), and negative surface charge, by coating with citrate groups (GdF₃: cit).⁴⁷

Unfortunately, the trans-metallization process could be happened (e.g. Gd can replace by Zn). This effect can be controlled by the stability of the complex: more stable chelate complexes, less likely to release Gd ions.⁴⁸ Headache, nausea, taste disturbance and skin rash are the most common side effects. Moreover anaphylactic reactions leading to death involving the respiratory and cardiovascular systems have been observed on 1 per 500,000 cases. Some studies have also shown that using gadolinium based contrast agents in patients suffering from kidney failure, increases the risk of nephrogenic systemic fibrosis (NSF).^{49,49-51} For those reasons, the FDA recommends avoiding these substances until there are no other viable alternatives.⁴⁸

Although there are some contrast agents based on manganese (II) complexes, Mn⁺² itself in the form MnCl₂ solution has been the most widely used, showing a contrast effect that reveals detailed physiological and biological information establishing a new category imaging, known as Manganese-enhanced MRI (MEMRI). In particular, MEMRI have been used for visualizing the anatomical structure of the brain as well as the neuronal activity which usually cannot be obtained by any other gadolinium (II) based contrast agent.

In this panorama, manganese, iron and copper ions and their derivatives could offer an alternative to the gadolinium-based contrast agent. Despite the smaller number of unpaired electrons and a lower magnetic moment manganese (II) ions are capable of shortening the T₁ of

water protons, thus increasing the signal intensity of T₁-weighted MR images and demonstrated comparable T₁ contrast power to gadolinium (III).

In addition, a great advantage in using Mn⁺² is its lower intrinsic toxicity at equivalent dose of Gd⁺³, since manganese is a natural cellular constituent.⁵² Mn⁺² ions play important roles in biological processes such as enzymes cofactors and the controlled release of neurotransmitters.⁵² Manganese also has an affinity for the myocardium and can act as biomarker in heart disease. Manganese ions compete with calcium for entry into cardiac cells. There the ions bind to macromolecules and influence the relaxation of cell and tissue water. Heart diseases gradually inactivate calcium transport mechanisms (due to lower metabolic activity). Thus, manganese uptake is reduced accordingly; manganese-induced changes of tissue relaxation reflect tissue calcium homeostasis and thus myocardial viability.

The only manganese-based contrast agent FDA and EMA approved is mangafodipir trisodium (Teslascan®, Mn-DPDP; GE Healthcare) dedicated to hepatocyte-selective detection.²⁹ Teslascan is an intravenous paramagnetic contrast medium for MRI. The active substance of Teslascan is mangafodipir trisodium, a manganese (Mn²⁺) chelate with the ligand fodipir (dipyridoxyl diphosphate or DPDP). Mangafodipir trisodium is metabolized (dephosphorylated) and partially transmetallated (manganese exchanged for zinc) after intravenous administration. Manganese released from mangafodipir is taken up by hepatocytes thereby increasing the signal intensity of normal liver tissue (Fig. 1.17). This may result in an improvement of the detection of liver metastases, which usually have no hepatocytes. The metabolites of fodipir are renal excreted, while the biliar route mainly excretes manganese. Approved in 1997 it was withdraw from USA market in 2003 and from European market in 2012.⁵³ During development of mangafodipir as an MRI contrast agent, it was discovered that it possessed MnSOD mimetic activity. Mitochondrial manganese superoxide dismutase (MnSOD) normally keeps reactive oxygen species (ROS) and reactive nitrogen species (RNS) in check, that participate in pathological tissue damage. Whereas MRI contrast depends on the release of Mn²⁺, the MnSOD mimetic activity depends on Mn²⁺ that remains bound to DPDP. Mangafodipir has been tested as a chemotherapy adjunct in cancer patients and as an adjunct to percutaneous coronary intervention in patients with myocardial infarctions, with promising results. The contrast enhancement in MR imaging relies on the release of manganese from the chelate, the therapeutic activity depends on manganese that remains bound to DPDP or PLED.¹⁹ Also Calmangafodipir [Ca₄Mn(DPDP)₅] (brand namePledOx) is being explored as a chemotherapy adjunct in cancer patients.⁵⁴

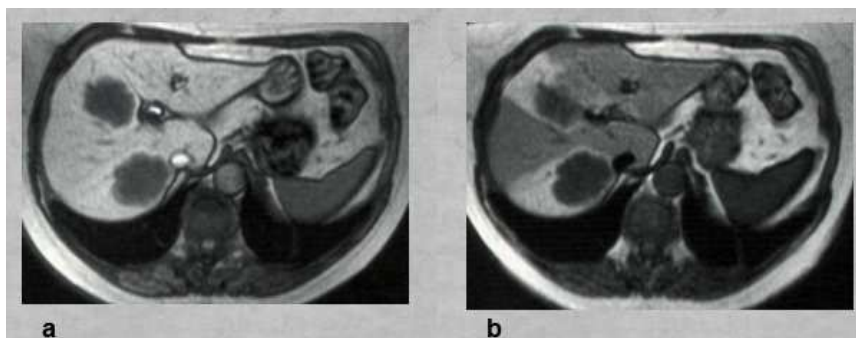


Figure 1.17 The uptake of Mn-DPDP (Mangafodipir) in the liver relies on the ability of hepatocytes to excrete metal ions. Manganese separates from the DPDP-complex and is taken up by the hepatocytes. T₁-weighted images. (a) The metastases are well delineated 15 minutes after the injection, and (b) even 24 hours after administration some of the contrast agent.²³

Another examples of the manganese-based CA mainly include aqueous-phase complexes, (hydrophilic dendritic Mn(II) complex 1 derived from diethylenetriamine pentaacetic acid (DTPA))²⁷ while only a few cases are reported of Mn-nanoscale materials (e.g. manganese oxide nanoparticles),³¹ metal-organic frameworks⁵⁵ and manganese-oxo clusters.⁵⁶

A key step forward in diagnostic technique could be given by the contribute of nanotechnology in the medical field, which has developed selective diagnostic nanocarriers to target specific organs and/or metabolic processes.²⁷

Among this scenario, manganese nanocomposites have been selected as useful probe for MRI. Manganese-based nanoparticles should have great paramagnetic properties (r_1) with negligible magnetic anisotropy (small r_2). For this reason nanoparticles are excellent candidate as T₁-CAs as they contain a large amount of metal ions with a high magnetic moment.²⁷ They shorten relaxation times of nearby protons, improve the contrast between lesions and normal tissues, thus leading to a better imaging quality and a reduced risk of misdiagnosis. Unlike T₂ contrast agents, the T₁ CAs need to have direct interactions with the surrounding water protons to affect proton relaxation times. In this perspective, MnO NPs small in diameter were prepared in order to have a large surface percentage of Mn⁺² ions and therefore higher r_1 relaxivities. Magnetic nanoparticles (MNPs) are the major class of nanoscale materials having the potential to revolutionize current clinical diagnostic and therapeutic techniques. Due to their unique physical properties and ability to interact at the cellular and molecular level, MNPs are being actively investigated as a new generation of magnetic resonance imaging (MRI) contrast agents³⁰ and as carriers for targeted drug delivery.²⁹

In addition, to provide positive contrast, T_1 -CAs should be easily absorbed and intracellular accumulated for cell imaging. Moreover, adequate nanoparticle shape for easy surface modification and for binding bioactive materials have to be designed. Finally, a favorable pharmacokinetics and an adequate dynamic for their efficient distribution towards biomarkers with minimal side effects is necessary.

The biomedical field principally embraces manganese based nanoparticles as diagnostic tools for magnetic resonance imaging. Current MRI contrast agents are in the form of either paramagnetic complexes or magnetic nanoparticles. Paramagnetic complexes, which are usually gadolinium (Gd^{+3}) or manganese (Mn^{+2}) chelates, accelerate longitudinal relaxation T_1 of water protons and exert bright contrast in regions where the complexes localize. Nowadays, the widely used positive contrast agent in clinic are gadolinium chelates in the form of Gd-diethylenetriamine pentaacetate (Gd-DTPA) and Gd-tetraazacyclododecanetetraacetic acid (Gd-DOTA), and its main clinical applications are focused on detecting the breakage of the blood-brain barrier (BBB) and changes in vascularity, flow dynamics, and perfusion. However, the dissociated gadolinium ions from gadolinium chelates could induce the risk of nephrogenic systemic fibrosis (NSF).^{49,50} Thus, many strategies, such as the loading of macromolecules and micelles, the fabrication of nanoscale objects, and so on, have been attempted to inhibit the toxicity and side-effect of released gadolinium ions together with retaining good contrast effect. Especially, the application of inorganic nanoparticles as contrast agent of MRI has gained considerable attention due to relatively high stability and good MRI function. For example, gadolinium compound-based crystalline nanoparticles, such as the Gd-containing nanoparticles of Gd_2O_3 , GdF_3 and $NaGdF_4$, provide a rigid crystal environment that is effectively prevent nanoparticles from releasing free gadolinium ions, and so that they have been mostly investigated as a new generation of positive contrast agents.⁵⁸ Concurrent Gd-based CAs, manganese enhancers are being developed.

The peculiar electronic configuration of manganese ion results in an efficient shortening of longitudinal relaxation time of proton in water together with the enhancement of magnetic resonance signal intensity. Furthermore, the toxicity of manganese ions is much lower than that of gadolinium ions. At present, the only Mn-based MRI contrast agent has been used in clinic is mangafodipirtrisodium (Mn-DPDP).⁵⁹ Mangafodipir, commercially sold under the brand name Teslascan, is a contrast agent delivered by intravenous injection to enhance contrast MRI of the liver. It was composed by the paramagnetic manganese (II) ion chelated by fodipir (dipyridoxyl diphosphate, DPDP). However, Mn-based complexes dissociate after administration to yield free

Mn⁺² because of the conversion between the six- and seven-coordinated states, which accounts for the *in vivo* instability of the Mn-DPDP chelate compared with gadolinium-based contrast agents. Due to manganese physiological role, exposure to Mn⁺² excess can induce deleterious effects on the central nervous system causing parkinsonism-like syndrome, especially in patients with liver failure. The *in vivo* instability of Mn-DPDP has raised especial concerns about its potential toxicity, which led to its gradual withdrawing from the US market in 2003⁶⁰ and the European market in 2012.⁵⁹ From this issue, the research of more stable manganese-chelating agents and/or of biocompatible and thermodynamic Mn compounds urges.⁶¹ To this aim, nanotechnological research proposed manganese compound-based crystalline nanoparticles (MnO NPs) as contrast agent for MRI with well defined morphology and high solubility. It is generally recognized the predominant contrast effect is only contributed by the manganese near to the NPs surface being closely in contact with the proton of water molecules. Therefore, it is essential to synthesize small MnO nanoparticles to provide large specific surface area for touching water molecules intimately. MnO NPs exhibit favorable behaviors in detection, localization, characterization and evaluation of hepatic lesions and provide clinical advantages over the existing Mn-based MRI contrast agent Mangafodipir. NPs offer a biocompatible profile further improved by coating strategies;⁴¹ however, the overall and systematic research on Mn-based contrast agents is still at a relatively early stage.⁶¹

2. Preliminary results on MAdCAM-1 targeted MnO NPs

Nanomedicine offers novel solutions for theranostic purposes in various clinical settings. A wide literature already exists about the translational potential of nanotechnology in cancer or infectious diseases, but the application of nanomedicine to IBD management has been only poorly investigated so far.⁶² The knowledge of an IBD specific targeting moieties could greatly contributed to the IBD active detection, specifically of CD.

Discriminating bowel wall thickening due to active inflammation from fibrotic stenosis was very important, since active inflammation is potentially reversible and requires timely pharmacological therapy, while fibrosis requires treatment by surgery.^{63,64} This issue is even more challenging in patients that have been previously subjected to gastrointestinal surgery, where discriminating between active IBD, pathological fibrosis and anastomotic scars is arduous.⁶⁴ Previous studies on anti-MAdCAM nanoparticle-based strategies for IBD are sporadic and mainly aimed to improve contrast-enhancement in bowel ultrasound⁶⁵ revealing an unexpected role of targeted nanomedicine for IBD.

In the light of the above, MAdCAM-1 overexpression was demonstrated to be a specific marker for IBD recognition and theranostic nanoplatform targeted toward MAdCAM-1 specifically designed for recognition of active inflammation foci in Crohn's disease was demonstrated to actively accumulated in inflamed sites. In addition the nanocomposite was demonstrated to be an efficient contrast enhancer for MRI diagnosis.

The rationale for choosing MAdCAM-1 as an appropriate target for IBD homing of nanoparticles resides in multiple advantages. First, MAdCAM-1 offers a high and early correlation with active bowel inflammation, as demonstrated by the agreement between MAdCAM-1 expression profile in immunohistochemistry and western blot (data not shown), as well as by the histological assessment of active inflammation on colonic mucosa after 5 days of DSS treatment (data not shown). Targeting leukocyte traffic in inflamed bowel mucosa, and particularly the interaction between $\alpha_4\beta_7$ integrins and MAdCAM-1, is currently considered a very promising strategy for IBD treatment with only a partial success for anti-MAdCAM-1 therapy in IBD.⁶⁶⁻⁶⁸

Another interesting feature of MAdCAM-1 is its over-expression also in extra-intestinal districts that are often involved in extra-intestinal manifestations of IBD, such as eyes, joints, liver and skin. In addition, aberrant homing of leukocytes in these sites could be responsible for such manifestations.⁶⁸ In this regard, a MAdCAM-1-targeted theranostic nanoplatform could be even more appealing, considering its potential targeting of both intestinal and extra-intestinal IBDs.

The diagnostic tool consisted of manganese oxide nanoparticles by solvothermal degradation biofunctionalized with anti-MAdCAM-1 antibody (MnO-aMC1 NPs) specific for the MAdCAM-1 recognition. A significant proportion of targeted nanoparticles was located in proximal colon at 24 h, allowing as to identify the sites of bowel inflammation, whereas untargeted nanoparticles were mostly washed out.

Active targeting of the endothelium within the inflamed bowel was demonstrated by TEM images on tissues, suggesting a prolonged window of interaction with relevant translational potential for theranostic purposes (Fig. 2.1).

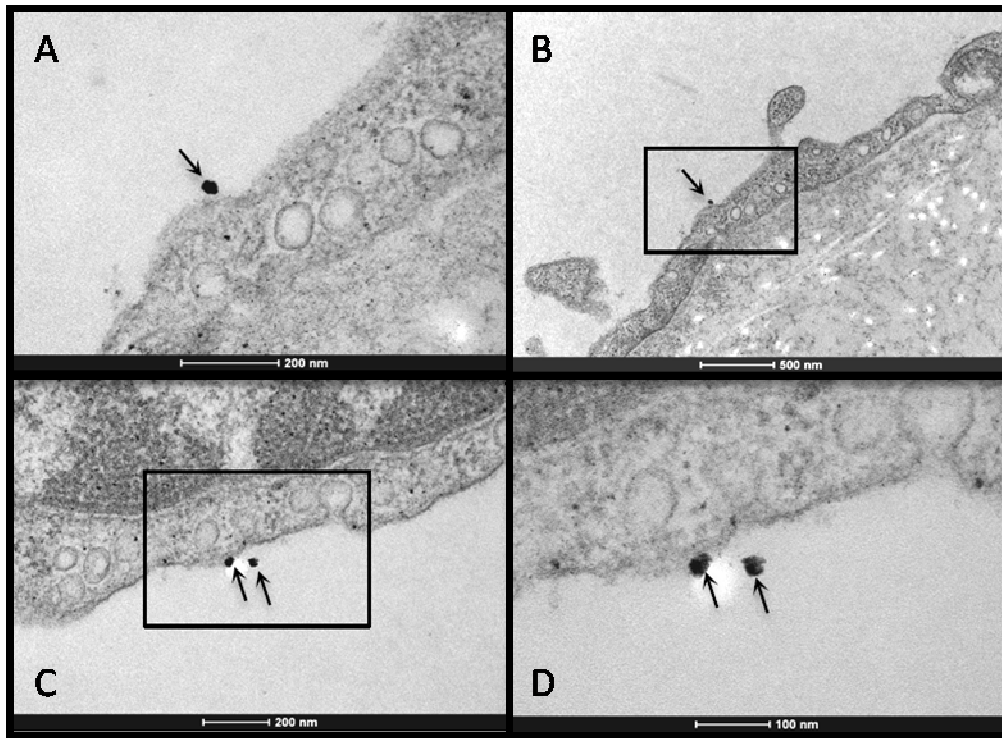


Figure 2.1. TEM images of proximal colon specimens isolated from DSS-treated mice injected with anti-MAdCAM-1-MnO-NP. Arrows point at nanoparticles within mucosal vessels and adhering to the endothelium of venules. Higher magnifications of MnO-aMC1 NPs (black boxes) are shown on the right of each single image. Scale bars(A) (C) 200 nm, (B) 500 nmm, (D) 100 nm.

A certain amount of MnO-aMC1 NPs was also detected in liver, kidneys and lungs that can be involved in extra-intestinal inflammatory damage in DSS-induced acute colitis.⁶⁹ However, histological analyses have not demonstrated clear damage in these tissues, thus the presence of targeted nanoparticles in these off-target districts could be probably attributable to excretion pathways.

Fluorescent-labeled MnO-aMC1 NPs are able to effectively and selectively localize at inflamed bowel tissue (Fig 2.2).

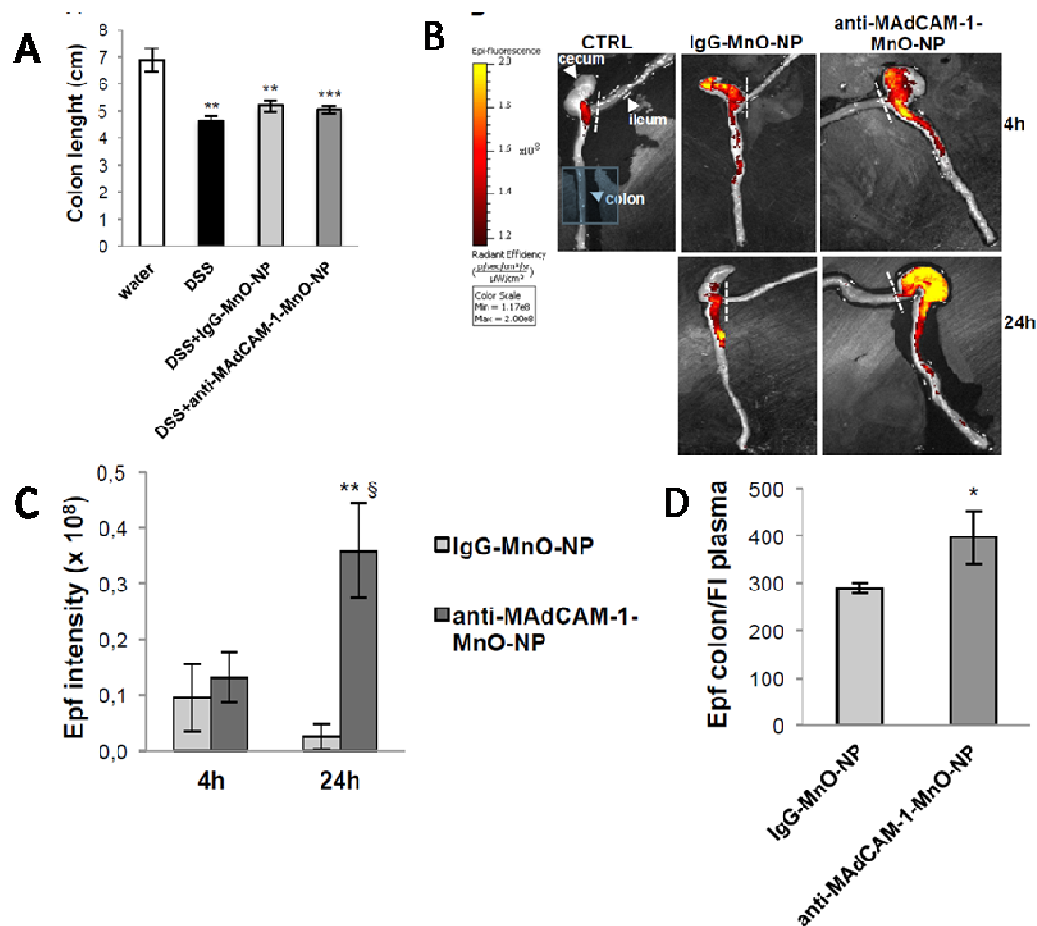


Figure 2.2. Analysis of dissected bowels isolated from DSS-treated mice exposed to MAdCAM-1-targeted nanoparticles (DSS + MnO-aMC1 NPs) or to control nanoparticles (DSS + MnO-IgG NPs). (A) Colon size reduction upon DSS treatment for 5 days. Length of colon removed from euthanized mice after injection of nanoparticles or control saline was compared to that of control mice drinking regular water. Results are means \pm SE in each group. ** $P < 0.01$, *** $P < 0.001$ versus control mice. (B) Epifluorescence (Epf) images of representative bowels isolated from DSS-treated mice exposed for 4 or 24 hours to control saline solution (CTRL), anti-MAdCAM-1-MnO-NP or IgG-MnO-NP. Epf intensity is expressed as radiant efficiency. Dashed lines indicate the end of ileum, and starting of colon. (C) Averaged Epf intensity of bowel isolated from DSS-treated mice exposed for 4 or 24 hours to anti-MAdCAM-1-MnO-NP or IgG-MnO-NP was measured within the entire colon, as described in Materials and Methods. Results are means \pm SE of 5 different bowels for each experimental condition. ** $P < 0.05$ anti-MAdCAM-1-MnO-NP versus IgG-MnO-NP; § $P < 0.05$ 24 hours versus 4 hours. (D) Epf intensity of bowels isolated from DSS-treated mice exposed for 24 hours to anti-MAdCAM-1-MnO-NP or IgG-MnO-NP was normalized toward the fluorescence intensity of plasma collected from the same animal before euthanasia. Results are means \pm SE of 5 mice per condition. * $P < 0.05$.

Table 2.1. Average epifluorescence intensity of isolated organs from DSS-treated mice exposed to MnO NPs conjugated with anti-MAdCAM-1 or IgG for 4 or 24 h. Data expressed as mean radiant efficiency ($W\text{ cm}^{-2}$).

	Anti-MAdCAM-1-MnO-NP ($\times 10^8$)		IgG-MnO-NP ($\times 10^8$)	
	4 h	24 h	4 h	24 h
Liver	0.124 \pm 0.089	0.102 \pm 0.054	0.002 \pm 0.002	0.88 \pm 0.034
Kidneys	0.178 \pm 0.098	0.114 \pm 0.064	0.027 \pm 0.027	0.348 \pm 0.103
Spleen	n.d.	n.d.	n.d.	n.d.
Heart	n.d.	n.d.	n.d.	n.d.
Lungs	0.106 \pm 0.065	0.092 \pm 0.103	0.042 \pm 0.042	0.12 \pm 0.05

MnO NPs magnetic properties were also investigated. MnO NPs has been denonstrated to improved performance as contrast-enhancer in magnetic resonance imaging at 1.5 T mainly as T_1 positive agent (data not reported).

These preliminary results suggest MAdCAM-1-targeted nanoparticles are promising theranostic tools for accurate detection and treatment of active bowel inflammation, even in early stages of development when damage could be only demonstrated by histopathology. Clinical potential of such nanoplatform was undeniable, considering the ability to discriminate active inflammation from fibro-stenosing alterations even in the post-surgical setting.

3. The goal

The natural history of Crohn's disease involves the inflammation of the transmural intestine which often leads to narrowing of the lumen causing bowel obstruction. Histologically, a mixture of inflammatory and mesenchymal cells is presented together with components of the extracellular matrix with different degrees of fibrosis. Inflammatory intestinal stenosis often responds quickly to treatment with high doses of steroids as well as to therapy with powerful anti-tumor activity. This could help to relieve the intestinal obstruction, but it exposes the patient to many side effects such as the deleterious effects of steroids on the growth and development of children. Moreover, intestinal stenosis which is mostly of fibrotic nature, will not respond to these medical treatments, but it will require surgical resection.

Currently, there are no clinical imaging modalities enable physician to specifically determine the level of fibrosis present in the intestinal stenosis.

From a clinical point of view, MRI targeted enhancement is a gold standard for IBD assessment and could better discriminate fibrotic stenosis from active inflammation. In this regard, MRI is proposed as a non-invasive technique for quantification of intestinal fibrosis in a mouse model with Crohn's disease.⁷⁰

Preliminary data on MAdCAM-1 targeted MnO NPs (paragraph ___) suggested MnO-aMC1 NPs very promising molecules for CD active targeting MR imaging. Anti-MAdCAM-1 targeting capability, joined with the contrast power of MnO NPs, allows a specific MR diagnosis of inflammatory bowel disease. An accurate contrast enhancement of active IBD, by properly homing manganese oxide to MAdCAM-1-overexpressing bowel sites, is expected to circumvent the discussed limitations and to avoid the non-specific enhancement.

To further enhance the contrast power of the manganese-based CA, a nanocontainer able to concentrate a great number of MnO NPs was designed. It allow to achieve remarkable r_1 relaxivity value and to decreases the toxicity of the contrast agent, resulting in an extreme safety for the organism. To aim these purposes, a manganese-based agent for enhancing the contrast in MR imaging is here discuss. A biocompatible and biodegradable co-polymeric matrix of poly(lactic-*co*-glycolic acid) was used to entrap the contrast agent in the form of organic colloidal MnO NPs (PLGA@MnO NPs).

Combining the benefit offered by the FDA approved polymer and the advantage of the paramagnetic behavior of manganese, PLGA@MnO nanocomposites could be a promising sources of CAs for future MRI application *in vivo*, thus enhancing the spatial resolution of images and providing an early stage diagnosis, with negligible side effect induced on body.

4. Materials and Methods

4.1. Chemicals and biological materials

Manganese Chloride Tetrahydrate ($\text{MnCl}_2 \cdot 4\text{H}_2\text{O}$, 99 %) Sodium Oleate (82 %), Oleic acid (analytical standard), Fluoresceinamin isomer I, Poly(isobutylene-alt-maleic anhydride) (MW 6,000 g mol⁻¹, Dodecylamine (98 %), Tetrahydrofuran (THF, 99.9%), Furfurylamine, Poly(DL-lactide-*co*-glycolide) (PLGA, MW 24000–38000 g mol⁻¹, 50:50) and Polyvinyl alcohol (PVA, MW 9000–

10000 g mol⁻¹, 80 % hydrolyzed), Ammonium persulfate ReagentPlus®, ≥ 99.99 %), 2-Mercaptoethanol (≥ 99.0 %), N,N,N',N'-Tetramethylethylenediamine (BioReagent, suitable for electrophoresis, ~ 99 %), Glycine (for electrophoresis, ≥ 99 %), Polyacrilamide, Comassi Blue Solution, Tween-20, bovine serum albumin (BSA), rabbit anti-GAPDH, CAPS (≥ 98.0 %), N-(3-Dimethylaminopropyl)-N'-ethylcarbodiimide hydrochloride (EDC ≥ 99.0 % (AT),) were purchased from Sigma Aldrich (MO, USA) acquired.

Hexane (97 %), Chloroform and Acetone (99 %) acquired from PanReac AppliChem.

DMEM without phenol red, Enhanced ChemiLuminescence (ECL) Western blotting reagent (GE Healthcare) from EuroClone LifeAblot® Plus kit were purchase from Euroclone.

Polyvinylidene difluoride membranes (Immobilon-P, EMD) were from Millipore Corporation (Billerica, MA-US).

Anti-MAdCAM-1 antibody clone MECA-367 was purchase from LifeSpanBioSciences (Seattle, WA).

α,ω-Bis-amino PEG (NH₂-PEG-NH₂, MW. 2000 g mol⁻¹) was purchase from RappPolymer (GmbH, Germany)

4.2. Synthesis of nanoparticles

4.2.1. Synthesis of manganese oxide nanoparticles

Once the reaction was completed, the solution was cooled down to room temperature and washed with acetone (three centrifugation at 6032 rcf, 6 minutes, Scanspeed 173OR, Labogene). After each wash, the supernatant was removed and the pellet of MnO nanoparticles were re-dispersed in organic solvent (chloroform or hexane) by sonication.

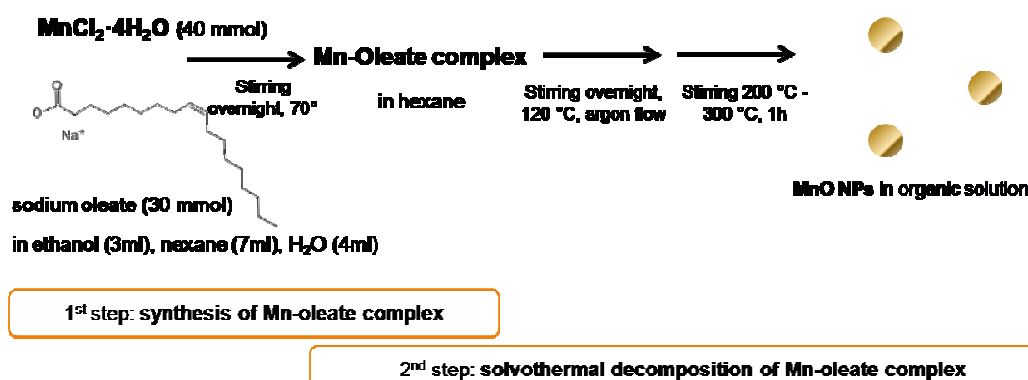


Figure 4.1. Schematic representation of the synthesis of manganese oxide nanoparticles (MnO NPs).

Table 4.1. Reaction conditions used for the synthesis of MnO nanoparticles.

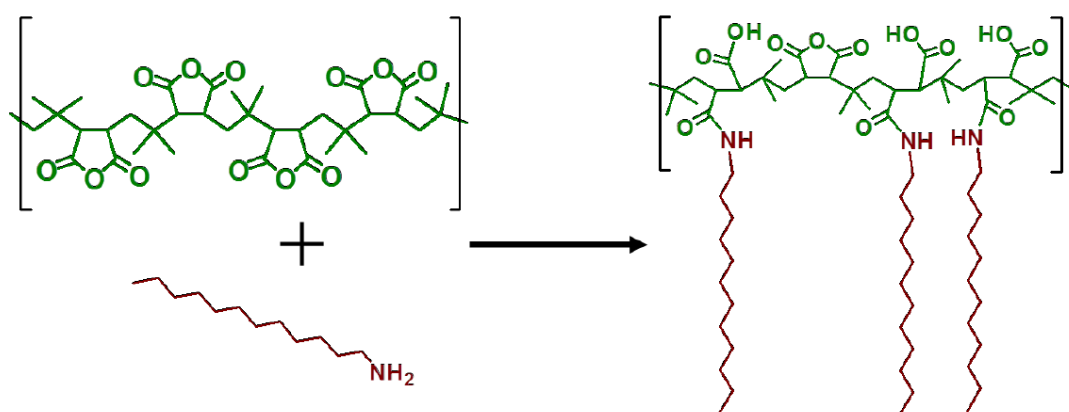
Shape	Solvent	T (°C)	t (min)
spherical	1-Hexadecene	280	60
star-like	1- Hexadecene	280	30
Cubic	1-Octadecene	300	15

4.2.2. Synthesis of polymer poly(Isobutylene-*alt*-maleic anhydride)

The synthetic procedure of the amphiphilic polymer (PMA) has been reported in previous publications.^{71,72} The polymer was synthesized using anhydrous tetrahydrofuran (THF) in order to avoid the maleic anhydride rings hydrolyzation during the reaction, and dodecylamine was used to modify the polymer. Briefly, 2.70 g (15 mmol) of the dodecylamine (98 %) were dissolved in anhydrous tetrahydrofuran (100 ml, 99.9 %). The solution was poured into a 250 ml round bottom flask containing 3.084 g (20 mmol expressed as monomer) of poly(isobutylene-*alt*-maleic

anhydride), average (MW 6000 g mol⁻¹). After agitation, the cloudy solution was sonicated for few seconds (20 s) and then heated to 60 °C for 3 h. In order to quantitatively react the maleic anhydride with the primary amine, the solution was concentrated to 30 - 40 ml by evaporation of the THF under reduced pressure (200 – 120 mbar). The concentrated solution was left under stirring overnight at 60 °C. Subsequently, the solvent was then slowly evaporated until the polymer was completely dry (pale yellow solid). Finally, the resulting polymer was redissolved in anhydrous chloroform and the final volume was adjusted to obtain a the final monomer concentration of 0.5 M. Maleic anhydride rings modifications occurs partially: assuming that all the maleic anhydride rings were active (100 %), the ratio of the dodecylamine-modified anhydride rings was chosen to be a 75 % of the total rings, leaving 25 % of them integral for further modification with molecules of biological interest *via* amide bonds. After the modification of the backbone (39 monomer units) with a 75 % dodecylamine, the molecular weight of the total (anhydrous) amphiphilic polymer is approximately 11400 g mol⁻¹. The rest of the anhydride rings could be opened using a basic water solution (e.g., NaOH 0.1 M or sodium borate buffer (SBB) pH 12) forming negatively charged carboxylic groups, providing colloidal stability in aqueous solutions (Fig. 4.2).

Figure 4.2. Structure of the amphiphilic poly(isobutylene-*alt*-maleic anhydride)-graft-dodecylamine (PMA) with poly(isobutylene-*alt*-maleic anhydride) hydrophilic backbone (green) and hydrophobic dodecylamine chains (bordeaux).



4.2.3. Manganese oxide nanoparticles phase transfer to organic solvent

In order to transfer nanoparticles from organic to water phase, MnO NPs were coated with an amphiphilic polymer poly(Isobutylene-*alt*-maleic anhydride) (PMA) following a protocol similar to that described by Lin and coworkers⁷³ The amount of amphiphilic polymer required for the coating

was calculating the total surface area of the hydrophobic nanoparticles by the equation 4.1, accordingly with previous study.⁷⁴

$$V_p = \frac{\pi C V d_{eff}^2 R_{p/area}}{C_p} \quad \text{eq. 4.1}$$

where C is the concentration calculated from UV-vis measure (mM) and V is the volume (nm³) measured by TEM analysis of the NPs solution, respectively. C_p and V_p are the monomer concentration (mM) and the volume (nm³) of the amphiphilic polymer dissolved in chloroform, respectively. d_{eff} is effective diameter of the NPs measured by TEM analysis. R_{p/area} is the number of polymer monomers which added per surface area of MnO NPs (monomer units nm⁻²).

Briefly, 0.04 ml of synthesized PMA (0.5 M) were added to 0.5 mg of MnO nanoparticles dispersed in chloroform (10 μl, 2.78 mg ml⁻¹). By using a rotary evaporator (40 °C, 40 rpm, vacuum, Heidolph, Laborota 4000 efficient, WB eco), the solution was dried and further re-dispersed sodium borate buffer (SBB) pH 12 (3 ml) by sonication. When the PMA polymer is added to the NPs, the dodecylamine chains (bordeaux) hydrophobically interact with the surfactant (black) present on the NP surface. By adding sodiumborohydrate buffer of pH 12 the anhydride rings on the poly(isobutylene-*alt*-maleic acid) backbone (green) are opened and carboxylic groups are formed. It is via this process that the NPs acquire hydrophilic properties and are transferred to the aqueous phase. Subsequently, three washings with Milli-Q water were carried out in a centrifuge (965 ref, 10 minutes, Scanspeed 173OR, Labogene) and the resulting PMA@MnO NPs nanoparticles were collected.

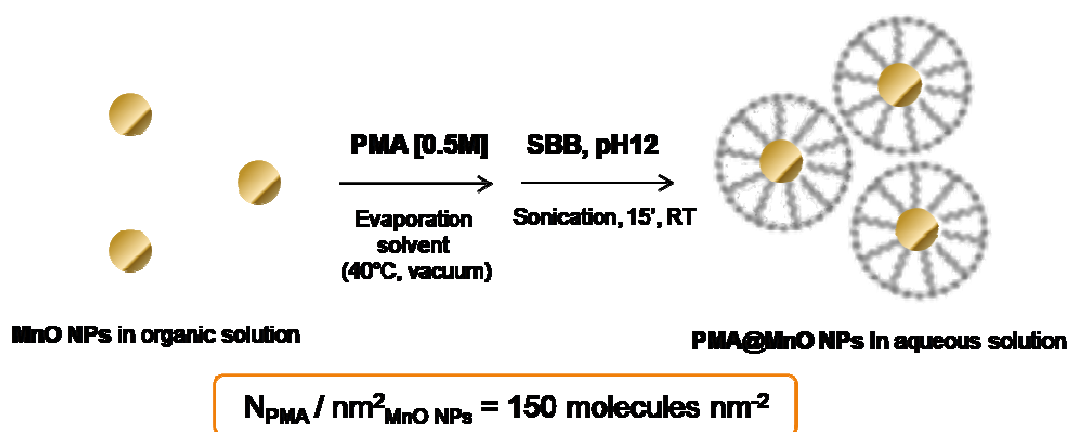


Figure 4.3. Schematic representation of PMA-coating of MnO NPs.⁷²

In order to prepare PMA conjugated with the Fluoresceinamine, isomer I (FITC-NH₂), FITC-NH₂ was added to PMA solution (molar ratio 5:1) and left under stirring 2h RT.

4.2.4. Synthesis of polypoly(D,L-lactide-co-glycolide) nanoparticles

Acid-terminated polypoly(D,L-lactide-co-glycolide) (MW 24000-38000 g mol⁻¹) nanoparticles (PLGA NPs) were synthesized by the single emulsion solvent evaporation method (Fig. 4.4).⁷⁵ Briefly, acid terminated PLGA (12.5 mg) was dissolved in chloroform (1 ml). The organic phase was added to 40 ml of a poly(vinyl alcohol) aqueous solution (PVA, MW 9000-19000 g mol⁻¹, 2%). The two phases form an emulsion under tip ultrasonication (Branson, Digital Sonifier) at 40% of amplitude for 30 seconds (twice) in ice-bath. The emulsion was left under stirring to completely evaporate the organic solvent (4 h). The sample was three-times centrifuged at 27237 rcf for 15 minutes at 4°C (Scanspeed 173OR, Labogene) and the pellet was re-dispersed in PVA (0.3%) solution. Finally, the sample was freeze-dried (Christ, alpha 1-2 LD).

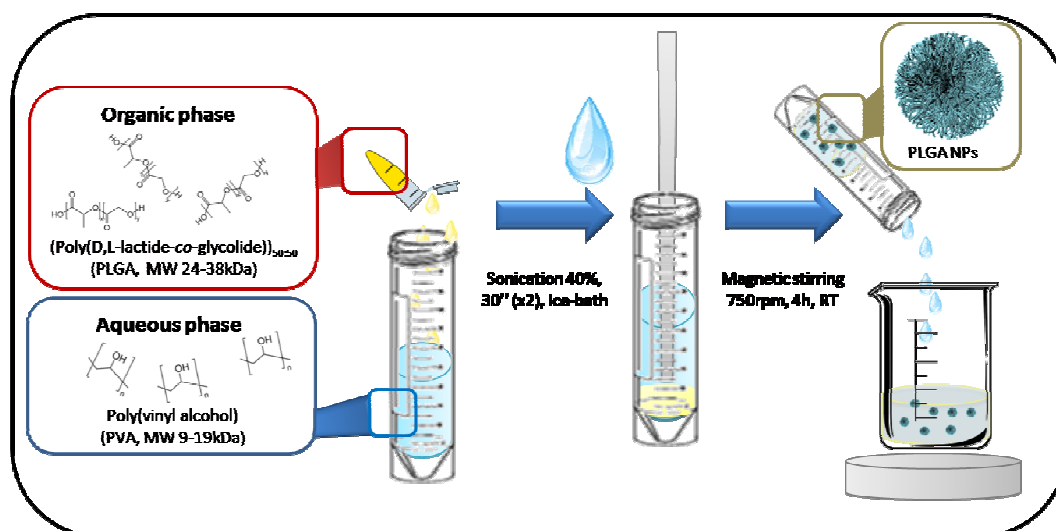


Figure 4.4. Depiction of synthesis of poly(D,L-lactide-co-glycolide) nanoparticles (PLGA NPs).

4.2.5. Synthesis of manganese oxide nanoparticles loaded polypoly(D,L-lactide-co-glycolide) nanoparticles

Acid-terminated poly(D,L-lactide-co-glycolide) (MW 24000-38000 g mol⁻¹) nanoparticles containing MnO NPs (PLGA@MnO NPs) were synthesized and treated as described above (Par. 3.2.4). The entrapment of spherical MnO NPs¹⁹ (Fig. 4.5) in PLGA NPs was obtained by added 8 mg of metallic NPs to the polymeric organic solution. After the synthesis, the sample was three-time centrifuged at 27237 rcf for 15 minutes at 4 °C (x 3) (Scanspeed 173OR, Labogene) and the

pellets was washed with PVA (0.3 %) solution. Finally the sample was freeze-dried (Christ, alpha 1-2 LD).

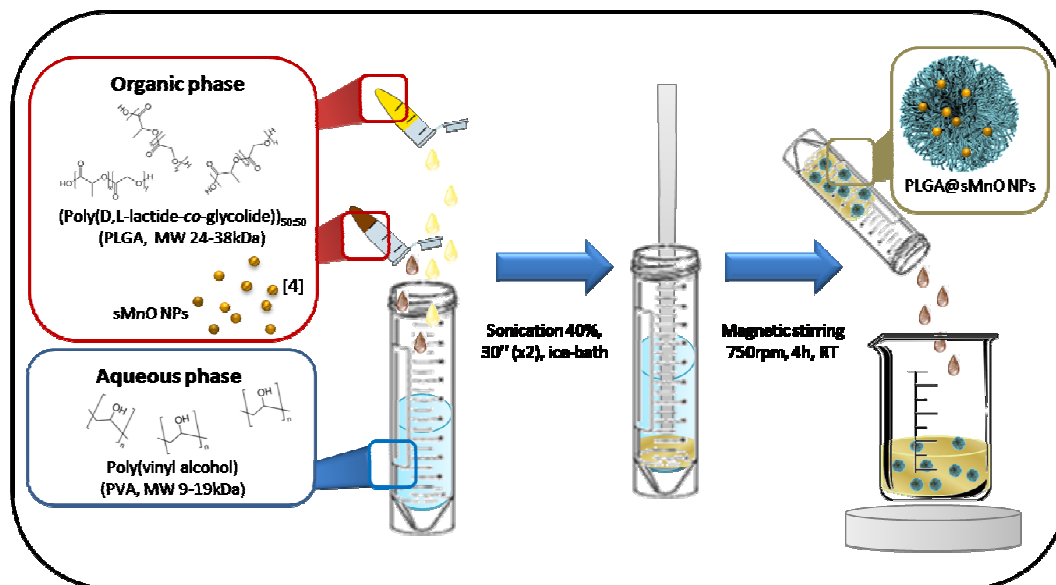


Figure 4.5. Depicted of synthesis of polypoly(D,L-lactide-*co*-glycolide) nanoparticles entrapping MnO NPs (PLGA@MnO NPs).

4.3. Nanoparticles Characterization

4.3.1. Reaction efficiency

To attest the efficiency of the reaction the lyophilized sample was weighted to calculate the yield of nanoparticles obtained (eq. 4.2):

$$\text{yeld (\%)} = \frac{\text{experimental mass of nanoparticles (mg)}}{\text{theoretical mass of nanoparticles (mg)}} * 100 \quad \text{eq. 4.2}$$

the experimental mass corresponds to the mass weight, while the theoretical mass is calculated as the sum of all the reagents (poly(lactic-*co*-glycolic acid) and MnO NPs added to reaction) while the amount of poly(vinyl alcohol) was negligible because mostly eliminated through centrifugation steps (Par. 3.2.4).

4.3.2. UV-visible analysis

Manganese oxide nanoparticles were quantified with UV-visible analysis at 248 nm, 272 nm and 268 nm in chloroform, dimethylsulfoxide (DMSO) and water, respectively. UV-vis analysis were

performed by NanoDrop2000c spectrophotometer (Thermo Scientific) in plastic cuvette for aqueous solution and quartz one for organic solution, with 1 cm optical pathway.

Protein directly quantification was performed by Bradford Protein Assay UV-visible analysis at 280nm.

4.3.3. Dynamic Light Scattering and ζ -potential analysis

In order to characterize the hydrodynamic radius, the size distribution of the nanoparticles as well as their dimensional evolution in suspension, Dynamic Light Scattering (DLS) was adopted. DLS is based on the statistical analysis of the fluctuations of the light scattered by a collection of particles suspended in a liquid. Brownian motions give rise to a randomly fluctuating intensity signal, whose correlation time is related to the Stokes-Einstein diffusion coefficient of the particles. The statistical analysis of the intensity fluctuations gives the average hydrodynamic radius of the particles.⁷⁶ The signal is generated by a number of particles, so that the information about the radius is statistical. Properly, refined analysis tools can access to the polydispersity of the size distribution and, in some cases, to its kurtosis. DLS therefore accesses the statistical properties of the particle motions in the liquid and it exploits the scattering of light to generate the needed signals containing the information. Dynamic light scattering (DLS) measurements were performed at 173° with a Zetasizer Nano ZS ZEN3600 from Malvern Instruments Ltd. (Worcestershire, UK) working at 4 mW of a He-Ne laser ($\lambda = 632.8$ nm). A disposable cuvette with 1 cm optical path length was used for the measurements. The samples were prepared by dilution with Milli-Q water. Each sample was allowed to equilibrate for 120 seconds prior to starting measurement. The measurements were performed at 25 °C. The hydrodynamic diameter was calculated using the Mie scattering theory, considering absolute viscosity and refractive index values of the medium: 0.8872 cP and 1.334 for water, 0.5420 cP and 1.442 for chloroform, 0.9200 cP and 1.430 for DMSO, respectively. The results are reported in Z-Average, Intensity and Number.

ζ -Potential measurements were elaborated on the same instrument by electrophoretic light scattering. ζ -potential values were automatically calculated from electrophoretic mobility using Zetasizer Software (Malvern Instruments Ltd., Malvern, UK). The dielectric constants 78.5, 0.100 and 36.70 were used for water, chloroform and DMF, respectively, and the Henry function of 1.5 were used for the calculations.

500 μl of PLGA NPs ($50 \mu\text{g ml}^{-1}$) were analysed by DLS and ζ -potential. The mean value of ten measurements give one record. All measurements were performed in triplicate, and the average values were calculated.

4.3.4. Inductively Coupled Plasma analysis

Samples for ICP analysis were digested overnight in 1ml of aqua regia (VHCl/NO₃ ratio = 3) in glass vials. Then samples were diluted with Milli-Q water to final volume of 4 ml. Samples were analyzed JY 2000 2 ICP Optical Emission Spectrometer (ICP OES) from HORIBA Scientific.

4.3.5. Stability test and degradation rate of nanoparticles

PMA@MnO NPs, PLGA NPs, PLGA@MnO NPs stability test was performed by measuring the variation of hydrodynamic diameter in time by Dynamic Light Scattering (par. 3.3.2). 500 μl of PLGA NPs ($50 \mu\text{g ml}^{-1}$) were analysed in different environments (Milli-Q-water, PBS 1X pH 7.2, DMEM) by DLS. The mean value of ten measurements provide one record. All measurements were performed in triplicate, and the average values were calculated.

4.3.6. Transmission Electron microscopy and Scanning Electron microscopy

Poly(lactide-co-glycolide) nanoparticles morphology and dimension were investigated by transmission electron microscopy (FEI 120kV Tecnai G2 Spirit BioTWIN) and digital images were obtained by a CCD Camera System and Leo Image software. Samples ($50 \mu\text{g ml}^{-1}$) were placed onto a formar-coated 300 mesh copper grid (Ted Pella, Inc.). The specimen on the copper grid was negatively stained with uranyl acetate (2 % w/w). Measure IT Olympus Software was used for the determination of the particle size distribution by measuring 150 – 200 particles (image processing).

Poly(lactide-co-glycolide) nanoparticles morphology and surface were investigated by scanning electron microscopy (JEOL JSM-6490LV), equipped with SE and BE detectors and an Oxford INCA EDXS system. The multipurpose sample preparation chamber Gatan Alto1000 is mounted directly to the SEM. Samples ($50 \mu\text{g ml}^{-1}$) were placed onto a formar-coated 300 mesh copper grid (Ted Pella, Inc.). The specimen on the copper grid was negatively stained with uranyl acetate (2 % w/w).

4.3.7. Metallic nanoparticles encapsulation efficiency and loading

Encapsulation efficiency (%), indicating the amount of nanoparticles recovered after NP formulation, was determined by UV-visible analyses (272 nm). PLGA NPs (1 mg) were dissolved

in 100 μl of DMSO at RT to solubilized the polymer and dissolve the nanoparticles. The mean value reported was calculate from a triplicate analyses. The encapsulation efficiency was calculated as the ratio between the mass of MnO NPs encapsulated in PLGA matrix and the total mass of MnO NPs added to the reaction (eq. 4.3):

$$\text{encapsulation efficiency (\%)} = \frac{\text{experimental mass of MnO NPs (ug)}}{\text{theoretical mass of MnO NPs (ug)}} * 100 \quad \text{eq. 4.3}$$

MnO NPs loading ($\mu\text{g mg}^{-1}$) into PLGA NPs is a parameter related to the amount of manganese oxide nanoparticles recovered after NP formulation. It is calculated as the ratio between the mass of MnO NPs encapsulated and the mass of total PLGA@MnO NPs (eq. 4.4).

$$\text{loading (\%)} = \frac{\text{experimental mass of MnO NPs (ug)}}{\text{mass of PLGA@MnO NPs (mg)}} * 100 \quad \text{eq. 4.4}$$

4.3.8. Relaxation analysis

The magnetic properties of PLGA@MnO NPs were established by a relaxometric analysis were performed by 0.5 T Time-Domain (TD) NMR Benchtop Systems (BRUKER, Minispec mq20). 120 μl of sample was analyzed by filling the bottom 8 mm of NMR glass tubes of 10 mm outer diameter. CPMG and saturation recovery sequences adapted for quantitative measurement in low field conditions^{77,78} were applied to determine T_2 and T_1 , respectively. Measurements were performed at different temperatures (303 K and 310 K) and in different environments (in water Milli-Q, in a saline and plasma mixture, and plasma). Sample were dissolved in water (120 μl) or plasma (120 μl) directly, while first in saline (50 μl) and then diluted to 120 μl with plasma for the analysis in the mixture. Relaxation rates (R) R_1 and R_2 are calculated as T_1^{-1} or T_2^{-1} respectively for several samples at different dilution, while relaxivity (r) r_1 and r_2 coincides to the angular coefficient of the calibration curve R_1 or R_2 versus concentration.

4.4. Cytotoxicity assay

The SVEC4-10 murine endothelial cells and Hela cervical cancer cell line were used as *in vitro* cell culture model and purchased by ATCC-LGC Standards (Sesto San Giovanni, IT). Cells were cultured in high glucose Dulbecco's modified Eagle medium (DMEM) supplemented with 10 % heat inactivated fetal bovine serum (FBS), 2 mM L-glutamine, 100 U ml⁻¹ penicillin, 0.1 mg ml⁻¹ streptomycin at 37 °C in a humidified atmosphere containing 5 % CO₂. At confluence, the cells were treated using trypsin-EDTA in a 1:4 to 1:6 split ratio, or they were used for experiments. All

cell culture materials were supplied by Euroclone S.p.A. (Milano, IT). Cell proliferation assay were performed on SVEC4-10 cells (5×10^3) onto 96-well tissue culture plates and incubated with different amounts of PMA@MnO NPs, PLGA NPs and PLGA@MnO NPs (from 0 $\mu\text{g ml}^{-1}$ to about 100 $\mu\text{g ml}^{-1}$). Cells were washed at the indicated times (24 h, 48 h, 72 h) with phosphate buffer saline (PBS 1X, pH 7.2) and tested with CellTiter 96®Aqueous Non-Radioactive Cell Proliferation Assay (Promega Italia s.r.l., Milano, IT), according to the manufacturers' instructions. Briefly, cells were incubated for 3 hours at 37 °C with 0.1 ml of 3-(4,5-dimethylthiazol-2-yl)-5-(3-carboxymethoxyphenyl)-2-(4-sulfophenyl)-2H-tetrazolium (MTS) and phenazinemethosulfate (PMS) stock solution previously diluted 1:6 in DMEM without phenol red. Cell viability quantification was performed by an optical absorbance reader (490 nm / 630 nm).

4.5. *In vitro* MRI analysis

The magnetic property of PMA@MnO NPs and PLGA@MnO NPs was characterized by MRI analysis were performed by 7 T preclinical magnetic resonance scanner equipped with 450/675 mT/m gradients (slew-rate: 3400-4500T/m/s; rise-time 140 μs) and a mouse body volume-coil (BRUKER, BioSpec 70/30 USR, Paravision 5.1). 500 μl of samples at different concentration were analyzed (from 0 mM to 1 mM Mn^{+2} ion concentration). RAREVTR (Rapid Acquisition with Relaxation Enhancement (RARE) with variable repetition time) and Multi Slice Multi Echo (MSME) sequences were applied to determine T_1 and T_2 , respectively. Measure were performed at 303 K and environment (saline and mixture saline and plasma (0.4 volume ratio)). Relaxation rates R_1 and R_2 are calculated as T_1^{-1} or T_2^{-1} , respectively, while relaxivity (r_1 and r_2) coincides to the angular coefficient of the calibration curve R_1 or R_2 versus concentration. The software processes the T_1 -map and provides the MR images in which the dynamic contrast is shown as a bright signal.

4.6. *In vivo* experimental IBD model

Male C57BL/6 mice (8 weeks old) were purchased from Charles River (Calco, IT), group housed (4 mice/cage) under standard laboratory conditions with free access to food and water, and allowed to acclimate for 1 week before inclusion in the experiment. The care and the use of laboratory animals was in accordance with an experimental protocol subjected to the direct approval of the Italian Ministry of Health. Colitis was induced by the addition of dextran sulphate sodium salt (DSS, 3% w/v, 40 kDa, MP Biomedicals, Santa Ana, US-CA) to the drinking water, by changing beverage each 2 days. For the set up of the model and analysis of MAdCAM-1 expression, 16 mice were divided into 4 groups: mice treated with DSS for 3 days (n=4), 5 days

(n=4), or 7 days (n=4), and mice drinking regular water (n=4) as control. Experiment was repeated twice, with comparable results. The mean DSS-water consumption was recorded over treatment for each group. Colitis was quantified with clinical activity, by scoring standard parameters of body weight change, stool consistency and fecal blood, which were determined daily for each mouse. Body weight change was scored 1 for 1-5 % body weight loss, 2 for 5-10 % body weight loss, 3 for 10-20 % body weight loss, 4 for > 20 % body weight loss; stools were scored 0 when normal, 1 when soft with well-formed pellets, 2 when soft without pellets, 4 in case of diarrhea; the presence of blood in the stools was evaluated as 0 when negative, 2 if positive to the Hemocult Sense assay (Beckman Coulter), 4 in case of macroscopic rectal bleeding. The scores assigned to each mouse were summed together to calculate the disease activity index (DAI), as previously described. After 3, 5 and 7 days of treatment, mice were euthanized, bowels were dissected from all mice and colon length was measured from the end of terminal ileum to the end of rectum. Then, dissected bowels were carefully washed with PBS by gentle flushing, and either fixed in 10% formalin for histological assessment and immunohistochemistry (n=2 bowels per group) or subdivided into proximal and distal part of colon, snap frozen and used for protein extraction and analysis of MAdCAM-1 expression (n=2 bowels per group).

4.6.1. Histological assessment

Bowel, liver, kidneys, spleen, heart and lung samples isolated from mice of each group were fixed with 10 % buffered formalin for at least 48 hours at room temperature and embedded in paraffin. Three micrometric sections were cut, stained with haematoxylin and eosin (H&E) and examined blindly. Bowels were scored by colitis severity: chronic and acute inflammatory infiltrate, erosion and ulceration of mucosa surface and loss of glandular crypts were the features analyzed.

4.6.2. Immunohistochemistry

For immunohistochemistry, 3 µm paraffin sections were cut, dewaxed in xylene and rehydrated in alcohol. Antigen unmasking was performed in microwave oven (citrate buffer pH 6) for 10 min. Endogenous peroxidase and unspecific binding sites were blocked by using appropriate reagents. Sections were incubated with an affinity-purified antibody anti-MAdCAM1 antibody for two hours at room temperature in a humid chamber. The reaction was revealed by nonbiotin peroxidase detection system with 3,3'-diaminobenzidine free base (DAB) as chromogen (haematoxylin counterstaining). The omission of primary antibody was used as negative control.

4.6.3. Protein extraction and western blotting

After ex vivo imaging by IVIS, the colon extracted from 3 mice per group were divided into proximal and distal portions, and immediately frozen in liquid nitrogen. Frozen tissues were weighted, homogenized with potter (Glas-Col homogenizer) in 20% w/v Triton lysis buffer (20 mM Tris-HCl pH 7.6, 150 mM NaCl, 1 mM EDTA, 10% Glycerol and 1% Triton X-100), containing 4% Protease Inhibitor Cocktail (Sigma-Aldrich S.r.l., Milan, IT), and cleared at 12,000 rpm for 20 minutes at 4°C. A 40 µg aliquot of protein was resuspended in Laemmli buffer, resolved on polyacrylamide gels under reducing conditions and transferred to polyvinylidene difluoride membranes. Membranes were blocked with 5% bovine serum albumin (BSA) in Tris buffer saline (TBS) with 0.1% Tween-20 for 1 hour at RT, and incubated with rat anti-MAdCAM-1 antibody (1:500 dilution, clone MECA-367) or with rabbit anti-GAPDH (1:5000 dilution), used as loading control. Antibodies conjugated to horseradish peroxidase (Abcam) were used as secondary antibodies, and the reaction was developed with the ECL star kit. Densitometric analysis of protein bands was performed with Image J software.

5. Result and discussion

5.1. Reaction efficiency

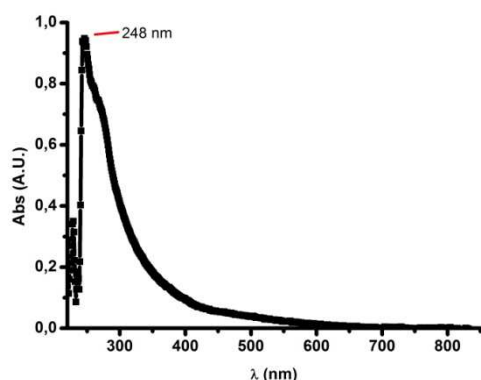
Reaction yield (%) was calculated for every lyophilized samples to attest the efficiency of the reaction. The yield was higher than 50% for more than 150 freeze-dried samples.

5.2. Calibration curves of manganese oxide nanoparticles

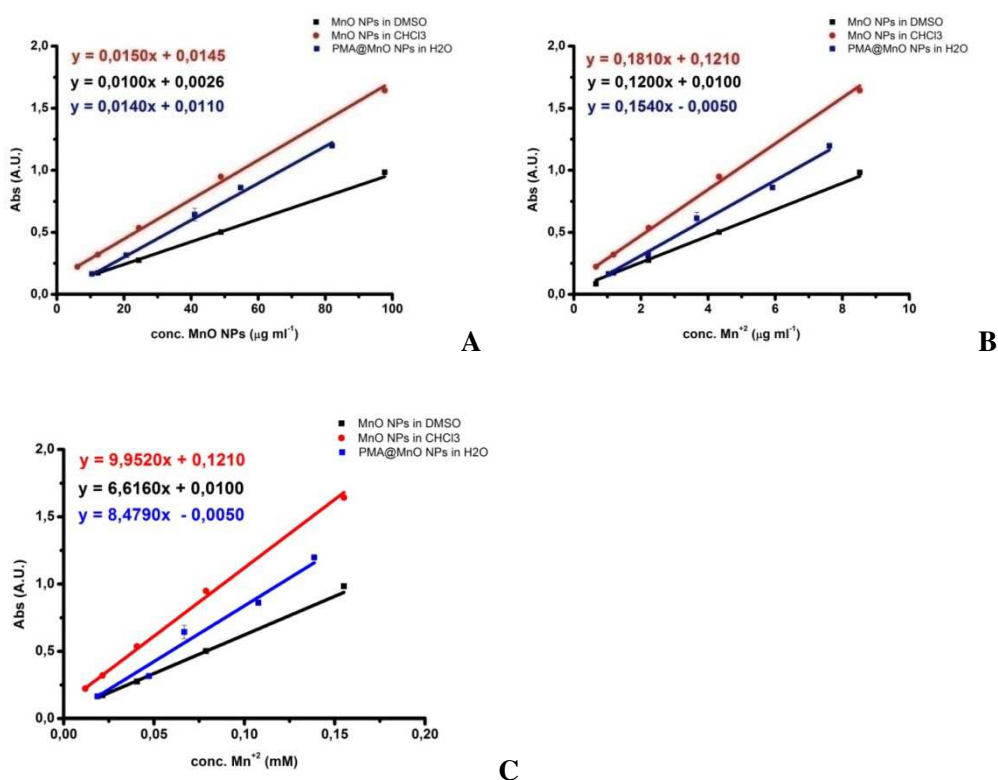
Manganese oxide nanoparticles synthesized and loaded on PLGA NPs were quantified by UV-visible analysis. For this purpose, calibration curves of manganese oxide nanoparticles in chloroform and dimethylsulfoxide for MnO NPs and in water for PMA@MnO NPs were performed. Samples at different concentrations were prepared by diluting MnO NPs (62.2 mg ml⁻¹) and PMA@MnO NPs (47.5 mg ml⁻¹) stock solutions to concentrations ranging from about 5 µg ml⁻¹ to 100 µg ml⁻¹.

Manganese oxide nanoparticles do not have a resonance plasmon band, but only exhibit a shoulder decreasing from a maximum absorption at a specific wavelength (Grf. 5.1.). The maximum absorption wavelength shifts depending on the particles coating and the environment they

are dissolved in. The absorption of MnO NPs in chloroform and dimethylsulfoxide and of PMA@MnO were measured at 248 nm, 272 nm and at 268 nm, respectively (Grf. 5.2 A, B and C).



Graph 5.1. Characteristic spectra of manganese oxide nanoparticles in chloroform. The maximum absorption was detected at 248 nm.



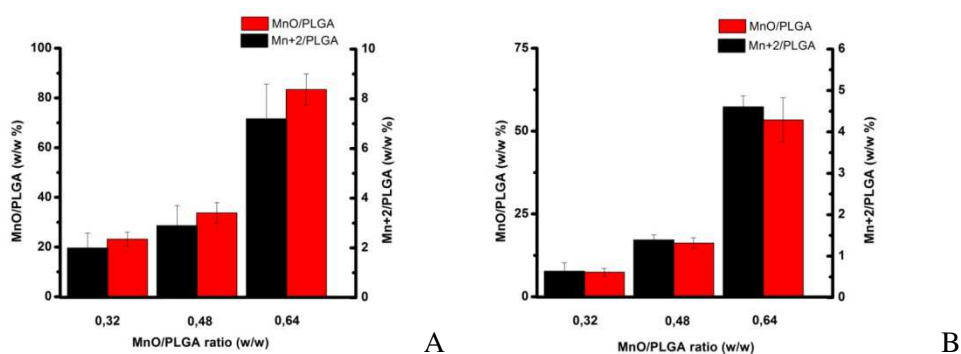
Graph 5.2. Absorbance dependence on concentration of MnO NPs ($\mu\text{g ml}^{-1}$) (A), Mn^{2+} ($\mu\text{g ml}^{-1}$) (B) and Mn^{2+} (mM) (C) at 248 nm in chloroform (red), at 272 nm in DMSO (black) and of PMA@MnO NPs at 226 nm in water Milli-Q (blue).

Absorbance of both MnO NPs and PMA@MnO NPs are linearly dependent on concentration of Mn^{+2} ions in the sample in the range of concentration analysed. The angular coefficient of MnO NPs is $0.015 \text{ ml } \mu\text{g}^{-1} \text{ cm}^{-1}$ ($0.1810 \text{ Mn}^{+2} \text{ ions } \mu\text{g}^{-1} \text{ cm}^{-1}$, $9.9520 \text{ Mn}^{+2} \text{ ions mM}^{-1} \text{ cm}^{-1}$) and $0.0100 \text{ ml } \mu\text{g}^{-1} \text{ cm}^{-1}$ ($0.1200 \text{ Mn}^{+2} \text{ ions } \mu\text{g}^{-1} \text{ cm}^{-1}$, $6.616 \text{ Mn}^{+2} \text{ ions mM}^{-1} \text{ cm}^{-1}$) in dymethylsulfoxide and in chloroform, respectively. The angular coefficient of PMA@MnO NPs is $0.0140 \text{ ml } \mu\text{g}^{-1} \text{ cm}^{-1}$ ($0.1540 \text{ Mn}^{+2} \text{ ions } \mu\text{g}^{-1} \text{ cm}^{-1}$, $8.479 \text{ Mn}^{+2} \text{ ions mM}^{-1} \text{ cm}^{-1}$), quite similar to that of MnO NPs in chloroform.

5.3. Encapsulation efficiency and loading of metal nanoparticles

In order to optimize the loading of metal nanoparticles on PLGA NPs to obtained a significant reduction of relaxation times of water protons by relaxometric analyses, different weight ratio between manganese oxide nanoparticles and PLGA polymer were investigated to synthesise an efficient contrast agent for MRI. Three different MnO NPs/PLGA (w/w) ratios (0.32, 0.48, 0.64) were explored, corresponding to 4.0 mg, 6.0 mg, 8.0 mg of MnO NPs, respectively, initially added to 12.5 mg of poly(lactic-*co*-glycolic acid) for the single emulsion reaction.

The encapsulation efficiency is calculated from the absorption at 272nm with the Lambert Beer Law (Grf. 5.3 A and B).



Graph 5.3. Encapsulation efficiency (%) (A) and loading (B) of MnO NPs in polymeric PLGA nanoparticles as a function of the weight ratio between metal nanoparticles or manganese ions and PLGA polymer.

Data demonstrated that the larger the amount of MnO NPs (mg) added to reaction, the higher the encapsulation efficiency and the nanoparticle loading inside the polymeric matrix. The loading of manganese nanoparticles increases from 23.2 % to 83.4 % (correspondent to Mn^{2+} ions from 2.0 %, 7.9 %) with the increasing in MnO NPs/PLGA (w/w) ratio from 0.36 to 0.72.

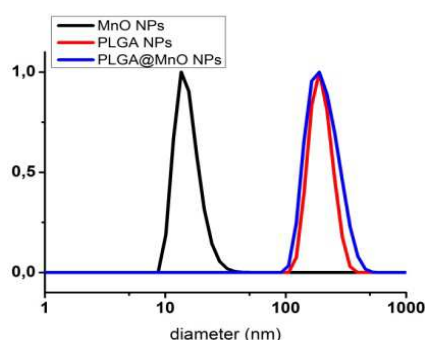
Data reported in table 5.1 were from analysis in triplicate.

Table 5.1. Encapsulation efficiency (%) and loading (%) of MnO NPs and Mn²⁺ ions in PLGA NPs depending on the MnO NPs/PLGA ratio used for emulsion.

MnO/PLGA ratio (w/w)	Encapsulation (%)		Loading (%)	
	MnO/PLGA (w/w %)	Mn ²⁺ /PLGA (w/w %)	MnO/PLGA (w/w %)	Mn ²⁺ /PLGA (w/w %)
0.32	23.18	2.00	7.42	0.64
0.48	33.75	2.90	16.20	1.39
0,64	83,41	7,20	53,38	4,61

5.4. Dynamic Light Scattering and ζ-potential analysis

Hydrodynamic diameter, polydispersity index (PDI), and ζ-potential (ζ-p) values of the prepared NPs are shown in table 4.2 and graph 4.4. The major goals in formulating polymeric nanoparticles is controlling the particle size, PDI, and ζ-potential, allowing MnO NPs encapsulation and optimizing MnO NPs release to achieve a site-specific regimen at a desired dose. MnO NPs in organic solvent showed a hydrodynamic diameter of 15.9 nm ± 0.21 nm, while PLGA NPs and PLGA@MnO NPs showed similar diameters (150.5 nm ± 8.0 nm and 163.0 nm ± 3.3 nm, respectively), indicating that the encapsulation of metallic nanoparticles didn't affect the PLGA NPs dimensions. PLGA and PLGA@MnO NPs were demonstrated to be stable considered anionic carriers with a ζ-potential of -33.5 mV ± 0.35 mV, -32.1 mV ± 0.99 mV, respectively. Characterization by TEM was coherent with DLS analysis. Micrographs of MnO NPs, PLGA NPs and PLGA@MnO NPs are shown (Grf. 4.5). Size distribution analyses showed NPs were monodispersed (Fig. 4.6).



Graph 5.4. Hydrodynamic diameter of MnO NPs, PLGA NPs and PLGA@MnO NPs by DLS analyses.

Table 5.2. Effective diameter, hydrodynamic diameter, polydispersity index and ζ-potential data of MnO NPs, PLGA NPs and PLGA@MnO NPs.

	Effective diameter (nm)		Hydrodynamic diameter (nm)		PdI		ζ-potential (mV)	
MnO NPs	9.7	± 1.3	15.85	± 0.212	0.130	± 0.034	-	-
PLGA NPs	129.5	± 35.1	150.5	± 8.017	0.058	± 0.028	-33.5	± 0.35
PLGA@MnO NPs	132.8	± 41.9	163.0	± 3.329	0.117	± 0.013	-32.1	± 0.99

5.5. Transmission Electron Microscopy (TEM)

TEM analysis of polymeric nanoparticles was not easy to perform, because they degraded under the electron beam. The degradation phenomenon was observed as particles coalescence or as dissolution (initial swelling followed by a substantial deflation until the disappearance of the particle). The nanoparticles staining with uranyl acetate (2 w/w%) favoured the image acquisition by decreasing NPs degradation. Unfortunately, analyzing PLGA nanoparticles containing metal particles, the colour could mask the presence of metal particles. Therefore, a compromise between the amount of dye added and the intensity of the electron beam was necessary.

Transmission Electron Microscopy revealed spherical shape polymeric PLGA nanoparticles monodispersed in size, both naked and loaded with MnO NPs (Graph. 5.5). TEM results correspond to DLS data: the encapsulation of manganese oxide nanoparticles in the PLGA matrix didn't affect the particles dimensions. In fact, PLGA NPs and PLGA@MnO NPs effective mean diameter were 129.5 nm ± 35.1 nm and 132.8 nm ± 41.9 nm, respectively.

Interestingly, at higher magnification MnO NPs loaded PLGA NPs were clearly visible and countable. Encapsulation of MnO NPs randomly occurred and it is not possible to control the amount of metal nanoparticles per PLGA NPs. Notably, the manganese particles remain single entities onto/into PLGA NPs and no aggregation was observed. Moreover, the PVA-shell surrounding the PLGA particles was observed.

The MnO NPs effective diameter measure was 9.7 nm ± 1.3 nm with a low polydispersity (Table 5.2).

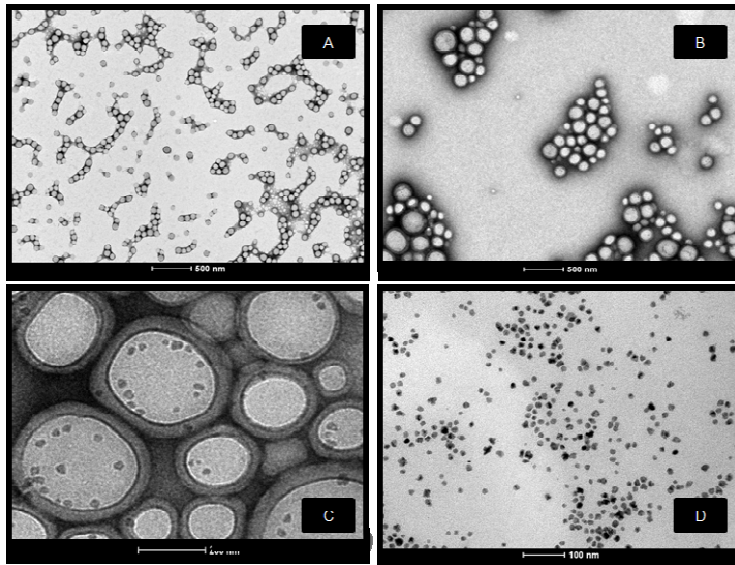
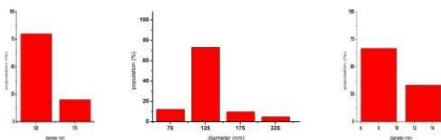
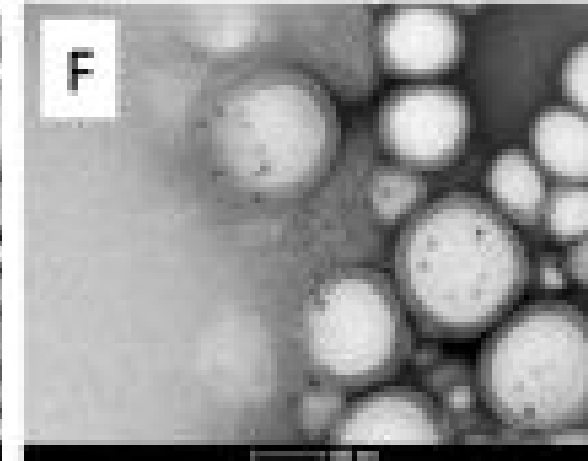
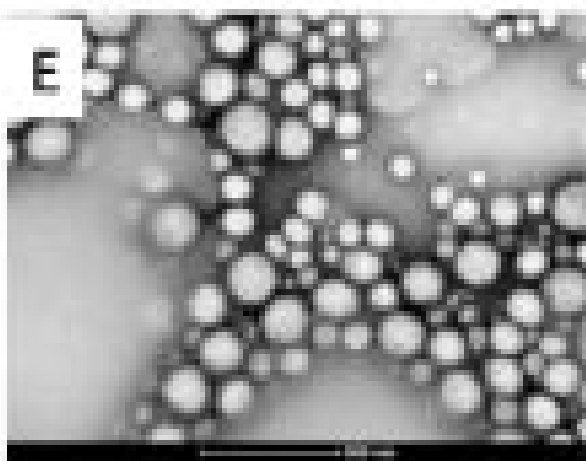
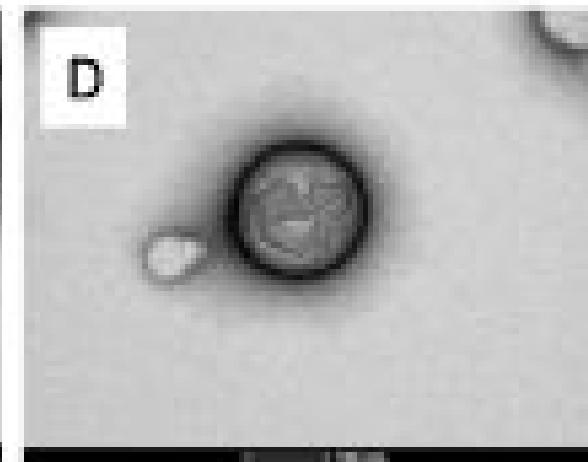
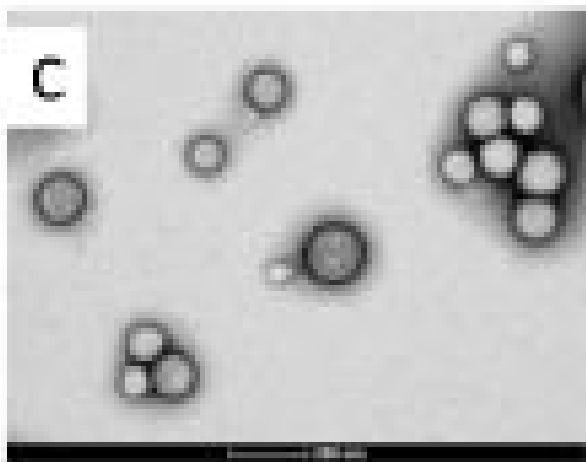
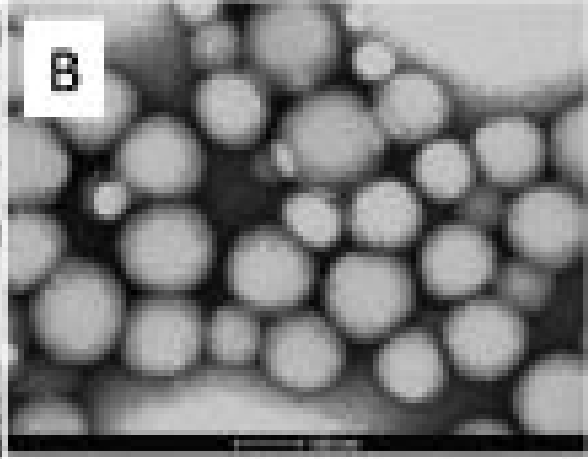
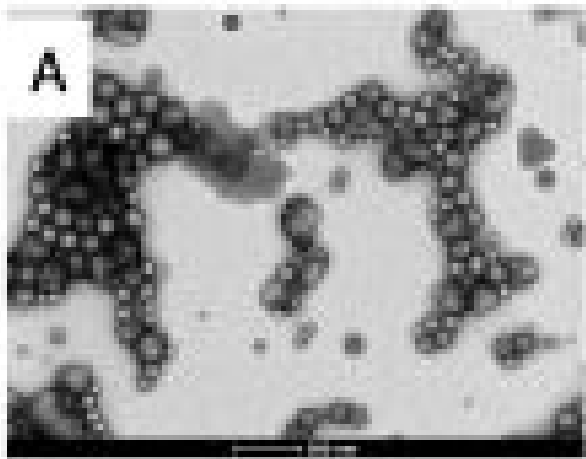


Figure 5.1. TEM images of (A) PLGA NPs (scale bar 500 nm) and (B), (C) PLGA@MnO NPs and (D) MnO NPs (scale bar 100 nm). Sample were negative stained with uranyl acetate (2% w/w).



Graph 5.5. (A) PLGA@MnO NPs, (B) PLGA NPs, (C) MnO NPs TEM size distribution analyses.

PLGA@MnO NPs degradation mechanism was investigated also by TEM images. To main mechanisms were described in literature: the bulk erosion and the surface erosion (Ch. ____, Par. __). PLGA NPs and PLGA@MnO NPs degradation mechanisms were identical. TEM images suggest an initial PVA-shell degradation one week after synthesis, followed by a consequently surface erosion of polymeric particles from outer to inner layers. Moreover, PLGA NPs swelling, deforming and increasing in diameter (Fig. 5.2 A, B, D, G, H and I). PLGA@MnO NPs degradation favor the escape of MnO NPs from polymeric matrix (Fig. 5.2E, F).



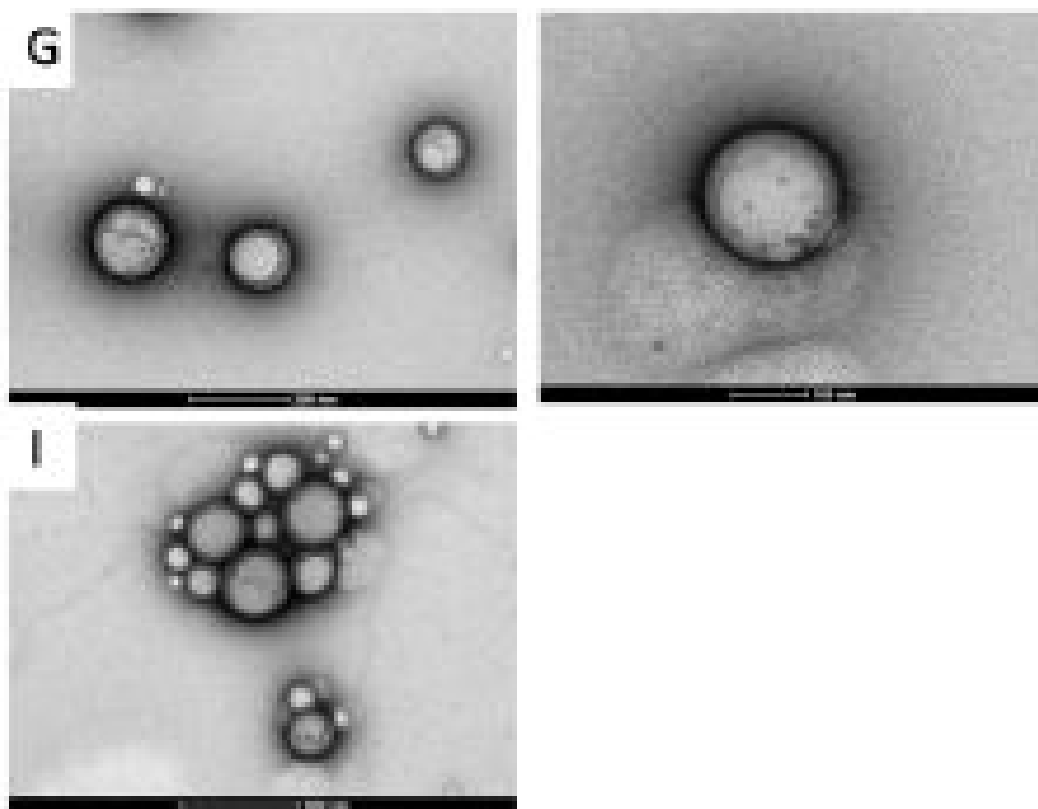


Figure 5.2. Degradation of PVA-shell of PLGA NPs one week after synthesis, scale bar (A) 500 nm (B) 100 nm, (C) 200 nm, (D) 100 nm. Degradation of PVA-shell of PLGA@MnO NPs one week after synthesis scale bar (E) 500 nm (F) 500 nm (G) 200 nm, (H) 100 nm, (I) 100 nm.

PLGA@MnO NPs in the mixture saline and plasma (0.7 :1) were analyzed by TEM (Fig. 5.3). PLGA NPs spherical structure was distinguished a tangle of proteins. In addition, PVA shell were ever visible as dark border around the polymeric particles. In this environment, it was not possible to establish if MnO NPs were still entrapped into PLGA matrix.

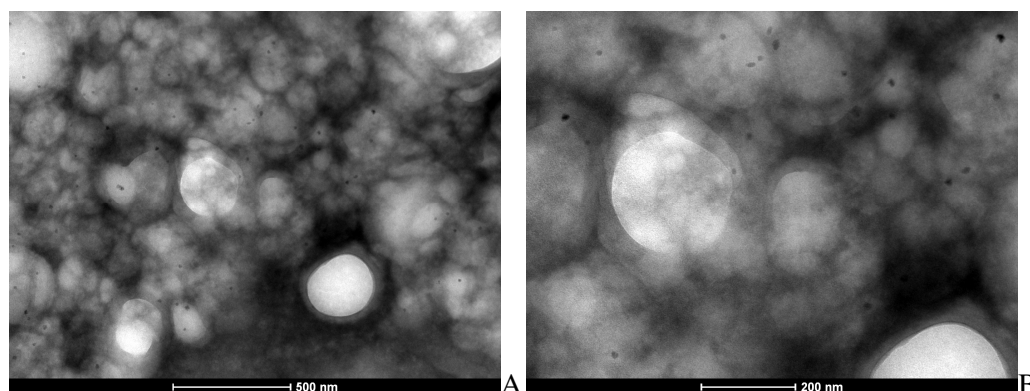
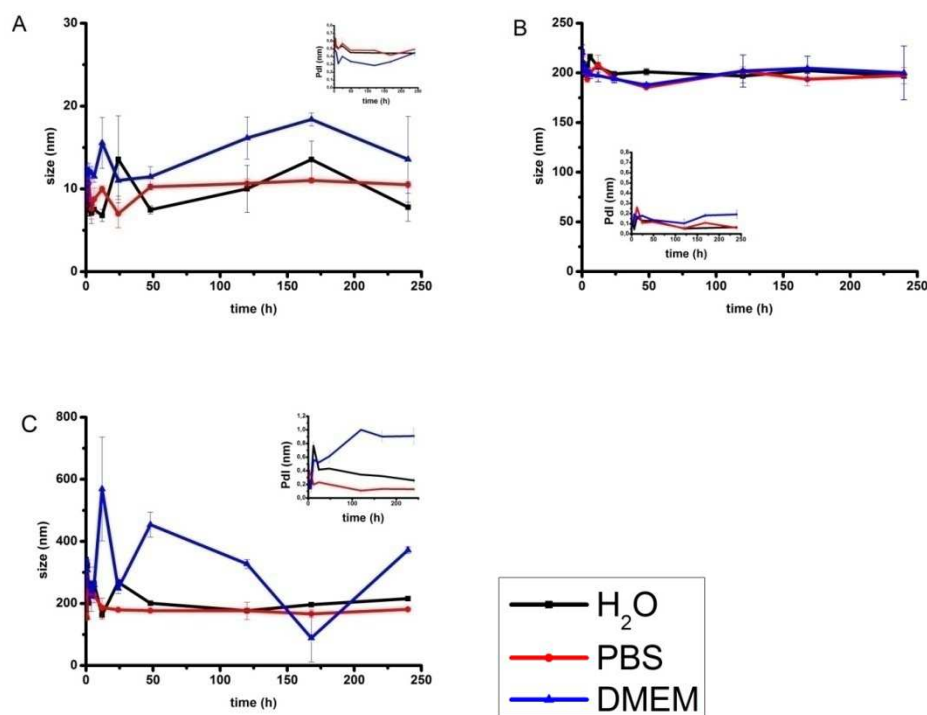


Figure 5.3. Tem images of PLGA@MnO NPs in saline plus plasma after 24 h, scale bar (A) 500nm, (B) 200 nm.

5.6. Stability test and degradation rate of PMA@MnO NPs, PLGA NPs and PLGA@MnO NPs

Stability test were performed by DLS. Samples of PMA@MnO NPs, PLGA NPs and PLGA@MnO NPs ($50 \mu\text{g ml}^{-1}$) were analysed in water Milli-Q, DMEM, and PBS 1X pH 7.2 (Graph 5.6).



Graph 5.6. Hydrodynamic diameter of (A) PMA@MnO NPs, (B) PLGA NPs and (C) PLGA@MnO NPs analysed in water Milli-Q, DMEM, and PBS 1X pH 7.2

The hydrodynamic diameter of MnO NPs (Grf. 5.6A) and PLGA@NPs (Grf. 5.6B) didn't vary significantly during the time of analysis, indicating nanoparticles were stable in time for at least 10 days. Also the polydispersity index didn't increase, corroborating the hypothesis of the stability. PLGA@MnO NPs showed different behaviour depending on the medium; they show high stability in water and in phosphate saline buffer 1X pH 7.2, while a fluctuating diameter and an increasing in polydispersity (Grf. 5.6C).

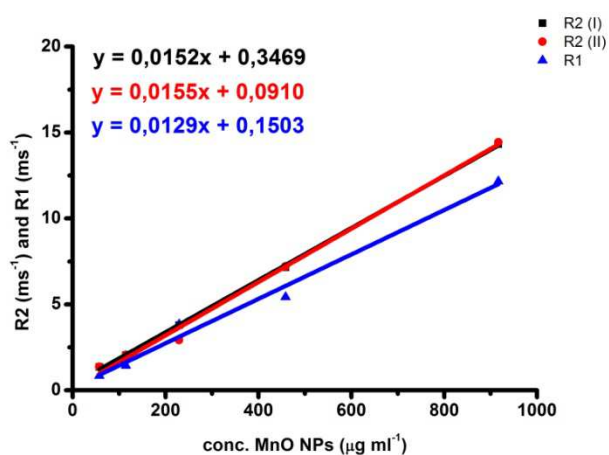
Manganese oxide degradation also was studied by TEM analyses for MnO NPs, PLGA NPs and PLGA@MnO NPs at time zero and after one week post synthesis (Fig. 5.3). MnO NPs were stable in time and no variations in diameter and polydispersity were observed (data not reported). Naked

and loaded polymeric particles started to degrade after one week: PVA was partially dissolved. Despite that size and polydispersity were not affected after seven days.

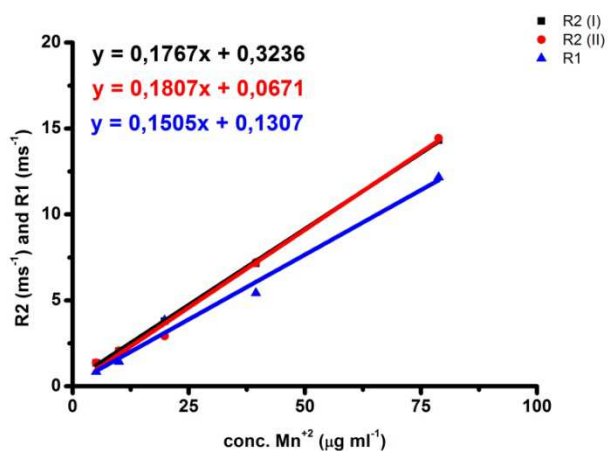
5.7. Relaxation analysis

In order to employ manganese oxide nanoparticles as contrast agents to ensure the particle enforcement power was primarily necessary. Relaxation measurements were firstly performed on PMA-coated manganese oxide nanoparticles and then on PLGA@MnO NPs to corroborate MnO NPs have maintained their contrast power even in presence of poly(lactic-co-glycolic acid) matrix.

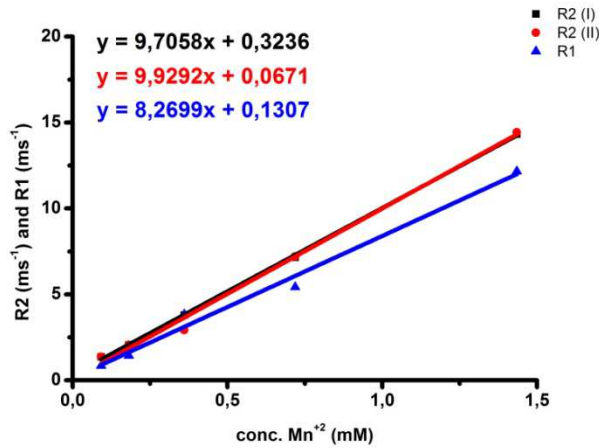
Relaxation analyses of PMA@MnO NPs were performed evaluating the particles capability of resounding with an external magnetic field of 0.5 T at 25 °C. The longitudinal (T_1) and transversal (T_2) relaxation times of samples at different Mn(II) ion concentrations in water Milli-Q and in saline mix with plasma (0.7 : 1) were acquired (Grf. 5.7).



A



B



C

Graph 5.7. Relaxation rates (A) R_1 and (B) R_2 as a function of (A) MnO NPs ($\mu\text{g ml}^{-1}$), (B) Mn^{+2} ($\mu\text{g ml}^{-1}$) and Mn^{+2} (mM) concentration in Milli-Q water at 303K.

Table 5.3. Relaxation rates R_1 and R_2 of PMA@MnO NPs in water Milli-Q and saline and plasma mix (0.7 : 1).

Sample: PMA@MnO NPs			in water Milli-Q			in saline and plasma (0.7 : 1)		
conc. MnO NPs ($\mu\text{g ml}^{-1}$)	conc. Mn^{+2} ($\mu\text{g ml}^{-1}$)	conc. Mn^{+2} (mM)	R_2 (I) (ms $^{-1}$)	R_2 (II) (ms $^{-1}$)	R_1 (ms $^{-1}$)	R_2 (I) (ms $^{-1}$)	R_2 (II) (ms $^{-1}$)	R_1 (ms $^{-1}$)
916,67	78,82	1,43	14,3225	14,4363	12,1655	5,3333	6,7568	4,4248
458,33	39,47	0,72	7,1582	7,2150	5,4259	3,9324	4,5413	2,9240
229,17	19,80	0,36	3,7836	2,9240	3,8329	2,7027	3,1069	1,9701
114,58	9,97	0,18	2,0425	2,0640	1,4286	2,1524	2,8580	1,5667
57,29	5,05	0,09	1,3596	1,3676	0,8475	-	-	-

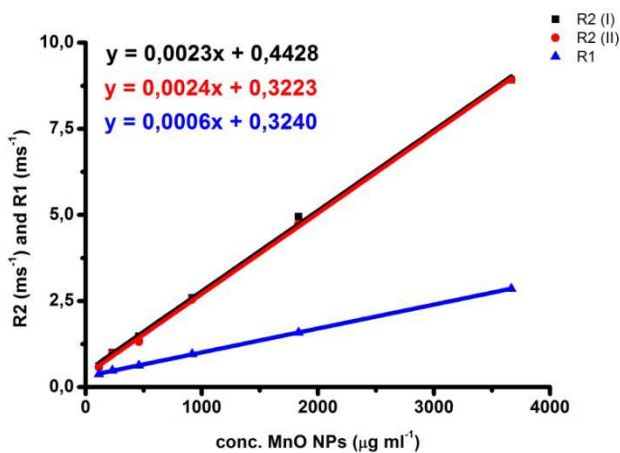
Relaxation rates R_1 and R_2 linearly depend on concentration of contrast agent in solution, either in water Milli-Q. r_1 and r_2 were estimated to be 8.2699 mM s^{-1} of Mn^{+2} ($0.1505 \mu\text{g ml}^{-1} \text{ s}^{-1}$ of Mn^{+2} , $0.0129 \mu\text{g ml}^{-1} \text{ s}^{-1}$ of MnO NPs), and 9.7058 mM s^{-1} of Mn^{+2} ($0.1767 \mu\text{g ml}^{-1} \text{ s}^{-1}$ of Mn^{+2} , $0.0152 \mu\text{g ml}^{-1} \text{ s}^{-1}$ of MnO NPs), respectively. PMA-coated MnO NPs were a highly sensitive T_1 positive MRI contrast agent ($r_2 / r_1 = 1.2$) in ultrapure water, but they also strongly broke down transversal relaxation time T_2 of water.

The exceptional relaxation data revealed the great potential of the manganese oxide nanoparticles as PLGA NPs-CA main tool.

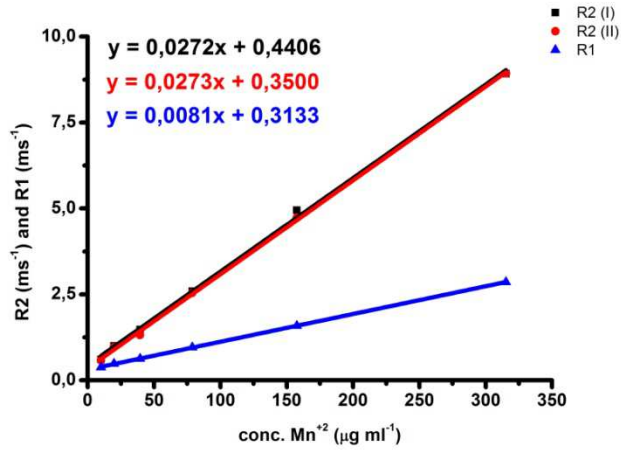
In order to investigate the influence of poly(lactic-*co*-glycolic acid) on the contrast power of MnO NPs, PLGA@MnO NPs were analyzed by Minispec instrument and the resulting R_1 and R_2 were

examined (Table 5.4). PLGA polymer modified the relaxation rates of metallic nanoparticles, by decreasing their contrast power with respect to PMA in water at 303K (Table 5.3). Despite of this, PLGA@MnO NPs contrast enhancement was still good for MR imaging. In addition, the polymeric coating provided a protection for the metal nanoparticles to degradation within the biological environment. Furthermore, PLGA coating decreased the cytotoxicity of MnO NPs (Par. 4.7) for human cells. For these reasons, a deeper knowledge on the properties of PLGA@MnO NPs CA was deserving to be investigated.

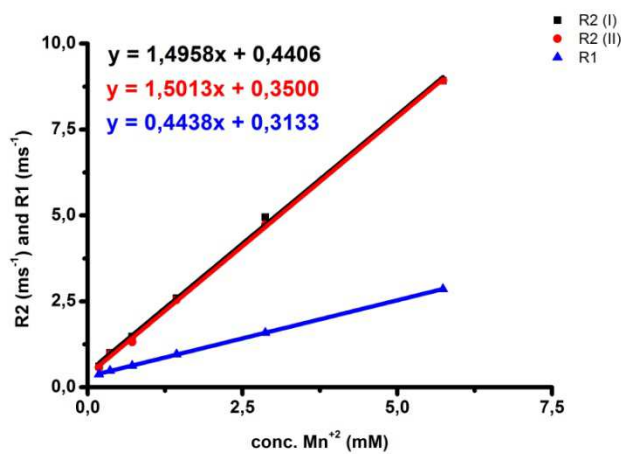
PLGA@MnO NPs relaxation times were linearity dependent on sample concentration (Grf.4.4, Tab.4.4). r_1 and r_2 extrapolated from the calibration curve were 0.4438 mM s^{-1} of Mn^{+2} ($0.0081 \text{ } \mu\text{g ml}^{-1} \text{ s}^{-1}$ of Mn^{+2} , $0.0006 \text{ } \mu\text{g ml}^{-1} \text{ s}^{-1}$ of MnO NPs), and 1.4959 mM s^{-1} of Mn^{+2} ($0.0272 \text{ } \mu\text{g ml}^{-1} \text{ s}^{-1}$ of Mn^{+2} , $0.0023 \text{ } \mu\text{g ml}^{-1} \text{ s}^{-1}$ of MnO NPs), respectively. PLGA-coated MnO NPs tremendously enhanced their T_1 positive contrast power ($r_2 / r_1 = 3.4$): it was three-fold powerful compared to PMA@MnO NPs in ultrapure water. PLGA carboxylic acid terminal groups hydrogen bonds with water could favor the spin-lattice relaxation, and thus increasing proton longitudinal relaxation rate, while strongly encumbered the spin-spin relaxation mechanism. Besides of that, PLGA@MnO NPs maintained the ability to decrease the transversal relaxation time T_2 of water. In general, relaxivity rates R_1 and R_2 decreased for PLGA compared to PMA embedded manganese oxide particles: The major consistence of PLGA than PMA layer onto magnetic NPs, could be responsible for impeding spin-spin and spin-lattice CA energy transfer to the surrounding medium. From these considerations PLGA@MnO NPs were proposed as valid contrast agents for future MRI application.



A



B



C

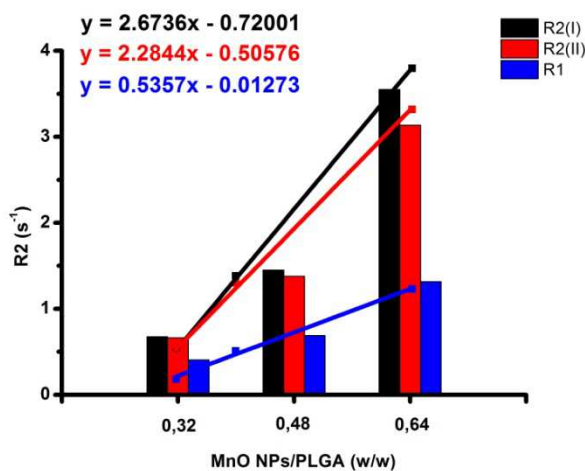
Graph 5.8. Relaxation rates (A) R_1 and (B) R_2 as a function of (A) MnO NPs ($\mu\text{g ml}^{-1}$), (B) Mn^{+2} ($\mu\text{g ml}^{-1}$) and Mn^{+2} (mM) concentration of PLGA@MnO NPs in Milli-Q water at 303K.

Table 5.4. Relaxation rates R_1 and R_2 of PMA@MnO NPs and PLGA@MnO NPs in water Milli-Q at 303K.

In water			Sample: PMA@MnO NPs			Sample: PLGA@MnO NPs		
conc. MnO NPs ($\mu\text{g ml}^{-1}$)	conc. Mn^{+2} ($\mu\text{g ml}^{-1}$)	conc. Mn^{+2} (mM)	R_2 (I) (ms $^{-1}$)	R_2 (II) (ms $^{-1}$)	R_1 (ms $^{-1}$)	R_2 (I) (ms $^{-1}$)	R_2 (II) (ms $^{-1}$)	R_1 (ms $^{-1}$)
3666,67	315,26	5,74	-	-	-	8,92	8,93	2,86
1833,33	157,63	2,87	-	-	-	4,95	4,73	1,59
916,67	78,82	1,43	14,32	14,44	12,1 7	2,59	2,54	0,96

458,33	39,47	0,72	7,16	7,22	5,43	1,48	1,32	0,63
229,17	19,80	0,36	3,78	2,92	3,83	1,00	0,97	0,48
114,58	9,97	0,18	2,04	2,06	1,43	0,61	0,58	0,38
57,29	-	-	1,36	1,37	0,85	-	-	-

Since contrast power was linearly dependent MnO NPs concentration, and therefore on Mn^{+2} ions concentration in the sample, more the increase of manganese oxide nanoparticles loaded on PLGA NPs, lower the screen by PLGA coating, and hence higher contrast power. To this aim, the same amount of nanocomposites encapsulating three different amount of metallic particles were analyzed. (Grf. 5.9).



Graph 5.9. Relaxation rates R_1 and R_2 of MnO NPs loaded PLGA NPs (0.32, 0.48 and 0.64 weight ratio (MnO NPs/PLGA) at $916.7 \mu g ml^{-1}$ of PLGA@MnO NPs in water Milli-Q at 303K.

Table 5.5. Relaxation rates R_1 and R_2 of MnO NPs loaded PLGA NPs (0.32, 0.48 and 0.64 weight ratio (MnO NPs/PLGA) at $916.7 \mu g ml^{-1}$ of PLGA@MnO NPsNPs in water Milli-Q at 303K.

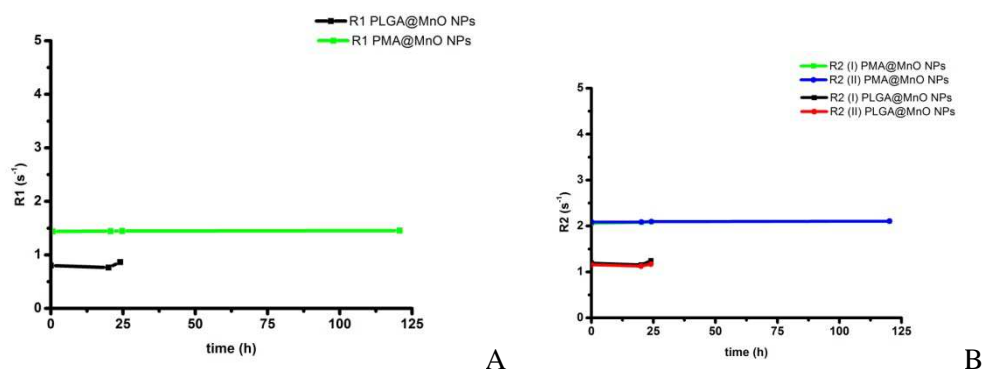
MnO NPs/PLGA (w/w)	conc. MnO NPs ($\mu g ml^{-1}$)	conc. Mn^{+2} ($\mu g ml^{-1}$)	conc. Mn^{+2} (mM)	T2 (I) (ms)	T2(II) (ms)	T1 (ms)
0.32	303,6	26,1	0,5	1484.2±0.7	1510.4±0.7	2470±80
0.48	378,8	130,0	2,4	689.7±0.4	725.1±0.4	1450±50
0.64	0,9	1,8	1,8	281.7±0.2	319±0.2	760±40

Highest relaxation rates were obtained from PLGA@MnO NPs with 0.64 MnO NPs/PLGA (w/w) ratio because of the higher amount of manganese ions in the sample. On the contrary, nil contrast power of 0.32 loading MnO NPs/PLGA (w/w) ratio was detected: T1 and T2 values were

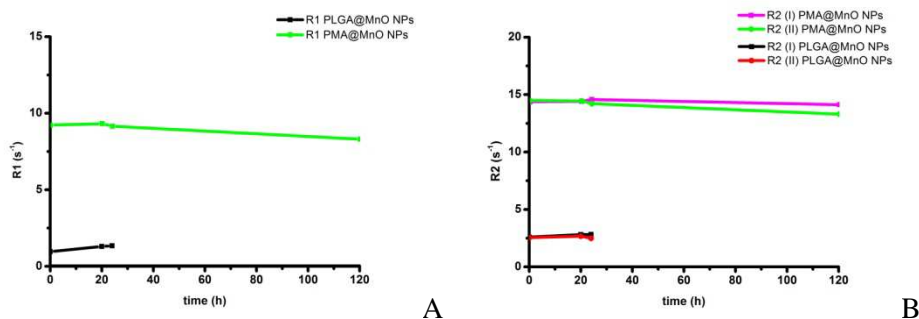
closed to water protons relaxation times. Graph showed more the amount of manganese oxide concentration in PLGA NPs, shorter the of relaxation times. Data confirmed MnO particles maintaining the capability to respond to an external magneticfield, even if reduced in presence of PLGA. Moreover, relaxation rates were linearly dependent on manganese concentration in PLGA NPS, accordingly with PMA@MnO NPs behavior in aqueous medium.

From these respects, PLGA@MO NPs with the major loaded value of manganese oxide nanoparticles were employed for the next experiments.

Stability of PMA-coated nanoparticles and PLGA@MnO NPs was investigated during time in ultrapure water at different concentration of MnO NPs ($114.58 \mu\text{g ml}^{-1}$ and $916.67 \mu\text{g ml}^{-1}$). The R_1 and R_2 constant values attested PMA@MnO NPs stability even after 10 days (Grf. 5.10 and 5.11). PLGA@MnO NPs stability was monitored for 24 h, a time sufficient for an *in vivo* MRI analysis (≤ 3 h) (Grf. 5.10 and 5.11).



Graph 5.10. Relaxation rates (A) R_1 and (B) R_2 of PMA@MnO NPs and PLGA@MnO NPs during time at $114.58 \mu\text{g ml}^{-1}$ of manganese oxide particles in water Milli-Q.

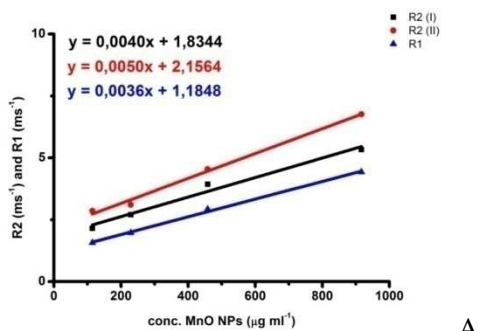


Graph 5.11. Relaxation rates (A) R_1 and (B) R_2 of PMA@MnO NPs and PLGA@MnO NPs during time at $916.67 \mu\text{g ml}^{-1}$ of manganese oxide particles in water Milli-Q.

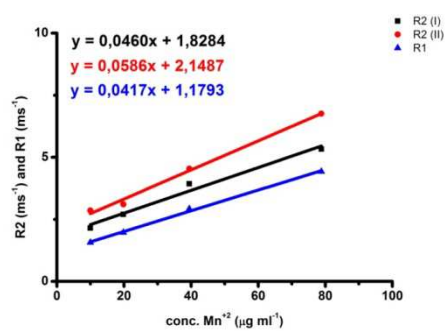
As previously demonstrated, the presence of the polymer affected the absolute value of the relaxation times T_1 and T_2 , but not modified the concentration-dependent behavior of the contrast agent.

In view of *anin vivo* application, PMA@MnO NPs and PLGA@MnO NPs capability as contrast agent in plasma was investigated.

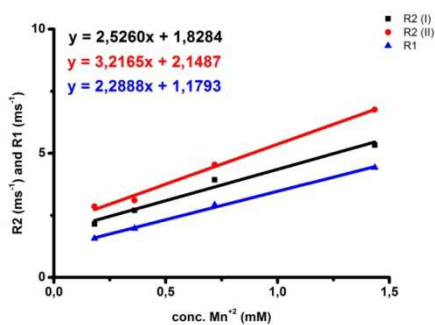
Relaxation rates R_1 and R_2 linearly depended on concentration of contrast agent in solution, either in water Milli-Q and in saline mix with plasma (0.7 : 1). In the mixture saline and plasma, r_1 and r_2 were estimated to be 2.2888 mM s⁻¹ of Mn⁺² (0.0417 μg ml⁻¹ s⁻¹ of Mn⁺², 0.0036 μg ml⁻¹ s⁻¹ of MnO NPs), and 2.5260 mM s⁻¹ of Mn⁺² (0.0460 μg ml⁻¹ s⁻¹ of Mn⁺², 0.0040 μg ml⁻¹ s⁻¹ of MnO NPs), respectively. PMA@MnO NPs were a highly sensitive T_1 positive MRI contrast agent ($r_2 / r_1 = 1.1$) in saline plus plasma and also strongly break down transversal relaxation time T_2 of the sample. PMA@MnO NPs contrast power as T_1 -enhancer unnoticeably decreased in the mixture saline and plasma instead of water. On the contrary, relaxivities r_1 and r_2 remarkably decreased in saline plus plasma: at higher concentrations of CA in solution, mixture R_1 and R_2 were three-fold lower than water relaxation rates (Table 5.6). Particles opsonization in plasma mix could be responsible for manganese contrast power decreasing; it could impede NPs-solvent interactions and limit the spin-spin and the spin-lattice relaxation mechanisms.



A



B



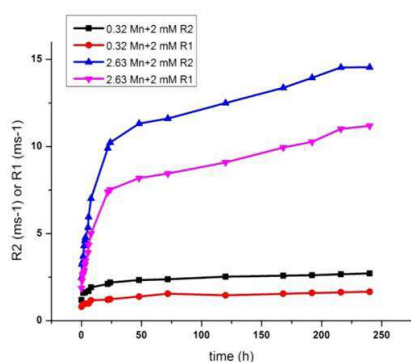
C

Graph 5.12. Relaxation rates of PMA@MnO NPs (A) R_1 and (B) R_2 as a function of (A) MnO NPs ($\mu\text{g ml}^{-1}$), (B) Mn^{+2} ($\mu\text{g ml}^{-1}$) and Mn^{+2} (mM) concentration in saline and plasma (0.7:1) at 303K.

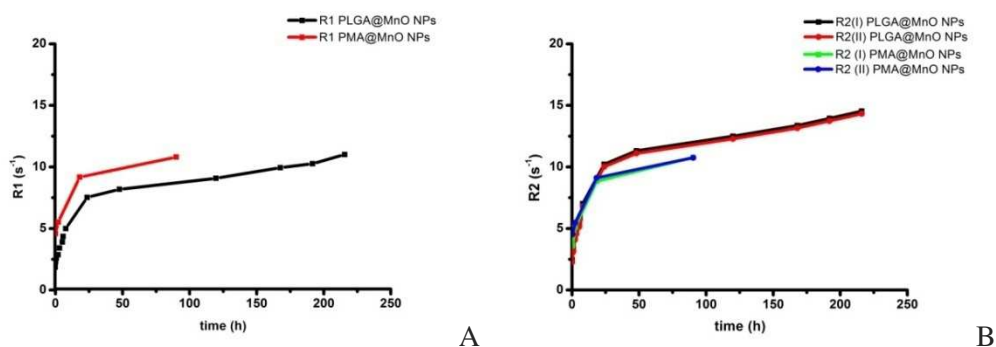
Table 5.6. Relaxation rates R_1 and R_2 of PMA@MnO NPs in saline mix with plasma (0.7 : 1) at 303K.

In saline and plasma			Sample: PMA@MnO NPs		
conc. MnO NPs ($\mu\text{g ml}^{-1}$)	conc. Mn^{+2} ($\mu\text{g ml}^{-1}$)	conc. Mn^{+2} (mM)	R_2 (I) (ms^{-1})	R_2 (II) (ms^{-1})	R_1 (ms^{-1})
916,67	78,82	1,43	5,3333	6,7568	4,4248
458,33	39,47	0,72	3,9324	4,5413	2,9240
229,17	19,80	0,36	2,7027	3,1069	1,9701
114,58	9,97	0,18	2,1524	2,8580	1,5667

Stability of PMA-coated nanoparticles and PLGA@MnO NPs was investigated during time in saline *plus* plasma at different concentration of MnO NPs ($114.58\mu\text{g ml}^{-1}$ and $916.67\mu\text{g ml}^{-1}$). PMA@MnO NPs and PLGA NPs R_1 and R_2 constant values increase in time was not significant at low concentration, as R_1 and R_2 values were close to blank (Grf. 5.13). PMA@ and PLGA@MnO NPs relaxivities r_1 and r_2 was not constant during time (Grf. 5.14). A deeper investigation on this phenomenon was necessary.

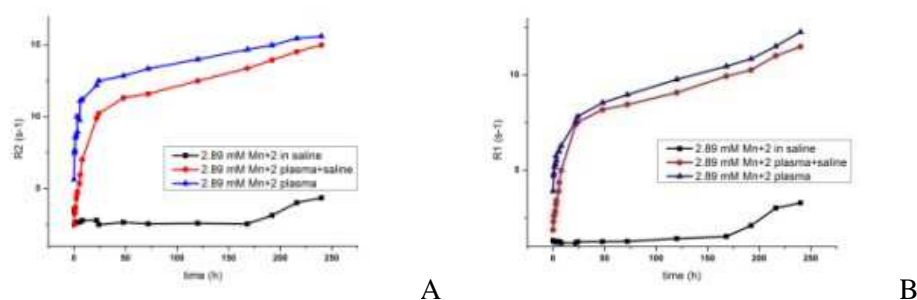


Graph 5.13. PLGA@MnO NPs (A) R_1 and (B) R_2 as a function of time at $114.58\mu\text{g ml}^{-1}$ ($78.82\text{ Mn}^{+2}\mu\text{g ml}^{-1}$, $1.43\text{ Mn}^{+2}\text{ mM}$) and $916.67\mu\text{g ml}^{-1}$ ($78.186\text{ Mn(II)}\mu\text{g ml}^{-1}$, $1.43\text{ Mn}^{+2}\text{ mM}$) MnO NPs entrapped in PLGA NPs.



Graph 5.14. (A) R_1 and (B) R_2 as a function of time at $916.67 \mu\text{g ml}^{-1}$ of MnO NPs entrapped in PLGA NPs ($78.816 \text{ Mn(II)} \mu\text{g ml}^{-1}$, $1.43 \text{ Mn(II)} \text{ mM}$) and coated with PMA ($916.67 \mu\text{g ml}^{-1}$ of MnO NPs entrapped in PLGA NPs ($78.186 \text{ Mn(II)} \mu\text{g ml}^{-1}$, $1.43 \text{ Mn(II)} \text{ mM}$) in the mixture saline and plasma (0.7 : 1).

PLGA@MnO NPs relaxivity grew over time in aqueous solution was nil, indicating NPs were preserved unaltered for at least one week in water, while a significantly different profile was observed in presence of plasma (Graph 5.15).



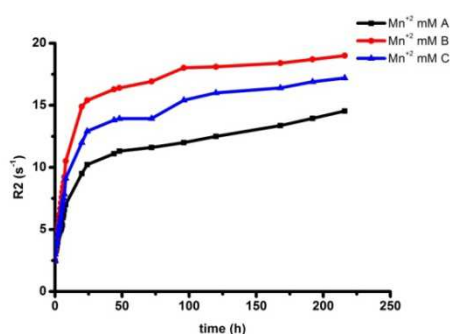
Graph 5.15. PLGA@MnO NPs (A) R_1 and (B) R_2 as a function of time at $916.67 \mu\text{g ml}^{-1}$ ($78.186 \text{ Mn}^{+2} \mu\text{g ml}^{-1}$, $1.43 \text{ Mn}^{+2} \text{ mM}$) in different in water MQ, in saline plus plasma (0.7 : 1) and in plasma.

Two hypotheses could justify the increase of R_1 and R_2 values in time. The first one suggests a faster polymer matrix enlargement or hydrolysis in plasma than in saline solution. As a consequence, the manganese-based contrast agent escaped from PLGA NPs, interacted with the environment and consequently decreased the relaxation times of the medium. A further investigation on the behavior of the PMA coated contrast agent reveal the same trend of PLGA@MnO NPs in plasma (Grf. 4.10). The increasing of relativity rates in time of both kinds of particles suggest a second hypothesis consisting in particles surface opsonization by plasmatic proteins and to the magnetization transfer (MT) mechanisms.²³ In magneticresonance imaging or NMR of macromolecular samples, such as protein solutions two types of water molecules, free (bulk) and bound (hydration) are present. Bulk water have many mechanical degrees of freedom

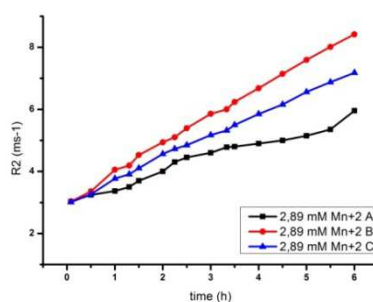
and the molecules motion exhibits a statistically averaged behavior. Because of this uniformity, most free water protons have resonance frequencies very near the average Larmor frequency of all such protons. Moreover, bulk water molecules are also relatively far from magnetic field perturbing macromolecules, such that free water protons experience a more homogenous magnetic field, which results in slower transverse magnetization dephasing and a longer T2. Conversely, hydration water molecules are mechanically constrained by extensive interactions with the local macromolecules and hence magnetic field inhomogeneities are not averaged out, resulting in faster dephasing of the magnetization that produces shorter T2 values. The presence of protein corona on the manganese-based contrast agent could favor this phenomena and hence, increase the relaxation rates R1 and R2 of the CA.

5.7.1. Reproducible manganese-loaded poly(lactic-co-glycolic acid) nanoparticles enhancement power

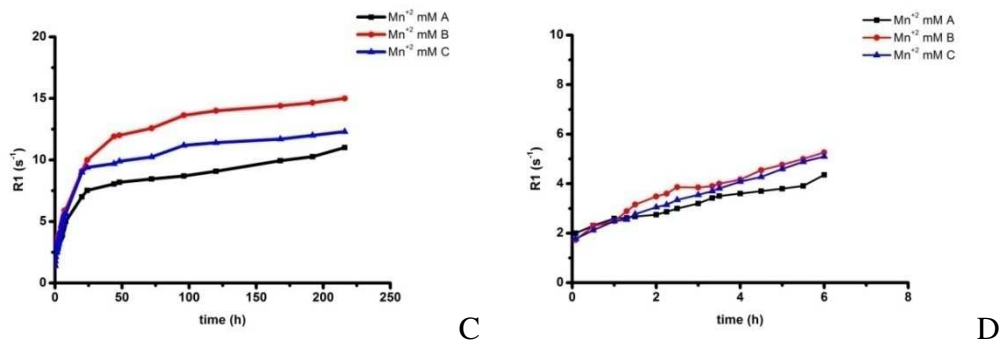
Different batches from the same protocol preparation of manganese-loaded polymeric nanoparticles were analyzed to confirm the reproducibility of relaxation analysis. As the loading of manganese oxide nanoparticles was the same for both the PLGA@MnO NPs, similar relaxation rates were expected by Minispec analysis. Data confirmed different batches gave a reproducible signal (data not shown). In addition, three relaxation rates profiles of the same PLGA@MnO NPs batch (120 μ l, 916.67 MnO NPs μ g ml⁻¹) in the mixture saline and plasma (0.7 : 1) from different persons, were reported (Grf 5.16). Relaxation rates profiles in time were superimposable, especially in the early hours of analysis (6h) (Fig. 5.16 C, D), attested the contrast ability of PLGA@MnO NPs was not influenced by different plasma. This is a considerable importance factor for the future *in vivo* diagnosis.



A



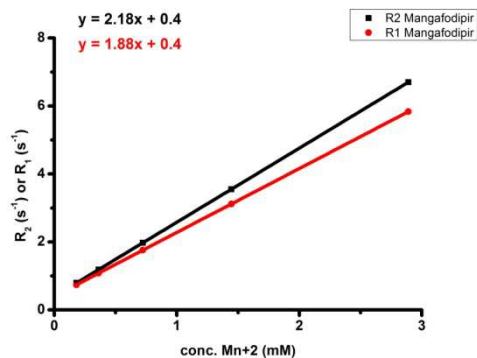
B



Graph 5.16. Relaxation rates trend in time (A, C in 250 h and B, D in 6 h) in different plasma mixtures by PLGA@MnO NPs (120 μ l, 916.67 MnO NPs μ g ml⁻¹).

5.7.2. A comparison with commercial manganese-based contrast agent

In order to employ PLGA@MnO NPs as MRI enhancer for *in vivo* diagnosis, a comparison with the commercially available manganese-based CA could provide significant information. A theoretical calibration curve of Mangafodipir was plotted by means of relaxivities r_1 and r_2 known from literature (1.88 and 2.18 at 37°C, respectively) (Grf. 5.17).⁷⁹



Graph 5.17. Theoretical calibration curves of Mangafodipir calculated from relaxivities r_1 and r_2 (1.88 and 2.18 at 37°C, respectively) reported in literature.⁷⁹

Otherwise, PMA@MnO NPs r_1 and r_2 were estimated to be 8.2699 Mn²⁺mM s⁻¹ (0.1505 Mn²⁺ μ g ml⁻¹ s⁻¹, 0.0129 MnO NPs μ g ml⁻¹ s⁻¹), and 9.7058 mM s⁻¹ of Mn²⁺ (0.1767 μ g ml⁻¹ s⁻¹ of Mn²⁺, 0.0152 MnO NPs μ g ml⁻¹ s⁻¹), respectively. These data proved the four-times T_1 and the fifth-fold T_2 higher contrast power of PMA@MnO NPs than Mangafodipir at the same concentration of administration. On the contrary, PLGA@MnO NPs r_1 and r_2 were five-times and two-fold lower than Magafodipir relaxivities.

In table 5.7 two situations of administrations were simulated. In the first simulation 78.84 Mn^{+2} μmol contained in PMA@, PLGA@MnO NPs and Mangafodipir were administered for MRI analysis. These moles of ions correspond to different weight amount of contrast agents. To inject the same amount of manganese ions, higher amount of PLGA@MnO NPs and Tesclscan were required. Moreover, even at the same Mn^{+2} dose, PLGA@MnO NPs and Mangafodipir provided a lower contrast enhancement. In the second simulation, 120 μl of PMA@, PLGA@MnO NPs and Mangafodipir (916.67 $\mu g ml^{-1}$) were administered to a body. This volume corresponded to different amount of injected manganese ions, responsible for generating the contrast in images. As a consequence, PMA@MnO NPs generated about three-times higher contrast images with respect to Mangafodipir. Otherwise, PLGA@MnO NPs enhancing capability was much lower in comparison with PMA-coated NPs and manganese complex.

Table 5.7. Comparisons between PMA@MnO NPs, PLGA@MnO NPs and Mangafodipir injections.

1st simulation									
conc PLGA@MnO NPs (mg)	conc MnO NPs (μg)	conc Mn2+ (μg)	conc. Mn2+ (μmol)	conc MnO NPs (μg)	conc Mn2+ (μg)	conc. Mn2+ (μmol)	con c mf (μg)	conc mn+2 (μg)	conc. mf (μmol)
88,03	916,94	78,84	1,44	916,94	78,84	1,44	173 3,08	78,84	1,44
		R2(l)	R1		R2(l)	R1		R2(l)	R1
		2,779	1,066		14,216	11,874		3,528	3,098

2nd simulation									
conc PLGA@MnO NPs (μg)	conc MnO NPs (μg)	conc Mn2+ (μg)	conc. Mn2+ (μmol)	conc MnO NPs (μg)	conc Mn2+ (μg)	conc. Mn2+ (μmol)	conc mf (μg)	conc mf (μg)	conc. mf (μmol)
0,92	9,55	0,95	0,02	916,94	78,84	1,44	916 ,94	41, 71	0,76
		R2(l)	R1		R2(l)	R1		R2(l)	R1
		0,429	0,408		14,21 6	11,874		2,0 55	1,827

Taking into account these results, it is possible to affirm PLGA@MnO NPs are very promising tools for MRI diagnosis. PLGA@MnO NPs contrast power is comparable with the commercial Tesclscan, suggesting a realistic possibility of an *in vivo* use. Moreover, the contrast enhancement

increases in the plasma mixture during time until proton relaxation rates given by PMA@MnO NPs as CA.

A final comparison between PMA@ and PLGA@MnO NPs was necessary (Table 5.8). Unfortunately, no data for Mangafodipir in plasma were disposable. The two situations proposed attested one time more the higher contrast power of PMA-coated nanoparticles in comparison with PLGA@MnO NPs of both at the same dose of Mn²⁺ (1st simulation) and of total amount of compounds injected (2nd simulation). This could be imputable to the presence of the PLGA coating that impeded the manganese-environment interaction, thus limiting the increasing of relaxation rates of protons in the surrounding of the CA. Interestingly, the contrast power of PLGA@MnO NPs increasing in time even to be very closed to PMA@MnO NPs.

Table 5.8. Comparisons between PMA@MnO NPs and PLGA@MnO NPs injections from analysis in plasma mixture.

1st simulation						
conc PLGA@MnO NPs (ug)	conc MnO NPs (ug)	conc Mn2+ (ug)	conc. Mn2+ (umol)	conc MnO NPs (ug)	conc Mn2+ (ug)	conc. Mn2+ (umol)
1,3	109,831	9,560	0,174	110,0	9,6	0,174
	time (h)	R2(l)	R1	time (h)	R2(l)	R1
	0	2,5	1,9	0	3,5	2,6
	3	4,8	3,4	3	-	-
	6	6,0	4,4	6	-	-
	24	10,2	7,5	18	8,8	6,2

1st simulation						
conc PLGA@MnO NPs (g)	conc MnO NPs (ug)	conc Mn2+ (ug)	conc. Mn2+ (umol)	conc MnO NPs (ug)	conc Mn2+ (ug)	conc. Mn2+ (umol)
1,3	109,831	9,560	0,174	1300,0	111,720	2,033
	time (h)	R2(l)	R1	time (h)	R2(l)	R1
	0	2,5	1,9	0	5,6	4,6
	3	4,8	3,4	3	-	-

6	6,0	4,4	6	-	-
24	10,2	7,5	18	-	-

5.7.3. *In vitro* Magnetic Resonance Imaging analysis

By investigating manganese particles as positive contrast agents for diagnostic MRI of chronic inflammatory bowel disease, only T1 longitudinal relaxation time values were reported. T1-weighted images from T1-maps (Fig. 4.4) showed a clear dose-dependent signal, both in saline and in the mixture of saline and plasma (0.7 : 1) (Fig. 4.5). Moreover the contrast power notably increased in plasma during time, while remained constant in saline. Data confirmed measurements from TD-NMR Benchtop Systems. PLGA@MnO NPs are good T1 contrast agent, while PLGA NPs give no MRI signal both in physiological medium and in plasma (data not shown). Finally, the contrast increase in time significantly for the higher concentration, both in saline and in the mixture of saline and plasma (Fig. 4.5). By plotting R1 values from MR analysis vs Mn(II) ion concentration (Grf. 4.18) TD-NMR results received a further confirmation. PLGA@MnO NPs were stable in saline as the calibration curves at different times were superimposed, providing to determine the relaxivity r_1 of the samples (about 0.3 mM s⁻¹). As expected, the relaxivity of PLGA@MnO NPs in presence of plasma rather increases over time for all the concentrations, indicating the contrasting power of the manganese-based agent intensify in time (from 0.3 mM s⁻¹ to 0.9 mM s⁻¹). In particular, it was observed the relaxivity value at time 0 h coincides with the value of the relaxivity of the samples in saline at any times, representing in the first minutes after PLGA@MnO NPs addition to plasma, the sample was not degraded, as in saline solution. By plotting R1 values from MR analysis vs time (Grf. 4.19) it was evident PLGA@MnO NPs were stable in saline while in presence of plasma an enhancement over time was observed for all the concentrations, indicating the T1 of the proton of the environment decrease in time. Moreover it was observed the MR R1 signal is not detectable below 0.015 Mn⁺² mM concentration.

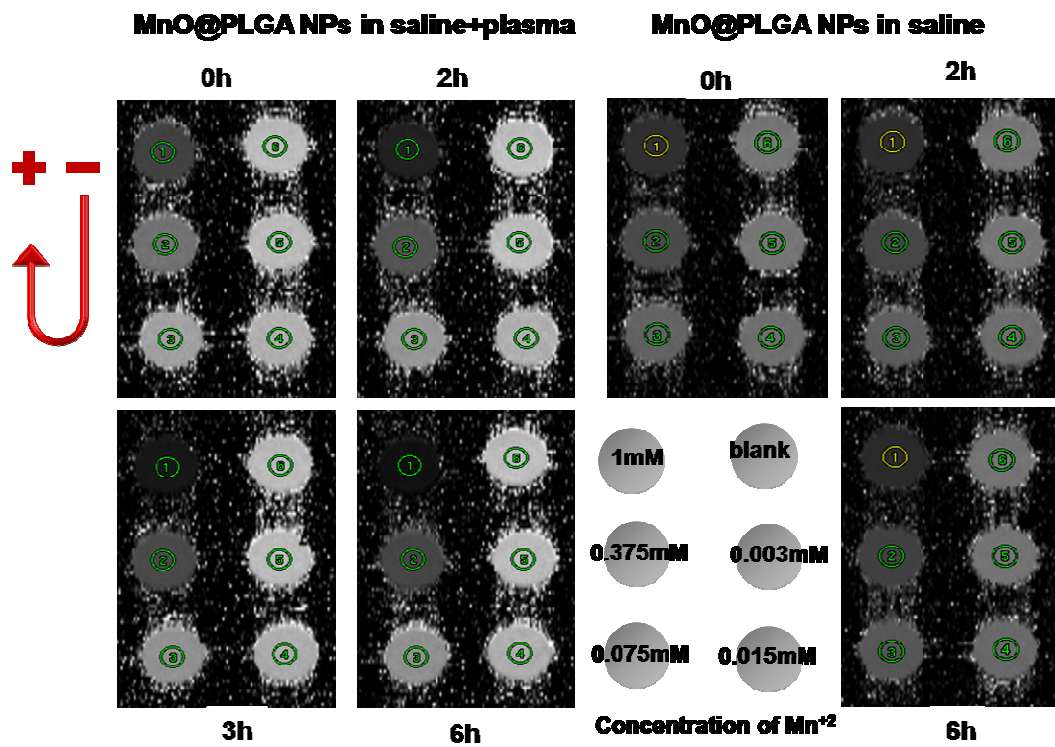


Figure 5.4. (A) T_1 -map image of PLGA@MnO NPs at different concentrations of Mn^{+2} ions in (A) the mixture plasma and saline, (B) in saline.

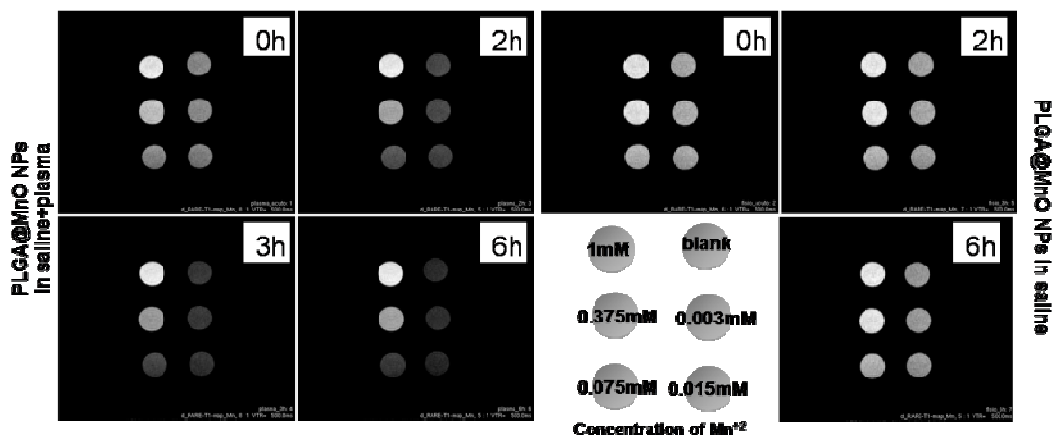
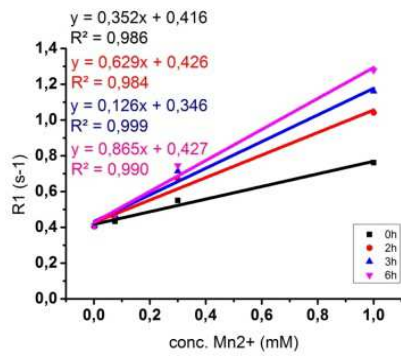
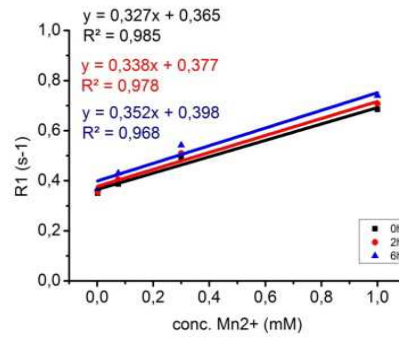


Figure 5.5. (A) T_1 -weighted image of PLGA@MnO NPs at different concentrations of Mn^{+2} ions in (A) the mixture plasma and saline, (B) in saline.

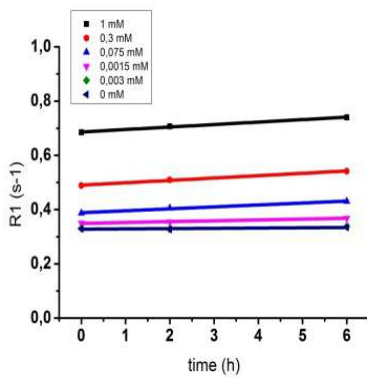


A

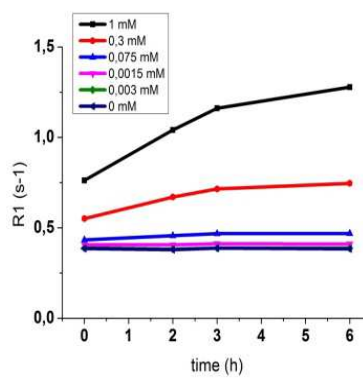


B

Graph 5.18. Plots of the R_1 of PLGA@MnO NPs in (A) the mixture saline and plasma and saline (B) as a function of Mn^{+2} ion concentration.



A



B

Graph 5.19. Plots of the R_1 of PLGA@MnO NPs different in Mn^{+2} ion concentration in (A) the mixture saline and plasma and saline (B) as a function of time.

Table 5.9. Relaxation times T_1 and T_2 of PLGA@MnO NPs different in Mn^{+2} ion concentration in the mixture saline and plasma and saline as a function of time.

t (h)	Mn (mM)	T1 (ms)		T2 (ms)	
		Plasma	Saline	Plasma	Saline
0	1	1312,71 ± 24.3	1460,77 ± 26.1	50,4418 ± 0.9	31,8375 ± 0.7
	0.375	1814,84 ± 30.4	2044,74 ± 28.1	83,8775 ± 1.3	62,0138 ± 1.4
	0.075	2307,83 ± 40.4	2586,29 ± 47.2	156,815 ± 3.2	132,649 ± 3.0
	0.003	2457,32 ± 43.0	2855,75 ± 59.2	193,708 ± 4.1	176,924 ± 3.6
	0.015	2572,89 ± 39.8	3023,78 ± 51.0	200,232 ± 3.3	192,281 ± 3.4
	0	2599,28 ± 41.2	3036,14 ± 45.5	202,04 ± 3.7	196,169 ± 3.7

2	1	960,595 ± 17.1	1414,43 ± 22.1	48,3037 ± 0.9	30,9657 ± 0.6
	0.375	1492,42 ± 24.4	1962,77 ± 29.0	67,5776 ± 1.8	59,507 ± 1.2
	0.075	2191,58 ± 34.2	2466,28 ± 45.0	104,185 ± 2.4	123,943 ± 2.9
	0.003	2464,41 ± 42.5	2823,97 ± 57.5	118,065 ± 2.0	176,135 ± 3.8
	0.015	2614,02 ± 17.45.0	3046,33 ± 52.3	121,474 ± 2.0	195,476 ± 3.7
	0	2635,64 ± 45.4	3055,94 ± 43.8	122,625 ± 1.9	201,204 ± 3.5
3	1	861,09 ± 11.3		53,8567 ± 1.0	
	0.375	1398,41 ± 22.8		73,0882 ± 1.6	
	0.075	2138,15 ± 39.0		106,635 ± 2.1	
	0.003	2428,13 ± 43.4		119,251 ± 2.2	
	0.015	2577,12 ± 46.8		122,571 ± 1.9	
	0	2578,06 ± 40.8		123,865 ± 1.9	
6	1	782,48 ± 12.5	1351,08 ± 21.7	54,3991 ± 1.0	31,7299 ± 0.7
	0.375	1340,9 ± 16.5	1845,31 ± 28.7	90,0093 ± 3.3	58,8893 ± 1.5
	0.075	2134,73 ± 34.4	2322,72 ± 37.4	110,717 ± 3.1	118,26 ± 2.6
	0.003	2434,52 ± 45.7	2714,16 ± 51.4	119,256 ± 2.1	177,002 ± 3.6
	0.015	2581,73 ± 39.4	2960,13 ± 38.9	122,171 ± 1.8	199,121 ± 3.7
	0	2610,51 ± 42.5	2987,87 ± 49.3	122,947 ± 1.7	204,569 ± 3.9

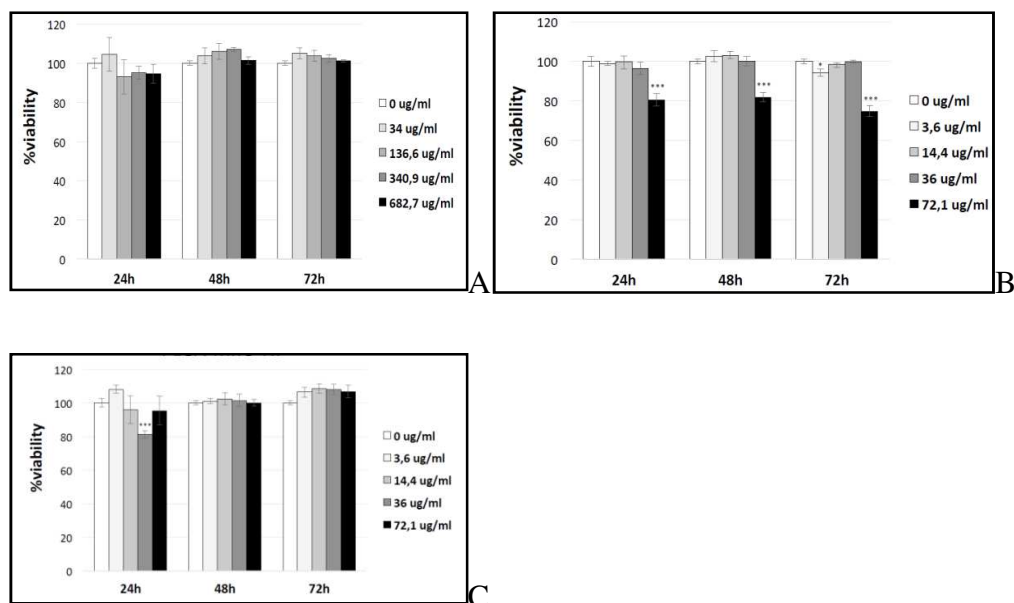
T₂ relaxation times values of saline and plasma mixture were measured in presence of PLGA@MnO NPs at times and concentrations described above. These data (Table 5.9) have not been thoroughly analyzed, but revealed the particles potential to act as a negative contrast agent, as already inferred from Minispec data (Par. 4.6.1).

5.8. Cytotoxicity assay

Toxicity is primarily due to the action of Mn⁺² as a calcium channel blocker with effects on muscle electrophysiology and contractility, and it has limited the use of manganese salts as paramagnetic contrast agents.^{79,80} Manganese complexes are relatively unstable *in vivo* and are dissociated in biological media. Indeed, manganese can be displaced by other divalent cations such

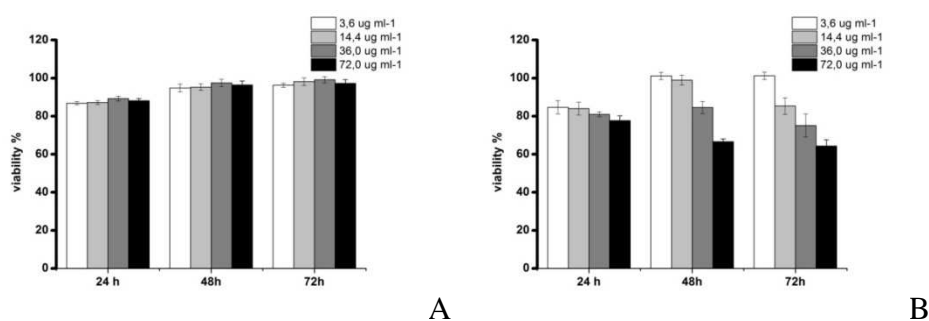
as calcium, magnesium, or zinc. Some concern exists about the potential long-term toxicity associated with the development and use of Mn-based contrast agents caused by the complex release.⁸¹ Free manganese was shown to be teratogenic and mutagenic in several models.³⁴ The teratogenic effect was also demonstrated after commercial MnDPDP injection.^{82,83} It was thus of great importance to show that PLGA@MnO NPs are non-toxic *in vitro* at concentrations of 1 mM. In view of the future application of PLGA@MnO NPs as contrast agents for the diagnosis of inflammatory bowel diseases, it is necessary to assess the toxicity of the nanoparticles on a cellular IBD model. Unfortunately, nowadays there is not an appropriate cellular IBD model and murine endothelial cellular SVEC-14-0 line is the most closed to IBD cells. Also tumor HeLa cell line, the oldest and most commonly used human cell line, was used to test the cytotoxicity of PLGA@MnO NPs. Cell toxic effect of NPs was investigated by incubating increasing concentrations of nanoparticles in both cell lines and assessing cell viability at different times (24, 48, 72 h). Cytotoxicity test on endothelial murine cells SVEC-14-0 demonstrated both PLGA NPs and PLGA@MnO NPs were extremely safe in the wide range of concentrations tested (0 $\mu\text{g ml}^{-1}$ to 682.7 $\mu\text{g ml}^{-1}$ of polymer particles corresponding to 0 $\mu\text{g ml}^{-1}$ and 72 $\mu\text{g ml}^{-1}$ of MnO NPs) (Grf. 5.20 A) and after 72 h of incubation, treated cell showed the highest cell viability percentage (100%) (Grf. 5.20B). Otherwise, a mild reduction in cell viability ($19.48\% \pm 3.15$) was detected upon incubation with 72.1 $\mu\text{g ml}^{-1}$ of PMA-coated nanoparticles at 24 h, remained unvaried at 48 h and decrease of about 25 % at 72 h (Grf. 5.20C), representing low cytotoxic effect. The cytotoxicity of MnO NPs was completely eluted thanks to the polymeric coating: without PLGA matrix, manganese oxide nanoparticles reduce cells viability to 80 % after 24 h of incubation, and decrease gradually of exposure time from 24 h to 72 h, while if clothed with the polymer, they allow cells to grow as the control. MnO@PLGA NPs are absolutely safe compared to the same concentration of PMA@MnO NPs tested, confirming that the polymeric PLGA coating advantages in reducing the toxicity of the metallic particles (Grf. 5.20 C).

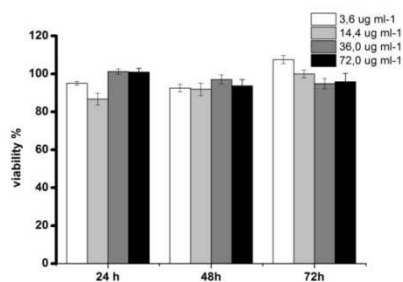
Cytotoxicity test on HeLa cell lines in the same experimental conditions gave similar results (Grf. 5.21).



conc PLGA NPs (mg ml ⁻¹)	conc MnO NPs (ug ml ⁻¹)	conc Mn2+ (ug ml ⁻¹)	conc. Mn2+ (mM)
6,35	317,22	54,94	1,00
2,38	118,96	20,60	0,38
0,48	23,79	4,12	0,08
0,10	4,76	0,82	0,02
0,02	0,95	0,16	0,00

Graph 5.20. *In vitro* cytotoxicity study on SVEC 4-10 cells. Cell viability was assessed by MTS assay. Reported values are means \pm standard error (SE) of six replicates, normalized on proliferation of untreated cells. *** $P < 0.001$. (A) Cells treated with 0, 34, 136.6, 340.9, 682.7 $\mu\text{g ml}^{-1}$ of PLGA NPs for 72 hours. (B) Cells treated with 0, 3.6, 14.4, 36, 72.1 $\mu\text{g ml}^{-1}$ of PMA@MnO NPs for up to 72 hours. (C) SVEC 4-10 cells cultured to 72 h with 0, 3.6, 14.4, 36, 72.1 $\mu\text{g ml}^{-1}$ of MnO NPs loaded on PLGA NPs, corresponding to 0, 34, 136.6, 340.9, 682.7 $\mu\text{g ml}^{-1}$ of PLGA NPs, respectively.





C

conc PLGA NPs (mg ml ⁻¹)	conc MnO NPs (ug ml ⁻¹)	conc Mn ²⁺ (ug ml ⁻¹)	conc. Mn ²⁺ (mM)
6,35	317,22	54,94	1,00
2,38	118,96	20,60	0,38
0,48	23,79	4,12	0,08
0,10	4,76	0,82	0,02
0,02	0,95	0,16	0,00

Graph 5.21. *In vitro* cytotoxicity study on HeLa cells. Cell viability was assessed by MTS assay. Reported values are means \pm standard error (SE) of six replicates, normalized on proliferation of untreated cells. *** $P < 0.001$. (A) Cells treated with 0, 34, 136.6, 340.9, 682.7 $\mu\text{g ml}^{-1}$ of PLGA NPs for 72 hours. (B) Cells treated with 0, 3.6, 14.4, 36, 72.1 $\mu\text{g ml}^{-1}$ of PMA@MnO NPs for up to 72 hours. (C) HeLa cells cultured to 72 h with 0, 3.6, 14.4, 36, 72.1 $\mu\text{g ml}^{-1}$ of MnO NPs loaded on PLGA NPs, corresponding to 0, 34, 136.6, 340.9, 682.7 $\mu\text{g ml}^{-1}$ of PLGA NPs, respectively.

5.9. MAdCAM-1 expression in experimental IBD model

With the final aim of testing MnO-NPs *in vivo*, we reproduced a murine model of inflammatory bowel disease by treating mice with 3% DSS in drinking water over 7 days. DSS treatment progressively induced loss of body weight, diarrhea and rectal bleeding, which were scored daily as clinical parameters associated with active colitis (Fig. 5.6 A, B, C). Disease progression was indicated by the disease activity index (DAI), calculated as the sum of clinical parameters observed during treatment, and revealed an acute phase of bowel inflammation starting after 5 days of DSS treatment (Fig. 5.6 D). Bowel damage was first assessed by measuring the length of colon dissected from mice at 3, 5 and 7 days of treatment. Colon length was only slightly reduced (by 10.3%) after 3 days of DSS treatment, while it drastically shortened by 33.7% and 35.9% after 5 and 7 days of DSS treatment, respectively, when compared to the length of colon from control non-treated mice

(Fig. 5.6 E). DSS-induced colon damage was then confirmed by histological analysis on bowel tissues (HE staining): after 5 days of DSS treatment inflammation and ulceration could be observed with loss of the epithelial lining of mucosa surface and glands (Fig. 5.6 F). These features were more severe in mice after 7 days of treatment. On the contrary, no inflammation was demonstrated in control mice and after 3 days of DSS treatment. Then, the MAdCAM-1 expression profile on intestinal mucosal vascular endothelium in control and DSS-treated mice. Immunohistochemistry revealed a progressive increase in MAdCAM-1 signal upon DSS treatment: only very few vessels were stained positive in control healthy mice and after 3 days of DSS treatment, while MAdCAM-1 staining dramatically increased at 5 and 7 days of treatment in the areas of histological damage (Fig. 5.7 A). This expression pattern correlated with the histologic assessment of inflammatory lesions, which pointed out the beginning of the acute phase of the disease at 5 days of DSS treatment. In parallel, we checked MAdCAM-1 protein expression on colon tissue homogenates by performing a western blotting analysis on samples of proximal and distal colon from control and DSS-treated mice (Fig. 5.7 B, C). We further observed that DSS treatment induced an over-expression of MAdCAM-1, which was only slightly expressed after 3 days of treatment, but appeared dramatically over-expressed after 5 days of treatment in both proximal and distal part of the colon. After 7 days of treatment the expression level of MAdCAM-1 protein was maintained high and did not increase further. Interestingly, we observed that, at 5 days of DSS treatment, MAdCAM-1 over-expression was significantly higher in the proximal part of the colon than in the distal one ($P = 0.013$) (data not shown). This expression profile was confirmed by immunohistochemistry on bowel tissues slides, and related to the inflammatory score of each bowel region (Table 5.10).

Table 5.10. Inflammation grade and MAdCAM-1 score in bowel specimens isolated from 4 mice treated with DSS for 5 days.

	Ileum				Proximal colon				Distal colon				
Inflammation grade	-	-	-	-				+++					+
MAdCAM-1 score	-	-	-	+				+++					+

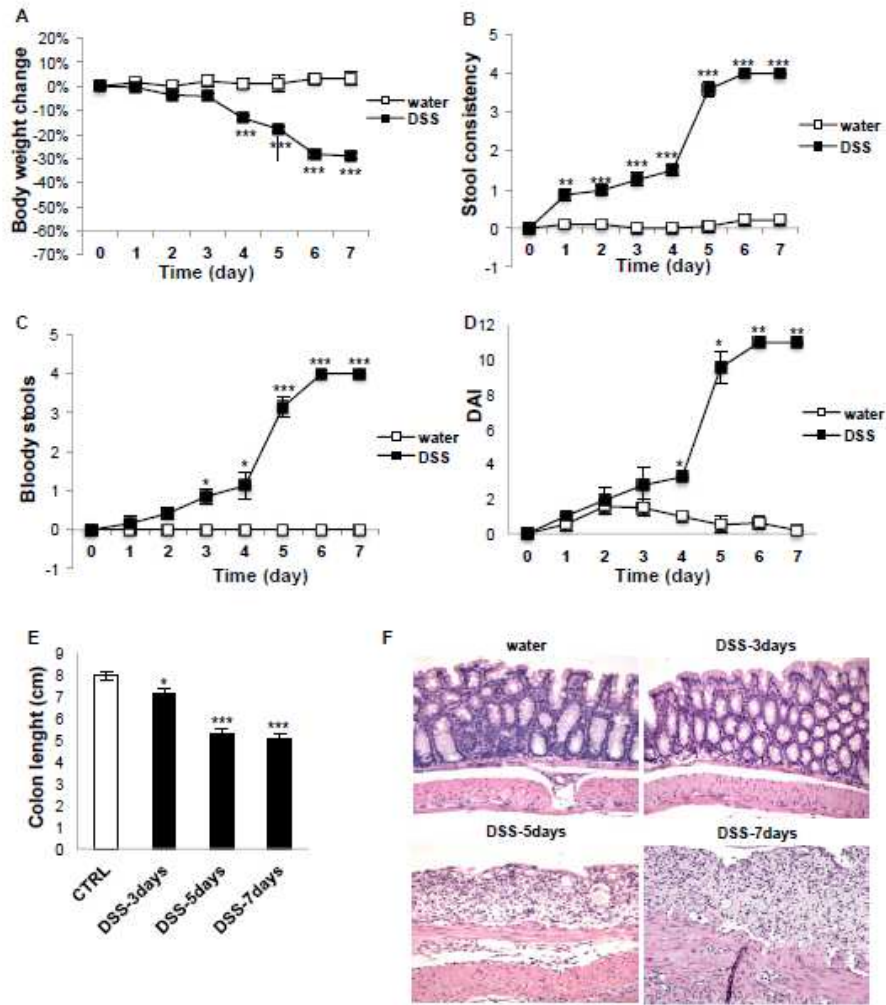


Figure 5.6. DSS-induced colitis in mice. Changes over time in body weight (A), stool consistency (B), and presence of blood in the stools (C) upon DSS treatment were monitored daily, scored as described in Materials and Methods, and compared to scores set for control group of mice drinking regular water. (D) Colitis severity was assessed for each group of animals by clinical disease activity index (DAI), which was calculated daily as described in Materials and Methods. (E) Colon length reduction upon DSS treatment was compared to that of control mice drinking regular water. Reported values are means \pm SE of all mice included in the study. * $P < 0.05$, ** $P < 0.01$, *** $P < 0.001$ DSS-treated *versus* control mice. (F) H&E of colon sections from control mice (water) or mice treated with DSS for 3, 5 or 7 days (20 \times magnification): in 5 and 7 days-treated mice, inflammation of the mucosa, ulceration and loss of epithelial lining were observed.

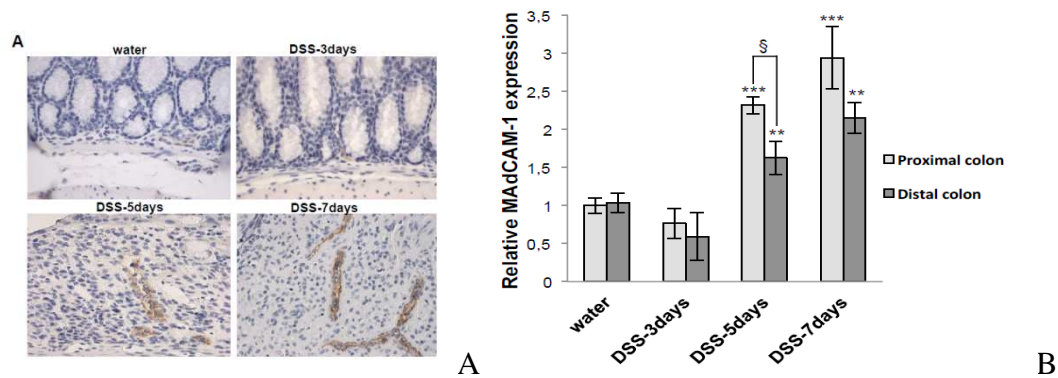


Figure 5.7. MAdCAM-1 expression pattern in colitic versus healthy bowel. (A) Representative pictures of MAdCAM-1 immunohistochemistry in colon specimens from control mice (water) or mice treated with DSS for 3, 5 or 7 days (40× magnification): rare and small vessels were MAdCAM-1 positive in control and 3 days-treated mice; on the contrary, MAdCAM-1 was intensively expressed in endothelial cells of large and wide vessels from 5 and 7-days treated mice. (B) Western blot of MAdCAM-1 protein expression in tissue homogenates of proximal and distal specimens of colon isolated from control (water) or DSS-treated mice.

6. Conclusion and Future perspectives

Inflammatory bowel disease (IBD) is the second most common chronic inflammatory disorder worldwide; however, a non-invasive means of accurately assessing the severity and extent of intestinal inflammation is not available yet. This study aims at valuing MRI technique as real-time and unambiguous practice for Crohn's disease detection by means of a highly efficient contrast agent. On this purpose, a high quality biocompatible manganese-based nanocomposite was prepared as contrast enhancer. The paramagnetic CA was constituted by monodispersed spherical manganese oxide nanoparticles (10 nm) synthesized by solvothermal reaction (Par. 3.2.5). MnO NPs were entrapped in a biocompatible and biodegradable matrix to further increase the stability and the human safety. Magnetic nanoparticles were captured by PLGA polymer *via* single emulsion method (Par. 3.2.1). The poly(lactic-co-glycolic acid) coated manganese oxide nanoparticles join the advantages of the low cytotoxicity of PLGA to the T_1 contrast power of the manganese paramagnetic ion.

Manganese oxide nanoparticles showed very promising results as positive contrast agents for MRI. Relaxation and MRI measurements at 1.5 and 3 T were coherent. Data showed concentration- and time-dependent relaxation rates of both PMA- and PLGA-coated NPs, with a longitudinal relaxivity r_1 ranging from 0.3 to 0.8 $\text{mM}^{-1} \text{s}^{-1}$ in plasma, significantly higher than r_1 of Gd-based

contrast agents and similar to r_1 Mangafodipir. A deeper knowledge about PMA@ and PLGA@MnO NPs behavior in plasma could be next investigated. In particular, PLGA polymer enclosed a great amount of manganese nanoparticles resulting in an enhanced contrast power in plasma comparable with those of free MnO NPs at similar concentrations. PLGA@MnO NPs offer the advantages of the low cytotoxicity compared to Gd(III)-based CA and Mangafodipir and the T_1 -contrast power of the manganese paramagnetic ion.

Cytotoxicity on Hela cells and SVEC-4-10 cell line was nil. This constitute a very important motivation to PLGA@MnO particles replacement gadolinium as MRI CA.

In addition, PLGA matrix has been proposed as a basic system for next engineering in order to obtain a contrast agent selective for a specific disorder. PLGA@MnO NPs was designed with carboxyl terminal groups allowing an easy functionalization with specific moieties (e.g. peptides, antibody) for the selective targeting cells in order to obtain active diagnosis. In order to provide the real-time and non-ambiguous MRI detection of Crohn's disease, PLGA@MnO NPs will be functionalized with the anti-MAdCAM-1 antibody, specifically to bind mucosal addressin cellular adhesion molecule-1 (MAdCAM-1), a mucosal-restricted addressin up-regulated during gut inflammation. The high level of antibodies receptors in the disease area attracts anti-MAdCAM-1-nanoparticles whose accumulation provides a high contrast in MRI diagnosis.

Furthermore the anti-MAdCAM-1-nanoparticles constitute a therapeutic vehicle: the anti-antibody binding MAdCAM-1 limits the immune response at the inflame site, thus restricting the damage to the intestinal mucosal. Additionally, other following functionalities as targeting motifs, therapeutic agents or second imaging component, can be loaded into PLGA nanoparticles, resulting in a multifunctional nanoplatform for an early detection, diagnosis, and personalized treatment of disease.

Finally, very promising relaxation and MR results also attested the ability of PLGA@MnO NPs to strongly decrease the relaxation times of the medium. A deeper investigation on aspect could provide a non-toxic and selective T_2 -CA for *in vivo* analysis.

The combination of all these properties renders our newly developed PLGA@MnO NPs a promising versatile nanoprobe for future applications for *in vivo* targeted diagnosis of tumor cells and inflamed tissues.

List of Figures, Graphs and Tables

Figure 1.1. Representation of colon in normal tissue, in Crohn's disease and in ulcerative colitis.⁴

Figure 1.2. Mechanism of interaction of MAdCAM-1 molecules and the receptor integrin $\alpha_4\beta_7$; inset, 3D-structure of MACAM-1, mucosal vascular addressin cell adhesion molecule 1.

Figure 1.3. (A) Representation of Damadian's invention of MRI; (B) Raymond Damadian, Larry Minkoff and Michael Goldsmith (from left to right) with Indomitable and its iced liquid helium and liquid nitrogen ports: the world's first supercooled, superconducting MR scanner and the world's first MRI machine.

Figure 1.4. The rotation of the electric charge proton origins a small current loop and generates the magnetic dipole moment μ and the consequently weak magnetic field.

Figure 1.5. Proton spins alignments and energy level occupation follows the Boltzmann distribution in a static magnetic field B_0 . The energy gap (ΔE) between spin-up (+ 1/2) and spin-down (- 1/2) states is directly proportional to the magnetic field strength (B_0) (Nuclear Zeeman splitting).

Figure 1.6. Net magnetization (M), the averaged sum of many individual quantum spins, can be treated as a regular vector in classical physics. Spins precession as Larmor frequency (ω_0) in the static magnetic field B_0 .²²

Figure 1.7. (a) Components $M_x(t)$, $M_y(t)$ and $M_z(t)$ of magnetization vector M ; (b) Magnetization vector at equilibrium; (c) Precession of magnetization vector at the Larmor frequency after a RF pulse in a static magnetic field; (d, e) Magnetization vector variation after the RF pulse; (f - i) M_z recovery in time along z axis; (l - o) M_{xy} decay in time in xy plane back to module value 0; (p) M spiralization after the RF pulse to restore the equilibrium state.

Figure 1.8. (A) Increased magnetization along the z axis. (B) Decay of the magnetization in the xy plane.

Figure 1.9. Ideal NMR signal is sinusoidal, while actual signal decay over time.¹⁸

Figure 1.10. The four classes of MRI images obtaining by varying TR and TE.²³

Figure 1.11. (A) Schematic representation of repetition time (TR) and echo time (TE); (B) Schematic representation of Free Induction Decay (FID) and echo time (TE).²³

Figure 1.12. Differences between (A) T_2 -decay and (B) T_1 -recovery curves lead to a sharper contrast.

Figure 1.13. Relaxivities r_1 and r_2 , extrapolated by plotting relaxation rates R_1 or R_2 versus the concentration of CAs.

Figure 1.14. Left. Influence of positive (T_1) and negative (T_2 , T_2^*) MR contrast agents upon signal intensity. Right. This figure gives an example of a clinical case where only the application of such a positive contrast agent helped the diagnostic process and showed the extent of the disease: Patient with breast cancer and recent neurological symptoms. The plain MR T_1 -weighted images (pre-contrast: a and c) do not reliably reveal brain lesions. However, the contrast-enhanced MR images (post-contrast: b and d) show a large number of metastases.²³

Figure 1.15. Different types of magnetism with the correspondent spin behavior and magnetic susceptibility value.

Figure 1.16. (A) Theoretical magnetization (M) versus the strength of the magnetic field (B) for different materials: depending on the particle size, materials exhibit either a multi-domain (green), single-domain (blue) or superparamagnetic (red) behavior; (B) Variation of the coercivity (H_C) of magnetic nanoparticles with size.

Figure 1.17. The uptake of Mn-DPDP (Mangafodipir) in the liver relies on the ability of hepatocytes to excrete metal ions. Manganese separates from the DPDP-complex and is taken up by the hepatocytes. T_1 -weighted images. (a) The metastases are well delineated 15 minutes after the injection, and (b) even 24 hours after administration some of the contrast agent.²³

Figure 2.1. TEM images of proximal colon specimens isolated from DSS-treated mice injected with anti-MAdCAM-1-MnO-NP. Arrows point at nanoparticles within mucosal vessels and adhering to the endothelium of venules. Higher magnifications of MnO-aMC1 NPs (black boxes) are shown on the right of each single image. Scale bars(A) (C) 200 nm, (B) 500 nmm, (D) 100 nm.

Figure 2.2. Analysis of dissected bowels isolated from DSS-treated mice exposed to MAdCAM-1-targeted nanoparticles (DSS + MnO-aMC1 NPs) or to control nanoparticles (DSS +-MnO-IgG NPs). (A) Colon size reduction upon DSS treatment for 5 days. Length of colon removed from euthanized mice after injection of nanoparticles or control saline was compared to that of control mice drinking regular water. Results are means \pm SE in each group. ** $P < 0.01$, *** $P < 0.001$ versus control mice. (B) Epifluorescence (EpF) images of representative bowels isolated from DSS-treated mice exposed for 4 or 24 hours to control saline solution (CTRL), anti-MAdCAM-1-MnO-NP or IgG-MnO-NP. Epf intensity is expressed as radiant efficiency. Dashed lines indicate the end of ileum, and starting of colon.(C) Averaged Epf intensity of bowel isolated from DSS-treated mice exposed for 4 or 24 hours to anti-MAdCAM-1-MnO-NP or IgG-MnO-NP

was measured within the entire colon, as described in Materials and Methods. Results are means \pm SE of 5 different bowels for each experimental condition. $**P < 0.05$ anti-MAdCAM-1-MnO-NP versus IgG-MnO-NP; $\S P < 0.05$ 24 hours versus 4 hours. (D) Epf intensity of bowels isolated from DSS-treated mice exposed for 24 hours to anti-MAdCAM-1-MnO-NP or IgG-MnO-NP was normalized toward the fluorescence intensity of plasma collected from the same animal before euthanasia. Results are means \pm SE of 5 mice per condition. $*P < 0.05$.

Figure 4.1. Schematic representation of the synthesis of manganese oxide nanoparticles (MnO NPs).

Figure 4.2. Structure of the amphiphilic poly(isobutylene-*alt*-maleic anhydride)-graft-dodecylamine (PMA) with poly(isobutylene-*alt*-maleic anhydride) hydrophilic backbone (green) and hydrophobic dodecylamine chains (bordeaux).

Figure 4.3. Schematic representation of PMA-coating of MnO NPs.⁷²

Figure 4.4. Depiction of synthesis of MnO NPs loaded polypoly(D,L-lactide-co-glycolide) nanoparticles (PLGA@MnO NPs).

Figure 4.5. Depicted of synthesis of polypoly(D,L-lactide-co-glycolide) nanoparticles entrapping MnO NPs (PLGA@MnO NPs).

Figure 5.1. TEM images of (A) PLGA NPs (scale bar 500 nm) and (B), (C) PLGA@MnO NPs and (D) MnO NPs (scale bar 100 nm). Samples were negatively stained with uranyl acetate (2% w/w).

Figure 5.2. Degradation of PVA-shell of PLGA NPs one week after synthesis, scale bar (A) 500 nm (B) 100 nm, (C) 200 nm, (D) 100 nm. Degradation of PVA-shell of PLGA@MnO NPs one week after synthesis scale bar (E) 500 nm (F) 500 nm (G) 200 nm, (H) 100 nm, (I) 100 nm.

Figure 5.3. TEM images of PLGA@MnO NPs in saline plus plasma after 24 h, scale bar (A) 500 nm, (B) 200 nm.

Figure 5.4. (A) T_1 -map image of PLGA@MnO NPs at different concentrations of Mn^{+2} ions in (A) the mixture plasma and saline, (B) in saline.

Figure 5.5. (A) T_1 -weighted image of PLGA@MnO NPs at different concentrations of Mn^{+2} ions in (A) the mixture plasma and saline, (B) in saline.

Figure 5.6. DSS-induced colitis in mice. Changes over time in body weight (A), stool consistency (B), and presence of blood in the stools (C) upon DSS treatment were monitored daily, scored as described in Materials and Methods, and compared to scores set for control group of mice drinking regular water. (D)

Colitis severity was assessed for each group of animals by clinical disease activity index (DAI), which was calculated daily as described in Materials and Methods. (E) Colon length reduction upon DSS treatment was compared to that of control mice drinking regular water. Reported values are means \pm SE of all mice included in the study. * $P < 0.05$, ** $P < 0.01$, *** $P < 0.001$ DSS-treated versus control mice. (F) H&E of colon sections from control mice (water) or mice treated with DSS for 3, 5 or 7 days (20 \times magnification): in 5 and 7 days-treated mice, inflammation of the mucosa, ulceration and loss of epithelial lining were observed.

Figure 5.7. MAdCAM-1 expression pattern in colitic versus healthy bowel. (A) Representative pictures of MAdCAM-1 immunohistochemistry in colon specimens from control mice (water) or mice treated with DSS for 3, 5 or 7 days (40 \times magnification): rare and small vessels were MAdCAM-1 positive in control and 3 days-treated mice; on the contrary, MAdCAM-1 was intensively expressed in endothelial cells of large and wide vessels from 5 and 7-days treated mice. (B) Western blot of MAdCAM-1 protein expression in tissue homogenates of proximal and distal specimens of colon isolated from control (water) or DSS-treated mice. (C) Densitometry of MAdCAM-1 bands normalized to GAPDH. Data are means \pm SE (n=4). * $P < 0.05$, ** $P < 0.01$, *** $P < 0.001$ DSS-treated versus control mice; § $P < 0.05$ proximal versus distal colon

Graph 5.1. Characteristic spectra of manganese oxide nanoparticles in chloroform. The maximum absorption was detected at 248 nm.

Graph 5.2. Absorbance dependence on concentration of MnO NPs ($\mu\text{g ml}^{-1}$) (A), Mn^{+2} ($\mu\text{g ml}^{-1}$) (B) and Mn^{+2} (mM) (C) at 248 nm in chloroform (red), at 272 nm in DMSO (black) and of PMA@MnO NPs at 226 nm in water Milli-Q (blue).

Graph 5.3. Encapsulation efficiency (%) (A) and loading (B) of MnO NPs in polymeric PLGA nanoparticles as a function of the weight ratio between metal nanoparticles or manganese ions and PLGA polymer.

Graph 5.4. Hydrodynamic diameter of MnO NPs, PLGA NPs and PLGA@MnO NPs by DLS analyses.

Graph 5.5. (A) PLGA@MnO NPs, (B) PLGA NPs, (C) MnO NPs TEM size distribution analyses.

Graph 5.6. Hydrodynamic diameter of (A) PMA@MnO NPs, (B) PLGA NPs and (C) PLGA@MnO NPs analysed in water Milli-Q, DMEM, and PBS 1X pH 7.2

Graph 5.7. Relaxation rates (A) R_1 and (B) R_2 as a function of (A) MnO NPs ($\mu\text{g ml}^{-1}$), (B) Mn^{+2} ($\mu\text{g ml}^{-1}$) and Mn^{+2} (mM) concentration in Milli-Q water at 303K.

Graph 5.8. Relaxation rates (A) R_1 and (B) R_2 as a function of (A) MnO NPs ($\mu\text{g ml}^{-1}$), (B) Mn^{+2} ($\mu\text{g ml}^{-1}$) and Mn^{+2} (mM) concentration of PLGA@MnO NPs in Milli-Q water at 303K.

Graph 5.9. Relaxation rates R_1 and R_2 of MnO NPs loaded PLGA NPs (0.32, 0.48 and 0.64 weight ratio (MnO NPs/PLGA) at $916.7 \mu\text{g ml}^{-1}$ of PLGA@MnO NPs in water Milli-Q at 303K.

Graph 5.10. Relaxation rates (A) R_1 and (B) R_2 of PMA@MnO NPs and PLGA@MnO NPs during time at $114.58 \mu\text{g ml}^{-1}$ of manganese oxide particles in water Milli-Q.

Graph 5.11. Relaxation rates (A) R_1 and (B) R_2 of PMA@MnO NPs and PLGA@MnO NPs during time at $916.67 \mu\text{g ml}^{-1}$ of manganese oxide particles in water Milli-Q.

Graph 5.12. Relaxation rates (A) R_1 and (B) R_2 as a function of (A) MnO NPs ($\mu\text{g ml}^{-1}$), (B) Mn^{+2} ($\mu\text{g ml}^{-1}$) and Mn^{+2} (mM) concentration in saline and plasma (0.7:1) at 303K.

Graph 5.13. PLGA@MnO NPs (A) R_1 and (B) R_2 as a function of time at $114.58 \mu\text{g ml}^{-1}$ ($78.82 \text{Mn}^{+2} \mu\text{g ml}^{-1}$, $1.43 \text{Mn}^{+2} \text{mM}$) and $916.67 \mu\text{g ml}^{-1}$ ($78.186 \text{Mn(II)} \mu\text{g ml}^{-1}$, $1.43 \text{Mn}^{+2} \text{mM}$) MnO NPs entrapped in PLGA NPs.

Graph 5.14. (A) R_1 and (B) R_2 as a function of time at $916.67 \mu\text{g ml}^{-1}$ of MnO NPs entrapped in PLGA NPs ($78.816 \text{Mn(II)} \mu\text{g ml}^{-1}$, $1.43 \text{Mn(II)} \text{mM}$) and coated with PMA ($916.67 \mu\text{g ml}^{-1}$ of MnO NPs entrapped in PLGA NPs ($78.186 \text{Mn(II)} \mu\text{g ml}^{-1}$, $1.43 \text{Mn(II)} \text{mM}$) in the mixture saline and plasma (0.7 : 1).

Graph 5.15. PLGA@MnO NPs (A) R_1 and (B) R_2 as a function of time at $916.67 \mu\text{g ml}^{-1}$ ($78.186 \text{Mn}^{+2} \mu\text{g ml}^{-1}$, $1.43 \text{Mn}^{+2} \text{mM}$) in different in water MQ, in saline plus plasma (0.7 : 1) and in plasma.

Graph 5.16. Relaxation rates trend in time (A, C in 250 h and B, D in 6 h) in different plasma mixtures by PLGA@MnO NPs ($120 \mu\text{l}$, $916.67 \text{MnO NPs} \mu\text{g ml}^{-1}$).

Graph 5.17. Theoretical calibration curves of Mangafodipir calculated from relaxivities r_1 and r_2 (1.88 and 2.18 at 37°C , respectively) reported in literature.⁷⁹

Graph 5.18. Plots of the R_1 of PLGA@MnO NPs in (A) the mixture saline and plasma and saline (B) as a function of Mn^{+2} ion concentration.

Graph 5.19. Plots of the R_1 of PLGA@MnO NPs different in Mn^{+2} ion concentration in (A) the mixture saline and plasma and saline (B) as a function of time.

Graph 5.20. *In vitro* cytotoxicity study on SVEC 4-10 cells. Cell viability was assessed by MTS assay. Reported values are means \pm standard error (SE) of six replicates, normalized on proliferation of untreated cells. *** $P < 0.001$. (A) Cells treated with 0, 34, 136.6, 340.9, 682.7 $\mu\text{g ml}^{-1}$ of PLGA NPs for 72 hours. (B) Cells treated with 0, 3.6, 14.4, 36, 72.1 $\mu\text{g ml}^{-1}$ of PMA@MnO NPs for up to 72 hours. (C) SVEC 4-10 cells

cultured to 72 h with 0, 3.6, 14.4, 36, 72.1 $\mu\text{g ml}^{-1}$ of MnO NPs loaded on PLGA NPs, corresponding to 0, 34, 136.6, 340.9, 682.7 $\mu\text{g ml}^{-1}$ of PLGA NPs, respectively.

Graph 5.21. *In vitro* cytotoxicity study on Hela cells. Cell viability was assessed by MTS assay. Reported values are means \pm standard error (SE) of six replicates, normalized on proliferation of untreated cells. *** $P < 0.001$. (A) Cells treated with 0, 34, 136.6, 340.9, 682.7 $\mu\text{g ml}^{-1}$ of PLGA NPs for 72 hours. (B) Cells treated with 0, 3.6, 14.4, 36, 72.1 $\mu\text{g ml}^{-1}$ of PMA@MnO NPs for up to 72 hours. (C) Hela cells cultured to 72 h with 0, 3.6, 14.4, 36, 72.1 $\mu\text{g ml}^{-1}$ of MnO NPs loaded on PLGA NPs, corresponding to 0, 34, 136.6, 340.9, 682.7 $\mu\text{g ml}^{-1}$ of PLGA NPs, respectively.

Table 1.1. Selected examples of clinical experience with emerging IBD therapies.¹

Table 1.2. Nuclear spin I and magnetic moment μ of nuclides.²¹

Table 1.3. Approximate values of T_1 and T_2 at 1.5 T of some elements of the human body.²³

Table 1.4. T_1 and T_2 properties for three different types of tissues.²³

Table 1.5. Overview of a number of MR contrast agents actually used in clinic, already withdrawn from the market, or being developed.²³

Table 2.1. Average epifluorescence intensity of isolated organs from DSS-treated mice exposed to MnO NPs conjugated with anti-MAcCAM-1 or IgG for 4 or 24 h. Data expressed as mean radiant efficiency (W cm^{-2}).

Table 4.1. Reaction conditions used for the synthesis of MnO nanoparticles.

Table 5.1. Encapsulation efficiency (%) and loading (%) of MnO NPs and Mn^{2+} ions in PLGA NPs depending on the MnO NPs/PLGA ratio used for emulsion.

Table 5.2. Effective diameter, hydrodynamic diameter, polydispersity index and ζ -potential data of MnO NPs, PLGA NPs and PLGA@MnO NPs.

Table 5.3. Relaxation rates R_1 and R_2 of PMA@MnO NPs in water Milli-Q and saline and plasma mix (0.7 : 1).

Table 5.4. Relaxation rates R_1 and R_2 of PMA@MnO NPs and PLGA@MnO NPs in water Milli-Q at 303K.

Table 5.5. Relaxation rates R_1 and R_2 of MnO NPs loaded PLGA NPs (0.32, 0.48 and 0.64 weight ratio (MnO NPs/PLGA) at $916.7 \mu\text{g ml}^{-1}$ of PLGA@MnO NPs in water Milli-Q at 303K.

Table 5.6. Relaxation rates R_1 and R_2 of PMA@MnO NPs in saline mix with plasma (0.7 : 1) at 303K.

Table 5.7. Comparisons between PMA@MnO NPs, PLGA@MnO NPs and Mangafodipir injections.

Table 5.8. Comparisons between PMA@MnO NPs and PLGA@MnO NPs injections from analysis in plasma mixture.

Table 5.9. Relaxation times T_1 and T_2 of PLGA@MnO NPs different in Mn^{+2} ion concentration in the mixture saline and plasma and saline as a function of time.

Table 5.10. Inflammation grade and MAdCAM-1 score in bowel specimens isolated from 4 mice treated with DSS for 5 days.

References

1. Strober, W., Fuss, I. & Mannon, P. The fundamental basis of inflammatory bowel disease. *J. Clin. Invest.* **117**, 514–521 (2007).
2. Molodecky, N. A. *et al.* Increasing Incidence and Prevalence of the Inflammatory Bowel Diseases With Time, Based on Systematic Review. *Gastroenterology* **142**, 46–54.e42 (2012).
3. Arihiro, S. *et al.* Differential expression of mucosal addressin cell adhesion molecule-1 (MAdCAM-1) in ulcerative colitis and Crohn's disease. *Pathol. Int.* **52**, 367–374 (2002).
4. Slideshow: A Visual Guide to IBD. *WebMD* Available at: <http://www.webmd.com/ibd-crohns-disease/ss/slideshow-inflammatory-bowel-overview>. (Accessed: 17th December 2016)
5. Grant, A. J., Lalor, P. F., Hübscher, S. G., Briskin, M. & Adams, D. H. MAdCAM-1 expressed in chronic inflammatory liver disease supports mucosal lymphocyte adhesion to hepatic endothelium (MAdCAM-1 in chronic inflammatory liver disease). *Hepatol. Baltim. Md* **33**, 1065–1072 (2001).
6. Souza, H., Elia, C., Spencer, J. & MacDonald, T. Expression of lymphocyte-endothelial receptor-ligand pairs, $\alpha 4\beta 7$ /MAdCAM-1 and OX40/OX40 ligand in the colon and jejunum of patients with inflammatory bowel disease. *Gut* **45**, 856–863 (1999).
7. Shyjan, A. M., Bertagnolli, M., Kenney, C. J. & Briskin, M. J. Human mucosal addressin cell adhesion molecule-1 (MAdCAM-1) demonstrates structural and functional similarities to the alpha 4 beta 7-integrin binding domains of murine MAdCAM-1, but extreme divergence of mucin-like sequences. *J. Immunol. Baltim. Md 1950* **156**, 2851–2857 (1996).
8. Oshima, T. *et al.* TNF- α induced endothelial MAdCAM-1 expression is regulated by exogenous, not endogenous nitric oxide. *BMC Gastroenterol.* **1**, 5 (2001).

9. Targan, S. R. Current limitations of IBD treatment: where do we go from here? *Ann. N. Y. Acad. Sci.* **1072**, 1–8 (2006).
10. Turkay, C. & Kasapoglu, B. Noninvasive methods in evaluation of inflammatory bowel disease: where do we stand now? An update. *Clinics* **65**, 221–231 (2010).
11. Van Assche, G. *et al.* The second European evidence-based Consensus on the diagnosis and management of Crohn's disease: Definitions and diagnosis. *J. Crohns Colitis* **4**, 7–27 (2010).
12. Fuss, I. J. *et al.* Both IL-12p70 and IL-23 are synthesized during active Crohn's disease and are down-regulated by treatment with anti-IL-12 p40 monoclonal antibody. *Inflamm. Bowel Dis.* **12**, 9–15 (2006).
13. Yen, D. *et al.* IL-23 is essential for T cell-mediated colitis and promotes inflammation via IL-17 and IL-6. *J. Clin. Invest.* **116**, 1310–1316 (2006).
14. Mechanisms in Medicine. *Novel Agents for the Treatment of Crohn's Disease.*
15. Chaparro, M., Guerra, I., Muñoz-Linares, P. & Gisbert, J. P. Systematic review: antibodies and anti-TNF- α levels in inflammatory bowel disease. *Aliment. Pharmacol. Ther.* **35**, 971–986 (2012).
16. MacKalski, B. A. & Bernstein, C. N. New diagnostic imaging tools for inflammatory bowel disease. *Gut* **55**, 733–741 (2006).
17. Bennewitz, M. F. *et al.* Biocompatible and pH-Sensitive PLGA Encapsulated MnO Nanocrystals for Molecular and Cellular MRI. *ACS Nano* **5**, 3438–3446 (2011).
18. Cleary, K. & Peters, T. M. Image-Guided Interventions: Technology Review and Clinical Applications. *Annu. Rev. Biomed. Eng.* **12**, 119–142 (2010).

19. Na, H. B. *et al.* Development of a T1 Contrast Agent for Magnetic Resonance Imaging Using MnO Nanoparticles. *Angew. Chem.* **119**, 5493–5497 (2007).
20. MRI: THE BASICS - HASHEMI, R.H. / BRADLEY, W.G. / LISANTI C.J. - Lippincott Williams & Wilkins - Risonanza magnetica :: Libreri. *Libreria Cortina Milano* Available at: <https://www.libreriacortinamilano.it/medicina/risonanza-magnetica/opere-di-carattere-generale/9780781741576/mri-the-basics.html?fc=controller>. (Accessed: 10th December 2016)
21. Nuclear Spin. Available at: <http://hyperphysics.phy-astr.gsu.edu/hbase/Nuclear/nspin.html>. (Accessed: 10th December 2016)
22. Bellin, M.-F. MR contrast agents, the old and the new. *Eur. J. Radiol.* **60**, 314–323 (2006).
23. 13-01 | Contrast agents • Magnetic resonance imaging | NMR MR MRI | Essentials, introduction, basic principles, facts, history | The primer of EMRF/TRTF. Available at: <http://www.magnetic-resonance.org/ch/13-01.html>. (Accessed: 10th December 2016)
24. Na, H. B., Song, I. C. & Hyeon, T. Inorganic Nanoparticles for MRI Contrast Agents. *ResearchGate* **21**, 2133–2148 (2009).
25. Considerazioni sui mezzi di contrasto per Risonanza Magnetica, R. POZZI MUCELLI La Radiologia Medica - Radiol Med 107 (Suppl 1 al N. 4): 32-33, 2004 Edizioni Minerva Medica – Torino - Cerca con Google. Available at: [https://www.google.it/search?q=Considerazioni+sui+mezzi+di+contrasto+per+Risonanza+Magnetica%2C+R.+POZZI+MUCELLI+La+Radiologia+Medica+-+Radiol+Med+107+\(Suppl+1+al+N.+4\)%3A+32-33%2C+2004+Edizioni+Minerva+Medica+%E2%80%93+Torino&oq=Considerazioni+sui+mezzi+di+contrasto+per+Risonanza+Magnetica%2C+R.+POZZI+MUCELLI+La+Radiologia+Medica+-+Radiol+Med+107+\(Suppl+1+al+N.+4\)%3A+32-33%2C+2004+Edizioni+Minerva+Medica+%E2%80%93+Torino](https://www.google.it/search?q=Considerazioni+sui+mezzi+di+contrasto+per+Risonanza+Magnetica%2C+R.+POZZI+MUCELLI+La+Radiologia+Medica+-+Radiol+Med+107+(Suppl+1+al+N.+4)%3A+32-33%2C+2004+Edizioni+Minerva+Medica+%E2%80%93+Torino&oq=Considerazioni+sui+mezzi+di+contrasto+per+Risonanza+Magnetica%2C+R.+POZZI+MUCELLI+La+Radiologia+Medica+-+Radiol+Med+107+(Suppl+1+al+N.+4)%3A+32-33%2C+2004+Edizioni+Minerva+Medica+%E2%80%93+Torino)

33%2C+2004+Edizioni+Minerva+Medica+%E2%80%93+Torino&aqs=chrome..69i57.346j0j4&sourceid=chrome&ie=UTF-8. (Accessed: 10th December 2016)

26. Pankhurst, Q. A., Connolly, J., Jones, S. K. & Dobson, J. Applications of magnetic nanoparticles in biomedicine. *J. Phys. Appl. Phys.* **36**, R167 (2003).
27. Manganese-based MRI contrast agents: past, present, and future - Documents. *Docslide.us* Available at: <http://docslide.us/documents/manganese-based-mri-contrast-agents-past-present-and-future.html>. (Accessed: 10th December 2016)
28. Ling, D. & Hyeon, T. Chemical Design of Biocompatible Iron Oxide Nanoparticles for Medical Applications. *Small* **9**, 1450–1466 (2013).
29. Gourtsoyiannis, N. C. *Clinical MRI of the Abdomen: Why, How, When*. (Springer Science & Business Media, 2011).
30. Corot, C., Robert, P., Idée, J.-M. & Port, M. Recent advances in iron oxide nanocrystal technology for medical imaging. *Adv. Drug Deliv. Rev.* **58**, 1471–1504 (2006).
31. Murph, S. E. H. *et al.* Manganese–gold nanoparticles as an MRI positive contrast agent in mesenchymal stem cell labeling. *J. Nanoparticle Res.* **14**, 658 (2012).
32. Shin, J. *et al.* Hollow manganese oxide nanoparticles as multifunctional agents for magnetic resonance imaging and drug delivery. *Angew. Chem. Int. Ed Engl.* **48**, 321–324 (2009).
33. Superparamagnetic iron oxide nanoparticles for MR imaging and therapy: design considerations and clinical applications - ClinicalKey. Available at: <https://www.clinicalkey.com/#!/content/playContent/1-s2.0-S1471489214000940?returnurl=http:%2F%2Flinkinghub.elsevier.com%2Fretrieve%2Fpii%2FS>

1471489214000940%3Fshowall%3Dtrue&referrer=https:%2F%2Fscholar.google.it%2F.

(Accessed: 17th December 2016)

34. Crossgrove, J. & Zheng, W. Manganese toxicity upon overexposure. *NMR Biomed.* **17**, 544–553 (2004).
35. Schrand, A. M. *et al.* Metal-based nanoparticles and their toxicity assessment. *Wiley Interdiscip. Rev. Nanomed. Nanobiotechnol.* **2**, 544–568 (2010).
36. Zhen, Z. & Xie, J. Development of Manganese-Based Nanoparticles as Contrast Probes for Magnetic Resonance Imaging. *Theranostics* **2**, 45–54 (2012).
37. Sun, C., Lee, J. S. H. & Zhang, M. Magnetic nanoparticles in MR imaging and drug delivery. *Adv. Drug Deliv. Rev.* **60**, 1252–1265 (2008).
38. Espinosa, A. *et al.* Duality of Iron Oxide Nanoparticles in Cancer Therapy: Amplification of Heating Efficiency by Magnetic Hyperthermia and Photothermal Bimodal Treatment. *ACS Nano* **10**, 2436–2446 (2016).
39. Hergt, R., Dutz, S., Müller, R. & Zeisberger, M. Magnetic particle hyperthermia: nanoparticle magnetism and materials development for cancer therapy. *J. Phys. Condens. Matter* **18**, S2919 (2006).
40. Lee, J.-H. *et al.* Exchange-coupled magnetic nanoparticles for efficient heat induction. *Nat. Nanotechnol.* **6**, 418–422 (2011).
41. Sapsford, K. E. *et al.* Functionalizing Nanoparticles with Biological Molecules: Developing Chemistries that Facilitate Nanotechnology. *Chem. Rev.* **113**, 1904–2074 (2013).
42. Ho, D., Sun, X. & Sun, S. Monodisperse Magnetic Nanoparticles for Theranostic Applications. *Acc. Chem. Res.* **44**, 875–882 (2011).

43. Niendorf, H. P. *et al.* Magnetic resonance imaging of intracranial tumors using gadolinium-DTPA. Initial experience with fast imaging. *Acta Radiol. Suppl.* **369**, 561–563 (1986).
44. Chikazumi, S. *Physics of Ferromagnetism*. (OUP Oxford, 2009).
45. Girardot, C. *et al.* Choroid plexus papillomas of the posterior fossa in adults: MR imaging and gadolinium enhancement. Report of four cases and review of the literature. *J. Neuroradiol. J. Neuroradiol.* **17**, 303–318 (1990).
46. Pishko, G. L., Astary, G. W., Mareci, T. H. & Sarntinoranont, M. Sensitivity analysis of an image-based solid tumor computational model with heterogeneous vasculature and porosity. *Ann. Biomed. Eng.* **39**, 2360–2373 (2011).
47. Hifumi, H., Yamaoka, S., Tanimoto, A., Citterio, D. & Suzuki, K. Gadolinium-based hybrid nanoparticles as a positive MR contrast agent. *J. Am. Chem. Soc.* **128**, 15090–15091 (2006).
48. McDonald, M. A. & Watkin, K. L. Investigations into the Physicochemical Properties of Dextran Small Particulate Gadolinium Oxide Nanoparticles. *Acad. Radiol.* **13**, 421–427 (2006).
49. Grobner, T. Gadolinium--a specific trigger for the development of nephrogenic fibrosing dermopathy and nephrogenic systemic fibrosis? *Nephrol. Dial. Transplant. Off. Publ. Eur. Dial. Transpl. Assoc. - Eur. Ren. Assoc.* **21**, 1104–1108 (2006).
50. Prince, M. R., Zhang, H. L., Prowda, J. C., Grossman, M. E. & Silvers, D. N. Nephrogenic systemic fibrosis and its impact on abdominal imaging. *Radiogr. Rev. Publ. Radiol. Soc. N. Am. Inc* **29**, 1565–1574 (2009).
51. Idée, J.-M., Port, M., Dencausse, A., Lancelot, E. & Corot, C. Involvement of gadolinium chelates in the mechanism of nephrogenic systemic fibrosis: an update. *Radiol. Clin. North Am.* **47**, 855–869, vii (2009).

52. Huang, H.-C., Barua, S., Sharma, G., Dey, S. K. & Rege, K. Inorganic nanoparticles for cancer imaging and therapy. *J. Controlled Release* **155**, 344–357 (2011).
53. Community list of not active medicinal products for human use. Available at: <http://ec.europa.eu/health/documents/community-register/html/h040.htm>. (Accessed: 10th December 2016)
54. Karlsson, J. O. G., Ignarro, L. J., Lundström, I., Jynge, P. & Almén, T. Calmangafodipir [Ca₄Mn(DPDP)₅], mangafodipir (MnDPDP) and MnPLED with special reference to their SOD mimetic and therapeutic properties. *Drug Discov. Today* **20**, 411–421 (2015).
55. Taylor, K. M. L., Rieter, W. J. & Lin, W. Manganese-Based Nanoscale Metal–Organic Frameworks for Magnetic Resonance Imaging. *J. Am. Chem. Soc.* **130**, 14358–14359 (2008).
56. Mertzman, J. E. *et al.* Surface attached manganese–oxo clusters as potential contrast agents. *Chem. Commun.* 788–790 (2009). doi:10.1039/B815424D
57. Dobson, J. Magnetic nanoparticles for drug delivery. *Drug Dev. Res.* **67**, 55–60 (2006).
58. Huang, H. *et al.* Fabrication and evaluation of tumor-targeted positive MRI contrast agent based on ultrasmall MnO nanoparticles. *Colloids Surf. B Biointerfaces* **131**, 148–154 (2015).
59. European Medicines Agency - Find medicine - Teslascan. Available at: http://www.ema.europa.eu/ema/index.jsp?curl=pages/medicines/human/medicines/000137/human_med_001088.jsp&mid=WC0b01ac058001d124. (Accessed: 16th December 2016)
60. Research, C. for D. E. and. Drug Approvals and Databases - January 2005: Additions and Deletions to the Drug Product List. Available at: <http://www.fda.gov/Drugs/InformationOnDrugs/ucm091413.htm>. (Accessed: 16th December 2016)

61. Li, J., Zhao, Z., Feng, J., Gao, J. & Chen, Z. Understanding the metabolic fate and assessing the biosafety of MnO nanoparticles by metabonomic analysis. *Nanotechnology* **24**, 455102 (2013).
62. Wu, L.-M., Xu, J.-R., Gu, H.-Y., Hua, J. & Hu, J. Is magnetic resonance imaging a reliable diagnostic tool in the evaluation of active Crohn's disease in the small bowel? *J. Clin. Gastroenterol.* **47**, 328–338 (2013).
63. Rimola, J. *et al.* Magnetic resonance imaging for evaluation of Crohn's disease: validation of parameters of severity and quantitative index of activity. *Inflamm. Bowel Dis.* **17**, 1759–1768 (2011).
64. Rimola, J. *et al.* Characterization of Inflammation and Fibrosis in Crohn's Disease Lesions by Magnetic Resonance Imaging. *Am. J. Gastroenterol.* **110**, 432–440 (2015).
65. Klibanov, A. L. in *Nanoparticles in Biomedical Imaging* (eds. Bulte, J. W. M. & Modo, M. M. J.) 327–341 (Springer New York, 2008).
66. Rivera-Nieves, J. Strategies that target leukocyte traffic in inflammatory bowel diseases: recent developments. *Curr. Opin. Gastroenterol.* **31**, 441–448 (2015).
67. Levesque, B. G. *et al.* Converging Goals of Treatment of Inflammatory Bowel Disease From Clinical Trials and Practice. *Gastroenterology* **148**, 37–51.e1 (2015).
68. Adams, D. H. & Eksteen, B. Aberrant homing of mucosal T cells and extra-intestinal manifestations of inflammatory bowel disease. *Nat. Rev. Immunol.* **6**, 244–251 (2006).
69. Ye, Y., Pang, Z., Chen, W., Ju, S. & Zhou, C. The epidemiology and risk factors of inflammatory bowel disease. *Int. J. Clin. Exp. Med.* **8**, 22529–22542 (2015).

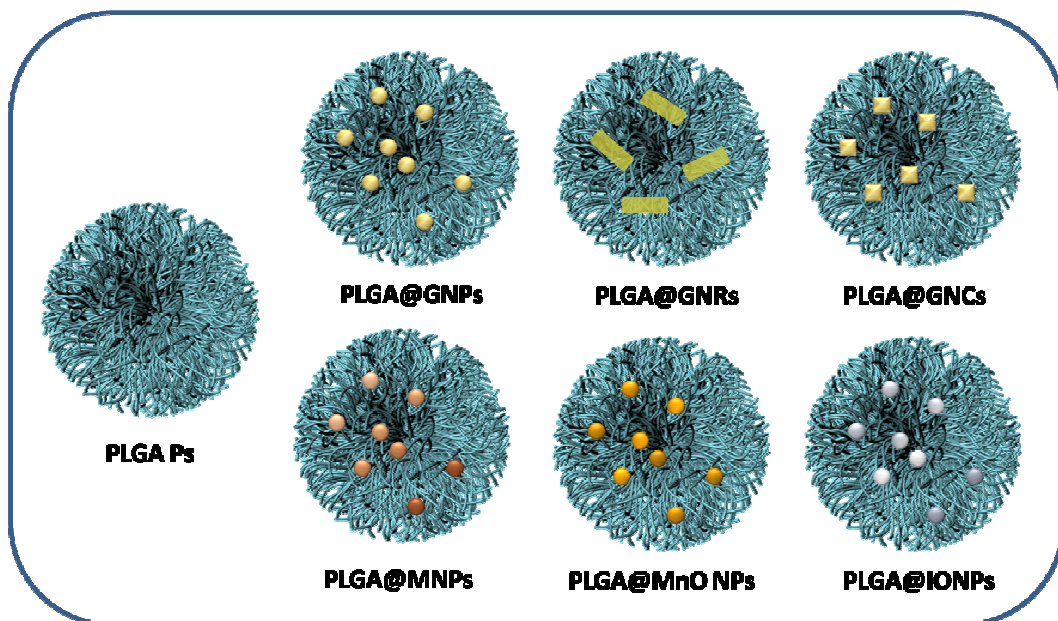
70. Ream, J. M. *et al.* MRI diffusion-weighted imaging (DWI) in pediatric small bowel Crohn disease: correlation with MRI findings of active bowel wall inflammation. *Pediatr. Radiol.* **43**, 1077–1085 (2013).
71. Kreyling, W. G. *et al.* In vivo integrity of polymer-coated gold nanoparticles. *Nat. Nanotechnol.* **10**, 619–623 (2015).
72. Orlando, A. *et al.* Iron oxide nanoparticles surface coating and cell uptake affect biocompatibility and inflammatory responses of endothelial cells and macrophages. *J. Nanoparticle Res.* **17**, 351 (2015).
73. Lin, C.-A. J. *et al.* Design of an amphiphilic polymer for nanoparticle coating and functionalization. *Small Weinh. Bergstr. Ger.* **4**, 334–341 (2008).
74. Hühn, D. *et al.* Polymer-coated nanoparticles interacting with proteins and cells: focusing on the sign of the net charge. *ACS Nano* **7**, 3253–3263 (2013).
75. Song, C. X. *et al.* Formulation and characterization of biodegradable nanoparticles for intravascular local drug delivery. *J. Controlled Release* **43**, 197–212 (1997).
76. Potenza, M. a. C. *et al.* Single particle optical extinction and scattering allows real time quantitative characterization of drug payload and degradation of polymeric nanoparticles. *Sci. Rep.* **5**, 18228 (2015).
77. Mauri, M., Thomann, Y., Schneider, H. & Saalwächter, K. Spin-diffusion NMR at low field for the study of multiphase solids. *Solid State Nucl. Magn. Reson.* **34**, 125–141 (2008).
78. Mauri, M., Mauri, L., Causin, V. & Simonutti, R. A method based on time domain nuclear magnetic resonance for the forensic differentiation of latex gloves. *Anal. Methods* **3**, 1802–1809 (2011).

79. Tirkkonen, B. *et al.* Physicochemical characterisation of mangafodipir trisodium. *Acta Radiol. Stockh. Swed.* 1987 **38**, 780–789 (1997).
80. Langer, G. A., Serena, S. D. & Nudd, L. M. Localization of contractile-dependent Ca: comparison of Mn and verapamil in cardiac and skeletal muscle. *Am. J. Physiol. -- Leg. Content* **229**, 1003–1007 (1975).
81. Haworth, R. A., Goknur, A. B. & Berkoff, H. A. Measurement of Ca channel activity of isolated adult rat heart cells using ⁵⁴Mn. *Arch. Biochem. Biophys.* **268**, 594–604 (1989).
82. Wolf, G. L. & Baum, L. Cardiovascular toxicity and tissue proton T1 response to manganese injection in the dog and rabbit. *AJR Am. J. Roentgenol.* **141**, 193–197 (1983).
83. Gallez, B., Bacic, G. & Swartz, H. M. Evidence for the dissociation of the hepatobiliary MRI contrast agent Mn-DPDP. *Magn. Reson. Med.* **35**, 14–19 (1996).

Chapter III

General Methods:

Gold Nanoparticles Phase Transfer to Organic Solvent and Developing of Metal *Core* Poly(lactic-co-glycolic acid) Nanoparticles



Index

1.	Introduction.....	135
1.1.	Metal Nanoparticle <i>Core</i> : Physics in Action.....	136
1.1.1.	Ligand Exchange Reaction	137
1.2.	Gold Nanoparticles	138
1.2.1.	Local Plasmon Resonance Band	138
1.2.2.	Synthesis of GNRs	140
1.2.3.	Gold Nanoparticles for Biological Applications	141
1.2.4.	Magnetic nanoparticles	144
1.2.5.	Synthesis of Iron Oxide Nanoparticles.....	145
1.2.6.	Applications of Iron Oxide Nanoparticles in Biomedical Research.....	145
1.2.7.	Quantum Dots for Biomedical Applications	148
2.	The goal	149
3.	Materials and Methods.....	150
3.1.	Materials.....	150
3.2.	Synthesis of nanoparticles.....	151
3.2.1.	Synthesis of Spherical Gold Nanoparticles	151
3.2.2.	Synthesis of Gold Nanorods	152
3.3.	Thiol-terminated Poly(D,L-lactide-co-glycolide) Acid and Poly(D,L-lactide) Acid Polymer Synthesis	153
3.4.	Gold Nanoparticles Phase Transfer to Organic Solvent	153
3.4.1.	Biphasic Phase Transfer Method	154
3.4.2.	Monophasic Phase Transfer Method	156
3.5.	Synthesis of Polypoly(D,L-lactide-co-glycolide) Nanoparticles	156
3.5.1.	Synthesis of Poly(D,L-lactide-co-glycolide) Nanoparticles by Single Emulsion Method	157

3.5.2. Synthesis of Spherical Gold Nanoparticles Incorporated Polypoly(D,L-lactide-co-glycolide) Nanoparticles.....	158
4. Nanoparticles Characterization.....	158
4.1.1. Stability in Organic Solvent.....	158
4.1.2. Dynamic Light Scattering and ζ -Potential Analysis.....	158
4.1.3. Inductive Coupled Plasma Analysis	158
4.1.4. Transmission Electron Microscopy and Scanning Electron Microscopy.....	159
5. Result and discussion	160
5.1. Gold Nanoparticles Kinetic Reaction	160
5.2. Gold Nanoparticles Phase Transfer to Organic Solvent	161
5.2.1. Biphasic Phase Transfer Method	162
5.2.2. Monophasic Phase Transfer Method	170
5.2.3. Inorganic Nanoparticles Characterization	171
5.2.4. Poly(lactic-co-glycolic acid) nanoparticles characterization.....	173
5.3. Inorganic Nanoparticles Entrapped in Poly(lactic-co-glycolic acid) Characterization	176
5.3.1. Particle Dimension, Size Distribution and ζ -Potential Analysis	177
6. Conclusions and Future Perspectives.....	180
List of Figures, Graphs and Tables.....	182
References.....	185

1. Introduction

In the context of drug delivery, poly(lactic-co-glycolic acid) (PLGA) represents one of the most used polymer, thanks to its cytocompatibility and extremely low toxicity. Major efforts in literature are focused on the modification of its chemical surface to develop carriers with suitable release profile. PLGA NPs aim at satisfy the payload delivery with appropriate duration, biodistribution and concentration for the intended therapeutic effect.

Taking a cue from PLGA application as molecules delivery vector, this work proposes poly(lactic-co-glycolic acid) polymer as nanovector for inorganic metal nanoparticle. Metal NPs themselves will act as therapeutic, diagnostic or theranostic agents.

Metallic nanoparticles assortment of different *cores* and ligand shells, sizes and shapes, are employed toward a lot of applications ranging from sensing, to catalysis, therapy, labeling, diagnosis, and controlled release. Their applications, however, are often hindered because of the lack of conditions that particles should satisfy (e.g., colloidal stability, chemical functionality, suitable size and shape, solubility, non-immunogenicity, etc.). In order to overcome this limitation, the appropriate modification of NP properties is an important issue to achieve. In this perspective, ligand exchange is one the most widely employed strategy to alter NP chemical or physical properties without change their size, shape and nature of material. As an example, preparing high-quality gold NPs in organic solvent is a tricky work; thus, the post-synthesis transfer from aqueous environment to organic *medium* is the best method. The strategy here exploited, allows to obtain stable nanoparticles in organic solvent for the subsequently encapsulation into PLGA matrix by single emulsion solvent evaporation technique.

Examples of metal particles entrapped in PLGA NPs in literature reported mainly iron oxide nanoparticles for diagnostic purpose,¹ but an efficient encapsulation method is still lacking. In order to satisfy this requirement, this work intends to develop a more profitable strategy to load metal nanoparticles in PLGA matrix, to arrange nanodevices for theranostic applications.

1.1. Metal Nanoparticle Core: Physics in Action

Materials scientists have performed exceptional accomplishments in the design of various types of materials that can be used for biomedical research (Fig 1.1). In particular, nanoparticles have become forefront scaffolds for designing bioactive materials. The *core* sizes of smaller nanoparticles impart unique properties arising from quantum confinement.² Above all, plasmonic nanoparticles, radioactive nanoparticles and magnetic nanoparticles are widely exploited as thermal agent for their optical and magnetic properties. The major biomedical applications are summarized in figure 1.1. The application of such materials in biomedicine however requires a directed design providing actuation and stability in complex environments such as living organisms. Some of the major features nanoparticles need to satisfy are the long-time circulation in blood, the targeting of disease and the low cytotoxicity.

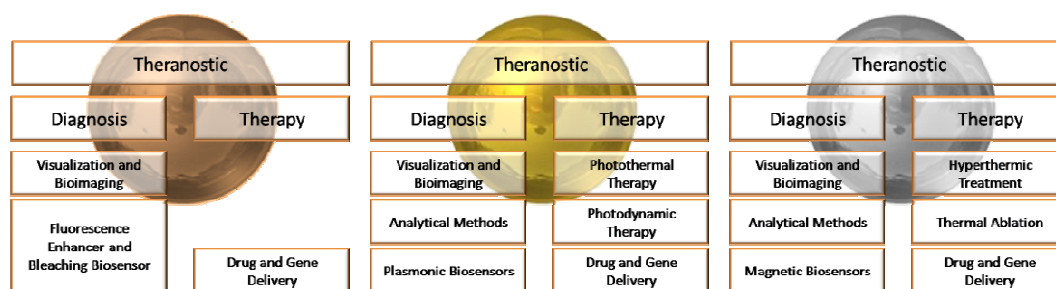


Figure 1.1. Major applications of manganese oxide, gold and iron oxide nanoparticles in biomedicine, respectively.

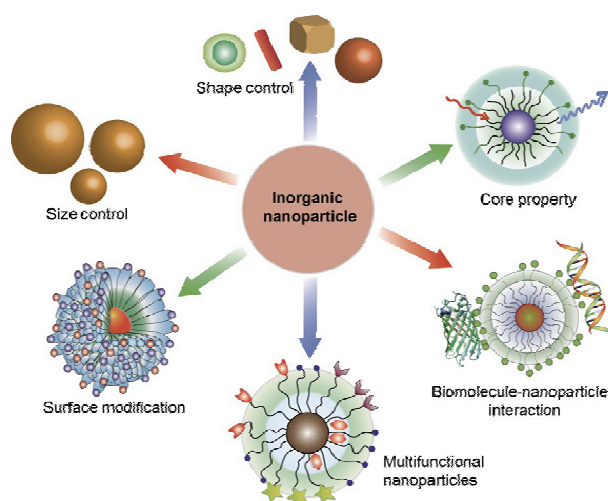


Figure 1.2. Main features to design promising nanoparticles for biomedicine.³

Toxicity is one of the most important problems concerning nanoparticles for medical application. Nanoparticles are more reactive than bigger particles of the same material and their pathogenicity is essentially due to the intrinsic properties of material they are made of. Toxicity also derived from nanoparticle dimensions that determine the permeability in tissues. Moreover, NPs are responsible for free radicals formation causing oxidative stress that damages the organism. Otherwise, this negative aspect could be exploited as a strategy to cure diseases, such as inducing cancer cell apoptosis. Finally, nanoparticles present an inorganic-bioorganic conjugation limit; the immobilization of biomolecules on solid surface can provoke protein unfolding and partially or totally compromises the biological molecular properties. Detailed studies on NP chemical structure modifications are being carried out to solve the problem.⁴

1.1.1. Ligand Exchange Reaction

A suitable NP coating is an excellent strategy to overcome these inconveniences, as it can limit cytotoxicity, prevent the fast clearance within the body, enhance the circulation-time in the blood streaming and maintain the functional activities of particles.

For this purpose, ligand exchange (LE) strategy is the mostly used method to change the nature and the polarization of nanoparticles and to prepare functionalized surfaces.⁵ LE strategy consists of mixing nanoparticles with free ligands, resulting in the replacement of the outgoing ligands with the incoming ones.^{5,6} The reaction mechanism is very intricate because it involves a lot of factors ranging from the nature of ligands and solvents to the NP size and shape, from *ligand to NP* ratio to *aqueous to organic phase* volume ratio.

NP ligand exchange, first suggested by Langford and Gray,² is a complex and multi-sided mechanism, as it comprises associative, dissociative and interchange mechanisms (Fig. 1.3). In addition, ligand substitution reaction rate depends on the electronic configuration of the atoms involved.⁶ Steric crowding at the nanoparticle surface could hamper associative mechanisms. Additionally, LE could be complicated by the particle polydispersity because of the strongly dependence on the arrangement of the ligands onto NP surface and accessibility of Au sites. For this reason, reproducibility in nanoparticle preparation provides equivalent surface sites to make the dynamic of the ligand exchange reaction repeatable.

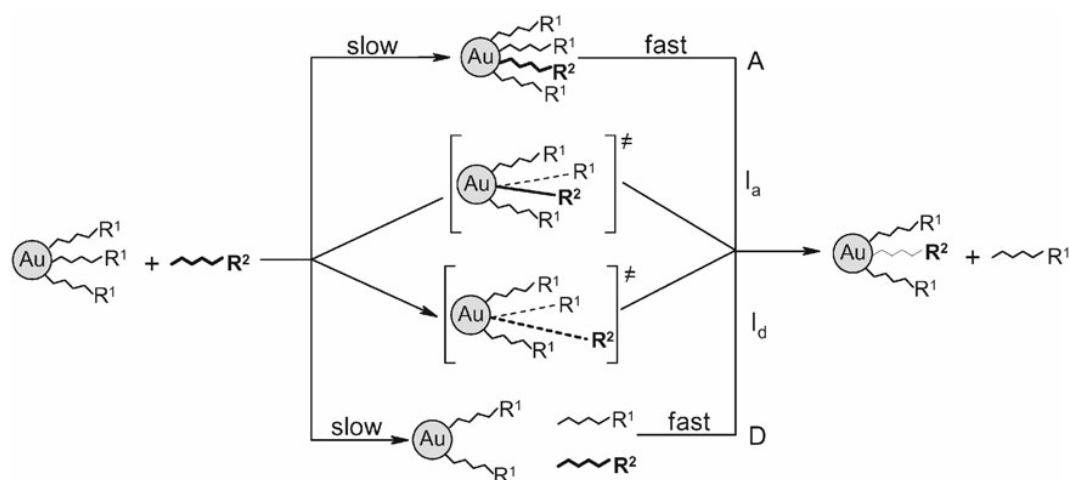


Figure 1.3. Possible mechanisms of ligand exchange reaction in nanoparticles; (A) associative, (D) dissociative and (I) interchange mechanisms

1.2. Gold Nanoparticles

The brilliant and fascinating colors of noble metal nanoparticles have attracted considerable interest since historical times as decorative pigments in stained glasses and artworks.⁷ In recent times, the tunable photophysical properties of metal nanocrystals, their efficient accessibility *via* optical and spectroscopic techniques, and the rapid advances in NP synthesis and fabrication have made metal nanostructures the forefront of nanotechnology research directed toward applications ranging from photonics⁸ to biomedicine.^{9,10}

1.2.1. Local Plasmon Resonance Band

As it was first pointed out by Gustav Mie in 1908,¹¹ the interaction of light with metal nanoparticles results in the collective oscillation of the metal-free electrons compared to the nanoparticle lattice in resonance with the light field. This phenomenon is known as surface plasmon resonance (LPR). LSP is the result of the confinement of a surface plasmon in particles of comparable to or smaller size than the wavelength of plasmon excitation light. For gold (Au), silver (Ag), and copper (Cu), the resonance condition is fulfilled at visible frequencies making them useful tools for optical applications. The large optical polarization associated with the SPR results in a huge local electric field enhancement at the surface and in the strong enhancement of particle light absorption and scattering at the SPR frequency.¹² The SPR frequency depends on a plethora of factors including nature of the metal, size and shape of the nanoparticle,^{12,13} dielectric properties of the surrounding medium,¹⁴ and inter-nanoparticle coupling interactions.^{8,15}

UV-vis-NIR *spectrum* reveals a lot of information about the characteristic of a plasmonic nanoparticle, through the analysis of both the wavelength peaks and the absorbance values. Spherical gold nanoparticles (GNPs) have a size-dependent LSPR band in the visible region of the light: smaller the size, lower the maximum wavelength peak is (Fig. 1.4 B). This behavior is naked-eye detected as colour change of sol (Fig. 1.4 A).

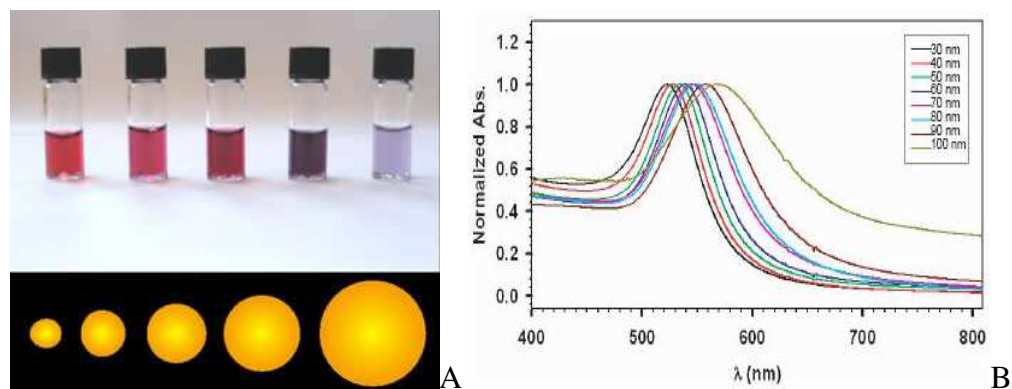


Figure 1.4. (A) Colloidal gold solutions increasing nanoparticle size; (B) typical spectra of gold spherical nanoparticles. LSPR band shift dependence on NPs size.

According to Gans' theory, the change of NP spherical shape into rods results in the emergence of a surface plasmon resonance (SPR) band at higher wavelength (nearer to IR region) in addition to the SPR band at lower wavelength (around 500 nm) (Fig. 1.5). Lower and shorter wavelengths are generated respectively by the oscillation of free electrons along the gold nanorods (GNRs) long (longitudinal) and short (transversal)-axis. The short-axis depolarization is not strongly dependent on the GNR aspect ratio (AR, defined as *longitudinal to transversal dimension* ratio) and it is always fixed around 500 nm. The longitudinal SPR band absorption is always higher than the transverse one, and its intensity increases with the growth of the aspect ratio. In addition, the full width at half-maximum and the longitudinal plasmon band profile are excellent parameters to value the size dispersion, whereas the LSPR band position provides a quick estimation of the aspect ratio. Moreover, nanoparticles concentration can be calculated by the absorbance at 400 nm. GNR aggregation can be monitored in time by the decrease of intensity and by the width of the longitudinal LSPR band, until the possible overlapping of the two plasmon bands.¹⁶

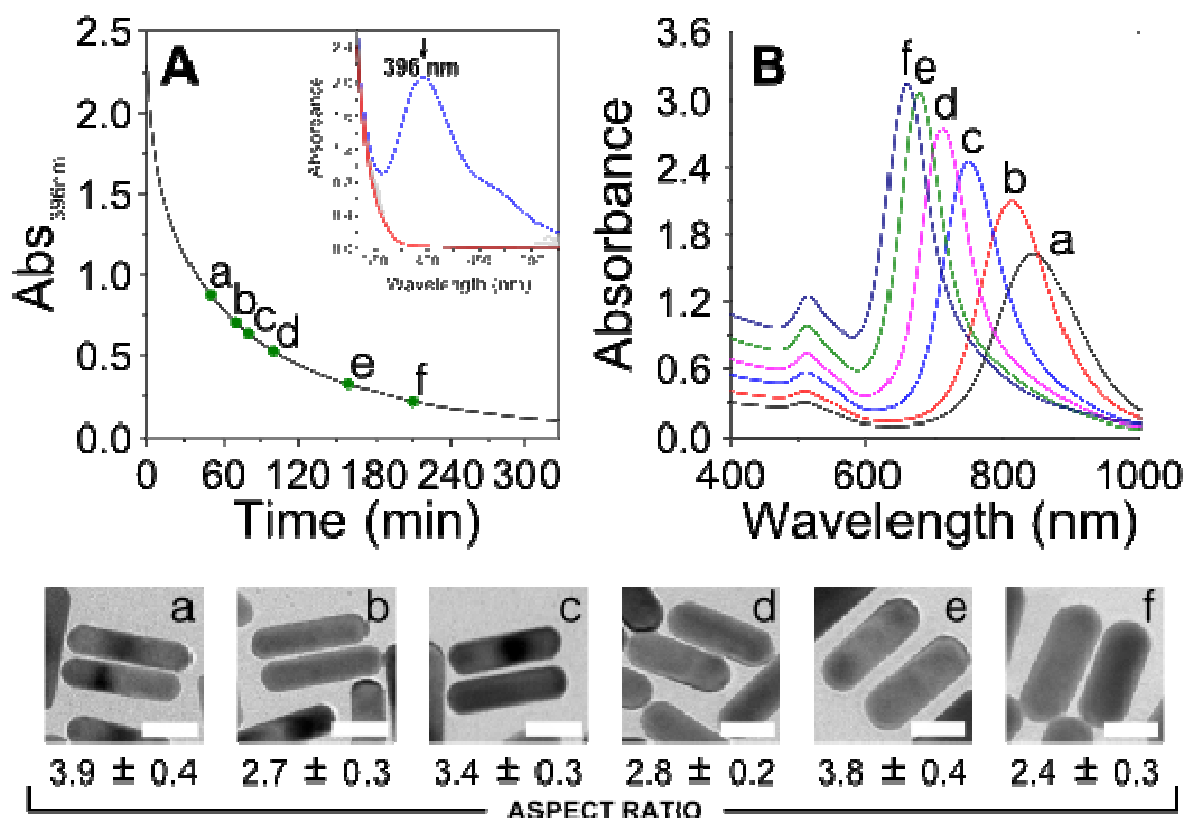


Figure 1.5. The extent of pre-reduction by 5-BrSA affects both the AR and the amount of reduced gold. A: Kinetic study of the pre-reduction (*inset*: full UV-vis spectra). B: UV-vis-NIR spectra of the various NR colloids obtained by changing the pre-reduction time. Abs₃₉₆: 0.88 (a); 0.71 (b); 0.64 (c); 0.53 (d); 0.33 (e); 0.22 (f). Bottom row: Representative TEM images of NRs obtained with different pre-reduction times (the labels correspond to those on the spectra in B). Scale bars: 20 nm.¹⁶

1.2.2. Synthesis of GNRs

Gold nanorods are the first successful example of anisotropic plasmonic nanostructure synthesized by wet chemistry. Preparing monodisperse, uniform in size and reproducible from batch to batch GNRs is a tricky work. The synthesis of GNRs requires both thermodynamic and kinetic controls, thus the parameters that should be taken into account increase significantly. Some general aspects to facing the improvement in performance and reproducibility of synthetic procedures are here described (Fig. 1.6).¹⁷



Figure 1.6. Optimization of synthesis methods achieved through careful tuning of various parameters such as reactant concentrations, which influence thermodynamic and kinetic aspects of seeded growth.¹⁷

Reducing agent solution must be added into seed solution in *one-pot* to achieve the simultaneous production of all nuclei and to guarantee the homogeneous distribution in the entire solution volume. It is also crucial that the reducing agent cannot complete the reduction of Au(I) into Au(0), that is, secondary nucleation during the growth step is prevented. In order to obtain the desired GNRs, the optimization of parameters is required. Higher the concentration of silver ions and lower the concentration of ascorbic acid, higher the aspect ratio is;¹⁸ lower the amount of seed, larger the nanorods and smaller the AR are; lower pH values, slower the growth kinetics and higher the GNR aspect ratio are.¹⁹

The quality of the water supply and the contaminant traces in the chemicals (mostly CTAB) used for synthesis are some of the main sources of irreproducibility.²⁰

Finally, scaling-up the synthesis of GNRs is a trivial task, because of the uniform diffusion of the reagent in solution and the temperature must be kept constant during reaction time.

1.2.3. Gold Nanoparticles for Biological Applications

The strongly enhanced tunable absorption and scattering of noble metal nanocrystals has made them a novel class of optical and spectroscopic tags for biological sensing, imaging and biomedical therapy to replace conventional chromophores and fluorophores. Besides their unique photophysical properties, several factors have motivated the use of noble metal in biomedicine, especially gold nanoparticles. These include easy synthesis in a wide range of sizes and shapes, facile surface conjugation to a variety of chemical and biomolecular ligands, biocompatibility, and high chemical and photostability.²¹ The predominant chemistry for modifying gold NPs is the self-assembly of

thiols *via* chemisorptions²² and small molecules, polymers and a variety of biomolecules can be anchored to AuNPs through thiol-terminated linkers.²³ Functionalized NPs can generate a net of interaction between highly specific molecules like antigen-antibody or complementary strains of DNA. Moreover nanoparticle *core* is responsible for detectable signals (both chemical and physical) because of the peculiar characteristics of the inorganic material which is made of. NPs are fundamental for cellular bioactivity exploration, for drug delivery system and new diagnostic techniques.³⁹

LSPR offers the advantage of the direct label-free detection method that relies on the measurement of refractive index changes accompanied with the binding of target analyte. Labeled-gold nanoparticles are employed for cancer imaging using laser confocal microscopy, and the dark-field imaging technique²⁴ to have great potential for molecular-specific detection and differentiation of cancerous cells from healthy cells.

The wavelength-dependent intensity of the LSPR is very sensitive to changes in AuNP dielectric environment, as well as to plasmon NP-NP coupling. This behavior, the efficient have been all used to develop biological sensors based on the colorimetric changes that result from selective binding interactions at the particle surface. The sensitivity of the SPR to the medium dielectric constant and inter-nanoparticle interactions has also been exploited for the optical detection of chemical and biological species: the huge local electric field resulting from the SPR leads to a strong enhancement of the spectroscopic signal from molecules in the vicinity of the nanoparticles.^{22,24} Important examples include metal plasmon-enhanced fluorescence,²⁶ which has a demonstrated utility in sensing platforms²⁷ and surface-enhanced Raman scattering (SERS) with enhancement factors large enough to allow single molecule detection.²⁸ In all these applications, a relevant condition for detecting molecules is to maximize the penetration of the radiation to tissue and to minimize the tissue autofluorescence by exciting the sample with wavelengths ranging from 750 nm to 1mm (NIR), within the biological transparency window. Therefore, much progress has been made toward the preparation NPs with localized surface plasmon resonances in this spectral range.

The absorption by AuNPs is efficiently converted *via* electron-electron and electron-phonon relaxations to heat in the time scale of picoseconds.²⁹ The plasmonic heating makes gold NPs potent photothermal agents at much lower laser intensities compared to strong conventionally absorbing dyes employed for this purpose, and thus they hold great promise for the photothermal therapy (PTT) of cancers and other disorders.³⁰ In particular, spherical gold nanoparticle applications as PTT agents

are limited to near-surface or skin-type cancers; for clinical therapy applications involving tumors located deep within bodily tissue, a NIR laser light in the region of the biological water window is required as human tissue has the highest transmissivity in this spectral region and hence, nanorods, nanocages or nanoshells can shift the absorption to the NIR region, to better respond to this necessity because of their longitudinal SPR band between 600 - 1100 nm.¹³

Most pharmacological approaches to cancer therapy are based on chemotherapeutic substances, which generally exhibit high cytotoxic activities but poor specificity for the intended biological target. This practice mostly results in a systemic distribution of the cytotoxic agents leading to side effects associated with chemotherapy.¹³ Different approaches of drug delivery are tested. The most common physiological routes can be followed by all kinds of nanoparticulates. The passive targeting route takes advantage of the biological function of the reticulo endothelial system (RES) deputed to the first clearance activity in mammalian organisms. Once unprotected particles are immersed in the blood stream, plasma proteins recognize them as invading entities and immediately adsorb nanoparticles on their surface. The parameters affecting of opsonization are related to the physical properties of the nanoparticle surface, including size, shape, charge and aggregation state. Many studies confirmed particles in the range 10 - 100 nm have optimal size for drug delivery treatments, as they have the longest blood circulation time.

Passive nanocarriers can be used to deliver drugs for the treatment of hepatic diseases, such as liver metastases, and to favor the internalization of antibiotics by phagocytic cells of the RES for the treatment of intracellular infections. The movement of nanoparticles inside a matrix or fluid depends directly on a multitude of factors such as temperature and viscosity of the *medium*, fluid flow, interaction between nanoparticles and fluid components and nanoparticles size and shape. The dynamics of nanoparticle transport *in vivo* through a vein or artery to an area of interest are far from being fully understood and modeled but there are nowadays several studies in this direction. In contrast with the passive delivery route, active targeting has the advantage of improving the accumulation of chemotherapeutics at the tumor site, but requires multiple synthetic steps to tailor the chemical properties of nanoparticles in order to achieve a suitably bioengineered nanocarrier.

With unique characteristics, such as strong surface plasmon absorption, stability, biosafety, and ease of modification, AuNP have long been exploited as a candidate material for building up functional agents for both imaging and therapy applications. Remarkably, the thiol-Au chemistry is successfully exploited to functionalized AuNPs to enhance AuNP-conjugates stability and to

attached biomolecular moieties for the active targeting of disease or to bring thermosensitive linker for the drug delivery.³¹ One noticeable disadvantage is its high cost of production, which may cast a shadow over applications that are otherwise of bright clinical perspectives.

1.2.4. Magnetic nanoparticles

Among all inorganic nanocomposites, magnetic nanoparticles (MNPs) show magnetic properties making them very interesting tools for biomedical applications, both for diagnosis and therapy. The size in the nanoscale allow nanoparticles to interact with biological environment and to acquire intrinsic physical properties (e.g., size-dependent optical, magnetic, electronic, catalytic properties and biological activities) that bulk material do not possess.²⁷ Magnetic nanoparticles exhibit the capability to interact and respond to an applied external magnetic field, and hence the ability to be manipulated by an external magnetic field to be addressed to a desire *situ* both *ex vivo* and *in vivo*, and to provide controllable means of magnetically tagging biomolecules, leading to potentially highly efficient bioseparation and highly sensitive biosensing. MNPs can also act as site-specific drug delivery system.^{4,30,35} In the last decades MNPs became also one of the most exploited nanoparticles for hyperthermic treatment, especially for cancer care.^{31,32,33} Their resonantly response to an external alternating magnetic field transform the magnetic energy in heat, and hence, warm the surrounding environment. In order to be employed for biomedical applications, magnetic nanoparticles have to be biocompatible with the organism without any relevant toxic effect. It is also necessary to have MNPs monodisperse for better controlling the biodistribution, bioelimination and the side effects. Moreover, drug in the form of antibody or chemical molecules could be loaded onto NPs surface, opening the possibility of using them as therapeutic agents. The possibility of functionalizing NPs joined with the possibility of loading drugs and their magnetic properties, make them a very attractive tool both for targeted diagnosis and therapy. In addition, the possibility of conjugating the inorganic nanoparticles with biochemical building blocks constitute a great possibility for designing novel hybrid systems able to interact with biological field, further enlarge the biomedical applications of inorganic nanomaterials.³⁴ Another important advantages for medical application³⁵ is the high-level accumulation of MNPs in the desired tissue.³⁶ Finally, magnetic nanoparticles can act as contrast enhancer to provide higher resolution in magnetic resonance imaging (MRI).¹¹ The main MNPs studied are promising tools for biomedical applications are based on iron (IONPs) and manganese (MnO NPs). MnO NPs are argued in chapter II, while IONPs are here briefly discussed.

1.2.5. Synthesis of Iron Oxide Nanoparticles

A great number of both physical and chemical methods have been explored to synthesize IONPs.⁴⁶ Physical methods offer the advantages of a mass and high-purity production of nanomaterials, while controlling NP size and shape is harder.⁴⁷ To overcome this drawback, chemical methods based on solution-phase colloidal chemistry have been investigated for the synthesis of high quality nanoparticles with control dimensions and morphology. The commonly chemical methods used include metal salt reduction, sol-gel process, reverse micelle technique, and thermal decomposition of iron organic precursors.⁴⁷ Between these methods, the most used is solvothermal decomposition consisting of a two-step synthesis: the first organo-metallic iron precursor (e.g., iron pentacarbonyl, iron cupferron, iron oleate, or iron acetylacetonate in a heated surfactant solution) and its further solvothermal decomposition to form iron oxide nanoparticles with high crystallinity and very low size distribution on a large scale.³²

1.2.6. Applications of Iron Oxide Nanoparticles in Biomedical Research

Iron oxide nanoparticles are very attractive for biomedical application address to medicine. The primary prerogative that makes the nanoparticles a fruitful investment in medical field is their dimensions comparable to those of biological moieties. Indeed, natural cellular constituents and synthetic nanoparticles can interact and generate some response getting closed. Iron is one of the most abundant metal elements in living organisms, and it is essential for several biological processes, such as oxygen transportation by hemoglobin and cellular respiration by redox enzymes.⁴⁰ Iron oxide nanoparticles (IONPs) can be incorporated into natural metabolic pathways of human body and exhibit lower toxicity and more biological tolerability in a broad range of concentrations, compared to other nanoparticles.⁴¹ In the last decade, investigations with several types of iron-based material have been carried out in the field of magnetic nanoparticles, such as maghemite, γ -Fe₂O₃, or magnetite, Fe₃O₄. Among them, magnetite is a very promising candidate since its biocompatibility has been already proven.⁴² IONPs doped with magnetically susceptible elements (e.g. MnFe₂O₄ and CoFe₂O₄) and metal alloys nanoparticles (e.g. FeCo and FePt) are also available, but their applications in biomedical field is limited by the potential toxicity and the rapid oxidation, nevertheless the magnetism of these ferrites and metal alloys is stronger than that of the corresponding pure iron oxide. The metabolism and the pharmacokinetic of intravenously injected IONPs have been well studied and, in addition to the biocompatibility, they offer important advantages for biomedical applications (Fig. 3.7), including drug delivery (DD), gene therapy, nanosensing, hyperthermic treatments and magnetic resonance imaging (MRI).⁴³ All applications

require nanoparticles with high magnetization values, size smaller than 100 nm, and a narrow particle size distribution.

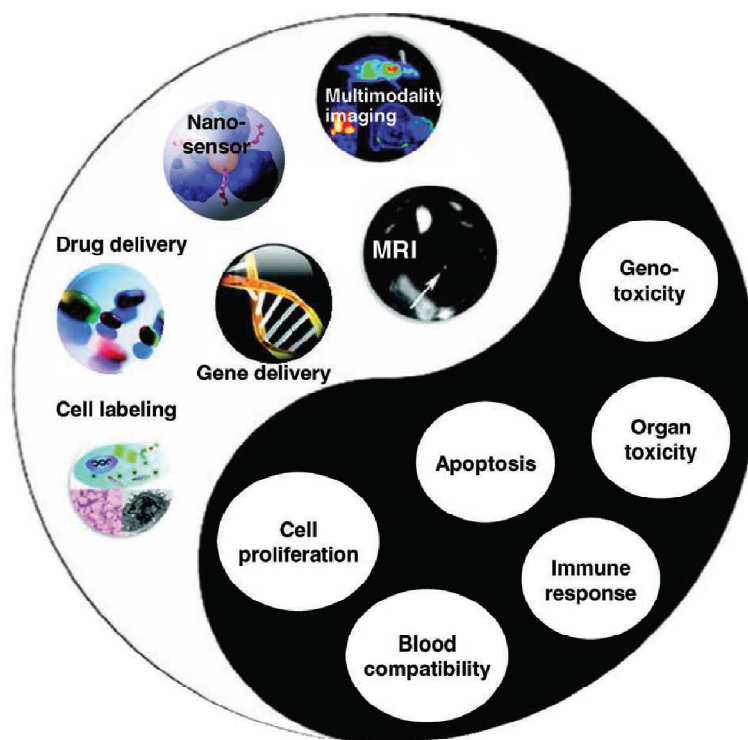


Figure 1.7. Schematic representation of biomedical applications and potential toxicity of magnetic iron oxide nanoparticles.⁴³

IONPs for biomedical applications often require a surface coating to decrease NP toxicity, to allow particles to overcome barriers to reach biological targets, and to prevent NPs from an early elimination by the immune system, thus increasing the circulating time of particles into a living organism. The NP surface coating is selected depending on the *in vivo* fates of these carriers and it needs to satisfy the requirements of low toxicity and biocompatibility, and preferentially should arrange particles to bind molecules (e.g., drugs, proteins, nucleotides, etc.) for the accumulation in a specific organs, tissues, or tumor masses.²⁹ In particular, nanoparticles can be functionalized with biological molecules (e.g., peptides, antibodies, ...), thereby providing a controllable way of tagging or addressing them.³⁸ The magnetic properties of IONPs can contribute to increase further NP localization in demanded *situ*, thus ameliorating the targeting mechanism to improve drug delivery efficiency,^{2,12} as magnetic nanoparticles can be driven to the site of interest also within the body by the use of an external magnetic field.

A more recent application, consist of iron-based particles as nanovector for gene therapy. Gene therapy takes advantage of positive charged polymeric-coated IONPs that electrostatically attach negatively charged nucleic acids (e.g. siRNA, mRNA, DNA, plasmid) as drugs to antagonize abnormal gene regulation and to treat diseases.^{44,45} The coating polymer is commonly a transfection agent (e.g., polyethylenimine PEI) able to penetrate cell membrane and hence to favour nucleic acids passage through the membrane, and to preserve DNAs/RNAs from recognition and degradation by nucleases to fulfill their task.

Furthermore, IONPs are commonly proposed as contrast agent for magnetic resonance imaging. Iron oxide nanoparticles shorten T_2 of the environment they accumulated in, thus enhancing the contrast in MR imaging, allowing a sensitive and accurate detection of biomarkers with excellent temporal and spatial resolution.³⁰ Currently, there are some iron oxide nanoparticle-based MR contrast agents that have already been used in clinical trials, or are undergoing clinical trials.

Additionally, IONPs ability to act as antennae in an external alternating magnetic field (AMF) to convert electromagnetic energy into heat, allow them to be a potential hyperthermic agents. This capability holds great promises in cancer therapy because tumor cells are more susceptible to elevated temperature than normal cells.³² As a consequence iron-based nanoparticles could act themselves as compact theranostic agents.

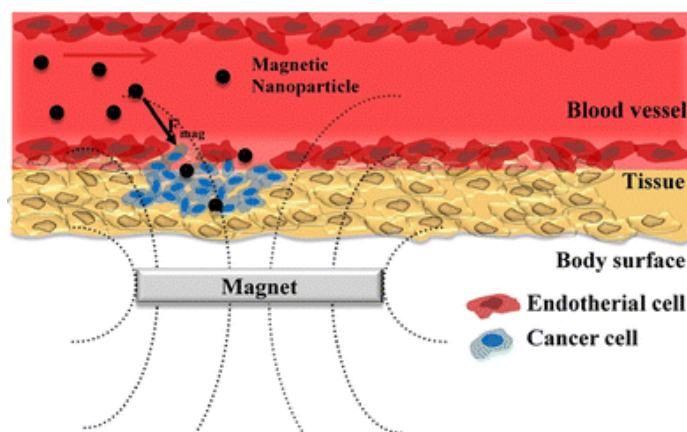


Figure 1.8. Schematic representation of magnetic drug delivery system under the influence of external magnetic field. F_{mag} is direction of external magnetic field are targeted.⁵⁶

1.2.7. Quantum Dots for Biomedical Applications

Quantum dots (QDs) provide very stable fluorescent probes of tunable size and very resistant to photobleaching. QDs also have great potential in photodynamic therapy (PDT) or fluorescence resonance energy transfer (FRET).

Tailoring the surface of QDs with suitable ligands may confer desirable properties such as high quantum yield and long-term stability under broad range of conditions (e.g., high electrolyte concentration, wide pH range). The translation of QDs to the clinic has been hampered by two major challenges: first, surface functionalization must reduce the intrinsic toxicity of the QD heavy metal *core*; second, QDs size and shape must be tuned to have an excitation and an emission wavelength in the biological window for imaging applications. QD as drug delivery system is less investigated, because of the *core* toxicity. Recent advances in QD synthesis have led to the emergence of less toxic Cd-free QDs, such as InAs/ZnSe and InAs/InP/ZnSe. Even if some effort are made to use QDs for DD by functionalizing the surface with targeting moieties (e.g. Trastuzumab) or adsorbed chemical drugs or genes (e.g. Doxorubicin, RNA) for cancer care, the investigation stopped at the imaging level and no therapeutic studies were pursued.

2. The goal

This chapter is focused on the development of a general method for the entrapment of metal nanoparticles in poly(lactic-co-glycolic acid) polymeric ones. The manganese-loaded PLGA NPs discussed in the previous chapter, has given the idea to trap NPs of different nature into PLGA matrix to obtain hybrid nanosystems for future biomedical applications. Metallic-based NPs entrapped into PLGA NPs join the fascinating properties of the metal nanomaterials with the extreme biocompatibility of poly(lactic-co-glycolic acid) polymer to make them very attractive medical tools.

To achieve this aim, gold nanoparticles (AuNPs) of spherical and rod shape, manganese and iron oxide nanoparticles have been encapsulated into PLGA matrix by single emulsion method. The strict requirements metal NPs need to satisfy for the reaction are the high concentration and stability in organic solvent.

While manganese- and iron-based particles are chiefly prepared in organic *medium*, aqueous-based syntheses are dominant to obtain precise morphology and size control of AuNPs. However, stable gold NPs in organic solvents are required for various applications such as the preparation of hydrophobic composites with water-insoluble polymers and the controlled assembly of nanoparticles on substrates upon evaporation of volatile solvents.

On this purpose, two different approaches based on the ligand exchange reaction, the biphasic and the monophasic method have been explored to obtain stable colloidal nanoparticles in organic solvent. Both the strategies are adaptable to whatever gold particles shape.

Summarizing, this work aims at setting up general protocols adaptable to particle of any size and shape to transfer efficiently metal nanoparticles to organic solvent and to entrap metal NPs into PLGA NPs. The methods have been set up in collaboration with prof. Marzan's group at CICBiomaGune, Spain.

3. Materials and Methods

3.1. Materials

Oleic acid, 5-bromosalicylic-acid (5-BrSA), Hexadecyltrimethylammonium bromide (CTAB, 95%), Poly(L-lactide), thiol terminated ($\text{H}(\text{C}_3\text{H}_4\text{O}_2)_n\text{OC}_2\text{H}_4\text{SH}$, average M_n 2.500, $\text{PDI} \leq 1.2$), poly(DL-lactide-co-glycolide) (PLGA, MW 24000–38000 g mol^{-1} , 50:50), thiol-terminated poly(lactic-co-glycolic acid), Poly(L-lactide) (PLA) polymer (M_n 2500, $\text{PDI} \leq 1.2$), Polyvinyl alcohol (PVA, MW 9000–10000 g mol^{-1} , 80 % hydrolyzed), Tetrahydrofuran (THF, 99.9%), N-(3-Dimethylaminopropyl)-N'-ethylcarbodiimide hydrochloride ($\text{EDC} \geq 99.0\%$ (AT), N-Hydroxysuccinimide (NHS, 98 %), Ethylenediaminetetraacetic acid (99.995% trace metals basis), 1-Dodecanethiol ($\geq 98\%$), 11-Mercaptoundecanoic acid (98%), Fluorescein isothiocyanate isomer I ($\geq 90\%$, powder), Hydrochloric acid (36.5-38.0%), Acrylamide 4k-Solution (40%) were purchased from Sigma Aldrich (MO, USA).

α,ω -Bis-amino PEG ($\text{NH}_2\text{-PEG-NH}_2$, MW. 2000 g mol^{-1}), thiol terminated Polyethylene glycol (MW, 750 and 5000 g mol^{-1}) were purchase from RappPolymer (GmbH, Germany)

Hexane (97 %), Chloroform and Acetone (99 %) acquired from PanReac AppliChem.

3.2. Synthesis of nanoparticles

3.2.1. Synthesis of Spherical Gold Nanoparticles

Gold nanoparticles were synthesized by seed mediated method (Fig. 3.1).³³ Briefly, a solution of 2.2 mM sodium citrate in Milli-Q water (150 ml) was heated with a heating mantle in a 250 ml three-necked round-bottomed flask for 15 minutes under vigorous stirring. A condenser was utilized to prevent the solvent evaporation. When the sample was boiling, HAuCl₄ aqueous solution (25 mM, 1 ml) was injected into the round-bottomed flask. The color of the solution changed from yellow to bluish gray and then to soft pink in 10 minutes. The resulting particles ($\sim 3 \times 10^{12}$ NPs ml⁻¹) have a mean diameter of about 10 nm and were coated with citrate ions that conferees high stability in aqueous medium. To allow the seeds growth to form GNPs in the same vessel, the solution was cooled down to 90 °C. At this point, sodium citrate (60 mM, 1 ml) and HAuCl₄ aqueous solution (25 mM, 1 ml) were sequentially injected (time delay of 2 minutes). After 30 minutes, HAuCl₄ solution (25 mM, 1 ml) was injected again. 30 minutes more, the reaction was brought to the completeness. The sample was then diluted by extracting 55 ml of sol and adding 53 ml of MQ water *plus* 2 ml of 60 mM sodium citrate. GNPs were centrifuged at 7684 rcf, 40 minutes (Scanspeed 173OR, Labogene) (x 3) to remove the exceeded reagents. The supernatant was removed and the pellet was re-dispersed in MQ water. 100 μ l were extracted for further characterization by transmission electron microscopy (TEM) and UV-vis spectroscopy.

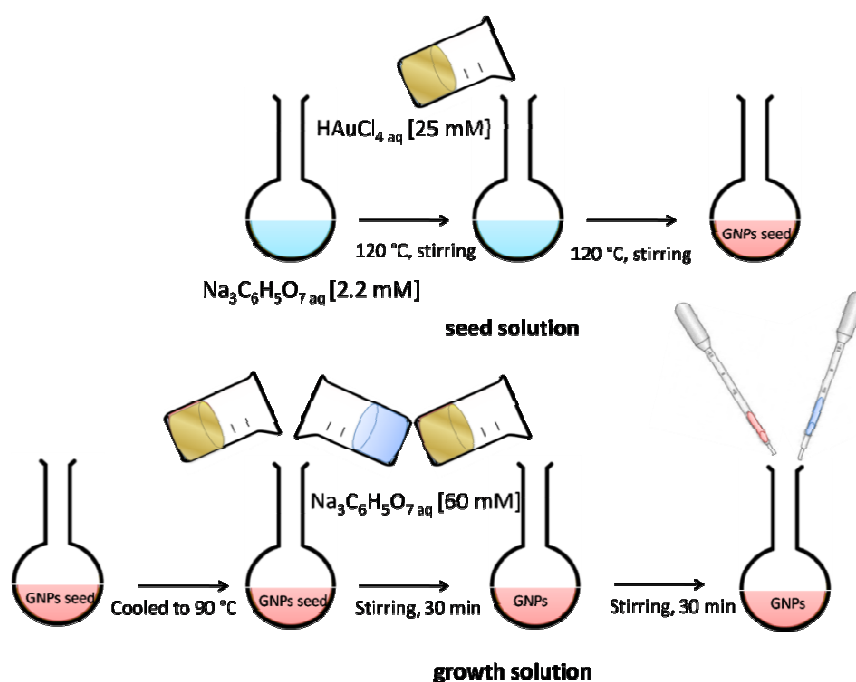


Figure 3.1. Spherical gold nanoparticles reaction scheme.

3.2.2. Synthesis of Gold Nanorods

Gold nanorods (GNRs) were synthesized by the seed mediated method (Fig. 3.2).¹⁵ Briefly, 25 μl of a 0.05 M HAuCl_4 aqueous solution were added to 4.7 ml of 0.1 M CTAB aqueous solution for the seed formation. 300 μl of a freshly prepared 0.01 M NaBH_4 solution were then injected under vigorous stirring. Excess sodium borohydride was consumed by keeping the seed solution for 30 minutes at room temperature before using it. The growth solution of gold nanorods was prepared following a modified Murray's protocol.^{15,16} Briefly, 50 mg of 5-bromosalicylic-acid (5-BrSA) were added to 25 ml of 0.1 M hexadecyltrimethylammonium bromide CTAB. When they are completely dissolved, 480 μl of 0.01 M AgNO_3 was added to the solution. The mixture was mildly stirred for 15 minutes at room temperature. Then 25 ml of 0.001 M HAuCl_4 solution was added to the solution: the pre-reduction step starts. The gold ions reduction from Au^{+3} to Au^{+1} was monitored by UV-visible analysis measuring the absorbance at 400 nm. Once the absorbance at 400 nm gets to 0.8, 130 μl of 0.1 M ascorbic acid (AA) solution was added under vigorous stirring, followed by 80 μl of seed solution. After 30 seconds, the stirring was stopped and the mixture was left undisturbed at room temperature for 4 h. Sample was centrifuged at 7684 rcf for 30 minutes at room temperature (RT). 5 μl of sample were extracted for TEM and UV-vis spectroscopy characterization.

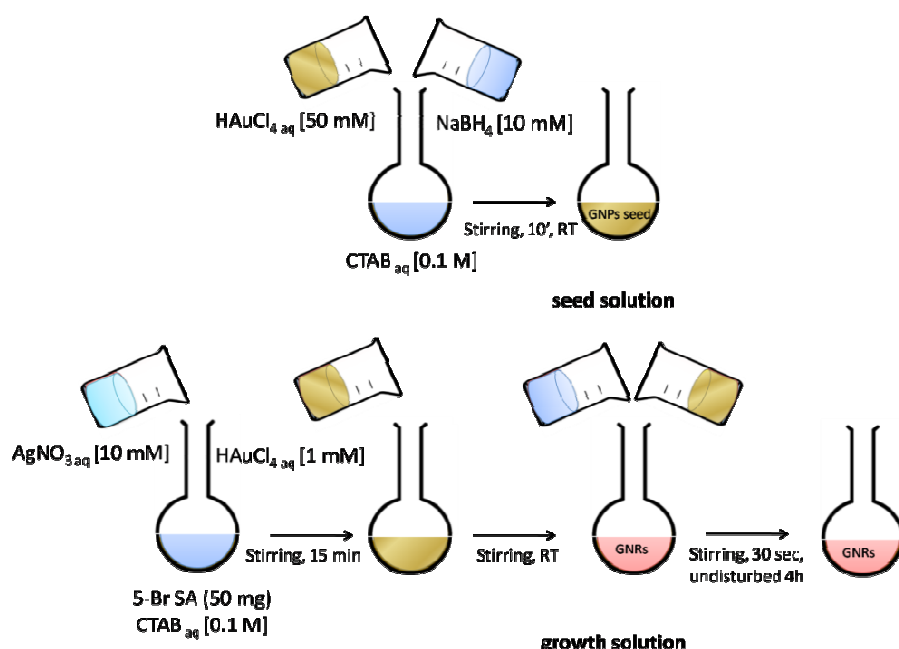


Figure 3.2. Schematic representation of the synthesis of spherical gold nanoparticles (GNPs) by seed-mediated method.

3.3. Thiol-terminated Poly(D,L-lactide-co-glycolide) Acid and Poly(D,L-lactide) Acid Polymer Synthesis

Acid-terminated poly(D,L-lactide-co-glycolide) (50 mg, LG. 50:50, MW 7000 - 17000 g mol⁻¹) was dissolved in chloroform (1.3 ml) to 38.5 mg ml⁻¹ final concentration. EDC (1.3 mg, 1 ml, 1.3 mg ml⁻¹) and NHS (0.8 mg, 1 ml, 0.8 mg ml⁻¹) solutions in chloroform were added to PLGA solution and left under stirring for 30 minutes at 400 rpm at RT to activate molecules for the amide coupling. Following, 6-mercaptoethylamine solution (0.67 mg, 1 ml, 0.67 mg ml⁻¹) in chloroform was added to the reaction. 6-mercaptoethylamine and PLGA polymer molar ratio was 3.

The thiol-terminated polymer was purified in separating funnel. The volume ratio between water and poly(D,L-lactide-co-glycolide) polymer was 5. The organic solution was recollected into a flask with *salamoia* (2 ml). The separation was repeated and the organic solution was recollected into a clean flask. Na₂SO₄ was added to dry the solution. The solution was finally filtered and collected.

The same protocol was adopted to prepare thiol- conjugated poly(L-lactide) (PLA) polymer (M_n 2500).

3.4. Gold Nanoparticles Phase Transfer to Organic Solvent

Ligand exchange reaction is a strategy for preparing functionalized metal nanoparticles, consisting of molecules displacement from particles surface with others ligands. In order to transfer gold nanoparticles from aqueous *medium* to organic solvent, two different approaches were explored (Fig. 3.3): the biphasic and the monophasic method.

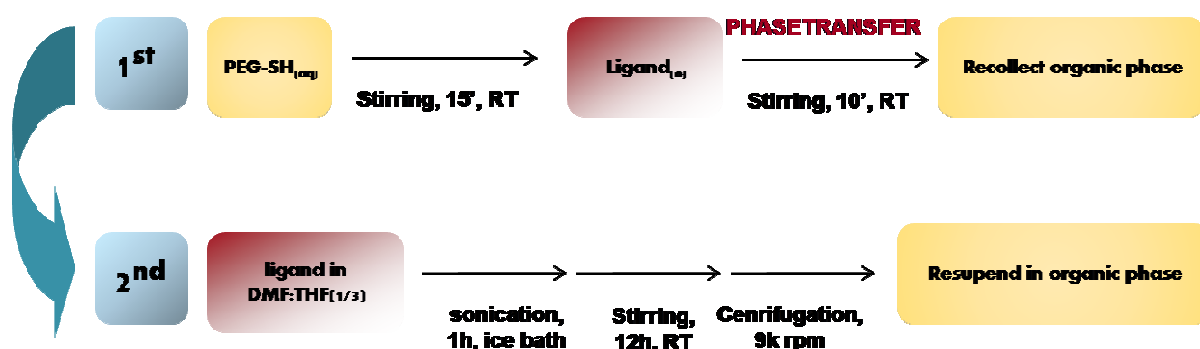


Figure 3.3. Scheme of monophasic and biphasic method for transferring gold NPs to organic phase.

3.4.1. Biphasic Phase Transfer Method

In order to obtain a highly stable gold colloidal solution in organic phase, a plethora of ligands and solvent mixtures were explored. The spectrum of solvent engaged comprises chloroform, dichloromethane, tetrahydrofuran (THF), a mixture of dimethylformamide (DMF) and THF (3:1) and ethylacetate (EtAc). The stuff of employed ligands consists of dodecanethiol (DDT), mercaptoundecanoic acid (MUA), carboxyl-terminated lipids, oleic acid (OA), thiol-terminated poly(lactic-co-glycolic acid (PLGA-SH) and thiol-terminated poly(lactic) acid (PLA-SH).

High molecular weight thiol-terminated poly(ethylene) glycol

(a) The phase transfer strategy made use of thiol-terminated polyethylene glycol (PEG-SH) and a drop of hydrochloric acid (HCl 37 %) to favour the phase transfer, *plus* the ligand (pure or in a mixture). Briefly, GNRs were centrifuged twice (7600 rcf, 20 minutes, RT) to remove the CTAB excess and resuspend in MQ water. 315, 473, 630 and 945 molecules of PEG-SH (MW 5k Da) - correspondent to 3, 6, 8, 10 and 16 μl of PEG-SH aqueous solution (2.58×10^{-7} M) - per GNRs, were added to CTAB@GNRs (2 ml, $\text{Abs}_{400} = 0.5$) under mild stirring (300 rpm, 15 minutes, RT). Then, DDT in chloroform (84, 770 and 1540 μl of 5 mM) was added to the solution under mild stirring (300 rpm, 30 minutes, RT). The amount of DDT ligand per NPs surface unit corresponds to 2487, 22800 and 45600, respectively. Finally, 20 μl of HCl (37 %) were added to the mixture. After 15 minutes NPs pass to organic phase: the upper aqueous phase (colourless) was eliminated while gold nanorods in organic phase were recollected. GNRs-DDT were centrifuged twice and resuspended in chloroform to eliminate unreacted molecules. UV-visible analysis monitored NP stability in time.

(b) The same protocol was adopted for the phase transfer in dichloromethane and ethylacetate. DDT was dissolved in dichloromethane or AcOEt to the final concentration of 5 mM prior to use.

(c) In the case of DDT-GNRs in chlorinated solvents (chloroform and dichloromethane), a next transfer to ethylacetate or THF was performed. Briefly, while evaporating CHCl_3 under N_2 flow, AcOEt or THF was dropping into the solution until the complete removal of the chlorinated solvent.

Low molecular weight thiol-terminated poly(ethylene) glycol

(a) The same experimental conditions were reiterated for low molecular weight thiol-terminated PEG (MW. 750 g mol^{-1}). GNRs were redispersed in MQ water. 946, 2838 and 8514 molecules of

PEG-SH (MW 750 g mol⁻¹) per GNRs of PEG-SH (16, 48 and 144 μl respectively, 0.1 mM) were added to CTAB@GNRs aqueous solution (2 ml, Abs₄₀₀ = 0.5) under mild stirring. The ligand addition follows the protocol previously described.

(b) Many others thiol-terminated ligands are explored for GNRs phase transfer such as 11-mercaptoundecanoic acid (MUA) and mercapto undecanoic alcohol (UA, from Marzan's laboratory, Donostia, Spain), both dissolved in CHCl₃ or AcOEt. Briefly, 48 μl of PEG-SH (MW 750 g mol⁻¹, 0.1 mM) were added to CTAB@GNRs aqueous solution (2 ml, Abs₄₀₀ = 0.5) under mild stirring (300 rpm, 30 min, RT) at PEG-SH molecules per GNRs of 946, 2838 and 8514, respectively. Next, 7600, 22800, 11400 MUA and UA molecules per GNRs were added.

Many of the tested conditions are reported in Table 4.1, paragraph 4.

(c) The same procedure was adopted with the PLGA-SH ligand. To prepare PLGA-SH stabilizing GNRs, 80 μl of PEG-SH in chloroform (0.1 mM, 750 Da) were added to CTAB-GNRs (2 ml, Abs₄₀₀ = 0.5). Then, 350 μl of PLGA-SH (700 μg, 2 mg ml⁻¹) were added to the mixture to transfer GNRs to organic *medium*. Solution was dried and re-suspended in hexane or CHCl₃. The HS-PLGA-GNRs transfer to THF / DMF (3 : 1) mixture was also conducted.

(d) The same procedure for PEGylated HS-PLGA-GNRs was repeated with thiol-terminated polylactic acid (PLA-SH) in the same amount of polymer per particle volume (2 ml).

All protocols described for GNRs are also explored for spherical gold nanoparticles transfer to organic solvent.

(e) The last attempt to particle phase transfer involved the use of oleic acid as a surface ligand, even if its carboxyl-terminal group has less affinity that thiol group to gold atom. Oleic acid (20 μl, 17.8 mg, density 0.89 g ml⁻¹) was added to DDT-AuNPs (473 N_{PEG}/N_{NPs}, 22800 N_{DDT}/N_{NPs}) in chloroform and left under stirring (400 rpm, 12 h) at RT to form oleic acid stabilized AuNPs (OA-GNPs and GNRs). A next centrifugation at 1500 rcf caused the collapse of OA-GNRs, but not of OA-GNPs. Hence, dialysis in membrane with 50k Da cut-off (Spectrum Labb. Com) in MQ water (12 h) was selected as alternative method for nanoparticles purification.

3.4.2. Monophasic Phase Transfer Method

1 mg of gold nanoparticles different in morphology and dimensions (GNPs, GNRs, GNCs) were concentrated in the smallest as possible water volume (less than 25 μl) by centrifuging at 7600 rcf for 20 minutes at RT. One and two centrifugations were required for GNRs and GNPs, respectively, to remove the high excess CTAB on citrate from AuNPs surface. Afterwards, gold particles were added slowly drop by drop to 1 ml of thiol-terminated poly(lactic-co-glycolic acid) (PLGA-SH) or poly(lactide acid) solution (6 mg, 6 mg ml^{-1}) in the mixture of water miscible solvents DMF/THF (1 : 3) under sonication (1 h) in ice-bath. Samples were further stirred in an orbital shaker (ThermoFisher) at 60 rcf, overnight. Finally, the NPs were twice centrifuged (7600 rcf, 20 minutes, 4 $^{\circ}\text{C}$) and redispersed in chloroform.

A note of attention should be paid on the phase transfer of gold nanocubes, which exhibited a lower stability in chloroform compared to the other gold treated particles. In order to prevent the precipitation of the nanocubes in a chlorinated solvent, a resuspension after the first centrifugation in the minimum possible volume of the solvent mixture (DMF/THF) was necessary (< 50 μl); then the colloidal solution was brought to the final volume (1 ml) with chloroform.

3.5. Synthesis of Polypoly(D,L-lactide-co-glycolide) Nanoparticles

In order to obtain polypoly(D,L-lactide-co-glycolide) nanoparticles with optimal in size and dispersity, PLGA polymers different for molecular weight (from 7000 to 54000 g mol^{-1}) and terminal group (methyl and carboxylic acid groups) were tested. Moreover, two different surfactants were experienced: poly(vinyl alcohol) (PVA, MW 9000-19000 g mol^{-1}) and PLURONIC F127 (or Poloxamer 407). Poly(vinyl alcohol) (PVA) is a water-soluble polymer with several hydroxyl groups that strongly influence PVA properties; hydrogen bonds by PVA are responsible for high water solubility, wide range of crystallinity, and high crystal modulus.¹⁷ PLURONIC F127 is a hydrophilic non-ionic surfactant. It is a triblock linear copolymer consisting of a central hydrophobic and poly(propylene oxide) (PPO) blocks (about 30 % units) flanked by two hydrophilic blocks of poly(ethylene oxide) (PEO) blocks (about 70 % units). PLURONIC is widely used in industry such as detergents, dispersants, stabilizers, foaming agents and emulsifiers. Pharmaceutical formulations based on PLURONIC F127 presents an excellent potential as drug delivery systems as results in increased circulation time and improves metabolic stability of the drug because the outer hydrophilic PEO chains of Pluronic acts as a protection from external conditions. PLURONIC F127

is less toxic than PVA polymer, but the last one is preferred because it gives more stable and smaller PLGA particles.

3.5.1. Synthesis of Poly(D,L-lactide-co-glycolide) Nanoparticles by Single Emulsion Method

Acid-terminated polypoly(D,L-lactide-co-glycolide) nanoparticles (PLGA NPs) were synthesized by the single emulsion solvent evaporation method (Fig. 3.4).¹⁹ Briefly, 12.5 mg of acid terminated PLGA 50:50 (MW 7000 – 170000 g mol⁻¹, or 24000-38000 g mol⁻¹, or 38000 – 54000 g mol⁻¹) were dissolved in 1 ml of organic solvent (chloroform, THF, acetone). The organic phase was added to 40 ml of a poly(vinyl alcohol) aqueous solution (2 % w/w) or PLURONIC F127 (7 % w/w). The two phases form an emulsion under tip-ultrasonication (Branson, Digital Sonifier) at 40 % of amplitude for 30 seconds (twice) in ice-bath. The emulsion was stirred (4 h) to evaporate completely the organic solvent. The sample was three-time centrifuged at 14000 rcf for 15 minutes at 4°C (Scanspeed 173OR, Labogene) and the pellet was re-dispersed in PVA (0.3 %) or PLURONIC F127 (0.5 %) solution. Finally, the sample was freeze-dried (Christ, alpha 1-2 LD) and stored at -20 °C.

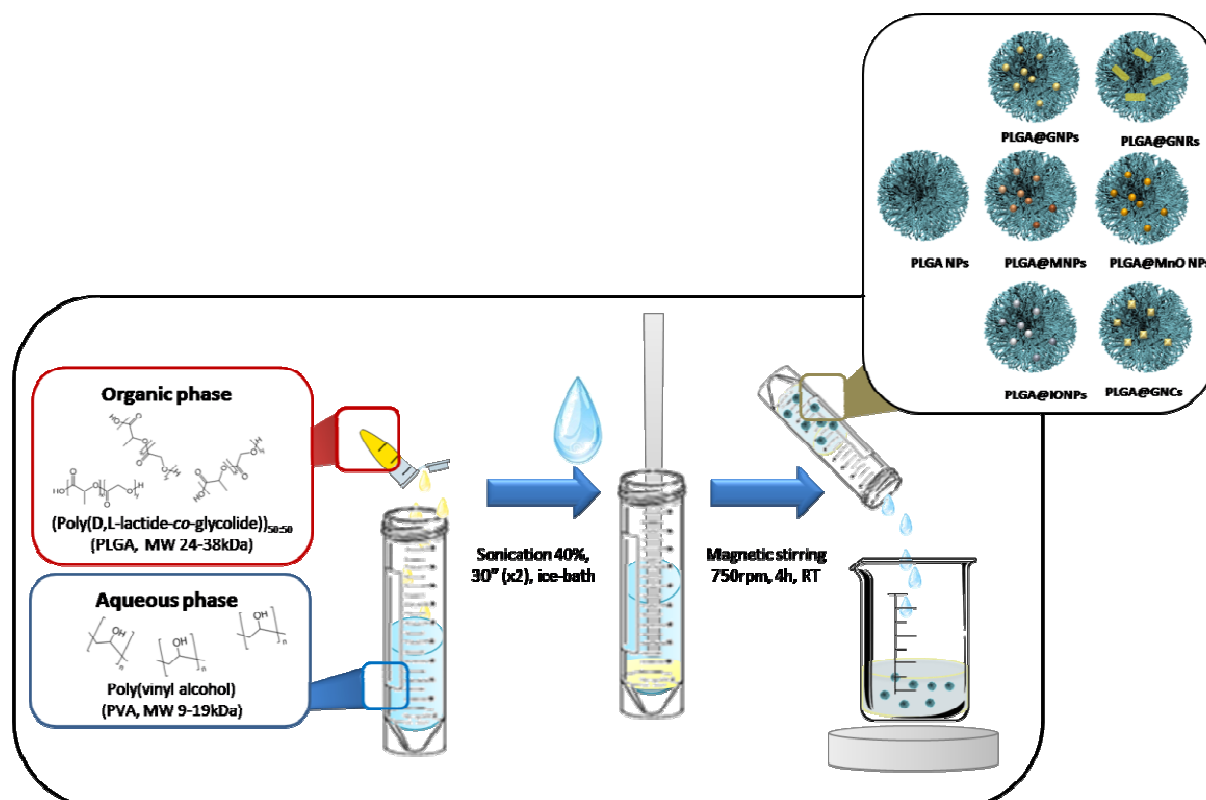


Figure 3.4. Depicted of synthesis of poly(D,L-lactide-*co*-glycolide) nanoparticles entrapping GNPs, GNRs, GNCs, MnO NPs, IONPs (PLGA@metal NPs).

3.5.2. Synthesis of Spherical Gold Nanoparticles Incorporated Polypoly(D,L-lactide-co-glycolide) Nanoparticles

Acid-terminated poly(D,L-lactide-co-glycolide) (MW 24000-38000 g mol⁻¹) nanoparticles containing MnO NPs (PLGA@MnO NPs) were prepared as described above (Par. 2.4). The entrapment of inorganic NPs (Fig. 3.4) in PLGA NPs was obtained by added 1 ml of particles (2 mg of GNP, GNRs and GNCs, 8 mg of MnO NPs and IONPs, 0.6 μmol of QDs) in CHCl₃ to the polymeric organic solution. The QDs entrapped were ellipsoidal Cd/Se quantum dots (6 nm X 12 nm).²² Also after the synthesis, samples were three-time centrifuged at 14000 rcf for 15 minutes at 4 °C (x 3) (Scanspeed 173OR, Labogene) and pellets were resuspended in PVA (0.3 %) or PLURONIC F127 (7 %) aqueous solution. Finally the sample was freeze-dried (Christ, alpha 1-2 LD).

4. Nanoparticles Characterization

4.1.1. Stability in Organic Solvent

To attest the stability of plasmonic gold nanoparticles after the phase transfer to organic solvent, UV-visible *spectra* were recorded by NanoDrop2000c spectrophotometer (Thermo Scientific) in cuvettes with 1 cm optical pathway.

4.1.2. Dynamic Light Scattering and ζ-Potential Analysis

In order to characterize the hydrodynamic radius, the size distribution of the nanoparticles as well as their dimensional evolution in suspension, Dynamic Light Scattering (DLS) was turned out to be a good method as discussed in chapter II, paragraph 4. ζ-potential values were automatically calculated from electrophoretic mobility using Zetasizer Software (Malvern Instruments Ltd., Malvern, UK). The dielectric constants 78.5 and 0.100 were used for water and chloroform, respectively, and the Henry function of 1.5 were used for the calculations.

The same sample (500 μl, 50 μg ml⁻¹) of PLGA NPs and PLGA loaded NPs were analyzed by DLS and ζ-potential. The mean value of ten measurements give one record. All measurements were performed in triplicate, and the average values were calculated.

4.1.3. Inductive Coupled Plasma Analysis

Samples for ICP analysis were prepared as described in chapter II, paragraph 4.

4.1.4. Transmission Electron Microscopy and Scanning Electron Microscopy

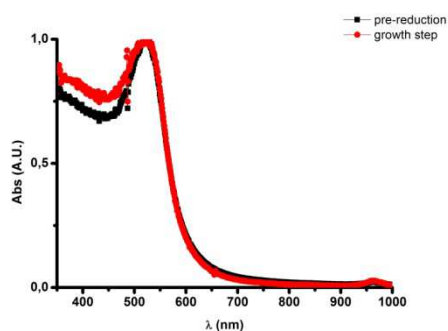
Poly(lactide-*co*-glycolide) nanoparticles morphology and dimension were investigated by transmission electron microscopy (FEI 120kV Tecnai G2 Spirit BioTWIN) and digital images were obtained by a CCD Camera System and Leo Image software. Samples were prepared as described in chapter II, paragraph 4. The specimen on the copper grid was negatively stained with uranyl acetate (2 % w/w).

5. Result and discussion

5.1. Gold Nanoparticles Kinetic Reaction

Spherical Gold Nanoparticles

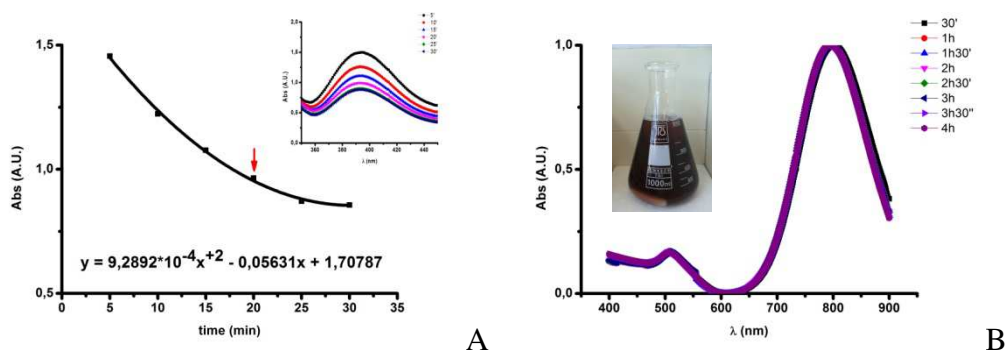
In order to obtain 30 nm-sized GNPs, the reaction was stopped at LSPR 525 nm (Grf. 4.1).



Graph 4.1. Kinetic optical study of gold nanoparticles synthesis. Position of the longitudinal LSPR band of GNPs (A) in the pre-reduction step at 90 °C and (B) in the growth solution at 90 °C.

Rod-Shape Gold Nanoparticles

In order to obtain GNRs with the longitudinal plasmon band around 800 nm, Au⁺³ absorbance at 400 nm in the pre-reduction step could reach a value between 0.80 and 0.85 (Grf. 4.2 A). At that time, reducing agent and seed solution were added to the growth solution. The following shift and the absorbance increase of the plasmon band were monitored until 4 h. The LPR band reaches its constant value after 1 h (Grf. 4.2 B). After 1 h, the absorbance at 400 nm was low. This means that there were Au⁺¹ ions left in solution that could be reduced over time even in the absence of AA molecules onto the NP surface and change the particle AR and monodispersity. To avoid this phenomenon, GNRs were centrifuged (7600 rcf, 20 min) within 24 h after the growth had started.



Graph 4.2. Kinetic optical study of gold nanorod synthesis. (A) Position of the longitudinal LSPR band as a function of time. Red row at the absorbance of 0.8. (*inset*: UV-vis spectra of seed in solution in time at 25 °C); (B) UV-vis spectra of growing single-crystal GNRs in solution at 25 °C.

5.2. Gold Nanoparticles Phase Transfer to Organic Solvent

In order to overcome the limitation of the ligand exchange mechanism to transfer efficiently AuNPs to organic solvent, it has been necessary to work concurrently on two fronts: to formulate reproducible and homogeneous gold nanorods from different batches to have equivalent surface active sites, and to set up a universal protocol from whatever nanoparticle shape and dimension.

In order to transfer GNPs to organic phase, removal of excess citrate in solution was profitable: a great excess of stabilizing agent could reduce the ligand replacement by competitive reaction onto particles surface. On the purpose to transfer GNRs from aqueous solution to organic solvent the removal of the CTAB excess was very important. As a matter of fact, CTAB could interact with ligands in solution generating micelles and subtract the incoming stabilizing molecules to the gold particle anchoring, and hence destabilize GNRs. As a consequence, aggregation of gold particles in solution was detected by a color changing from brilliant red to violet/black corresponding to an absorbance decrease and a wavelength shift of the LPR band. The total particle degradation derives from the Au^0 oxidation to Au^+ . Consequently, the gold solution appears uncolored and no plasmon band was detected.

If centrifugation was considerably important to remove the excess citrate and CTAB, to centrifuge too many times caused the NPs collapse: the lack of surfactant molecules onto particles surface destabilized the colloidal solution. As a consequence the cleaning procedure was of crucial significance to prevent NPs aggregation or degradation during phase transfer. Optimum results were obtained for twice-centrifuged GNRs and for one-centrifuged GNPs at 7500 rcf for 20 minutes at RT. In addition, high concentrated GNRs after centrifugation (≥ 2) lost stability in time and may aggregate in water. On the contrary, centrifuged GNPs were stable even at a very high concentration

Due to the high surface area to volume ratio and the high curvature of small nanoparticles, the number of ligands required is quite large and comparable with the number of *core* atoms. Moreover, the protecting ligands were exposed to solvents and external reagents and could determine the physical-chemical properties of the inorganic particle. For this reason to find the suitable ligand to

transfer AuNPs to organic phase for the following entrapment in PLGA matrix is of primary importance.

Aqueous-based GNPs are dominant, however, GNPs stable in organic solvents are required for many applications.³ Due to the major difficulty to prepare AuNPs with a range of sizes in organic solvents two approaches to transfer further nanoparticles in organic solvents were discussed: (1) phase transfer of GNPs from aqueous media to organic solvents across the liquid–liquid interface; (2) ligand exchange with hydrophobic molecules in one phase.

The results of the transfer phase by (1) biphasic and (2) monophasic methods were argued below.

5.2.1. Biphasic Phase Transfer Method

In order to load gold nanoparticles into PLGA NPs many efforts were made to have NPs stable in organic solvent. A lot of parameters have to be taken into account to transfer efficiently gold nanoparticles, such as the amount of ligand molecules per particles, the volume ratio between aqueous and organic phases, and the nature of the molecules involved, and nanoparticles shape and dimension.

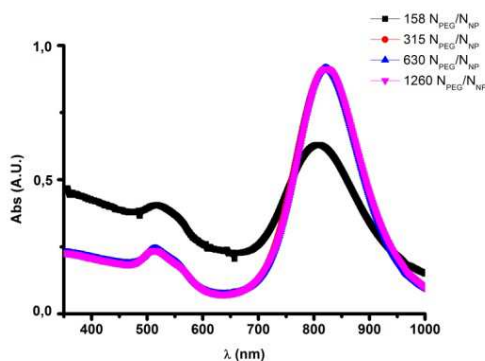
The first method to transfer gold nanoparticles to organic *medium* based on ligand exchange mechanism, reported a net phase transfer of NPs from aqueous to organic solvent. The process was visible naked-eye.

Table 4.1 summarizes all the experimental conditions to transfer gold nanoparticles, both sphere and rods, to organic phase. A great variety of ligands were explored and different solvent mixtures were experienced to obtain highly stable colloidal organic sol.

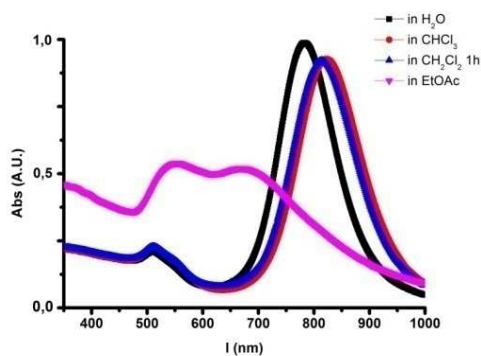
(b) The transfer of GNRs in ethylacetate and THF failed: the colloidal sol turned immediately from red into purple/blue and then into transparent indicating first aggregation and then the oxidation of GNRs. Also, gold nanorods were instable in a mixture of these solvents with chloroform or dichloromethane (1:1). In few minutes NPs solution collapsed and the LPR bands broadened and decreased in intensity till nil absorbance at plasmon resonance wavelength (data not reported).

The following attempts were performed in chloroform and dichloromethane.

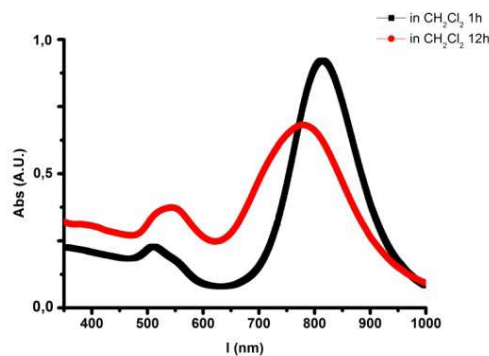
(a) GNRs phase transfer was performed adding high molecular weight PEG-SH (MW 5000 g mol⁻¹) and DDT at different molecules ratio per particles (Tab. 2.1). UV-visible analysis in time attested the stability for GNRs transfer with more than 315 PEG molecules per particle ($\geq 6 \mu\text{l}$, 0.1 mM, Grf. 4.3). UV-visible analysis in time attested the minor stability for GNRs transfer with 2487 DDT molecules per particle (data not reported). The transfer occurred efficiently with 473 - 945 $N_{\text{PEG}}/N_{\text{NPs}}$ and 22800 – 45600 $N_{\text{DDT}}/N_{\text{NPs}}$: the plasmon bands of gold nanorods shifted from 783 nm to longer wavelength (821 nm) maintaining its profile (Grf. 4.4 A and Fig. 4.4 A).



Graph 4.3. UV-vis spectra of gold nanorods transfer to organic phase with different amount of PEG-SH 0.1 mM: 3, 6, 10, 16 μl correspondent to 158, 3115, 630, 1280 PEG molecules per particles.



A



B

Graph 4.4. UV-vis spectra of gold nanorods (A) in water and transfer to organic solvent (CHCl_3 , CH_2Cl_2 and EtOAc); (B) in dichloromethane after 1 h and 12h.

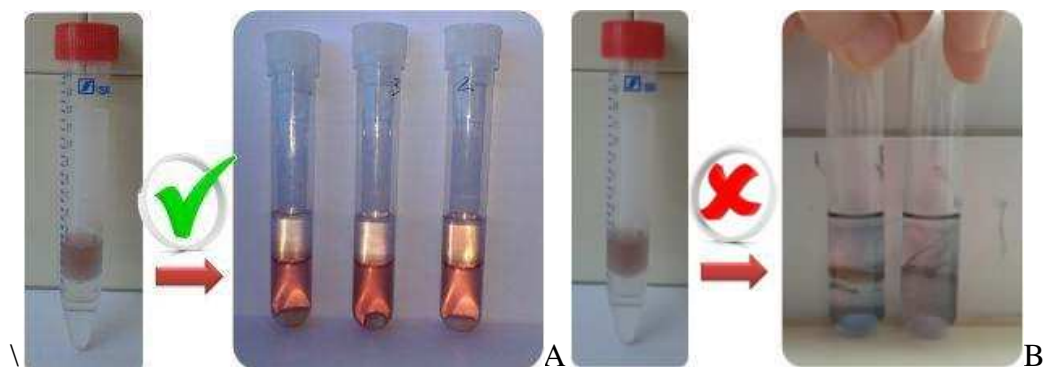
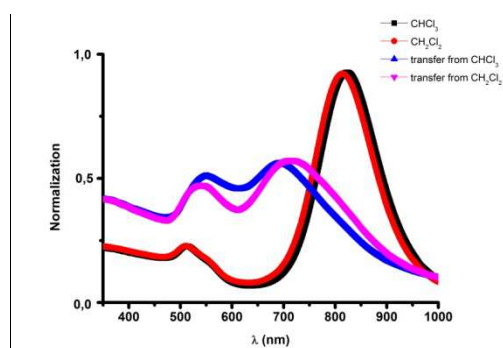


Figure 4.1. Gold nanorods ligand exchange with thiol-terminated PEG (MW. 5k Da) and DDT transfer to (A) chloroform and (B) ethylacetate.

A slightly aggregation of GNRs transfer to dichloromethane is detectable within 12 h. (Grf. 4.4 B).

(c) In the case of DDT-GNR in DCM and CHCl_3 , particles were next transferred from chlorinated solvents to AcOEt. GNRs immediately collapsed and the plasmon bands appear shifted and partially overlapped (Grf. 4.5). A further redispersion in chlorinated solvent restores the stability.



Graph 4.5. DDT-GNRs transfer from CHCl_3 or DCM to AcOEt UV-vis spectra.

The method discussed above is a simple and efficient protocol to transfer AuNPs from water to organic solvent by using thiolated ligands: PEG-SH as a phase transfer agent, and DDT as supplementary stabilizer. The NPs stability in organic solvent exhibited the typical red colored of gold colloidal solution (Fig. 4.1 A), and the corresponding UV-vis *spectrum* indicated no nanoparticle aggregation (Grf.4.3 A and 4.4). Data showed a LSP band red-shift without significant broadening for both GNPs and GNRs, in agreement with the LSPR dependence on the refractive index of the medium. The remarkable ability of PEG-SH molecules to transfer gold NPs from water

to chloroform relies on the unique hydrophilic–hydrophobic character of PEG molecules: since PEG is soluble in both water and chloroform, it was hypothesized well solvated PEG molecules maintain thiol group availability to replace the lid onto particles surface in both water and chloroform, thus resulting in a fast capping and avoiding NPs aggregation and assembly at the liquid-liquid interface.

Interestingly, it was noted gold NPs transferred spontaneously and completely to dichloromethane (DCM) or chloroform, but no phase transfer was observed into hexane or toluene (data not reported), where PEG has poor interaction and low solubility. In addition to acting as a phase transfer agent, PEG-SH is a known capping agent to stabilize nanoparticles in aqueous and organic media resulting in remarkable stability of GNPs during the phase transfer process and in the organic layer.

For free PEG molecules in water, it has been reported that the entropy enhancement of PEG molecules in CHCl_3 is the driving force of the phase transfer to chlorinated solvent; indeed, the phase transfer of PEG from water to CHCl_3 is an endothermic process because the bound with water is energetically favored than that in CHCl_3 .³⁷ However, PEG molecules on AuNPs may behave differently than free PEG molecules in solution, and thus the entropy gained is not enough to drive efficiently the phase transfer. Therefore, another hypothesis suggests PEG molecules partition into the aqueous phase with spontaneous assembly at the surface of nanoparticles in water. Addition of common solvents to PEG-AuNPs in water disrupts the hydrogen bonds between PEG molecules and water and thus decreases the energy barrier related to solvation in water. A significant decrease in the solvation energy barrier couple to entropy gain in CHCl_3 drives the transfer of GNPs from water to CHCl_3 .³⁸ DDT molecules gave their contribution as stabilization enhancer once the particles have been transferred.. DDT thiol-terminal group anchored gold surface while the hydrophobic chain was exposed to the non-polar solvent, and hence favored the dispersion of DDT-AuNPs. The detailed mechanism of the phase transfer of AuNPs from water to CHCl_3 is under investigation.

Table 4.1. List of solvents and ligand amounts used to GNRs phase transfer to organic solvent.

Solvent	PEG-SH (MW)	N _{PEG-SH} / NRs	N _{DDT} / NRs	N _{MUA} / NRs	N _{OH} / NRs	stable	Resusp. in	stable
CHCl_3		473		-	-	X		X
		630	11400	-	-	VX	AcOEt	X
		945		-	-	VX		X

	156		-	-	X	-	
	315		-	-	X	-	
	473	22800	-	-	V		X
	630		-	-	V	AcOEt	X
	945		-	-	V		X
	156		-	-	X		X
	315		-	-	V		X
	473	45600	-	-	V	AcOEt	X
	630		-	-	V		X
	945		-	-	V		X
AcOEt	630	22800	-	-	X	-	
	945		-	-	X	-	
	473		-	-	X		X
	630		-	-	VX	AcOEt	X
	945		-	-	VX		X
	156		-	-	X	-	
	315		-	-	X	-	
CH₂Cl₂	473	22800	-	-	V		X
	630		-	-	V	AcOEt	X
	945		-	-	V		X
	156		-	-	X		X
	315		-	-	V		X
	473	45600	-	-	V	AcOEt	X
	630		-	-	V		X
	945		-	-	V		X
CHCl₃	946	22800	-	-	X	-	
			-	-		CHCl ₃ : AcOEt (1:1)	X
	2838	22800	-	-	X	THF	X
			-	-		CHCl ₃ : THF (1:1)	X
	8514	22800	-	-	V		V
		45600	-	-	V	THF	V
			22800	-	NO	-	
	2838		-	22800	IP	-	
		11400	-	11400	V	AcOEt	X
			-	22800	NO		
	8514	22800	-	V		THF	V
		45600	-	V			V
	2838		22800	V		AcOEt	X
CH₂Cl₂	946	22800	-	-	X	-	
	2838	22800	-	-	X	CHCl ₃ : AcOEt (1:1)	X
			-	-		THF	X

			-	-		CHCl ₃ : THF (1:1)	X
	8514	22800	-	-	V	THF	V
		45600	-	-	V		V
		-	22800	-	NO	-	
	2838	-	-	22800	IP	-	
		11400	-	11400	V	AcOEt	X
		-	-	22800	NO		
	8514	22800	-	V		THF	V
		45600		V			V
	2838		22800	V		AcOEt	X
			22800		IP		X V
				22800	IP	THF	X
AcOEt	2838	15200		7600	IP	-	
				7600	IP	-	
		11400		11400	NO	-	
				11400	NO	-	
THF	2838		22800		1		X
				22800	1	THF	V X

V = phase transfer performed efficiently; X = phase transfer failed.

(e) The same experimental procedure employed with PEG (MW 5000 Da) was repeated with 750 Da PEG-SH. Only the conditions correspondent to 8514 $N_{\text{PEG}}/N_{\text{NPs}}$ and 22800 or 45600 $N_{\text{DDT}}/N_{\text{NPs}}$ ratios gave stable GNRs in organic solvent. Similar results were achieved in chloroform and dichloromethane.

For spherical gold nanoparticles (GNPs) phase transfer PEG and DDT employed with 473 $N_{\text{PEG}}/N_{\text{NPs}}$ and 22800 $N_{\text{DDT}}/N_{\text{NPs}}$ ratios gave stable particles in chloroform (data not shown).

Summarizing, the biphasic transfer method for PEGylated DDT-GNPs was efficient for certain ligands per particles ratio in chloroform. PEGylated DDT-GNPs were stable for about 12 h in dichloromethane, while they collapsed immediately in ethylacetate.

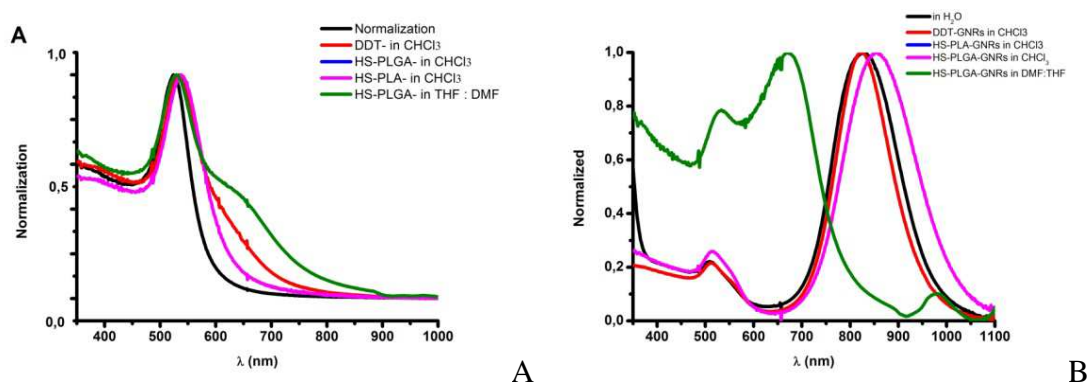
In order to find the suitable ligand to transfer AuNPs to organic phase and for the subsequently encapsulation in poly(lactic-co-glycolic acid) particles, a screening of different molecules was carried out.

(f) MUA-NPs and UA-NPs were prepared by following the protocol previously described for PEGylated DDT-NPs. Mercapto-undecanoic acid didn't allow the phase transfer and GNRs still remains stable in aqueous *medium*. Otherwise, mercapto-undecanoic alcohol favored the phase

transfer more than MUA, but not enough to allow GNRs to pass completely to the organic solvent, and GNRs massed at the interphase. An additional centrifugation step didn't contribute to the transfer outcome. Also, mixing DDT molecules with MUA or UA in presence of PEG-SH didn't improve the transfer to chloroform.

Oleic acid made GNPs able to pass to chloroform (data not shown), while GNRs still remained in aqueous *medium* even adding a great amount of OA (400 – 800 μ l, 0.75 M).

(g) PLGA-SH ligand combined with PEG-SH was then explored to transfer both spherical and rods particles. HS-PLGA-AuNPs were stable in CHCl_3 ; a following transfer to THF/DMF (3:1) mixture causes NPs aggregation (Grf. 4.6). The amount of polymer used is listed in table 4.2 and 4.3. When resuspended in CHCl_3 , HS-PLGA-GNRs show a brilliant red color. UV-vis, analysis confirms the stability of the solution in CHCl_3 (Grf. 4.6). On the contrary the particles collapsed in EtOAc and hexane (data not shown).



Graph 4.6. UV-vis spectra of (A) GNPs and (B) GNRs stabilized with various ligands and in different environments.

Table 4.2. List of ligand exchange experimental conditions for transfer GNPs to organic phase.

NPEG-SH	NPEG/NNP	PLGA-SH (ml) in CHCl_3	PLGA-SH (mg) in THF/DMF	DDT (ul)	trasfer	resuspension in	stability
21	42299	375			IP	CHCl_3	V
42	84597				IP	CHCl_3	V
84	169194				IP	CHCl_3	V
42	84597	75			IP	CHCl_3	V
21	42299	15			NO		
		0,1			NO		
9	28200	167			NO		
		83			NO		

-	-	83			HT	THF/DMF	V
		1			1	CHCl3	V
9	28200	41,5			V	CHCl3	V
	28200	11			NO	CHCl3	V
	28200	3			HT	CHCl3	V
900	2820000	41,5			NO		
-	-	-	42	42	NO		
9	28200	-			48	IP	CHCl3
-	-	-	-			NO	
-	-	-	42		V	H2O	V
		42			V	H2O	V
-	-	84	84		V	H2O	V
						NO	

Table 4.3. List of ligand exchange experimental conditions for transfer GNRs to organic phase.

VPEG-SH (ul)	N _{PEG} /N _{NP}	DDT(ul)	PLGA-SH (ul)	transfer	resuspension in	stable in CHCl3
23	6129	-	145	IP	CHCl3	
23	6129	-	203	V		V
61	15942	-	145	V		V
66	17435	-	320	V		V
-	-	-	0	V		X
47	2558	-	407	V		v
47	2558	-	407	V		V
23	1279	-	407	V		V
12	639	-	-	V		V
12	639	-	-	V		V
-	639	-	407	X		X
6	320	-	407	X		V
9	4944	24	24	V		V
9	4944	49	-	V		X
9	4944	24	24	V		V
9	4944	49	-	V		V
-	-	-	10	V	X	

This method is highly sensitive to the size and shape of anisotropic nanoparticles. The ratio between the amount of ligand molecules to NPs needs to be adjusted to have the *optimum* phase transfer. Otherwise a partial aggregation or some product damage during the phase transfer could occur (Fig. 4.2). In addition a scale up of the reaction is not achievable easily.

To overcome these limitations, an alternative phase transfer method was investigated.



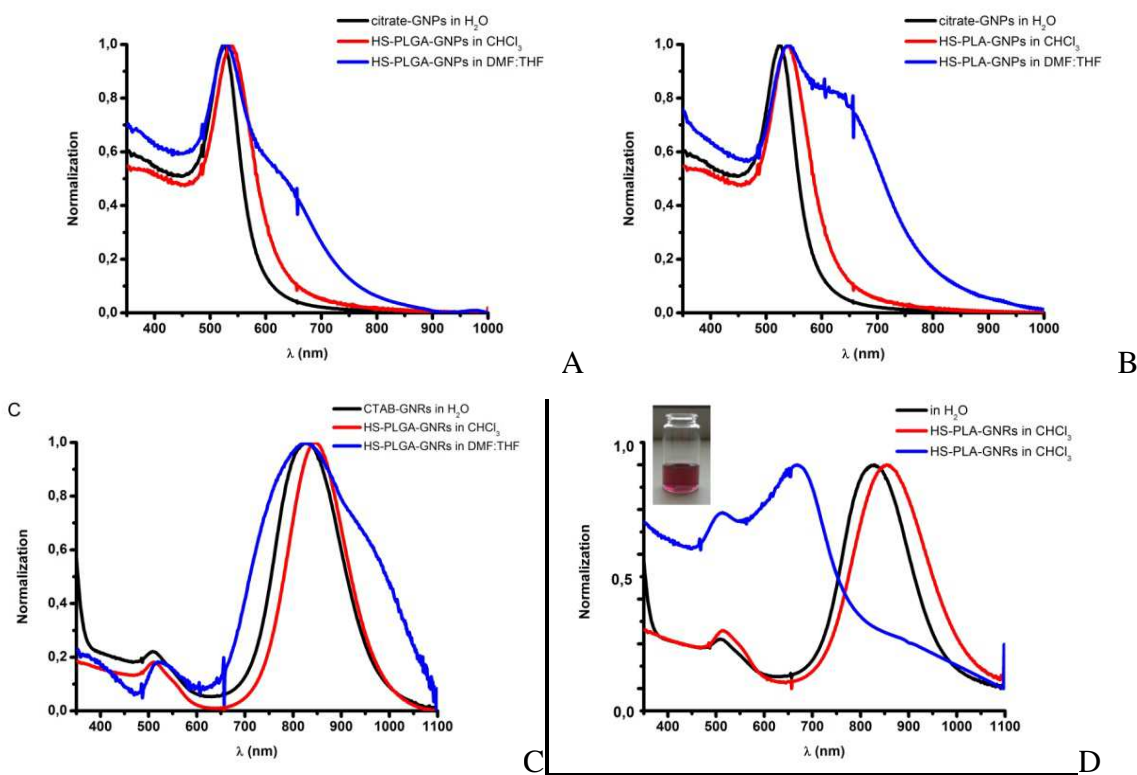
Figure 4.2. PEGylated DDT-GNRs (PEG-SH, MW. 5000 g mol⁻¹) and DDT transfer to chloroform. Some gold nanoparticles (black/purple) were lost during the phase transfer for the insufficient amount of ligands.

5.2.2. Monophasic Phase Transfer Method

Monophasic method follows a simple and highly efficient protocol to transfer AuNPs from water to organic solvent (chloroform) by means of thiol-terminated poly(lactic-co-glycolic acid) (PLGA-SH) and thiolated poly(lactic) acid (PLA-SH) as phase transfer agents.

At the same time, this procedure constituted a strategy to concentrate effectively the nanoparticles in the organic phase, enabling wider applications.

AuNPs seemed to collapse in THF/DMF (3:1) mixture as they turned deep purple, but once THF/DMF was evaporated and NPs were redispersed in chloroform, AuNPs exhibited a brilliant fuxia or bordeaux color and the correspondent UV-vis spectra indicated no particle aggregation. Moreover, the LSPR band appeared red-shifted without any significant broadening, in agreement with the LSPR band dependency on the refractive index of the *medium* (Grf. 4.7).



Graph 4.7. UV-vis spectra of GNPs and GNRs functionalized with thiolated (A), (C) PLGA and (B), (D, inset: HS-PLA-GNRs transfer to chloroform by monophasic method) PLA in chloroform and DMF/THF (3:1) mixture.

5.2.3. Inorganic Nanoparticles Characterization

Transmission Electron microscopy revealed spherical 30 nm-sized citrate- and HS-PLA-GNPs with a very high monodispersity (< 0.05). GNRs dimensions were about 44 nm x 11 nm with AR of 4.0. Both spherical and rod shape particles were not aggregated.

Manganese and Iron oxide nanoparticles were roughly spherical and no aggregation was observed. The effective diameter of magnetic NPs was reported in table 4.4.

The volume per particle calculated from TEM images was 8181.2 nm³, 4875.9 nm³, 117649.3 nm³, and 477.9 nm³ for GNPs, GNRs, GNCs, and magnetic NPs respectively.

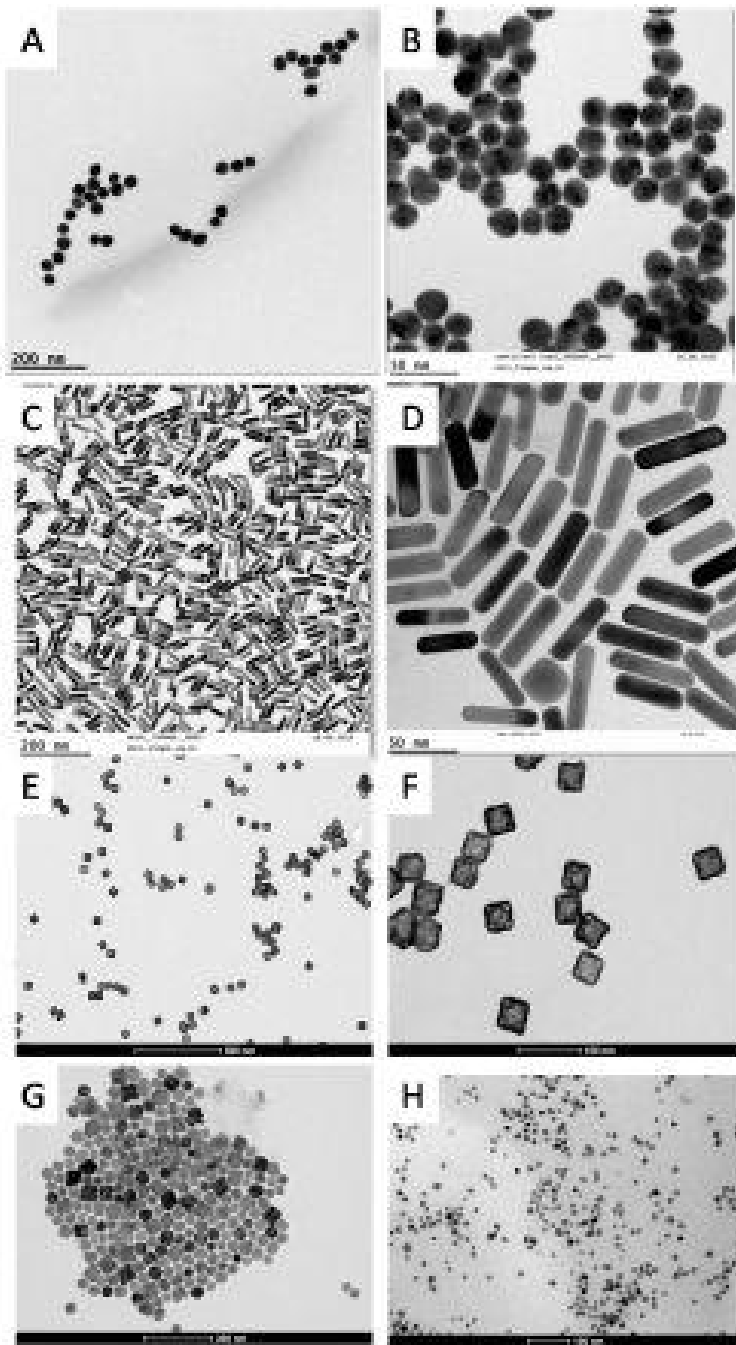


Figure 4.3. Transmission electron micrograph of (A) citrate-GNPs, (B) HS-PLA-GNPs, (C) CTAB-GNRs, (D) HS-PLA-GNPs, (E) PVP-GNCs;²³ (F) HS-PLA-GNCs; (G) IONPs, (H) MnO NPs. Scale bar (E) 500 nm; (A), (C), (G) 200 nm; (B), (D) 50 nm.

Table 4.4. Effective diameter of inorganic nanoparticles and PdI. TEM data were from analysis of 150 particles. DLS measurement were from triplicate analysis.

Particle	Mean size (nm)	Hydrodynamic diameter (nm)	PdI	ζ -potential (mV)
Citrate-GNPs	15.1 \pm 0.9	25.63 \pm 0.76	0.06 \pm 0.02	-30.4 \pm 4.1
HS-PLA-GNPs in CHCl ₃	14.6 \pm 1.2	16.9 \pm 8.5	0.392 \pm 0.153	-
CTAB-GNRs	(44.4 \pm 6.2) x (11.3 \pm 1.8)	-	-	+42.7 \pm 3.5
HS-PLA-GNRs in CHCl ₃	(44.8 \pm 7.1) x (12.5 \pm 1.4)	-	-	-
PVP-GNCs	44.2 \pm 3.1 (border: 6.9 \pm 1.3)	49.15 \pm 5.601	0.223 \pm 0.009	- 26.0 \pm 2.7
HS-PLA-GNCs in DMF/THF	40.8 \pm 5.4 (border: 6.9 \pm 1.3)	32.71 \pm 5.9	0.221 \pm 0.047	-
IONPs	9.51 \pm 0.65	37.89 \pm 0.692	0.177 \pm 0.009	-
MnO NPs	9.7 \pm 1.3	15.85 \pm 0.212	0.130 \pm 0.034	-
QDs	-	64.44 \pm 15.94	0.588 \pm 0.188	-

5.2.4. Poly(lactic-co-glycolic acid) nanoparticles characterization

In the single emulsion method, the organic solvent diffusion to the external phase produces PLGA nanoparticles. In order to optimized the poly(lactic-co-glycolic acid) nanoparticles (PLGA NPs) synthesis many parameters have been experienced and summarized in table 4.5. Sonication conditions were finally optimized at amplitude 40 % for 30 seconds (x 2) at low temperature. The nature of the organic phase plays an important role in determining the NP mean size since nanoparticles are formed by the emulsion droplets after organic solvent diffusion. NP size is dependent on the stability of the emulsion droplets, which can collide and coalesce among themselves

In order to evaluate the effect of the organic *media* on PLGA NPs formation, various solvents (AcOEt, CHCl₃, THF) were employed. AcOEt and THF are partially water-miscible and good solvents for poly(lactic-co-glycolic acid) polymer. Chlorinated solvents are immiscible with water and dissolve excellently PLGA. Highly monodispersed and small PLGA NPs were obtained for AcOEt < CHCl₃ < THF maintaining constant the other parameters. Graph 4.8 showed the size distributions of PLGA NPs prepared with different organic phases, maintaining constant all the others parameters (volume of aqueous and organic phase, volume ratio aqueous to organic phase, amount of polymer and stabilizer, sonication time and amplitude), while PVA (2 %) solution was

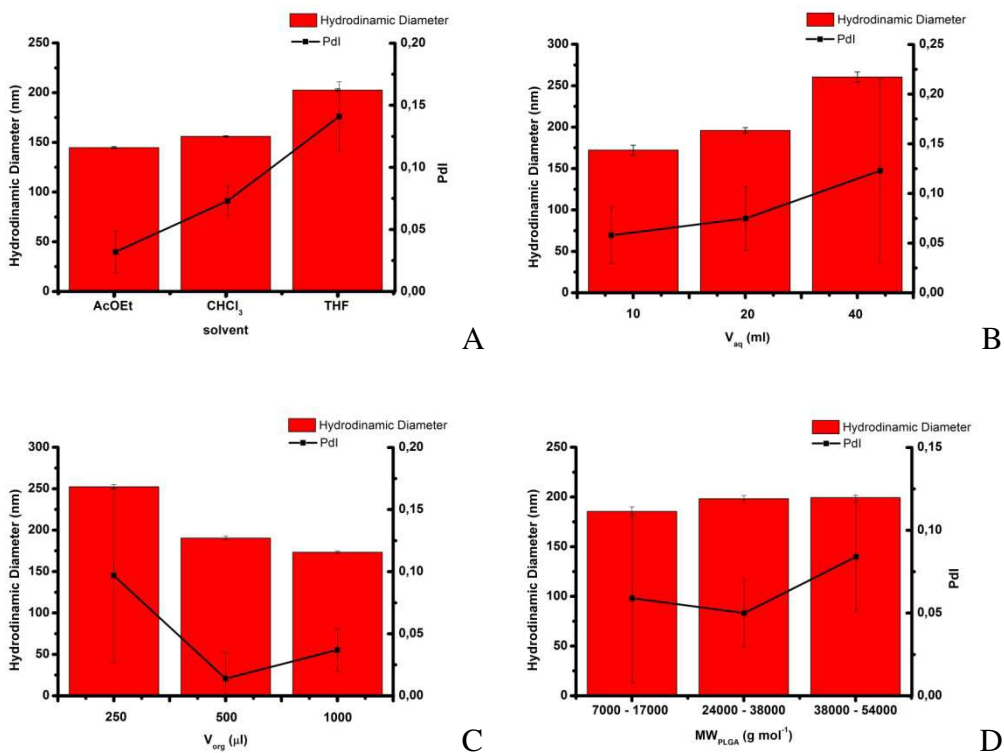
used as stabilizer (Grf. 4.8 A). The PLGA NPs obtained with EtOAc had lower polydispersity and lower diameter. Nevertheless chloroform was used to prepare PLGA NPs incorporating inorganic particles because of the highest stability of metal NPs in this solvent. Conversely, the ζ -potential was similar between PLGA NPs synthesized in these solvents.

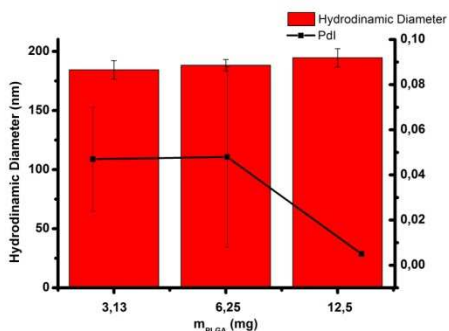
Lower the organic to aqueous phase volume ratio was - achieved by increasing the PVA volume (CHCl_3 1 ml was taken constant), or by decreasing the organic volume (PVA 2 % 40 ml constant) -, bigger the particle size was (Grf. 4.8 B and D). Pdl was very low for all the conditions tested (Table 4.5)

Finally, NP hydrodynamic diameter slightly increased with the increasing of the polymer molecular weight (Grf. 4.8 D) or with the increasing of PLGA mass added to the reaction, taking constant the other parameters (Grf. 4.8 E). All samples were highly monodispersed.

In order to decide which is the best stabilizer for PLGA NPs synthesis, many tests have been carried out in parallel with poly(vinyl alcohol) and PLURONIC F127. PVA was chosen as one of the most suitable stabilizer because it allowed the synthesis of more stable and monodispersed PLGA NPs (Table 4.6)

The scale-up of the reaction was almost efficient (data not reported).





E

Graph 4.8. The effect of (A) different organic phase solvents, (B) aqueous and (C) organic phase volume increasing; (D) polymer PLGA molecular weight increasing and (E) PLGA mass on size distributions of PLGA NPs (PVA 2 % was used as a stabilizer).

Table 4.5 List of the experimented condition for PLGA NPs synthesis.

organic solvent	PLGA (mg)	MW _{PLGA} (g mol ⁻¹)	Vorg (ml)	Vaq (ml)	Z-Average (nm)		Pdl		Z-pot (mV)	
ChCl3	6,5	24 - 38	500	20	156	0,6429	0,073	0,012	-31,9	1,18
AcOEt					154,7	1,015	0,032	0,017	-23,3	2,8
THF					202,6	1,29	0,341	0,028	-30,9	0,7
ChCl3	6,5	24 - 38	500	10	172,3	5,873	0,058	0,028	-33,5	0,351
				20	196	3,4	0,075	0,032	-33,5	0,577
				40	260,6	6,108	0,123	0,092	-32,1	1,5
ChCl3	6,5	24 - 38	250	20	252,3	2,651	0,097	0,07	-35,4	0,755
			500		190,4	2,45	0,014	0,021	-33,7	0,802
			1000		173,3	1,55	0,037	0,017	-32,3	0,462
ChCl3	6,5	lug-17	500	20	185,5	4,697	0,059	0,051	-29,3	0,1
		24 - 38			198,2	3,444	0,05	0,02	-31,2	0,635
		38 - 54			199,4	2,483	0,084	0,033	-32	1,32
CHCl3	3,3	24 - 38	250	10	179,2	2,29	0,051	0,033	-30,8	1,32
	6,4		500	20	189,6	8,671	0,049	0,021	-28,9	2,3
	12,9		1000	40	208,5	12,43	0,111	0,014	-33,2	0,3

Table 4.6. PVA and PLURONIC-stabilized PLGA NPs size dimension and polydispersity by sonication at amplitude 40 % for 30 seconds (x 2).

	Hydrodynamic diameter (nm)		Pdl	
PLURONIC F127 (7 %)	258,1	± 2,87	0,119	± 0,015

PVA (2 %)	190,4	± 2,45	0,0140	± 0,021
------------------	-------	--------	--------	---------

The materials adopted for the next PLGA NPs synthesis comprise PVA as stabilizer agent, acid terminated PLGA NPs 50:50 (MW 24000 – 38000 g mol⁻¹) to form NPs, and chloroform as organic solvent.

5.3. Inorganic Nanoparticles Entrapped in Poly(lactic-co-glycolic acid) Characterization

Inorganic nanoparticles showed their characteristic colors if entrapped even in PLGA matrix. As PLGA NPs do, PLGA@metal NPs became more and more transparent during the reaction time, as the organic solvent evaporated and the typical opalescence of the emulsion disappeared for a colloidal stable solution.



Figure 4.4. Photos of PLGA@GNPs, @GNRs, @GNCs and @MnO NPs after (A) 30 minutes and (B) 3 h after reaction has been started, respectively.

5.3.1. Particle Dimension, Size Distribution and ζ -Potential Analysis

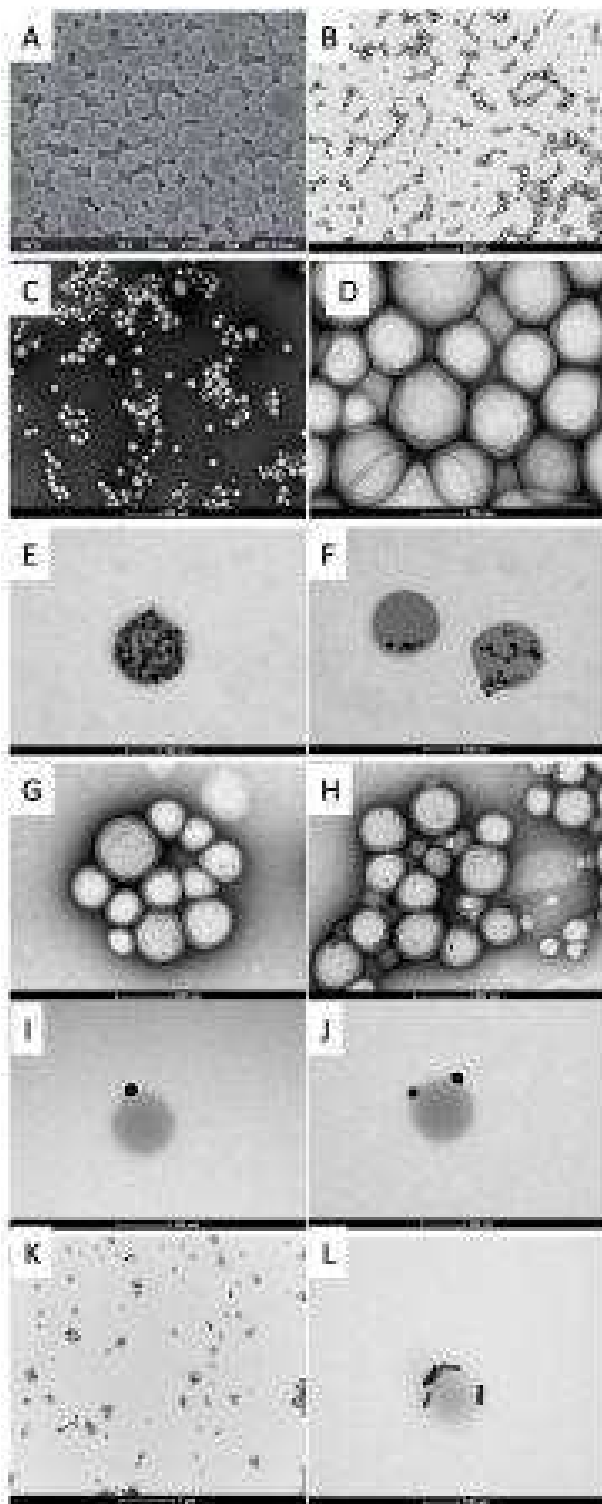
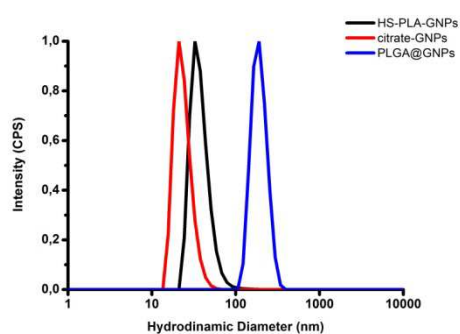


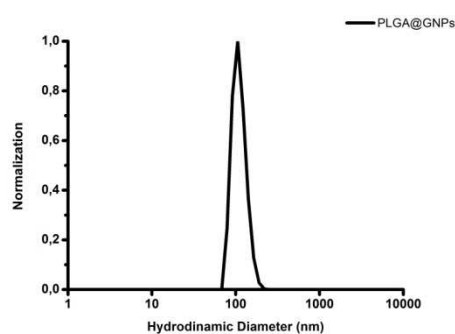
Figure 4.5. (A) Scanning and (B - H) transmission electron micrographs of PLGA@ (A), (B) IONPs; (C). (D) MnO NPs (E), (F) HS-PLA-GNPs; (G), (H) HS-PLA-GNRs. Scale bar (K) 1 μ m; (B) (C) 500 nm; (G) (H) 500 nm; (D) (E) (F) (I) (J) (L) 100 nm.

Table 4.7. Effective diameter of inorganic nanoparticles and PdI. TEM data were from analysis of 150 particles. DLS measurements were from triplicate analysis.

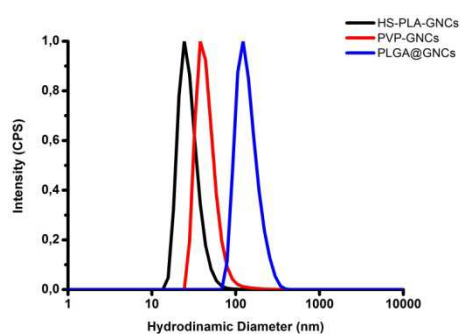
Particle	Effective diameter (nm)	Hydrodynamic diameter (nm)	PdI	ζ -potential (mV)
PLGA NPs	129.5 ± 35.1	150.5 ± 8.017	0.058 ± 0.028	-33.5 ± 0.35
PLGA@GNPs	$141.13.4 \pm 13.35$	172.8 ± 26.72	0.18 ± 0.167	-24.43 ± 0.862
PLGA@GNRs	138.9 ± 20.9	130.2 ± 15.58	0.402 ± 0.113	-16.5 ± 2.62
PLGA@GNCs	-	159.6 ± 15.25	0.183 ± 0.055	-30.3 ± 2.12
PLGA@MnO NPs	132.8 ± 41.9	163.0 ± 3.329	0.117 ± 0.013	-32.1 ± 0.99
PLGA@IONPs	150.0 ± 51.1	163.0 ± 2.411	0.028 ± 0.02	-37.5 ± 1.11
PLGA@QDs NPs	-	138.1 ± 7.26	0.079 ± 0.023	-30.1 ± 0.756



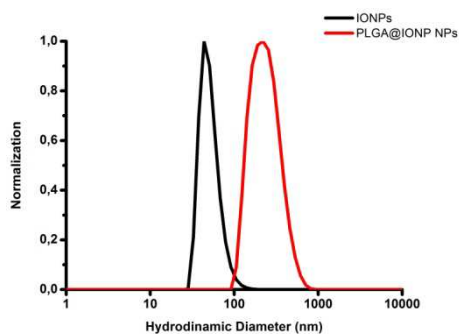
A



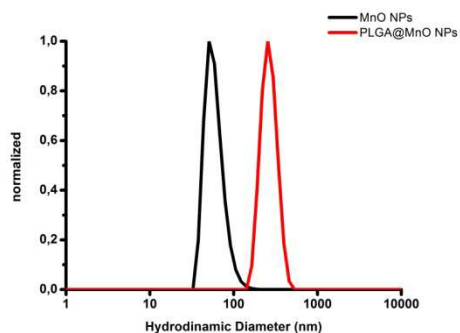
B



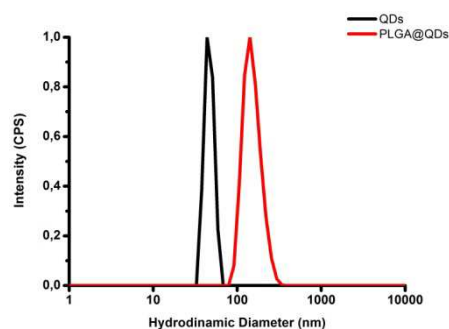
C



D



E



F

Graph 4.9. DLS micrograph of different coated (A) GNPs, (B) GNRs, (C) GNCs, (D) IONPs, (E) MnO NPs, (F) QDs.

TEM images showed PLGA NPs, both naked and entrapping inorganic structures, have a spherical shape with a diameter around 150 nm (Fig. 4.6). In addition a PVA polymeric shell from 10 to 20 nm bordered NPs.

DLS data showed the presence of inorganic particles didn't significantly affect PLGA NPs size dimensions (Grf. 4.9, Tab. 4.8). ζ -potential was still highly negative for all the samples and contributed to NP stabilization (Tab. 4.8).

6. Conclusions and Future Perspectives

Two main issues have been developed in this chapter: the phase transfer of gold nanoparticles to non-polar solvent and the loading of some metal particles onto/in PLGA NPs. General results of both the topics are reported.

Firstly, general strategies for the facile phase-transfer of water-soluble metal nanoparticles to non-polar solvent have been presented. Major efforts have been concentrated on the transfer of Au particles to chloroform as organic solvent. Thiol-terminated ligands - most successfully PEG-SH plus DDT and PLA-SH – have allowed the phase transfer of gold nanoparticles to organic medium. The choice of both the ligand molecules and the solvent was critical in performing the complete phase transfer of AuNPs without aggregation.

Two main strategies have been investigated by testing a plethora of ligands and solvents: (1) the phase transfer of AuNPs from aqueous media to organic solvents across the liquid-liquid interface (or biphasic); (2) the ligand exchange with hydrophobic molecules in water-miscible organic solvents (DF/THF = 3:1) followed by the replacement of the *medium* (monophasic method). The success of the phase transfer has been attested by UV-visible and by transmission electron microscopy analyses.

The phase transfer set up by biphasic method has a main drawback: the thiol-group amount per GNRs surface unit needs to be optimized for a variable preparation for size and shape, thus makes the application of this methods more laborious than the monophasic one. Moreover, some questions on the reproducibility of this method for anisotropic nanoparticles are still opened; indeed GNR phase transfer is highly sensitive to dimensions, AR and stirring. Finally, the scale-up of the reaction is not easy achievable. In order to overcome these limitations, the research of a more efficient phase transfer method was undertaken.

Thiol-terminated poly-lactide (PLA-SH) was the ligand selected for citrate and CTAB exchange in the monophasic method. The strategy consists of mixing a highly concentrated aqueous sol of AuNPs with an organic water-miscible solvent containing the ligand to form HS-PLA-AuNPs in a single phase. The further centrifugation allowed replacing solvent mixture with non-polar solvent. This approach was demonstrated to be highly efficient for nanoparticles of different size and shape. The resulting PLA-SH-stabilized AuNPs maintained the initial size and shape, and were highly

stable in organic solution. They could be dissolved in various organic solvents (except for ethylacetate) and readily dried, purified, and redissolved. This method could be interesting for the use of a wide range of metallic cores in organic solvents.

The second result to focus on is the general method for entrapping metal particles into poly(lactic-co-glycolic acid) matrix. In this work it has been reported an ameliorative process to incorporate thiol-PLA-coated NPs and OA-coated magnetic nanoparticles compare to those presented in literature. Some aspects are still unsolved. Sure, the encapsulation efficiency and the loading of metal particles in polymer particles could be further improved. Also a confirmation about the position of metal particles with respect to PLGA NPs is necessary to better understand the mechanisms that intervene between inorganic colloid and poly(lactic-co-glycolic acid) chains.

Indeed, to control the number of metal NPs entrapped in the polymer matrix is an interesting challenge as the internalization is predominantly controlled by hydrophobic weak interactions.

This general approach is an attractive strategy toward the fabrication of heterogeneous nanostructures based on inorganic platforms and functional cargo molecules (e.g. drugs, vaccines, nucleic acids, quantum dots, magnetic nanoparticles) located within the PLGA matrix. The hybrid prepared particles join the advantages of the biodegradability and the high biocompatibility of PLGA polymer with the unique properties of inorganic nanoparticles, to obtain potential systems for numerous biomedical applications. PLGA loading plasmonic gold particles could be employed for photothermal therapy and diagnosis; iron oxide particles entrapped in the polymer NPs could act as hyperthermic therapeutic agent or MR contrast agent; manganese oxide nanoparticle-loaded PLGA NPs are demonstrated to be high performing CA (Chapter II). All the system could incorporate also active therapeutics molecules.

Future attempts will be focused on the application of PLGA@inorganic NPs described above, by functionalizing particles with targeting moieties to even enhance their efficacy as theranostic agents.

List of Figures, Graphs and Tables

Figure 1.1. Major applications of manganese oxide, gold and iron oxide nanoparticles in biomedicine, respectively.

Figure 1.2. Main features to design promising nanoparticles for biomedicine.³

Figure 1.3. Possible mechanisms of ligand exchange reaction in nanoparticles; (A) associative, (D) dissociative and (I) interchange mechanisms

Figure 1.4. (A) Colloidal gold solutions increasing nanoparticle size; (B) typical spectra of gold spherical nanoparticles. LSPR band shift dependence on NPs size.

Figure 1.5. The extent of pre-reduction by 5-BrSA affects both the AR and the amount of reduced gold. A: Kinetic study of the pre-reduction (*inset*: full UV-vis spectra). B: UV-vis-NIR spectra of the various NR colloids obtained by changing the pre-reduction time. Abs₃₉₆: 0.88 (a); 0.71 (b); 0.64 (c); 0.53 (d); 0.33 (e); 0.22 (f). Bottom row: Representative TEM images of NRs obtained with different pre-reduction times (the labels correspond to those on the spectra in B). Scale bars: 20 nm.¹⁶

Figure 1.6. Optimization of synthesis methods achieved through careful tuning of various parameters such as reactant concentrations, which influence thermodynamic and kinetic aspects of seeded growth.¹⁷

Figure 1.7. Schematic representation of biomedical applications and potential toxicity of magnetic iron oxide nanoparticles.⁴³

Figure 1.8. Schematic representation of magnetic drug delivery system under the influence of external magnetic field. F_{mag} is direction of external magnetic field are targeted.⁵⁶

Figure 3.1. Spherical gold nanoparticles reaction scheme.

Figure 3.2. Schematic representation of the synthesis of spherical gold nanoparticles (GNPs) by seed-mediated method.

Figure 3.3. Scheme of monophasic and biphasic method for transferring gold NPs to organic phase.

Figure 3.4. Depicted of synthesis of poly(D,L-lactide-*co*-glycolide) nanoparticles entrapping GNPs, GNRs, GNCs, MnO NPs, IONPs (PLGA@metal NPs).

Figure 4.1. Gold nanorods ligand exchange with thiol-terminated PEG (MW. 5k Da) and DDT transfer to (A) chloroform and (B) ethylacetate.

Figure 4.2. PEGylated DDT-GNRs (PEG-SH, MW. 5000 g mol⁻¹) and DDT transfer to chloroform. Some gold nanoparticles (black/purple) were lost during the phase transfer for the insufficient amount of ligands.

Figure 4.3. Transmission electron micrograph of (A) citrate-GNPs, (B) HS-PLA-GNPs, (C) CTAB-GNRs, (D) HS-PLA-GNPs, (E) PVP-GNCs;²³ (F) HS-PLA-GNCs; (G) IONPs, (H) MnO NPs. Scale bar (E) 500 nm; (A), (C), (G) 200 nm; (B), (D) 50 nm.

Figure 4.4. Photos of PLGA@GNPs, @GNRs, @GNCs and @MnO NPs after (A) 30 minutes and (B) 3 h after reaction has been started, respectively.

Figure 4.5. (A) Scanning and (B - H) transmission electron micrographs of PLGA@(A), (B) IONPs; (C). (D) MnO NPs (E), (F) HS-PLA-GNPs; (G), (H) HS-PLA-GNRs. Scale bar (K) 1 μ m; (B) (C) 500 nm; (G) (H) 500 nm; (D) (E) (F) (I) (J) (L) 100 nm.

Graph 4.1. Kinetic optical study of gold nanoparticles synthesis. Position of the longitudinal LSPR band of GNPs (A) in the pre-reduction step at 90 °C and (B) in the growth solution at 90 °C.

Graph 4.2. Kinetic optical study of gold nanorod synthesis. (A) Position of the longitudinal LSPR band as a function of time. Red row at the absorbance of 0.8. (*inset*: UV-vis spectra of seed in solution in time at 25 °C); (B) UV-vis spectra of growing single-crystal GNRs in solution at 25 °C.

Graph 4.3. UV-vis spectra of gold nanorods transfer to organic phase with different amount of PEG-SH 0.1 mM: 3, 6, 10, 16 μ l correspondent to 158, 3115, 630, 1280 PEG molecules per particles.

Graph 4.4. UV-vis spectra of gold nanorods (A) in water and transfer to organic solvent (CHCl₃, CH₂Cl₂ and EtOAc); (B) in dichloromethane after 1 h and 12h.

Graph 4.5. DDT-GNRs transfer from CHCl₃ or DCM to AcOEt UV-vis spectra.

Graph 4.6. UV-vis spectra of (A) GNPs and (B) GNRs stabilized with various

Graph 4.7. UV-vis *spectra* of GNPs and GNRs functionalized with thiolated (A), (C) PLGA and (B), (D, *inset*: HS-PLA-GNRs transfer to chloroform by monophasic method) PLA in chloroform and DMF/THF (3:1) mixture.

Graph 4.8. The effect of (A) different organic phase solvents, (B) aqueous and (C) organic phase volume increasing; (D) polymer PLGA molecular weight increasing and (E) PLGA mass on size distributions of PLGA NPs (PVA 2 % was used as a stabilizer).

Graph 4.9. DLS micrograph of different coated (A) GNPs, (B) GNRs, (C) GNCs, (D) IONPs, (E) MnO NPs, (F) QDs.

ligands and in different environments.

Table 4.1. List of solvents and ligand amounts used to GNRs phase transfer to organic solvent.

Table 4.2. List of ligand exchange experimental conditions for transfer GNPs to organic phase.

Table 4.3. List of ligand exchange experimental conditions for transfer GNRs to organic phase.

Table 4.4. Effective diameter of inorganic nanoparticles and PdI. TEM data were from analysis of 150 particles. DLS measurement were from triplicate analysis.

Table 4.5 List of the experimented condition for PLGA NPs synthesis.

Table 4.6. PVA and PLURONIC-stabilized PLGA NPs size dimension and polydispersity by sonication at amplitude 40 % for 30 seconds (x 2).

Table 4.7. Effective diameter of inorganic nanoparticles and PdI. TEM data were from analysis of 150 particles. DLS measurements were from triplicate analysis.

References

1. Lee, S.-J. *et al.* Magnetic enhancement of iron oxide nanoparticles encapsulated with poly(d,l-lactide-co-glycolide). *Colloids Surf. Physicochem. Eng. Asp.* **255**, 19–25 (2005).
2. Irrera, A. *et al.* Quantum confinement and electroluminescence in ultrathin silicon nanowires fabricated by a maskless etching technique. *Nanotechnology* **23**, 75204 (2012).
3. Huang, H.-C., Barua, S., Sharma, G., Dey, S. K. & Rege, K. Inorganic nanoparticles for cancer imaging and therapy. *J. Controlled Release* **155**, 344–357 (2011).
4. Polito, L. *et al.* Resolving the Structure of Ligands Bound to the Surface of Superparamagnetic Iron Oxide Nanoparticles by High-Resolution Magic-Angle Spinning NMR Spectroscopy. *J. Am. Chem. Soc.* **130**, 12712–12724 (2008).
5. Langford, C. H. & Gray, H. B. *Ligand Substitution Processes*. (W. A. Benjamin, Inc., 1966).
6. Caragheorghopol, A. & Chechik, V. Mechanistic aspects of ligand exchange in Au nanoparticles. *Phys. Chem. Chem. Phys.* **10**, 5029–5041 (2008).
7. Daniel, M.-C. & Astruc, D. Gold nanoparticles: assembly, supramolecular chemistry, quantum-size-related properties, and applications toward biology, catalysis, and nanotechnology. *Chem. Rev.* **104**, 293–346 (2004).
8. Hutter, E. & Fendler, J. H. Exploitation of Localized Surface Plasmon Resonance. *Adv. Mater.* **16**, 1685–1706 (2004).
9. Jain, P. K., El-Sayed, I. H. & El-Sayed, M. A. Au nanoparticles target cancer. *Nano Today* **2**, 18–29 (2007).
10. Rosi, N. L. & Mirkin, C. A. Nanostructures in Biodiagnostics. *Chem. Rev.* **105**, 1547–1562 (2005).

11. Mie, G. Beiträge zur Optik trüber Medien, speziell kolloidaler Metallösungen. *Ann. Phys.* **330**, 377–445 (1908).
12. Kelly, K. L., Coronado, E., Zhao, L. L. & Schatz, G. C. The Optical Properties of Metal Nanoparticles: The Influence of Size, Shape, and Dielectric Environment. *J. Phys. Chem. B* **107**, 668–677 (2003).
13. Lee, K.-S. & El-Sayed, M. A. Gold and Silver Nanoparticles in Sensing and Imaging: Sensitivity of Plasmon Response to Size, Shape, and Metal Composition. *J. Phys. Chem. B* **110**, 19220–19225 (2006).
14. Ghosh, S. K., Nath, S., Kundu, S., Esumi, K. & Pal, T. Solvent and Ligand Effects on the Localized Surface Plasmon Resonance (LSPR) of Gold Colloids. *J. Phys. Chem. B* **108**, 13963–13971 (2004).
15. Jain, P. K., Eustis, S. & El-Sayed, M. A. Plasmon Coupling in Nanorod Assemblies: Optical Absorption, Discrete Dipole Approximation Simulation, and Exciton-Coupling Model. *J. Phys. Chem. B* **110**, 18243–18253 (2006).
16. Scarabelli, L., Grzelczak, M. & Liz-Marzán, L. M. Tuning Gold Nanorod Synthesis through Prereduction with Salicylic Acid. *Chem. Mater.* **25**, 4232–4238 (2013).
17. Scarabelli, L., Sánchez-Iglesias, A., Pérez-Juste, J. & Liz-Marzán, L. M. A ‘Tips and Tricks’ Practical Guide to the Synthesis of Gold Nanorods. *J. Phys. Chem. Lett.* **6**, 4270–4279 (2015).
18. Perezjuste, J., Pastorizasantos, I., Lizmarzan, L. & Mulvaney, P. Gold nanorods: Synthesis, characterization and applications. *Coord. Chem. Rev.* **249**, 1870–1901
19. Ward, C. J., Tronndorf, R., Eustes, A. S., Auad, M. L. & Davis, E. W. Seed-Mediated Growth of Gold Nanorods: Limits of Length to Diameter Ratio Control. *J. Nanomater.* **2014**, e765618 (2014).
20. Smith, D. K. & Korgel, B. A. The importance of the CTAB surfactant on the colloidal seed-mediated synthesis of gold nanorods. *Langmuir ACS J. Surf. Colloids* **24**, 644–649 (2008).

21. Jain, P. K., Huang, X., El-Sayed, I. H. & El-Sayed, M. A. Review of Some Interesting Surface Plasmon Resonance-enhanced Properties of Noble Metal Nanoparticles and Their Applications to Biosystems. *Plasmonics* **2**, 107–118 (2007).
22. Sperling, R. A., Gil, P. R., Zhang, F., Zanella, M. & Parak, W. J. Biological applications of gold nanoparticles. *Chem. Soc. Rev.* **37**, 1896–1908 (2008).
23. Alexis, F., Pridgen, E., Molnar, L. K. & Farokhzad, O. C. Factors Affecting the Clearance and Biodistribution of Polymeric Nanoparticles. *Mol. Pharm.* **5**, 505–515 (2008).
24. Sönnichsen, C. Drastic Reduction of Plasmon Damping in Gold Nanorods. *Phys. Rev. Lett.* **88**, (2002).
25. Myroshnychenko, V. *et al.* Modelling the optical response of gold nanoparticles. *Chem. Soc. Rev.* **37**, 1792–1805 (2008).
26. Aslan, K., Lakowicz, J. R. & Geddes, C. D. Plasmon light scattering in biology and medicine: new sensing approaches, visions and perspectives. *Curr. Opin. Chem. Biol.* **9**, 538–544 (2005).
27. Aslan, K., Lakowicz, J. R., Szmajcinski, H. & Geddes, C. D. Metal-Enhanced Fluorescence Solution-Based Sensing Platform. *J. Fluoresc.* **14**, 677–679 (2004).
28. Alvarez-Puebla, R. A. & Liz-Marzán, L. M. SERS-Based Diagnosis and Biodetection. *Small* **6**, 604–610 (2010).
29. Huang, X. & El-Sayed, M. A. Gold nanoparticles: Optical properties and implementations in cancer diagnosis and photothermal therapy. *J. Adv. Res.* **1**, 13–28 (2010).
30. Huang, X., El-Sayed, I. H., Qian, W. & El-Sayed, M. A. Cancer Cell Imaging and Photothermal Therapy in the Near-Infrared Region by Using Gold Nanorods. *J. Am. Chem. Soc.* **128**, 2115–2120 (2006).
31. Xie, J., Lee, S. & Chen, X. Nanoparticle-based theranostic agents. *Adv. Drug Deliv. Rev.* **62**, 1064–1079 (2010).

32. Laurent, S. *et al.* Magnetic Iron Oxide Nanoparticles: Synthesis, Stabilization, Vectorization, Physicochemical Characterizations, and Biological Applications. *Chem. Rev.* **108**, 2064–2110 (2008).
33. Volsi, A. L. *et al.* Inulin coated plasmonic gold nanoparticles as a tumor-selective tool for cancer therapy. *J. Mater. Chem. B* **4**, 1150–1155 (2016).
34. Ye, X. *et al.* Improved size-tunable synthesis of monodisperse gold nanorods through the use of aromatic additives. *ACS Nano* **6**, 2804–2817 (2012).
35. Bercea, M., Darie, R. N., Niță, L. E. & Morariu, S. Temperature Responsive Gels Based on Pluronic F127 and Poly(vinyl alcohol). *Ind. Eng. Chem. Res.* **50**, 4199–4206 (2011).
36. Song, C. X. *et al.* Formulation and characterization of biodegradable nanoparticles for intravascular local drug delivery. *J. Controlled Release* **43**, 197–212 (1997).
37. Alkilany, A. M., Yaseen, A. I. B., Park, J., Eller, J. R. & Murphy, C. J. Facile phase transfer of gold nanoparticles from aqueous solution to organic solvents with thiolated poly(ethylene glycol). *RSC Adv.* **4**, 52676–52679 (2014).
38. Zhang, Q., Li, W., Wen, L.-P., Chen, J. & Xia, Y. Facile Synthesis of Ag Nanocubes of 30 to 70 nm in Edge Length with CF₃COOAg as a Precursor. *Chem. Weinh. Bergstr. Ger.* **16**, 10234–10239 (2010).

List of Publications

R. Vago, V. Collico, S. Zupponea, D. Prosperi, M. Colombo, Nanoparticle-mediated delivery of suicide genes in cancer therapy, *Pharmacological Research***111** 619–641 (2006).

M. Colombo, S. Mazzucchelli, V. Collico, S. Avvakumova, L. Pandolfi, F. Corsi, F. Porta, and Davide Prosperi, Protein-Assisted One-Pot Synthesis and Biofunctionalization of Spherical Gold Nanoparticles for Selective Targeting of Cancer Cells, *Angew. Chem.***124**, 1 –5 (2012)

J. J. Plata, V. Collico, A. M. Marquez, and . Fdez. Sanz, Understanding Acetaldehyde Thermal Chemistry on the TiO₂ (110) Rutile Surface: From Adsorption to Reactivity, **J. Phys. Chem. C**, 115, 2819–2825 (2011)

G. Fumagalli, M.S. Christodoulou, B. Riva, I. Revuelta, C. Marucci, V. Collico, D. Prosperi, S. Riva, D. Perdicchia, I. Bassanini, A. García-Argáez, L. Dalla Via and D. Passarella, Self-assembled 4-(1,2-diphenylbut-1-en-1-yl) aniline based nanoparticles: podophyllotoxin and aloin as building blocks, under revision on *Organic & Biomolecular Chemistry*.

Targeting Mucosal Addressin Cell Adhesion Molecule-1 by Manganese Oxide Nanoparticles Selectively Identifies Colitis in Murine Model of Inflammatory Bowel Disease, submitted.

Magnetic Hyperthermia Mediated by Iron Oxide Nanoparticles Activates Lipolysis and Modulates Adipocyte Metabolism, M. R. Marinozzi, M. Colombo, L. Pandolfi, V. Collico, C. Lasconi, F. Boschi, M. Malatesta, S. Tambalo, A. Sbarbati, L. Calderan, and D. Prosperi, submitted.